A Lattice Boltzmann Method for the Simulation of Light Transfer in Turbid Media and its Application in Computational Studies on Microalgae Growth Kinetics

vorgelegt von

M.Sc.

Christopher Benjamin McHardy

von der Fakultät III - Prozesswissenschaften

der Technischen Universität Berlin

zur Erlangung des akademischen Grades

Doktor der Ingenieurwissenschaften

- Dr.-Ing. -

genehmigte Dissertation

Promotionsausschuss:

Vorsitzender:	Prof. Dr.-Ing. Harald Kruggel-Emden
Gutachterin:	Prof. Dr.-Ing. habil. Cornelia Rauh
Gutachter:	Prof. Dr.-Ing. habil. Kai Sundmacher
Gutachter:	Prof. Dr.-Ing. habil. Antonio Delgado

Tag der wissenschaftlichen Aussprache: 30. September 2019

Berlin 2019

Abstract

One of the major challenges in the 21st century is the exploitation of new sustainable and environmental friendly resources. It is often mentioned that the production of biomolecules from microalgae has large potential to contribute to a bio-based economy. However, to date it is still challenging to establish competitive products from microalgae. A major issue thereby is the limitation of cell growth by light, which occurs in every photobioreactor from a certain point in time. It is known that the efficiency of the light-to-biomass conversion decreases under strong illumination, but also that it increases if the illumination occurs with flashing light; a phenomenon known as flashing-light effect. Hence, researchers try to create flashing light regimes in photobioreactors - often by intensive mixing of the cell culture in order to shuttle algae cells between light and dark zones.

The objective of this work is to evaluate the interplay of light distribution, hydrodynamic mixing and cellular reaction kinetics in photobioreactors with a special focus on the flashing-light effect. Numerical simulation is a desirable tool to study complex kinetic problems with spatio-temporal dependencies for engineering purposes and will be applied in this work. Therefore, a new numerical model for the simulation of the light distribution in a photobioreactor is developed within the lattice Boltzmann framework. Subsequently, the model is combined with other sub-models for reaction kinetics and hydrodynamics to investigate the interplay of light distribution, light exposure and cell growth in a bubble column photobioreactor and to evaluate the impact of different operation conditions.

The spatio-temporal distribution of light is the key element for efficient photobiotechnological production processes. The developed lattice Boltzmann model takes absorption and three-dimensional scattering of light into account and was validated by means of Monte Carlo simulations and experiments. The results of this work demonstrate that the model is capable of simulating three-dimensional light transfer for a broad range of optically active media, although further research is needed to improve boundary conditions and to enable the simulation of light transfer in more complex geometries. Therefore, an important result of this work is that the lattice Boltzmann approach provides in principle a suitable methodological framework for three-dimensional simulations of light propagation in participating media.

Concerning the transport of light in a bubble column photobioreactor, it is shown by means of multiphysical simulations of the multiphase flow and light propagation that the presence of a gaseous phase has only a small effect on the spatial light distribution and, therefore, on the microbial growth kinetics. Thus, this factor can be neglected in light propagation models, what leads to a drastic reduction of

the computational costs. This finding is explained by the fact that the absorption of light by the cell culture is clearly the dominating feature at most wavelengths, what causes the light intensity to be low at points where gas bubbles are located so that the absolute effects of the gas phase on light distribution are weak. The results may differ from these findings for other configurations than the investigated ones, e.g. other sparger types, much higher gas superficial velocities or smaller gas bubbles. However, the general trend that an increase of the biomass concentration counteracts any beneficial effect of the gas phase on the distribution of light can also be expected in these cases.

Additional simulations of the investigated bubble column photobioreactor consider also the motion of individual algae cells and the dynamics of the photosynthetic reactions under fluctuating light exposure. For different states of operation and emission characteristics of the light source, it is shown that the shuttling of algae cell between light and dark zones of the culture is not fast enough to induce the flashing-light effect in a population of the green microalgae *C. reinhardtii*. Therefore, it is unlikely that hydrodynamic mixing is a suitable strategy to induce the flashing-light effect and to improve the productivity of photobioreactors, which is however often considered as promising in the literature. A further discussion on the topic indicates that the flashing-light effect will also be not induced by means of hydrodynamic mixing in tubular photobioreactors because shear damage of the cells and the increasing demand for mixing energy limit the reachable light/dark frequencies. In contrast, further simulations indicate that the productivity of photobioreactors can be enhanced by means of pulsed light emission even on the scale of conventional photobioreactors. Pulsed illumination can only be realized by means of artificial light sources. LED appear most promising for this purpose because they unify several beneficial operation characteristics and offer additional opportunities such as the adaption of emission spectra and intensity during cultivation processes in order to achieve tailored light regimes. Therefore, a possible future scenario could be the efficient production of metabolites with a high market value from microalgae in indoor cultivation systems with tailored light regimes under industrial conditions.

Zusammenfassung

Eine der wichtigsten Herausforderungen des 21. Jahrhunderts ist die Erschließung neuer, nachhaltiger und umweltfreundlicher Ressourcen. Der Produktion von Biomolekülen aus Mikroalgen wird in diesem Kontext ein großes Potenzial zugeschrieben, um zu einer biobasierten Wirtschaft beizutragen. Bis heute ist es jedoch schwierig, wettbewerbsfähige Produkte aus Mikroalgen zu gewinnen. Ein großes Hindernis für die Produktion von Mikroalgen ist die Limitierung des Zellwachstums durch die Verfügbarkeit von Licht, die in jedem Photobioreaktor ab einem bestimmten Zeitpunkt auftritt. Es ist bekannt, dass die Effizienz der Photosynthese und damit die der Umwandlung von Licht in Biomasse bei starker Beleuchtung abnimmt, hingegen aber ansteigt, wenn die Beleuchtung pulsierend erfolgt. Dieses Phänomen ist als Flashing-light Effekt bekannt. Um diesen Effekt zu nutzen, versuchen Wissenschaftler durch den Eintrag von Mischungsenergie Algenzellen schnell zwischen den hellen und dunklen Zonen eines Reaktors zu bewegen und dadurch definierte hell-/dunkel Regime in Photobioreaktoren zu erzeugen.

Ziel dieser Arbeit ist es, die Wechselwirkung von Lichtverteilung, hydrodynamischem Mischen und zellulärer Reaktionskinetik in Photobioreaktoren unter besonderer Berücksichtigung des Flashing-light Effekts zu untersuchen. Numerische Simulationen sind ein geeignetes Werkzeug, um komplexe kinetische Probleme unter räumlich und zeitlich veränderlichen Reaktionsbedingungen in einem ingenieur-wissenschaftlichen Kontext zu untersuchen und werden in dieser Arbeit angewendet. Hierfür wurde innerhalb des lattice Boltzmann Frameworks ein neues numerisches Modell zur Simulation der Lichtverteilung in einem Photobioreaktor entwickelt. Anschließend wurde das Modell mit weiteren Teil-modellen für Reaktionskinetik und Hydrodynamik kombiniert, um das Zusammenspiel von Lichtverteilung, Lichtexposition und Zellwachstum in einem Blasensäulen-Photobioreaktor zu untersuchen und den Einfluss verschiedener Betriebsparameter zu bewerten.

Die räumlich-zeitliche Verteilung von Licht ist das Schlüsselelement für effiziente photobiotechnologische Produktionsprozesse. Das entwickelte lattice Boltzmann Modell berücksichtigt die Absorption und dreidimensionale Streuung von Licht und wurde durch Monte Carlo Simulationen und Experimente validiert. Die vorliegende Arbeit zeigt, dass das Modell in der Lage ist, Lichtverteilungen für eine große Bandbreite optisch aktiver Medien zu simulieren, auch wenn weitere Entwicklungen erforderlich sind, um Randbedingungen zu verbessern und so die Simulation der Lichtausbreitung in komplexeren Geometrien zu ermöglichen. Ein wichtiges Ergebnis dieser Arbeit ist daher, dass der

gewählte lattice Boltzmann Ansatz grundsätzlich einen geeigneten methodischen Rahmen für Simulationen der drei-dimensionalen Lichtausbreitung in optisch aktiven Medien bietet.

Im Hinblick auf die Verteilung von Licht in Blasensäulen-Photobioreaktoren wird mittels multiphysikalischer Simulationen der Mehrphasenströmung und der Lichtausbreitung gezeigt, dass die Gasphase nur in geringem Maß die räumliche Lichtverteilung und die mikrobielle Wachstumskinetik beeinflusst. Somit kann dieser Faktor in Modellen für die Lichtausbreitung vernachlässigt werden, was zu einer drastischen Reduzierung des Rechenaufwands führt. Diese Beobachtung lässt sich dadurch begründen, dass die Absorption von Licht bei den meisten Wellenlängen eindeutig gegenüber der Lichtstreuung dominiert, wodurch niedrige Lichtintensitäten an Orten vorliegen, an denen sich Gasblasen befinden, so dass die Gasphase insgesamt nur einen geringen Einfluss auf die lokale Lichtintensität ausübt. Die Ergebnisse können für andere Begasertypen, wesentlich höhere Gasdurchsatzgeschwindigkeiten oder sehr kleine Gasblasen abweichen. Jedoch ist auch für diese Fälle der generelle Trend zu erwarten, dass die stetige Erhöhung der Biomassekonzentration einer günstigen Wirkung der Gasphase auf die Lichtverteilung entgegenwirkt.

In weiteren Simulationen des betrachteten Blasensäulen-Photobioreaktors wird zusätzlich die Bewegung einzelner Algenzellen, die damit verbundene fluktuierende Lichtexposition und deren Auswirkungen auf die Dynamik der Photosynthese berücksichtigt. Die Analyse zeigt für verschiedene Reaktorbetriebszustände und Emissionscharakteristiken der Lichtquelle, dass die Bewegung der Zellen zwischen hellen und dunklen Zonen des Reaktors nicht schnell genug erfolgt, um den Flashing-light Effekt in einer Population der grünen Mikroalge *C. reinhardtii* zu induzieren. Es ist deshalb unwahrscheinlich, dass die in der Literatur häufig vorgeschlagene Strategie durch hydrodynamisches Mischen den Flashing-light Effekt zu fördern eine signifikante Steigerung der Produktivität von Photo-bioreaktoren nach sich zieht. Eine weiterführende Diskussion des Themas deutet darauf hin, dass der Flashing-light Effekt auch nicht durch hydrodynamisches Mischen in rohrförmigen Photobioreaktoren induziert wird, da Scherbelastungen der Zellen und der zunehmende Bedarf an Mischungsenergie die erreichbaren hell-/dunkel-Frequenzen begrenzen. Ein weiteres Ergebnis der Arbeit ist, dass die Produktivität von Photobioreaktoren mittels gepulster Lichtquellen erhöht werden kann. Gepulste Beleuchtung kann nur durch künstliche Lichtquellen realisiert werden, wofür LED als beste Wahl erscheinen, da sie mehrere vorteilhafte Betriebsmerkmale vereinen und zusätzliche Möglichkeiten bieten, um maßgeschneiderte Lichtregime durch die dynamische Modulation von Emissionsspektren und der Intensität während der Zellkultivierung zu erzeugen. Ein mögliches Zukunftsszenario könnte daher die effiziente Produktion von Hochwertmetaboliten aus Mikroalgen in Indoor-Kultivierungssystemen mit maßgeschneiderten Lichtregimen unter industriellen Bedingungen umfassen.

Acknowledgment

This thesis was created between November 2013 and May 2019 as part of my work as a research associate at the Department of Food Biotechnology and Food Process Engineering of the Technical University of Berlin. During that time I received support from many people, who enabled me to complete this thesis and whom I would like to thank for their help.

First of all, I like to thank Prof. Dr.-Ing. habil. Cornelia Rauh for the possibility to work at her institute, the scientific freedom and the intellectual and financial support of my work. I also like to thank Prof. Dr.-Ing. habil. Kai Sundmacher and Prof. Dr.-Ing. habil. Antonio Delgado for their time and effort for examining my thesis as well as Prof. Dr.-Ing. Harald Kruggel-Emden for chairing the examination committee.

Especially, I like to thank Dr.-Ing. Giovanni Luzi, with whom I have had a fruitful and productive collaboration for several years and who has a significant share in the success of this work. Thank you Giovanni for your help! I also like to thank my friends and former colleagues Dr.-Ing. Alessandro Cubeddu, Dr.-Ing. Tobias Horneber and Dipl.-Ing. Matthias Schulz, who supported me in many helpful discussions, especially during the first years of my work. Thanks also to Albert Mink and Dr. Mathias J. Krause from Karlsruhe Institute of Technology, who asked the right questions and gave me thought-provoking impulses what led to further improvements of my work. Moreover, I like to thank Dr. Roland Hass, who gave me access to the laboratory at innoFSPEC / University of Potsdam as well as Dr. Marvin Münzberg, Stefanie Schönfelder, Annika Barg and Sabrina Lach for their help with the setup and conduction of experiments. A special thank also goes to all co-authors of my publications for their contribution.

Although this thesis is focused on numerical simulations, experiments are an important part of scientific work and therefore I have established cultivation methods for microalgae at the institute. This could have not been done without the help of Irene Hemmerich and Linda Krüger, who supported me a lot in this task and in the supervision of my students. Thanks a lot for your help! I also like to thank my students Justus Knappert, Suhyang Lee, Alexander Rudolph, Nicole Schröer, Jonas Hunsiker, Stephanie Haas, Christoph Gerstenberg, Deborah Becker, Byeongwoo Ko, Thierry Djike, Bastian Eysel, Milan Esser, Natascha Friese and Sophie Kieschke for their great efforts in the experimental work. Thanks also to all of my recent and former colleagues at TU Berlin for the good working atmosphere!

Finally, I like to thank you, Maike, for your love, your daily support and all the things we share together. You are the most important person in my life! Λ

Content

List of Figures

List of Tables

List of Symbols

Latin symbols

a	[-]	Scaling constant
A_a	[m^2 kg^{-1}]	Absorption cross-section
A_s	[m^2 kg^{-1}]	Scattering cross-section
A_0	[m^2]	Cross-section of photobioreactor
b	[-]	Backscattering fraction
c	[m s^{-1}]	Speed of light
c_i	[-]	Discrete lattice speed
$c_{i,max}$	[-]	Maximum discrete lattice speed
c_m	[-]	Particle mass fraction
c_s	[m s^{-1}]	Speed of sound
$\tilde{c}_s$	[-]	Lattice speed of sound
$\boldsymbol{c}_i$	[-]	Discrete lattice velocity vector
C	[-]	Courant number
C_f	[-]	Fanning friction factor
d_p	[m]	Particle diameter
d_s	[m]	Diameter of an optical fiber
D	[m^2]	Radiation diffusion coefficient
D_r	[m^2 s^{-1}]	Radial dispersion coefficient
D_x	[m^2 s^{-1}]	Axial dispersion coefficient
D_0	[m]	Diameter of photobioreactor
e	[J kg^{-1}]	Specific kinetic energy
f	[kg m^{-6} s^3]	Particle distribution function
f_i	[-]	Discrete particle distribution function
f^{eq}	[kg m^{-6} s^3]	Equilibrium distribution function
f_i^{eq}	[-]	Discrete equilibrium distribution
f^{neq}	[kg m^{-6} s^3]	Non-equilibrium part of the particle distribution function
f_t	[s^{-1}]	Characteristic frequency for turbulent mixing
$\boldsymbol{F}$	[J m^{-2} s^{-1}]	Radiation flux vector
$\boldsymbol{F}_{ex}$	[kg m s^{-2}]	External force vector
g	[-]	Asymmetry factor

$\tilde{g}$	[-]	Scaled asymmetry factor
h	[J s]	Planck constant
H_0	[m]	Height of photobioreactor
I	[μE m^{-2} s^{-1}]	Light intensity
I_s	[μE m^{-2} s^{-1}]	Saturation intensity
I_c	[μE m^{-2} s^{-1}]	Compensation intensity
I_0	[μE m^{-2} s^{-1}]	Source intensity
j_λ	[-]	Measured spectrometer counts at wavelength λ
$j_{\lambda,0}$	[-]	Noise spectrometer counts at wavelength λ
k_i	[m^{-1}]	Discrete slope coefficient in the lattice Boltzmann model
K	[μE m^{-2} s^{-1}]	Kinetic constant
l	[m]	Measuring path
l_K	[m]	Kolmogorov length scale
l_{mpf}	[m]	Mean free path
l_{tr}	[m]	Transport mean free path
l_T	[m]	Taylor length scale
L	[μE m^{-2} s^{-1} sr^{-1}]	Radiance
L_0	[m]	Macroscopic length
m	[kg]	Particle mass
n	[-]	Refractive index
$\boldsymbol{n}$	[-]	Unit vector
N	[-]	Number of nodes in numerical grid
N_{ph}	[-]	Number of photons in Monte Carlo method
p	[-]	Grid convergence order
$p_{i,j}$	[-]	Coefficient to correct scattering in Geist's model
p_l	[Pa]	Static pressure of a liquid
P	[s^{-1}]	Rate of photosynthesis
P_{max}	[s^{-1}]	Maximum rate of photosynthsis
$\boldsymbol{P}$	[J m^{-3}]	Radiation pressure tensor
q_{abs}	[μE m^{-3} s^{-1}]	Volumetric light absorption rate
$q_{abs,nd}$	[-]	Dimensionless volumetric light absorption rate
Q		Quantile
r	[-]	Grid refinement factor
R	[J kg^{-1} K^{-1}]	Fundamental gas constant
S	[μE m^{-2} s^{-2}]	Source term for local emission of radiance
$S_{k,j}$		Sensitivity of kth model output with respect to the jth model input

t	[s]	Time
t_D	[s]	Duration of the dark period
t_F	[s]	Duration of the flash period
t_K	[s]	Kolmogorov time scale
Δt	[s]	Time step
T	[K]	Absolute temperature
u	[m s^{-1}]	Macroscopic velocity
u_g	[m s^{-1}]	Gas superficial velocity
u_K	[m s^{-1}]	Eddy velocity on the Kolmogorov scale
u_0	[m s^{-1}]	Characteristic macroscopic velocity
$\boldsymbol{u}$	[m s^{-1}]	Velocity vector
V_g	[m^3]	Gas volume
V_{tot}	[m^3]	Reactor volume
V_p	[m^3]	Particle volume
$\dot{V}_g$	[m^3 s^{-1}]	Gas volume flow rate
w	[-]	Parameter of the linear scattering phase function
w_i	[-]	Quadrature weighting coefficient
W_0	[m]	Macroscopic width
x	[m]	Position coordinate
x_1	[-]	Fraction of activated photosynthetic units
x_2	[-]	Fraction of damaged photosynthetic units
x_3	[-]	Fraction of resting photosynthetic units
Δx	[m]	Grid spacing
$\boldsymbol{x}$	[m]	Position vector
$\boldsymbol{x}_B$	[m]	Boundary location vector
X	[kg m^{-3}]	Concentration of dry biomass
X_A	[kg m^{-2}]	Surface area-specific concentration of dry biomass
y	[m]	Position coordinate
y_k		kth Model output
z	[m]	Position coordinate

Greek symbols

α	[μE m^{-2}]	Kinetic constant for PSU activation
α_C	[m^{-1}]	Optical coefficient in Cornets model
α_s	[-]	Size parameter
β	[μE m^{-2}]	Kinetic constant for PSU damage

γ	[s^{-1}]	Kinetic constant for PSU relaxation
$\dot{\gamma}$	[s^{-1}]	Viscous shear rate
Γ	[-]	Degree of light integration
δ	[s^{-1}]	Kinetic constant for PSU repair
δ_C	[m^{-1}]	Optical coefficient in Cornets model
δ_0	[m]	Thickness of viscous sublayer
ϵ	[-]	Error measure
ϵ_g	[-]	Gas hold-up
ϵ_k	[J kg^{-1} s^{-1}]	Rate of turbulent kinetic energy dissipation
η_l	[Pa s]	Dynamic viscosityof a liquid
θ_j		j^{th} Model input
$\boldsymbol{\theta}_0$		Base state vector of model inputs
Θ	[rad]	Scattering angle
$\boldsymbol{\Theta}$	[-]	Update matrix in Geist's model
κ	[-]	Scaling parameter in the lattice Boltzmann model
λ	[m]	Wavelength of radiation
μ	[s^{-1}]	Specific growth rate
μ_a	[m^{-1}]	Absorption coefficient
$\tilde{\mu}_a$	[m^{-1}]	Scaled absorption coefficient
μ_s	[m^{-1}]	Scattering coefficient
$\tilde{\mu}_s$	[m^{-1}]	Scaled scattering coefficient
μ_s'	[m^{-1}]	Reduced scattering coefficient
ν	[m^2 s^{-1}]	Kinematic viscosity of fluid
ν_F	[s^{-1}]	Frequency of light pulsation
ν_l	[m^2 s^{-1}]	Kinematic viscosity of liquid
ξ_i	[m s^{-1}]	Discrete particle speed
$\boldsymbol{\xi}$	[m s^{-1}]	Particle velocity vector
$\boldsymbol{\xi}_i$	[m s^{-1}]	Discrete particle velocity vector
o	[-]	Order of derivative
ρ	[kg m^{-3}]	Mass density
ρ_l	[kg m^{-3}]	Mass density of a liquid
ρ_p	[kg m^{-3}]	Mass density of a particle
σ	[rad^{-1}]	Differential collision cross-section
Σ_R	[-]	Richardson extrapolated numerical solution
Σ_1	[-]	Numerical solution on a fine grid

Σ_2	[-]	Numerical solution on a coarse grid
τ	[s]	Characteristic time for particle collisions
$\tilde{\tau}$	[-]	Dimensionless relaxation time
τ_f	[s]	Characteristic time scale of the flow
τ_F	[-]	Duty cycle of light pulses
τ_{int}	[s]	Spectrometer integration time
τ_p	[Pa]	Viscous shear stress on particles
τ_v	[s]	Particle response time to changes in the flow
τ_w	[Pa]	Wall shear stress
τ_λ	[-]	Optical depth at wavelength λ
ϕ_{FLE}	[-]	Measure for the flashing-light effect
ϕ_{PD}	[-]	Measure for effects due to reduced photodamage
ϕ_v	[-]	Particle volume fraction
ϕ_{x_1}	[-]	Dimensionless measure for the flashing-light effect
ϕ_{12}	[-]	Measure for the numerical error between two grids 1 and 2
Φ	[-]	Scattering phase function
$\Phi_{i,j}$	[-]	Probability density for discrete scattering from $\boldsymbol{n}_j$ into $\boldsymbol{n}_i$
$\tilde{\Phi}_{i,j}$	[-]	Scaled probability density for discrete scattering from $\boldsymbol{n}_j$ into $\boldsymbol{n}_i$
Φ_{HG}	[-]	Henyey-Greenstein phase function
Φ_l	[-]	Linear phase function
$\boldsymbol{\Phi}$	[-]	Discrete scattering matrix
ω	[-]	Scattering albedo
$\tilde{\omega}$	[-]	Scaled scattering albedo
Ω_C	[kg m^{-6} s^2]	Collision operator
$\boldsymbol{\Omega}$	[sr]	Solid angle

Dimensionless numbers

C	Courant number
Eo	Eötvös number
Kn	Knudsen number
Ma	Mach number
Mo	Morton number
Re	Reynolds number
St	Stokes number
Ta	Tadaki number
We	Weber number

List of Abbreviations

ADA	Anomalous Diffraction Approximation
ADP	Adenosin Diphosphate
ATP	Adenosin Triphosphate
BE	Boltzmann equation
BGK	Bathnagar-Gross-Krook
BLE	Boltzmann-Lorentz equation
CARPT	Computer-Automated Radioactive Particle Tracking
CFD	Computational fluid dynamics
D	Dimensional
DA	Diffusion Approximation
DOM	Discrete Ordinate method
DSMC	Direct simulation by Monte Carlo
DVBE	Discrete velocity Boltzmann equation
ETC	Electron transfer chain
EUR	Euro
FLE	Flashing-light effect
G3P	Glycerinaldehyde 3-phosphate
HG	Henyey-Greenstein
IQR	Interquartile range
LBM	Lattice Boltzmann method
LED	Light emitting diode
L/D	Light/Dark
LHC	Light harvesting complex
MAPE	Mean average percentage error
MC	Monte Carlo
MCM	Monte Carlo method
MDOM	Modified discrete ordinate method
MOC	Method of Characteristics
NADPH	Nicotinamide adenine dinucleotide phosphate
NPQ	Non-photochemical quenching

ODE	Ordinary differential equation
PAR	Photosynthetically active radiation
PBR	Photobioreactor
PCE	Photon conversion efficiency
PE	Photosynthetic efficiency
3-PGA	3-Phosphoglycerate
PI	Photosynthesis-Irradiance
PS	Photosystem
PSU	Photosynthetic unit
RHS	Right-hand side
RK	Runge-Kutta
RMSE	Root mean square error
ROS	Reactive oxygen species
RTE	Radiation transfer equation
RT-LBM	Radiation transfer lattice Boltzmann method
RuBP	Ribulose-1,5-biphosphate

Publications and Contributions

Peer-reviewed articles

McHardy, C., Horneber, T., Rauh, C. (2016). New lattice Boltzmann method for the simulation of three-dimensional radiation transfer in turbid media. Optics Express, 24 (15), 16999-17017, 2016.

McHardy, C., Horneber, T., Rauh, C. (2018). Spectral Simulation of Light Propagation in Participating Media by Using a Lattice Boltzmann Method for Photons. Appl. Math. Comput. 319(15), 59-70, 2018.

McHardy, C., Luzi. G., Lindenberger, C., Agudo, J.R., Delgado, A., Rauh, C. (2018). Numerical Analysis of the Effects of Air on Light Distribution in a Bubble Column Photobioreactor. Algal Research, 31, 311-325, 2018.

McHardy, C., Becker, D., Rauh, C. (2018). Similarity of Field Quantities in Scaled Radiation Transfer Lattice Boltzmann Simulations (RT-LBM). PAMM, 18(1):e201800195, 2018.

McHardy, C., Thünnesen, J., Horneber, T., Kostova, J., Hussein, M. A., Delgado, A., Rauh, C. (2018). Active control of foams by physically based destruction mechanisms. PAMM, 18(1), e201800351, 2018.

Luzi, G., McHardy, C., Lindenberger, C., Rauh, C., Delgado, A. (2019). Comparison between different strategies for the realization of flashing-light effects - pneumatic mixing and flashing illumination. Algal Research, 38:101404, 2019.

Conference proceedings

McHardy, C., Horneber, T., Rauh, C. (2015). Lattice Boltzmann Method for the Simulation of Radiation Transport in Microalgae Biosuspensions. In: Proceedings der 23. GALA-Fachtagung Lasermethoden in der Strömungsmesstechnik, 58-1 bis 58-10, 08.-10. September 2015, Dresden. Hrsg.: Czarske, J., Büttner, L., Fischer, A., Ruck, B., Leder, A., Dopheide, D.

Luzi, G., McHardy, C., Agudo, J. R., Rauh, C., Delgado, A. (2016). Numerical simulation of fluid flow and light distribution inside bio-reactors. In: Proceedings der 24. GALA-Fachtagung Experimentelle Strömungsmechanik, 17-1 bis 17-8, 06.-08. September 2016, Cottbus. Hrsg.: Egbers, C., Ruck, B., Leder, A., Dopheide, D.

McHardy, C., Luzi, G., Agudo, J. R., Delgado, A. and Rauh, C. (2017). Hybrid Numerical Simulation of Fluid Flow and Light Distribution in a Bubble Column Photobioreactor. In: Proceedings of the 5th International Conference on Photonics, Optics and Laser Technology - Vol. 1: PHOTOPTICS, pages 304-311

Luzi, G., McHardy, C., Agudo, J. R., Delgado, A., Rauh, C. (2017). Influence of Fluid Flow and Light Distribution on Single Cells in a Bubble Column Photobioreactor. In: Proceedings of the 14th International Conference Multiphase Flow in Industrial Plant, 2017, Desenzano, Italy.

McHardy, C., Luzi, G., Agudo, J. R., Rauh, C., Delgado, A. (2017). Comparison of different models for computation of light distribution inside photobioreactors. In: Proceedings der 25. GALA-Fachtagung Experimentelle Strömungsmechanik, 28-1 bis 28-8, 05.-07. September 2017, Karlsruhe. Hrsg.: Ruck, B., Gromke,C., Leder, A., Dopheide, D.

McHardy, C., Rudolph, A., Panckow, R., Kostova, J., Wegener, M., Rauh, C. (2018). Morphologische Charakterisierung von Schäumen bei der Abfüllung nicht-karbonisierter Getränke. In Proceedings der 26. GALA-Fachtagung Experimentelle Strömungsmechanik, 46-1 bis 46-8, 05.-07. September 2018, Rostock. Hrsg.: Grundmann, S., Brede, M., Ruck, B., Leder, A., Dopheide, D.

Conference talks

McHardy, C., Rauh, C.: Application of numerical simulation techniques to design PEF processes. School on applications of Pulsed Electric Fields for food processing, 07.-12.02.2015, Fisciano (SA), Italy.

McHardy, C., Horneber, T., Rauh, C.: Lattice Boltzmann Method for the Simulation of Radiation Transport in Microalgae Biosuspensions. Fachtagung Lasermethoden in der Strömungsmesstechnik, 08.-10.09.2015, Dresden, Germany.

McHardy, C., Horneber, T., Rauh, C.: Spectral Simulation of Light Propagation in Participating Media by Using a Lattice Boltzmann Method for Photons. 5th European Seminar on Computing ESCO 2016, 06.-10.06.2016, Pilsen, Czech Republic.

Agudo, J.R., Park, J., Luzi, G., McHardy, C., Rauh, C., Delgado, A.: Experimental studies on gas hydrate formation under submarine conditions. 9th International Conference on High Pressure Bioscience and Biotechnology (HPBB 2016), 25.-29.07.2016, Toronto, Canada.

Luzi, G., McHardy, C., Agudo, J. R., Rauh, C., Delgado, A.: Numerical simulation of fluid flow and light distribution inside bio-reactors. Fachtagung Experimentelle Strömungsmechanik, 06.-08.09 2016, Cottbus, Germany.

McHardy, C., Luzi, G., Agudo, J. R., Delgado, A., Rauh, C.: Hybrid Numerical Simulation of Fluid Flow and Light Distribution in a Bubble Column Photobioreactor. 5th International Conference on Photonics, Optics and Laser Technology, 27.02-01.03. 2017, Porto, Portugal.

McHardy, C., Luzi, G., Agudo, J. R., Rauh, C., Delgado, A.: Comparison of different models for computation of light distribution inside photobioreactors. Fachtagung Experimentelle Strömungsmechanik, 05.-07.09 2017, Karlsruhe, Germany.

McHardy, C.: Mikroalgen als Rohstoff in der Lebensmittelindustrie. Kurzlehrgang Emerging und Crosslink Technologies: Unausgeschöpfte Potentiale in der Lebensmittel-, Getränke- und Biotechnologie inkl. medizinischen Biotechnologie, 20.-22.09.2017, Berlin, Germany.

McHardy, C., Thünnesen, J., Horneber, T., Kostova, J., Hussein, M. A., Delgado, A., Rauh, C.: Prognose des Schaumbildungsvermögens und forcierte Schaumzerstörung mittels akustischer Resonanzanregung in Fruchtsäften. Jahrestreffen der ProcessNet-Fachgruppe Lebensmittelverfahrenstechnik, 05.-06.03.2018, Berlin, Germany.

McHardy, C., Becker, D., Rauh, C.: Similarity of Field Quantities in Scaled Radiation Transfer Lattice Boltzmann Simulations (RT-LBM). 89th GAMM Annual Meeting, 19.-23.03.2018, Munich, Germany.

McHardy, C., Thünnesen, J., Horneber, T., Kostova, J., Hussein, M. A., Delgado, A., Rauh, C.: Active control of foams by physically based destruction mechanisms. 89th GAMM Annual Meeting, 19.-23.03.2018, Munich, Germany.

McHardy, C., Rudolph, A., Panckow, R., Kostova, J., Wegener, M., Rauh, C: Morphologische Charakterisierung von Schäumen bei der Abfüllung nicht-karbonisierter Getränke. Fachtagung Experimentelle Strömungsmechanik, 06.-08.09 2018, Rostock, Germany.

Poster contributions

McHardy, C., Horneber, T., Rauh, C.: Lattice Boltzmann Method for the Simulation of Radiation Transport in Microalgae Biosuspensions. Particle Simulations, 21.-24.09.2015, Erlangen, Germany.

McHardy, C., Horneber, T., Rauh, C.: Effects of Light Modeling on the Prediction of Microalgae Growth. 4th BioProScale Symposium, 06.-08.04.2016, Berlin, Germany.

McHardy, C., Horneber, T., Rauh, C.: Effects of Light Modeling on the Prediction of Microalgae Growth. 9th Bundesalgenstammtisch, 26.-27.09.2016, Jülich, Germany.

McHardy, C., Luzi, G., Agudo, J.R., Delgado, A., Rauh, C.: Lattice Boltzmann Simulation of Light Distribution in a Bubble Column Photobioreactor. Spring School: Lattice Boltzmann Methods, 06.-10.03.2017, Hammamet, Tunisia.

McHardy, C., Luzi, G., Agudo, J.R., Delgado, A., Rauh, C.: Lattice Boltzmann Simulation of Light Distribution in a Bubble Column Photobioreactor. 10th Bundesalgenstammtisch, 11.-12.09.2017, Merseburg, Germany.

McHardy, C., Luzi, G., Lindenberger, C., Delgado, A., Rauh, C.: Evaluating the Enhancement of Light Integration in a Bubble Column by Pneumatic Mixing. 11th Bundesalgenstammtisch, 27.-28.09.2018, Karlsruhe, Germany.

McHardy, C., Djike, T., Jänich, I., Boguslawski, S., Rauh, C.: Zellaufschluss von Chlorella vulgaris durch druckunterstützen Hochleistungsultraschall. 11th Bundesalgenstammtisch, 27.-28.09.2018, Karlsruhe, Germany.

McHardy, C., Knappert, J., Djike, T., Jänich, I., Boguslawski, S., Rauh, C.: Performance of emerging technologies for microalgae cell disruption - Pulsed Electric Fields and Ultrasound. AlgaEurope, 04.-06.12.2018, Amsterdam, The Netherlands.

McHardy, C., Rudolph, A., Horneber, T., Kostova, J., Fidos, K., Rauh, C.: Dynamics of Foam Formation during the Bottling of Non-carbonated Beverages. Jahrestreffen der ProcessNet-Fachgruppe Lebensmittelverfahrenstechnik, 04.-06.03.2019, Lausanne, Switzerland.

Part I.

Fundamentals and Theoretical Background

1. Introduction

In times of a growing world population and an increasing demand for food protein against the background of global warming and declining fossil and non-fossil raw materials, new sustainable and environmental friendly resources need to be exploited. It is often mentioned that the production of biomolecules from microalgae has large potential to contribute to a bio-based economy [1]. The driving idea of obtaining valuable biomass from sunlight and carbon dioxide appears promising and the hope is not unfounded since many studies have proven the potential of microalgae with calculations of area yields and productivities [2, 3].

Although worldwide huge effort has been spent in research and development to boost the commercial utilization of microalgae, so far it has been realized only in parts. A major reason for this is that microalgae cultivation is only cheap at first glance and significant costs result from investments, photobioreactor operation and downstream processing [4]. A good example to illustrate this is the goal of gaining biofuels from microalgal lipids. The intention becomes clear as some species are able to accumulate usable lipids up to 70% of their cell mass, which is claimed to lead to a much higher area productivity compared to common plants being utilized for biodiesel production [2, 5]. In the practical implementation however, the energy demand for cell cultivation and several required downstream processes [6] even raised concerns about the net energy gain, although it turned out to be positive under reasonable conditions [7–9]. Similarly, the large scale production of food protein must still be considered as a perspective since microalgal biomass contributes less than with 2% to the alternative protein market, though a contribution of up to 18% is predicted until 2054 [10].

To date it is still challenging to establish competitive products from microalgae. The concentration of dry biomass in phototrophic algae cultures at the production scale is typically restricted to the single digit g/L range, while concentrations two orders higher in magnitude can be reached under heterotrophic conditions [11, 12]. Also, one is usually interested in intracellular metabolites so that the cell as the target of the cultivation process must be further processed downstream in order to gain the desired products [13, 14]. In consequence of the costly production, only niche markets exist for different products such as pigments, polyunsaturated fatty acids or dried biomass. On the other hand, the favorable properties of different microalgal metabolites for neutraceutical applications, natural food additives, technofunctional ingredients or biopharmaceutical products justify the unvarying research interest [15–18].

A major challenge for a competitive production of microalgae is the limitation of cell growth by light, occurring in every photobioreactor from a certain point in time. The limitation is caused by the decay of the light intensity due to absorption by the cell culture and its resultant inhomogeneous distribution in space. The situation is even worse since a simple increase of the light energy input steepens the intensity gradient, what results in a disadvantageous light distribution and a low efficiency of light utilization [19]. The latter is reflected in the photon conversion efficiency, which relates the energy content of the biomass to the supplied light energy [20]. In typical photobioreactors values in the order of 2-3% can be achieved [21], while the theoretical maximum is in the order of 10% related to the visible part of the spectrum [20]. It is straightforward that a higher photon conversion efficiency favors the economics of the production by increasing the amount of achievable biomass. A desirable goal for biotechnologist and engineers is therefore to search for means to improve the performance of photobioreactors by increasing the photosynthetic efficiency.

From the process engineering perspective, the kinetics of the system govern the problem and an optimal state can be achieved for matching rates of energy demand and supply under the constraint of minimal losses. Under the presumption that light propagation is by far the fastest process in photobioreactors, the light intensity field determines the local energy supply, while the spatiotemporal energy demand is defined by the concentration of the biomass and mixing. This point of view considers that the energy demand of individual cells can either be governed by local steady states of the photo- and biochemical reactions involved in photosynthesis, or alternatively by the dynamics of these reactions, both depending on the temporal characteristics of light exposure to single cells [22]. In the latter case of fast dynamics, a phenomenon termed the flashing-light effect occurs, which is known for increasing the photon convergence efficiency [23]. Although the utilization of the flashing-light effect by technological means already received considerable effort, e.g. [24–28], controversies about its practical relevance still exist [29, 30], not least because of a wide variety of different photobioreactor designs. Therefore, further research is required to evaluate practically relevant processing conditions for their impact on the efficiency of cell growth and to enhance existing cultivation strategies in order to improve the competitiveness and sustainability of microalgae production.

1.1. Scope and outline of the thesis

The scope of the thesis is to evaluate the occurrence of the flashing-light effect in bubble column photobioreactors and the evaluation of its technological potential. As said above, the dynamic energy balance of the biomass is governing the problem, being determined by the microbial reaction kinetics, the local light supply and hydrodynamic mixing. Numerical simulation is a desirable tool to study complex kinetic problems under spatio-temporally varying reaction conditions for engineering purposes and will be applied in this work. Therefore, a new model is developed within the lattice Boltzmann framework

for the simulation of the light distribution. Subsequently, the model is combined with other sub-models for reaction kinetics and hydrodynamics to investigate the interplay of light distribution, light exposure and cell growth in bubble column photobioreactors and to evaluate the impact of different operation conditions. The key questions for this work are therefore:

1. Does the lattice Boltzmann approach provide a suitable methodological framework for three-dimensional simulations of light propagation in participating media?
2. How does the presence and motion of the gaseous phase affect the light exposure of single cells?
3. Can the flashing-light effect be induced in a microalgae population by means of hydrodynamic mixing in typical bubble column photobioreactors?
4. Are there alternative ways to induce the flashing-light effect in a microalgae population and consequently to improve the reactor productivity?

The thesis is organized in three parts. In part I the fundamentals of photosynthesis and microalgae cultivation are outlined and the theoretical background for the modeling of light transfer and the lattice Boltzmann method is provided. Part II contains four research articles which represent the major contribution to ongoing research and aim to answer the aforementioned key questions. The chapters 5 and 6 cover the development of the new numerical method for the computation of light transfer in turbid media. In chapters 7 and 8 the method is utilized for the comprehensive modeling of a photobioreactor including the flow field and kinetics of photosynthesis in order to investigate the relevance of different process conditions for the productivity of photobioreactors. In part III a continuing discussion of the methods and results of part II is presented followed by an overall conclusion and outlook.

1.2. Notation

For the sake of the readers convenience it shall be briefly said that the list of symbols does not cover the notation used in part II, as the articles therein were published as stand-alone contributions. All symbols in the articles are explained in the respective texts whereas the provided list of symbols covers the notation used in parts I and III.

2. Algal Photosynthesis and Cultivation

The aim of this chapter is to provide basic information about the metabolism of microalgae, photosynthetic reaction kinetics and their relation to the available light energy. On the reactor scale, light is the limiting factor for photosynthetic cell growth and its availability is characterized by gradients in space and time. In this context, the light exposure of individual cells is also affected by hydrodynamic mixing. The chapter reviews the state of the art in photobioreactor technology with a special emphasis on cylindrical bubble columns.

2.1. Engineering perspective on the principles of photosynthesis

2.1.1. Photosynthetic reaction scheme

The major pathway for microalgae to gain energy is photosynthesis. The mechanisms of photosynthesis are extensively described in several textbooks, e.g. [31–33], and therefore just a brief review of the different reactions will be provided here. Generally, photosynthesis consists of light-dependent, photochemical reactions for the generation of chemical energy in terms of ATP and NADPH (light reaction) and on the other hand light-independent, enzymatic reactions in which the chemical energy is utilized to fixate CO_2 into organic carbon (dark reaction). Figure 2.1 provides a schematic of the different reactions in order to illustrate the below standing text.

The starting point of the light reaction is the absorption of light energy in light harvesting complexes (LHC). LHC are located in the thylakoid membranes of the cellular chloroplasts and are composed of different pigments, particularly chlorophyll a and b but also several carotenoids. Thereby, the different pigments absorb light dominantly at specific wavelengths and the overall absorption spectrum results from the superposition of the absorption spectra of the present pigments. Once impinging light energy has been absorbed, it is passed towards the core of a LHC to a photosynthetic reaction center, consisting of a pair of chlorophyll molecules. The two existing types of reaction centers are termed either photosystem (PS) II or I while the respective paired chlorophyll molecules (pigments) are named P680 and P700 according to the wavelength of their absorption maximum. The photosystems are associated with large protein complexes having the function of an electron transfer chain (ETC), which connects the two systems PS II and PS I. The received light energy is utilized to lift the central chlorophyll molecules to an excited state, which allows to transfer excited electrons to the ETC. The concomitant initial loss of electrons in the P680 reaction center is compensated by the oxidation of water, which

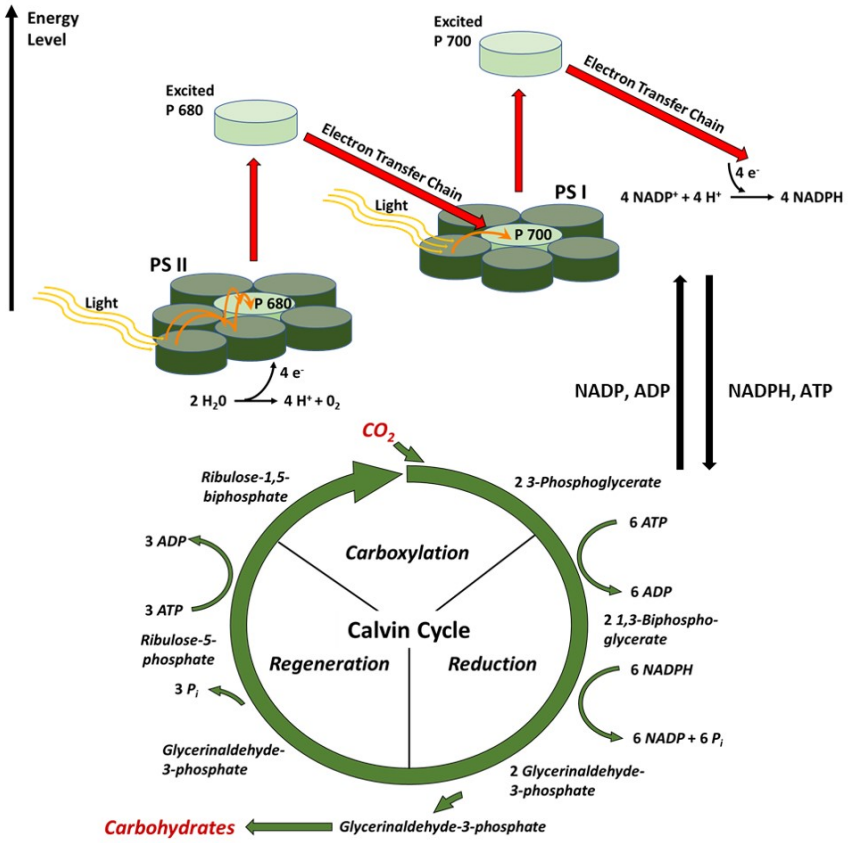

Figure 2.1.: Schematic of photosynthesis reactions. The light-dependent production of reduction equivalents (so-called z-scheme of photosynthesis) is shown in the upper part. The production of ATP is also light-dependent and coupled to a transmembrane proton-gradient which is established during the reactions of in the electron transfer chain (not shown). In the lower part the reactions of the light-independent Calvin cycle are depicted, wherein the produced NADPH and ATP are regeneratated during the production of organic carbon from CO_2.

therefore acts as the electron source for photosynthesis. Thereby, molecular oxygen is formed as a by-product, allowing the indirect measurement of the photosynthetic reaction rate via oxygen evolution [34]. Within the ETC, the supplied electrons are finally used to reduce NADP+ to the reduction equivalent NADPH. Simultaneously, a proton gradient across the thylakoid membranes is generated which drives the production of ATP by the enzyme ATPase. The chemical equation of the entire light reaction reads [32]

$$4\,\mathrm{NADP^+} + 2\,\mathrm{H_2O} + 4\,\mathrm{ADP} + 4\,\mathrm{P_i} \xrightarrow{8\ \text{photons}} 4\,\mathrm{NADPH} + 4\,\mathrm{ATP} + \mathrm{O_2}$$

The reaction time of the different processes is in the order of 10^{-14} seconds for light absorption, 10^{-6} seconds for the photochemical reactions and $5...10 \cdot 10^{-3}$ seconds for the ETC, which is the rate limiting step of the light reaction [35].

In the dark reaction, the chemical energy and electrons are used to fixate CO_2 into organic carbon. The cycle of enzymatic reactions in which this occurs is termed Calvin cycle. A key enzyme of the Calvin cylce is RubisCo, which adds CO_2 to a 5-carbon sugar[1] in a carboxylation reaction yielding 2 molecules of 3-phosphoglycerate (3-PGA), which are 3-carbon molecules. The formed 3-PGA is further reduced to Glycerinaldehyde 3-phosphate (G3P), which as the main product of the Calvin cycle can be further metabolized to a hexose in order to drive different metabolic reactions including glycolysis and respiration. The chemical equation for 6 runs of the dark reaction is

$$6\,CO_2 + 18\,ATP + 12\,NADPH + 12\,H^+ \longrightarrow C_6O_6H_{12} + 18\,ADP + 18\,P_i + 12\,NADP^+ + 6\,H_2O$$

and the reaction time of a single run is in typically in the order of $10^{-1} - 10^{0}$ seconds [35]. It should be noted at this point that the kinetics of the light reaction are approximately two to three orders of magnitude faster in comparison to the dark reaction, which causes the occurrence of different limiting regimes depending on the amount of absorbed light energy, see 2.1.2. The overall chemical equation of photosynthesis results from the coupling of light and dark reactions and is given by the equation

$$nCO_2 + nH_2O + light \longrightarrow (CH_2O)_n + nO_2$$

2.1.2. Kinetics and efficiency

Due to the dependence of the light absorption rate on the local light intensity, the overall turnover rate of photosynthesis is also a function of it. This relation is usually expressed in terms of the PI-curve[2] [36] (also Blackman curve); a typical example is sketched in Figure 2.2. The PI-curve is characterized by different regimes [37]. At low light intensity (light limited), the turnover rate of photosynthesis can be approximated by first order kinetics. Under these conditions, the overall reaction rate is limited by the availability and absorption of light and the consequential limitation of the dark reaction due the exhaust of its educts. Frequently, a negative value for the rate of photosynthesis can be found in literature at very low light intensities. This is caused by the frequently applied recording of PI-curves in terms of the net oxygen evolution [34, 38]. At almost dark conditions, the oxygen consumption by respiration may exceed the photosynthetic oxygen production so that the net oxygen evolution rate is negative. A characteristic point of the PI-curve is the compensation intensity I_c, where the photosynthetic oxygen production is just sufficient to compensate the respiration losses and the net oxygen evolution equals zero. I_c is therefore related to the cellular catabolism and is specific for each species [39].

A characteristic measure for the light intensity at which the reaction regime changes is the saturation intensity I_s. Figure 2.2 shows that the turnover rate becomes more or less constant at higher light in-

[1] Ribulose-1,5-biphosphate (RuBP).

[2] P stands for the rate of photosynthesis while I represents the irradiance or light intensity.

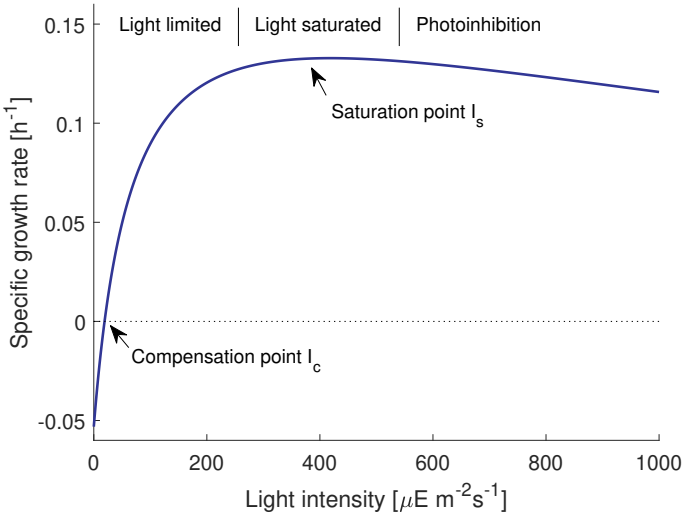

Figure 2.2.: PI-curve of the green algae *Chlamydomonas reinhartdii* predicted by the kinetic model in [40]. The maximum growth rate is $\mu = 0.133$ h^{-1} at 400 μE m^{-2} s^{-1}.

tensities than I_s (light saturated). In this regime, light energy is harvested in excess and the maximum turnover rate of the enzymatic dark reaction becomes limiting for the overall reaction. Cells respond to the energy surplus under these conditions by a variety of mechanisms, including non-photochemical quenching (NPQ)[3] and so-called alternative electron pathways[4] [35]. The dissipation rate for the absorbed energy increases with light intensity and comes along with a reduced efficiency regarding the required number of photons to fixate one molecule of CO_2. Under ideal conditions, the photosynthetic efficiency (PE) is about 8-12 photons per molecule of CO_2 while this ratio can reach values higher than 50 under high light conditions [38]. A related quantity is the photosynthetic conversion efficiency (PCE, also bioenergetic yield) which measures the amount of absorbed light energy being finally stored in the biomass [20]. The theoretical maximum of the PCE is in the order of 10% for the photosynthetically active (PAR) part of the light spectrum [20] and about 5% for full sunlight [41]. Due to nutrient limitations, microalgae operate in natural habitats at much lower PCE than the theoretical maximum and a significant amount of energy is dissipated as heat [42]. Also in photobioreactors, values of the PCE far from the theoretical maximum and inverse relations to the incident light intensity are reported [43, 44] and up to 80 % of this inefficiency can be explained by energy dissipation [20]. Consequently, the goal of a high photon conversion efficiency is in conflict with the supply of light at high intensities in order to achieve high growth rates [35].

A potential solution for this dilemma provides the finding that the PCE increases under high-light conditions if the illumination occurs with flashing light [23, 45], a phenomenon known as flashing-

[3] NPQ contains the heat dissipation of light energy via different mechanisms. One of these is the xanthophyll cycle where secondary carotenoids are synthesized and stored in the LHC in order to dissipate the excess energy, see e.g. [35] for details.

[4] Alternative electron pathways compensate an overreduction of the ETC by providing alternative pathways to the electron transfer to $NADPH_2$.

light effect (FLE). Mechanistically, this effect is explained by a closer match of the time scales of the light and dark reactions [46] or more precisely, it harmonizes the time-averaged energy fluxes of both reactions and therefore reduces the need for energy dissipation. This explanation is based on considering the dark reaction as a bottleneck for the overall rate of photosynthesis (see 2.1.1). However, a full explanation of the FLE is still pending and it should be mentioned that also other theories for the mechanism of enhancement exist [47]. Since the first reports of the FLE, a tremendous amount of theoretical and practical research was carried out in order to investigate the effects of flash intensities, frequencies and duty cycles on growth rates of different microalgae and the related photosynthetic (conversion) efficiencies, e.g. see [28, 29, 34, 48–54] or [55, 56] for reviews. The flashing light regime ideally results in full light integration, meaning that growth under flashing light occurs at a similar rate as under continuous illumination of similar light intensity [45]. Thus, full or partial light integration is accompanied with an increase of the PCE. Although differences between various species exist [57], there is a convention that flash frequencies of several Hz and short duty cycles are required to improve the photosynthetic efficiency under high-light conditions [56]. For example, full light integration in the model algae *Chlamydomonas reinhardtii* occurs at frequencies higher than 50 Hz [34], while 10 Hz flashes might be sufficient for *Nannochloropsis salina* [52]. The scattering of results and also the fact that some researchers report no effect of flashing light on cell growth at all [29] makes it difficult to assess optimal flashing regimes and the real potential of the FLE for the improvement of algal growth in technical reactor systems. Also it should be noted that many experiments were performed in optically thin cultures and are thus not representative for large scale cultivation systems where the light exposure of single cells is governed by a continuously varying light intensity and hydrodynamic mixing, see section 2.2. In order to take these relations into account, some studies aim at mimicking representative conditions for photobioreactors with light/dark cycles in the order of several seconds [24, 58–62]. An alternative way to investigate the occurrence of the FLE in photobioreactors is the development of numerical models coupling the transient change of the physical environment with kinetic models for photosynthesis (see 2.1.3).

Recalling Figure 2.2, it can be seen that the turnover rate decreases at very high light intensity due to the light-induced damaging of the photosystems (photoinhibition). The damaging of the photosystems, particularly of PS II, is proportional to the received light intensity. Under strong irradiance, photoinhibition cannot be compensated any longer by intracellular repair mechanisms and, consequently the rate of photosynthesis decreases [63]. This effect is even pronounced by the formation of reactive oxygen species (ROS) as a by-product of photosynthesis. The increased formation of ROS under strong light contributes indirectly to photoinhibition by targeting the synthesis of the D1 protein, which is part of the repair mechanism of PS II [63]. On longer time scales, a typical cellular response to light stress is the adaption of their pigmentation (photoacclimation) including the reduction of the chlorophyll content

and the formation of carotenoids in order to reduce the size of the LHC and enhance the antioxidative capacity respectively [64, 65].

2.1.3. Kinetic models for photosynthesis on different time scales

For the purpose of photobioreactor engineering it is necessary to describe the kinetics of photosynthesis quantitatively. In this context, a large body of kinetic models has been developed, see e.g. the reviews [37, 66, 67] for an overview. In the following, two fundamental different approaches for light dependent kinetic modeling will be presented based on a selection from the many models being present in literature. A summary of the model characteristics is provided in table 2.1.

A common approach to capture the kinetics of photosynthesis is the expression of the cellular response to light by one-equation models mimicking the hyperbolic shape of the PI-curve. Examples for kinetic models of this type are the hyperbolic tangent model [68] or Monod-type kinetics with light intensity I playing the role of a substrate, thus

$$P = P_{max} \frac{I}{K + I} \propto \mu \tag{2.1}$$

where P is the rate of photosynthesis, K a kinetic constant and μ the specific growth rate. Extensions of these models were proposed to increase the prediction accuracy, e.g. by considering substrate inhibition to account for photodamage [36, 40]. Another modification is the consideration of absorbed instead of incident light [69] and therefore of the wavelength-dependency of light and the cellular absorption characteristics. Also limitations by nutrients (e.g. carbon or nitrogen) are sometimes considered by multiplicative Monod-type kinetics [66]. The characteristic time scale of this class of models is given by cellular doubling time μ^{-1}, which is usually in the order of hours to days. Thus, they are suitable for the simulation of whole batch cultivations with durations in the order of several days. For process simulations, the kinetic model must be coupled with a light-attenuation model (see chapter 3) to take into account the spatio-temporal variation of light intensity in a reactor (see 2.2.2) and the related variance of local growth conditions. A representative reaction rate for a reactor system can be obtained

Table 2.1.: Characteristics of different kinetic models according to [37].

Type	Time scale	Consideration of light history and FLE	Possible model couplings
One-equation models	μ^{-1}	no	Coupling with light distribution for local growth rates of the culture
Photosynthetic factory models	dark reaction	yes	Coupling with light distribution and particle tracking and/or flow models for dynamic growth rates of single cells in light fields

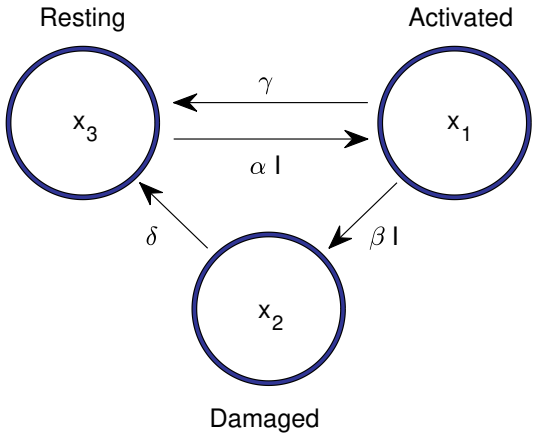

Figure 2.3.: Schematic of the Eilers and Peeters model. The rate of PSU activation is $\alpha I x_3$. Light-dependent photodamage occurs at rate $\beta I x_1$. The rates of the dark reaction and PSU-repair are given by γx_1 and δx_2 respectively.

by integrating the local prediction $\mu(\mathbf{x})$ over the whole reactor volume[5] [37]. It should be noted that the motion of individual cells and their expose to fluctuating light is not considered by this modeling approach.

A second class of models aims at predicting the overall photosynthetic reaction kinetics by the coupling of models for the single reactions, namely light and dark reaction as well as photoinhibition. Although there are different approaches [53], the most common representatives of this class are the photosynthetic factory models, firstly introduced by Eilers and Peeters [70]. The basic assumption behind the photosynthetic factory models is the existence of photosynthetic units (PSU) which can be activated by light absorption. Activated PSU either relax again towards the resting state and drive the dark reaction with the absorbed energy. Alternatively, if light is absorbed in excess, photodamage of activated PSUs transfer them into an inactive state whereby the carried energy is dissipated. Thus, three possible states for PSUs are considered: activated (x_1), damaged (x_2) or at rest (x_3), with x_i being the dimensionless fraction of the total cellular PSUs in the respective state. The transition rates between the single states account for the rates of involved partial reactions and the total rate of photosynthesis is usually given by the transition rate from the activated to the resting state. Figure 2.3 illustrates the basic principle of the Eilers and Peeters model. According to this scheme, the transition rates of the activated and damaged states are given by the following set of equations

$$\frac{dx_1}{dt} = \alpha I x_3 - (\beta I + \gamma) x_1 \tag{2.2}$$

$$\frac{dx_2}{dt} = \beta I x_1 - \delta x_2 \tag{2.3}$$

$$x_3 = 1 - x_1 - x_2 \tag{2.4}$$

[5] This procedure is also termed μ-integration.

where the model parameters α, β, γ and δ account for the kinetic constants of light-dependent activation and damaging of PSU, as well as for their recovery in the photosynthetic dark reaction and by repair, respectively. Several modifications and extensions of the original reaction scheme of Eilers and Peeters were proposed by different authors, taking into account different possibilities for states transitions, different models for the single reaction rates or models accounting for changes in the total number of PSU in order to represent photoacclimation [71–78]. A comparison of the different models including a parameter sensitivity analysis was recently carried out by Rudnicky et al. [79] showing that all compared models were able to reproduce experimental data although some of the model parameters have little effects on the solution. The characteristic time scale of the photosynthetic factory models is approximately given by the dark reaction rate, being much smaller than the cell growth rate. Because the dynamics of photosynthesis are resolved, photosynthetic factory models are suitable to investigate the effects of fluctuating environmental conditions on the dynamics of photosynthesis. This also includes the investigation of the FLE (see 2.1.2) on the reactor scale if the kinetic model is coupled to additional models for the light distribution and the hydrodynamic mixing of cells [30, 80–84]. However, it should be also mentioned that photosynthetic factory models are not suitable for the simulation of whole batch cultivations due to their high temporal resolution and the related computational costs.

2.2. Cultivation of microalgae in photobioreactors

2.2.1. General requirements and photobioreactor types

In contrast to other fields of biotechnology where stirred tank reactors are the dominating reactor type, the dependence of cell growth on light availability causes a large variety of reactor types being utilized in photobiotechnology. Common features of all reactor designs are transparent surfaces and a large surface-to-volume ratio in order to provide the cell culture with a sufficient amount of light energy from external sources. Both, technical and natural light sources are used with a clear dominance of sunlight at the production scale. Other requirements for photobioreactors include an effective gas-liquid mass transfer for the supply of CO_2 and the removal of dissolved oxygen as well as sufficient mixing to ensure homogeneous light exposure of all cells. Thereby shear and tensile stresses must kept at a low level to prevent mechanical cell damage.

Different types of photobioreactors and recent advances in their design have been extensively reviewed, e.g. see [41, 85–91]. A crucial difference exists between open and closed cultivation systems from which only the latters are termed photobioreactors. Among these, the most commonly employed types are horizontal or vertical tubular reactors with typical tube diameters of a few centimeters. Design variants include for example helical tubular reactors [92] or tubes with static mixers [93, 94]. Horizontal tubular reactors are operated by pumping the cell suspension through transparent tubes having lengths up to several hundred meters. Typically, they are operated in the weakly turbulent regime at Reynolds

numbers Re in the order of 10^3 to 10^4 to ensure proper mixing of the cell culture [95]. Therewith related is a relative high demand of mixing energy [88]. For gas exchange, the cell suspension is passed through a degasser (e.g a bubble column) after flowing through the tubular light collector. However, the accumulation of oxygen along the tubes may cause the inhibition of RubisCo [85] (see 2.1.1). In contrast, vertical tubular photobioreactors are often operated as bubble column or air-lift reactor, where mixing is realized by gas sparging. They are typically operated at low to moderate gas superficial velocities $u_g < 0.4$ m s^{-1} [96] and provide several advantages like excellent mass transfer characteristics, low shear stress and low requirements for mixing energy [88, 96]. Other types of photobioreactors are flat-panel air-lift reactors [25] or internally illuminated reactors [97] from those the latter are currently not found at production scale.

Several researchers compared the performance and economics of photobioreactor operation. Wolf et al. [21] observed a maximum photon conversion efficiency (PCE, see 2.1.2) in a tubular reactor system of 2.5% (related to the total solar spectrum) for the cultivation of *Chlorella sorokiniana* under outdoor conditions. Results in a similar order are reported for other species [98, 99]. The biomass production costs, on the other hand, were estimated at the 100 ha scale in the order of 4-6 EUR per gram dry mass with little differences between different reactor systems [100, 101]. The theoretical minimum of production costs for tubular or flat panel photobioreactors was estimated by Acien et al. [4] with 0.7 EUR per gram dry mass under the prerequisite of an increased reactor productivity (among others). Recalling that the theoretical maximum of the PCE related to the PAR region of sunlight is in the order of 10% [20], it becomes clear that improving the PCE and thereby the reactor productivity offers great potential to make photobioreactor technology economically more feasible. Apart from genetical engineering [102, 103], the technical realization of the FLE (see 2.1.2) in the reactor environment provides a possible way to reach this goal. For gas-sparged photobioreactors it is reported that improved pneumatic mixing might be suitable to increase the biomass yield [60, 104]. Other researchers suggest the utilization of artificial light sources to provide flashing light with tailored characteristics in order to meet the photosynthetic requirements [27, 50, 105, 106]. However, several technical hurdles need to be overcome prior to a technical realization of flashing light sources on the production scale [106]. Also new concepts targeting an improved PCE by means of internal light sources [97] or special reactor designs with improved mixing characteristics [93] are reported in the literature. However, according to the analysis of Acien et al. [4], equipment costs contribute crucially to the overall production costs and therefore limit the economical realization of some innovations. In any case, evaluating the potential of the different approaches to improve the PCE requires knowledge about the light distribution and hydrodynamics in a PBR configuration.

2.2.2. Light distribution in photobioreactors

As mentioned before, the availability of light is one of the most important factors for the growth of microalgae in photobioreactors. Above all, this is due to the tight relation of light intensity and the rate of photosynthesis. Reviews concerning the issue of light distribution in photobioreactors are provided by Ogbonna and Tanaka [19] or Wang et al. [107]. Generally, the light distribution in a photobioreactor is mainly affected by the type, shape, orientation and emission characteristics of the light sources, the reactor geometry and in particular by the radiation characteristics and concentration of the cells. Moreover, it is often mentioned that the presence of the gaseous phase affects the light distribution in gas-sparged photobioreactors [108–110]. The cell radiation characteristics include the probabilities for photons to be absorbed or scattered by cells as well as the angular distribution of scattered photons. The cell suspension itself is usually treated as a homogenized participating optical medium, instead of considering the interaction of light with individual cells. At the scale of the suspension, the radiation characteristics are related to the cell mass fraction as well as the morphology and pigmentation of the cells. Further details about this topic will be provided in section 3.1.

The light intensity in photobioreactors always underlies spatial gradients due to the attenuation of light by the cell culture. Thereby, the strength of the light-matter interaction is proportional to the light intensity itself causing very steep gradients at the spectral absorption peaks. Consequently, at these wavelengths all light can already be absorbed a few millimeters away from the source, which was also confirmed experimentally [111, 112]. On the other hand, the strength of the light-cell interaction varies at different wavelengths due the spectral distribution of absorption and scattering characteristics. Because the absorption spectrum of green algae species is peaked in the blue and red parts [113, 114], the relative contribution of green light to the local polychromatic light intensity increases along the light path [112]. The weak absorptivity of green light again causes a flattening of the spatial light intensity gradient [115]. It is often neglected that additional heterogeneity of the light intensity distribution can be caused by reflection or refraction at the various interfaces and even dark regions may arise due to these effects [116]. This issue may be addressed by illuminating cylindrical geometries radially from all sides. It was shown that an almost homogeneous light distribution can be obtained due to the superimposing emission of the different sources [117, 118]. In the usual case of batch or semi-batch operation, additional temporal gradients exist in consequence to the evolution of cell density, cell size and the possible adaption of the pigmentation [119–121]. On longer time scales also the diurnal and seasonal variations of sunlight contribute to temporal light gradients in case of outdoor cultivation, affecting the cellular composition [107] and in turn the radiation characteristics of the cell culture.

Recalling that the reaction kinetics of photosynthesis are determined by the light intensity cells are exposed to, it is clear that the cell growth rate in photobioreactors must underlie spatio-temporal dependencies. For instance, parts of the culture can be exposed to high light intensity near illuminated

surfaces and photosynthesis becomes light saturated or even photodamage of the photosynthetic apparatus can take place. In contrast, above a certain cell density, the existence of spatial intensity gradients cause that parts of a cell culture are located under conditions where the light intensity is below the saturation point and thus, the rate of photosynthesis is light-limited or zero (see 2.1.2). It is well accepted that the volumetric productivity of a photobioreactor is the highest if the lowest available light intensity equals the compensation intensity [29], meaning that the energy demand for respiration can be satisfied by photosynthesis. In case of a high cell density, e.g. $10 - 20\,\mathrm{g/L}$, the related steep intensity gradient requires extreme short light paths in the sub-centimeter scale to satisfy the optimality condition. In order to achieve a more homogeneous light distribution and thus, to overcome the contradiction of short light paths and reactor scale-up, researchers suggest for instance reactors with internal illumination (see 2.2.1). However, externally illuminated photobioreactors exist almost exclusively in practice, typically with light paths of a few centimeter and consequently dark parts of the culture. Therefore, a typical property of photobioreactors is the very inhomogeneous spatial distribution of photosynthetic reaction rates due to the gradients of light intensity. The non-linear relations between light intensity, light spectrum and the cellular reaction kinetics necessitate to consider the spatial inhomogeneity of the light intensity field for the prediction of a representative culture growth rate [19].

Due to hydrodynamic mixing, individual cells move through the reactor and are exposed to a time-dependent fluctuating light intensity. The received temporal light signal is sometimes termed as light regime [122, 123] and contains the incident light intensity, the frequency of the light/dark cycles as well as the duty cycle as characteristic variables. It is clear that the light regime is a decisive determinant for the occurrence of the FLE in photobioreactors. Brindley et al. [123] pointed out that the light regime in real photobioreactors is not well represented by sharp light/dark transitions, which typically appear when thin-cultures are illuminated with flashing-light sources in laboratory experiments. Under such conditions, the effects of mixing on photosynthesis are potentially overestimated [54]. In order to take the continuous variation of light intensity in photobioreactors into account, they proposed a characterization of the light regime with a duty cycle being computed from the volumetric average light intensity [123]. However, the definition presumes a perfect mixing of the culture and ideal cell trajectories from the reactor center to the walls and vice versa. For three-dimensional multiphase flows, e.g. in bubble columns, this presumption hardly holds since the trajectories of the tracer-like cells are mainly governed by chaotic and non-regular vortices [124]. Consequently, to date an accurate description of light regimes in a photobioreactor under certain operation conditions requires the simulation of the light distribution and the multiphase flow.

2.2.3. Hydrodynamics and mixing

Hydrodynamic mixing is an important requirement for photobioreactor operation and ensures that all cells within a culture experience similar conditions on time scales longer than a characteristic mixing time. In bubble column reactors, this time scale is usually in the order of seconds [125]. On the other hand, an improvement of photobioreactor productivity can be achieved when the shuttling of single cells between light and dark zones in the reactor is fast enough to match the time scales of the photosynthetic reaction kinetics [41]. As outlined before, the limiting time scale is the one of the dark reaction, which is in the order of milliseconds (see 2.1.2). For the external illumination of a cylindrical photobioreactor, this is related to a radial movement of single cells at frequencies of several Hz over amplitudes which are related to the spatial light intensity gradient. Due to the large variety of existing photobioreactor designs, a comprehensive discussion of the hydrodynamic features for all of these reactors would go beyond the scope of this literature review. Instead, the focus of this section lies on the review of hydrodynamics in cylindrical bubble columns with special emphasis on bubble column photobioreactors. Reviews capturing the hydrodynamics in other photobioreactor designs are provided by Refs. [89, 126]. Literature reviews concerning the characteristics of bubble column reactors in general can be found e.g. in Refs. [127–130].

The major design parameters of bubble column reactors contain the diameter and aspect ratio of the column as well as the sparger design [130]. Bubble column photobioreactors are usually characterized by large aspect ratios with typical column diameters in the order of a few centimeters, whereas the column height can reach several meters. Typical values of diameters and aspect ratios are summarized in table 2.2. According to these data, aspect ratios H_0/D_0 of photobioreactors range from order 10^1 to 10^2, whereas for conventional bubble column bioreactors the aspect ratio takes values from 2 to 5 [127]. With regard to the spargers (gas distributors) a large variety of designs is known, capturing simple dip tube spargers, ring or spider spargers, porous plates and membranes. It can be concluded from table 2.2 that all of these types can be found in photobioreactors. The type and hole diameter of the sparger has a strong impact on the number and size of primary bubbles by affecting the effective gas flow rate through each hole and the magnitude of the local adhesive and detachment forces [128]. Thereby, the characteristic operation parameter is the gas superficial velocity $u_g = \dot{V}_g/A_0$ which relates the gas volume flow rate $\dot{V}_g$ to the cross-section A_0 of the column. The provided data in table 2.2 show that typical values for u_g range from 10^{-4} to 10^{-2} m s^{-1} .

Based on the typical design and operation of bubble column photobioreactors, certain operation characteristics can be expected. The most important quantity is the bubble size distribution (BSD) determining the global and local gas hold-ups, the gas-liquid mass transfer and the overall flow field.

Table 2.2.: Design and operation characteristics of some bubble column photobioreactors.

Scale	D_0 [m]	H_0/D_0	u_g [m s^{-1}]	Sparger	Ref
Lab	0.070	6.04	$5.9 \cdot 10^{-3}$	n.s.*	[131]
Lab	0.030	62.5	$1 \cdot 10^{-3}$ ... $5 \cdot 10^{-3}$	Nozzle, ∅ n.s.*	[132]
Pilot	0.185	6.21	$9.3 \cdot 10^{-4}$ ... $3.7 \cdot 10^{-3}$	Nozzle, ∅ 10 mm	[133]
Pilot	0.130	7.69	$5.4 \cdot 10^{-4}$ ... $8.2 \cdot 10^{-3}$	Ring, 15 holes, ∅ 1 mm	[80]
Pilot	0.193	10.36	$1.1 \cdot 10^{-2}$	Spider, 17 holes, ∅ 1 mm	[96]
Production	0.05	120	n.s.*	Membrane	[134]

* not specified

According to the approximate flow maps provided by Shah et al. [135] and Zhang et al.[6] [136], the two-phase flow in bubble column photobioreactors can be expected to occur mainly in the so-called (pseudo-) homogeneous regime, although the typical high aspect ratios might support the transition to the slug flow regime at $u_g > 10^{-2}$ m s^{-1} [137]. The (pseudo-) homogeneous regime is characterized by mono- to polydisperse bubble size distributions and a small impact of bubble break-up or coalescence phenomena. Confirmatory, Besagni et al. [130] conclude in their extensive literature review that for a given sparger design the bubble sizes in the homogeneous flow regime are mainly determined by the fluid properties and remain more or less constant among different gas superficial velocities. The shape of bubbles of a certain size rising in a fluid can be estimated from combinations of the Eötvös (Eo), Reynolds (Re) and Morton (Mo) numbers [138]. More recently, the prediction of the bubble aspect ratio in terms of the Weber number $We = Re^2 Mo^{0.5} Eo^{-0.5}$ or the Tadaki number $Ta = ReMo^{0.23}$ has been proposed [139].

The size and shape of a bubble determine its rising velocity and therefore the time until it reaches the liquid surface. Eventually, bubble-bubble interactions also affect the rising velocity in bubble swarms. Since the bubble generation rate for a given sparger is closely related to the gas superficial velocity, it also determines the overall gas hold-up[7] ϵ_g. In the (pseudo-) homogeneous regime ϵ_g is approximately linearly related to u_g and takes values less than 0.15 [130]. There is evidence that the gas hold-up is inversely related to the column diameter if $D_0 < 0.1...0.15$ m [127, 130]. In contrast, concerning the column aspect ratio, no effect on the gas hold-up was observed, if $H_0/D_0 > 5$ [140].

The presence of velocity gradients in the liquid phase cause the action of lift forces on the gas bubbles. While large bubbles are concentrated at the column center, small ones migrate towards the column wall and create a non-uniform distribution of the void fraction leading to a destabilization of the multiphase flow [141]. In consequence, the occurrence of a randomly meandering bubble plume is a typical characteristic of the flow in bubble columns at higher gas superficial velocities beyond the homogeneous regime [142, 143], see also figure 2.4. The bubble plume is the driving force for the

[6] The dimensions column in this work were $D_0 = 0.0826$ m and $H_0 = 2$ m. Therefore the design is close to the one of photobioreactors.

[7] $\epsilon_g = V_g/V_{tot}$, V_g: dispersed gas volume, V_{tot}: total volume of the gas-liquid dispersion.

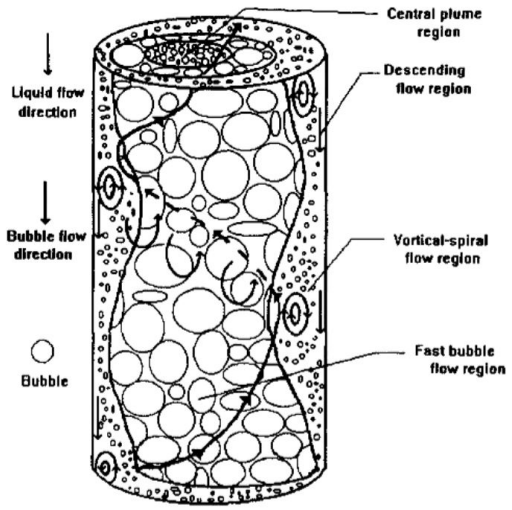

Figure 2.4.: Transient flow patterns in a three-dimensional bubble column flow [142]. With permission from John Wiley and Sons.

multiphase flow and it was shown in numerous experimental (e.g. [144, 145]) and numerical (e.g. [146–148]) investigations that the high void fraction in the column center causes an up-flow of the liquid phase while the down-flow occurs along the column walls in consequence to mass conservation. It is well established that dynamic vortices appear between the central bubble plume and the column wall [142], which have a significant impact on the mixing of passive tracers [149]. With regard to the desired radial motion of microalgae cells in photobioreactors, it can be estimated that the most species behave as passive tracers[8]. Consequently, these vortices can be expected to play an important role for the light regime to which cells are exposed to and thus, for the possible productivity enhancement by the FLE.

To take radial mixing into account, Camacho Rubio et al. [152] extended the established concept of quantifying mixing in bubble columns by an axial dispersion coefficient D_z and introduced an additional radial dispersion coefficient D_r. The achieved biomass growth of *Phaeodactylum tricornutum* was shown to correlate with this quantity, although just a weak sensitivity of D_r to u_g was reported. Luo et al. [153] and later Luo and Al-Dahhan [124] tracked radiative tracers (CARPT technique) to investigate the radial cycling of particles in different bubble-sparged photobioreactors. The overall radial motion of the particles is determined by the different time and length scales of the flow field, ranging from fast shuttling over small distances due to turbulence and small vortices to the slower motion along large spiral trajectories being determined by the bubble plume oscillations. An alternative way

[8]The Stokes number $St = \tau_v/\tau_f$ is an estimator for ability of a particle to follow the flow [150]. Therein, $\tau_v = \frac{\rho_p d_p^2}{18\eta_l}$ measures the particle response time to changes in the flow, while τ_f is a characteristic time scale of the flow. Microalgae cell are typically characterized by diameters d_p in the order of micrometers and mass densities ρ_p slightly higher as water. Assuming the material properties of a growth medium being similar to water, τ_v can be expected in the order of 10^{-7} to 10^{-8} seconds. A measure for the characteristic time scale of the flow field is the oscillation of the bubble plume, which occurs on time scales in the order of 10^0 to 10^1 s [143, 151]. Therefore, $St \ll 1$ which means that cells follow the flow passively.

to access bubble-induced radial mixing in photobioreactors is based on simulations of the flow field and cell motion. Thereby, a simplified and computationally less demanding approach is the modeling of the cell motion by superimposing convective motion with a random walk model, whereas for the latter a diffusion constant (eddy diffusivity) is related to the reactor operation parameters, e.g. the gas superficial velocity [30, 154]. This approach is related to the modeling of axial and radial tracer dispersion, however, its benefit for investigating mixing patterns in microalgae cultures is limited. First, the eddy diffusivity is not a constant and strongly depends on the radial position [155], what becomes particularly important if the determination of light regimes is pursued. Second, the determination of the eddy diffusivity underlies certain uncertainties as outlined by Joshi et al. [156]. Finally, the irregular tumbling of the bubble plume should also be taken into account for mixing studies [149].

A more sophisticated approach is the full simulation of the multiphase flow including cell tracking by means of computational fluid dynamics (CFD). Although in recent years systematic studies have been conducted to evaluate the ability of different turbulence models and interfacial closures to correctly capture the dynamical flow structures (e.g. [157, 158]), there is still no general agreement about these issues. Besagni et al. [130] provide an up-to date review of recent developments in the field of multiphase flow simulation, whose detailed discussion goes beyond the scope of this chapter. CFD is also often applied to investigate flow patterns and mixing in photobioreactors (see e.g [159, 160]). However, the results should be critically reviewed because the multiphase flow is often modeled inadequately. A common issue is that researchers neglect several interface forces, although agreement exists that the complete set of drag, lift, virtual mass, turbulent dispersion and wall lubrication forces should be considered for an accurate description of the multiphase flow [130]. For example, in their study on mixing effects on cell growth Nauha and Alopaeus [161] consider just the action of the drag force on the gas phase. Consequently, they achieve the result of straightly ascending bubbles being in conflict to the experimental observation of an oscillating bubble plume. In a second study [162], they extended their model by including a lift force while still neglecting the counteracting effects of turbulent dispersion [141]. Seo et al. [163] aimed at comparing different modeling approaches to simulate the flow in a bubble column photobioreactor. However, in their study they considered only drag, lift and virtual mass forces and assumed laminar flow conditions. These examples indicate that a careful modeling of the flow is required to capture the conditions in photobioreactors correctly. This is particularly important for investigations on bubble induced mixing, light regimes and cell growth. Finally, it should be stated that little knowledge is available on how the presence of algae cells and their increasing concentration during the cultivation process affect the liquid properties and the flow field. In a recent study Ojha and Al-Dahhan found that the gas hold-up was significantly reduced at higher biomass concentration, which was related to a growth-associated increase of the mixture viscosity at constant surface tension [164]. The increase of the dynamic viscosity at higher cell concentration was also reported by other au-

thors [165]. However, as reviewed by Besagni et al. [130], controversial results concerning the effects of viscosity on the bubble column operation characteristics are reported in the literature and further research about this issue will be necessary in future.

2.3. Concluding remarks

In the previous sections it was outlined that different processes on various time and length scales affect the operation and productivity of bubble column photobioreactors. On the one hand, the reaction kinetics of photosynthesis determine the overall cell growth (see 2.1.1). Under high light conditions, the light and dark reaction occur on mismatching time scales and, consequently the overall photosynthesis becomes light-saturated (see 2.1.2). On the other hand, mixing of the cells induces a fluctuating light exposure, which potentially synchronizes the reaction speed of both reactions if the light/dark frequencies are high enough. The underlying physiological effect is called flashing-light effect (FLE). The length scale over which the shuttling of single cells must occur to induce the FLE depends on the steepness of the light intensity gradient (see 2.2.2). It will be outlined in the next chapter, that a characteristic length scale of the light field is given by the inverse of the extinction coefficient of the cell suspension, which is related to the cell concentration. The intensity of pneumatic mixing in bubble columns depends mainly on the gas superficial velocity (see 2.2.3). Hence, each unique combination of mixing, light supply, cell concentration and reaction kinetics determine the overall productivity of a bubble column photobioreactor.

The existing literature contains contradictory information about the practical relevance of the FLE in photobioreactors so that further investigations of the topic are needed. Similarly, it is not clear whether the presence of a gaseous phase affects the light distribution and, consequently, the efficiency of light utilization and cell growth. In chapters 7 and 8 of this work, a multiphysical simulation model will be developed and coupled to cellular reaction kinetics in order to answer these questions. A further discussion of the topic is provided in chapter 10, which also links the obtained results to other types of photobioreactors.

3. Radiation Transfer Models and Numerical Methods

The chapter reviews models for light propagation with an emphasis on photobioreactor engineering. Aspects concerning the radiation characteristics of microalgae cell cultures will be discussed first. Thereafter, the most important models, namely Lambert's law and the Radiation Transfer Equation, will be introduced. Moreover, because of their relevance for photobioreactor research and lattice Boltzmann modeling of radiative transfer, additional common approximations of the RTE like the 2-Flux models or the Diffusion Approximation will be briefly reviewed. A short overview of numerical methods utilized for radiative transfer calculations complements the description of the different models.

3.1. Radiation characteristics of photosynthetic cells

All of the here considered models (see 3.2 and 3.3) have in common that radiation transfer in a homogenized participating optical medium is assumed. The definition of a participating medium contains specific absorption and scattering characteristics which determine the probability of light-matter interactions per unit length. Mathematically, this is expressed in the respective absorption and scattering coefficients μ_a and μ_s. As mentioned before (see 2.2.2), the radiation characteristics of a cell culture are related to the cell morphology, pigmentation and cell concentration and therefore vary constantly in time. A practical concept to obtain absorption and scattering coefficients is the consideration of optical cross-sections as a normalized measure for the interaction probability. In case of light absorption, μ_a can be expressed by a linear relationship

$$\mu_a = A_a X \tag{3.1}$$

where A_a is the cell-specific, cell mass-specific or pigment mass-specific absorption cross-section ($[\mathrm{m}^2/\mathrm{cell}]$ or $[\mathrm{m}^2/\mathrm{kg}]$) and X $[\#/\mathrm{m}^3]$ is the respective particle or pigment concentration in the suspension [166]. For scattering, linear relationships are only valid if independent scattering can be assumed, which occurs at low particle concentrations or a small scattering cross-section. Baillis and Sacadura [167] propose a scattering regime map in order to estimate whether independent scattering can be assumed, and consequently the relation

$$\mu_s = A_s X. \tag{3.2}$$

holds. The quantities in Eq. (3.2) are similar to those in Eq. (3.1) except that the index s denotes for scattering. Assuming typical values for microalgae cultures, one finds that linearity can be accepted[1]. Another important quantity is the scattering phase function Φ which describes the probability distribution for scattering with respect to the single scattering angle $\Theta = \mathrm{acos}((\mathbf{n} \cdot \mathbf{n}')/(|\mathbf{n}||\mathbf{n}'|))$, where $\mathbf{n}$, $\mathbf{n}'$ represent unit vectors in spherical coordinates. A general notation for Φ is [168]

$$\Phi(\cos(\Theta)) = 2\frac{\mathrm{d}I'(\cos(\Theta))}{\int_{-1}^{1} I'(\cos(\Theta))\,\mathrm{dcos}(\Theta)} \tag{3.3}$$

while the specific shape of the function depends on the chosen scattering model, e.g. Mie theory. Important properties of the scattering phase function are reciprocity and the conservation of energy. The latter directly follows from Eq. (3.3), thus

$$1 = \frac{1}{2}\int_{-1}^{1} \Phi\,\mathrm{dcos}(\Theta) \tag{3.4}$$

The cosine of the average scattering angle is given by the first angular moment of Φ and is known as the asymmetry factor g. Therefore,

$$g = \frac{1}{2}\int_{-1}^{1} \cos(\Theta)\Phi\,\mathrm{dcos}(\Theta). \tag{3.5}$$

In a weakly absorbing[2] but scattering medium, the direction of photon propagation becomes increasingly randomly after multiple scattering events, being accompanied with a transition from ballistic to diffuse radiation transport [169, 170]. In this context, the transport or reduced scattering coefficient $\mu_s' = \mu_s(1-g)$ is a determinant of radiative transfer, which is also reflected by its relation to the diffusion coefficient in the radiative Diffusion Approximation (DA, see 3.3.5). Related to this, it is part of similarity relations for radiation fields (see 3.3.2), which are applied to scale radiation characteristics in order to improve the performance of numerical solvers (see 3.3.3).

The optical cross-sections A_a and A_s as well as the scattering phase function Φ are related to the morphology, size and composition of the cells. The governing physical quantities are the size distribution of the suspended cells and their complex index of refraction [171]. The real part determines the scattering of light while light absorption is reflected in the imaginary part. The link to the optical cross-sections and the angular scattering patterns is provided by Mie theory, see [171–173]. Also

[1] The estimation of independent scattering is based on the size parameter $\alpha_s = \pi d_p/\lambda$ and the particle volume fraction $\phi_v = X/\rho_p$ where d_p, V_p, ρ_p, λ, denote for the particle diameter, particle volume, volume-specific particle dry mass and radiation wavelength [167]. Typical values for microalgae cultures range from $d_p = 10^{-6}...\ 3\cdot10^{-5}$ m, $\rho_p \approx 2000$ kg m^{-3} and $\lambda = 400...\ 700\cdot10^{-9}$ m. These parameters result in sizes parameters of order $\alpha_s \approx 10^0...\ 10^2$. Typical biomass concentrations in PBR range from $X = 1...\ 10$ kg m^{-3} so that cell volume fractions in the range of $\phi_v \approx 5{\cdot}10^{-4}...\ 5{\cdot}10^{-3}$ can be expected. According to the scattering map in Ref. [167], independent scattering can be expected within this parameter window.

[2] Strong absorption counteracts the equilibration process.

computationally cheaper but less accurate approximations of Mie scattering exist, e.g. the Anomalous Diffraction Approximation (ADA) [174]. The forward peaked Mie scattering of microalgae cells is often approximated by the Henyey-Greenstein (HG) phase function Φ_{HG} [175], being defined as

$$\Phi_{HG}(\Theta) = \frac{1}{4\pi} \frac{1 - g^2}{(1 + g^2 - 2g\cos(\Theta))^{3/2}} \tag{3.6}$$

Typical values for the asymmetry factor of microalgae are $g > 0.95$ [110, 114, 176, 177]. Then, the HG phase function reflects the strong forward scattering of the cells but also tends to underestimate the amount of backscattering, whose contribution to scattering is however normally small for microalgae. This issue can be addressed in principle by superimposing two or more phase functions with different asymmetry factors [178]. Though, in the context of photobioreactor engineering this approach is rarely applied and usually single parameter phase functions are assumed.

Measurements of the complex index of refraction are challenging and a model-based determination provides an alternative [176]. Thereby, a major difficulty lies in the complicated cellular structure and the impact of inner cell organelles and cell wall on the optical cell properties [176, 179]. In order to reflect this, algae cells are sometimes modeled as coated spheres assuming different optical properties for the cell hull and organelles [180–182]. Models must also take into account that the index of refraction is not a fixed quantity, rather than being affected by the physical and chemical environment during the cultivation [183]. For example, different growth conditions and environmental stress factors affect the cell size or the intracellular contents of lipids and pigments and in turn the optical properties of the cell culture [121, 183, 184]. Because of these difficulties direct or indirect measurements of the absorption and scattering coefficients in cell suspensions are more common. A number of papers deal with the development of measurement techniques, e.g. [185–187][3], and a large body of measured data is nowadays available for several species [113, 114, 120, 121, 177, 178, 189–193].

3.2. Lambert's law and modifications

3.2.1. Lambert's law

Lambert's law (also Beer-Lambert's law, Boguer's law) is the simplest model to calculate radiation transfer in participating media and the spatial distribution of the radiation intensity. The basic underlying assumption is that absorption fully governs the radiation-matter interaction and no scattering of radiation takes place. Under this assumption, radiation transfer reduces to a one-dimensional problem if the source also emits collimated radiation. An common way to derive Lambert's law is to postulate it in its differential form

$$\frac{\mathrm{d}I}{\mathrm{d}x} = -\mu_a I \tag{3.7}$$

[3] see also the techniques reviewed in [188].

and obtain by integration the analytical solution of (3.7)

$$I(x) = I_0 \exp(-\mu_a x) \tag{3.8}$$

with the boundary condition $I(x_0) = I_0$. This derivation corresponds to a special solution of the Radiation Transfer Equation, see 3.3.1. The quantities I_0 and μ_a are usually functions of wavelength. Therefore, the predicted intensity profiles depend on wavelength and the polychromatic radiation intensity must be obtained by integration across the light spectrum. Thus,

$$I(x) = \int_{\lambda_1}^{\lambda_2} I_{0,\lambda} \exp(-\mu_{a,\lambda} x) \mathrm{d}\lambda \tag{3.9}$$

where the index λ accounts for wavelength dependency of the indexed quantities. An alternative but less accurate approach is to average $I_{0,\lambda}$ and $\mu_{a,\lambda}$ across the spectrum and compute the polychromatic intensity by means of the spectrum-averaged quantities and Eq. (3.8).

Although Lambert's law is by far the most used model to calculate radiation transfer in photobioreactors, e.g. see [30, 69, 80, 194], some authors point out that realistic light intensity profiles are non-exponential even at single wavelengths [111, 195]. This deviation is caused by the disregardance of scattering which occurs naturally in particulate suspensions. Lambert's law provides only an acceptable approximation if the suspensions are dilute or if the path length of radiation transfer is small. Under these conditions single scattering of radiation can be expected and its effect on the radiation intensity can be incorporated into the absorption coefficient [188]. In these cases the term extinction coefficient should be preferred because it covers the two different mechanisms of radiation-matter interaction. An example for this approach is given in the work [196], where the contribution of absorption to extinction was modeled in a linear dependency of the intracellular pigment content and a constant offset accounting for scattering. At high cell concentrations or long propagation paths multiple scattering must be expected. Because photons propagate no longer unidirectional, the path length inside the medium is not similar to the macroscopic distance $\Delta x = x - x_0$. Consequently, the exponential relation between absorption probability and position x is not accurate. Moreover, because of the three-dimensional nature of scattering, the assumption of one-dimensionality can not necessarily be maintained.

3.2.2. Modifications of Lambert's law

In order to increase the prediction accuracy and retain a simple analytical model at the same time, different modifications of Lambert's law have been proposed. Béchet et al. [37] mention some of these models in their comprehensive review. Usually, modification of Lambert's law target the form of the exponent in Eq. (3.8). Empirically based approaches are given in the works [197][4] or [198,

[4]The exponent is modeled as hyperbolic function with respect to biomass concentration.

199][5]. These models neglect wavelength-dependency of the extinction coefficients and aim at directly predicting the polychromatic radiation intensity. Fuente et al. [115] proposed the utilization of Kirk's correlation [200] for computing the extinction coefficient. Similar to the approach of Grima et al. [196] (see 3.2.1), Kirk's correlation considers the contribution of absorption and scattering but relates them in a non-linear way. A different approach is the modeling of polychromatic light propagation by Mittag-Leffler functions [201]. Here, the first order derivative in Eq. (3.7) is replaced by a fractional derivative of order $o \in [0, 1]$. The choice of $o = 1$ yields again Lambert's law which is therefore a special solution of the Mittag-Leffler functions. The model is motivated by mimicking the spatial variation of the absorption efficiency in phototrophic cultures, being accompanied with changes in the light spectrum along the light path. However, the benefit is questionable since similar shaped light intensity profiles can be obtained by solving Eq. (3.9).

Although the mentioned models are not difficult to compute, problems may arise with their application. Usually the models are based on empirical relations, restricting their universality and necessitating previous testing of their accuracy in each specific case. Second, in all these models information propagates just downstream from the source or in other words, the exponential structure of Lambert's law is accompanied with the assumption of collimated radiation in the whole domain of interest. This is, however, clearly contradictory to the three-dimensional nature of scattering which also includes backscattering. With regard to light fields in photobioreactors, the importance of this simplification will depend greatly on the spectrum of the light source and the cultivated species. The light field at wavelengths close to the absorption maximum of a species is probably well approximated. On the contrary, most species do not absorb much light from the green part of the spectrum and scattering becomes a more prominent factor. Thus, the prediction error by utilizing Lambert's law or its modifications will increase under such conditions. The class of 2-Flux models (see 3.3.4) may provide a suitable alternative.

3.3. The Radiation Transfer Equation and its approximations

3.3.1. Radiation Transfer Equation

The Radiative Transfer Equation (RTE) is a balance equation for radiance $L(\boldsymbol{x}, \boldsymbol{n}, t)$, which takes its interaction with the surrounding matter by absorption and scattering into account. By utilizing certain approximations, it can be derived from Maxwell's equations [202]. Since radiance is directly related to the photon distribution function [203], the RTE is a mesoscopic, Boltzmann-type kinetic equation. In the framework of kinetic theory, an equation with identical structure (except the sink term $-\mu_a L$) is known as the Boltzmann-Lorentz equation (BLE), describing the kinetics of point-like particles colliding with stationary particles of much higher mass [204, 205], see 4.1.2. This scenario can be interpreted

[5]The exponent is modeled as product of two hyperbolic function with respect to biomass concentration and path length.

to be similar to the scattering of massless photons by matter. For a non-emitting medium, the RTE reads [206]

$$\frac{\partial L}{c\partial t} + \boldsymbol{n}\nabla L = \mu_s \left(-L + \frac{1}{4\pi} \int_{4\pi} \Phi L' \mathrm{d}\boldsymbol{\Omega}' \right) - \mu_a L \tag{3.10}$$

Therein, $\boldsymbol{x}$ is the spatial coordinate, t is the time, $\boldsymbol{n}$ is a unit vector pointing into the direction of light propagation and c is the speed of light. All other quantities have similar meanings as defined in the previous sections. The wavelength-dependency of the transport coefficients is not explicitly noted in Eq. (3.10), but usually exists as discussed in section 3.1. Radiation sources and the effects of domain boundaries need to be incorporated into boundary conditions. At sources, Dirichlet boundary conditions for radiance L are usually defined to model the emission characteristics of a source [206]. Dirichlet boundary conditions can also be defined at the domain boundaries. For example, setting L to zero reflects a typical condition for an absorbing black wall or free outflow. In contrast, at reflective walls the boundary values are modeled with respect to the impinging radiance [206].

The angular moments of radiance link the solution of the mesoscopic RTE to the macroscopic radiation field. The local light intensity $I(\boldsymbol{x}, t)$ is given by the zero_{th} angular moment of radiance

$$I(\boldsymbol{x}, t) = \int_{4\pi} L(\boldsymbol{x}, \boldsymbol{n}, t) \, \mathrm{d}\boldsymbol{\Omega} \tag{3.11}$$

and higher order moments with physical meaning are the radiation flux

$$\boldsymbol{F}(\boldsymbol{x}, t) = \int_{4\pi} \boldsymbol{n} L(\boldsymbol{x}, \boldsymbol{n}, t) \, \mathrm{d}\boldsymbol{\Omega} \tag{3.12}$$

and the radiation pressure tensor

$$\boldsymbol{P}(\boldsymbol{x}, t) = \frac{1}{c} \int_{4\pi} \boldsymbol{n}\, \boldsymbol{n} L(\boldsymbol{x}, \boldsymbol{n}, t) \, \mathrm{d}\boldsymbol{\Omega} \tag{3.13}$$

While in earlier publications Lambert's law and its modifications were frequently applied (see 3.2), more recently researchers increasingly utilize the RTE to predict light propagation in photobioreactors [110, 188, 195], which is justified by its higher accuracy [111, 195]. Thereby, solutions of the RTE are obtained in one [110, 111], two [195] or three [195, 207] dimensions with different numerical techniques, depending on the complexity of the geometry and the required computational costs. For one-dimensional predictions also analytical solutions of the RTE exits [208, 209], see 3.3.4. However, recent developments in the PBR technology point towards more complex geometries, including for example static mixers [93, 210] or internal illumination sources [97]. It is questionable whether light transfer can still be captured correctly with one-dimensional analytical models and therefore simulations of light transfer are desired. However, solving the RTE in 3D is still computationally demanding,

since the problem to be solved must be discretized in 7 dimensions (3 spatial, 2 angular, 1 temporal and 1 wavelength), see 3.3.3.1.

3.3.2. Scaling of radiation transfer problems

In order to simplify the computation of radiation transfer problems, scaling of the RTE was proposed. The basic underlying idea is to simplify the computation of anisotropic scattering by scaling the scattering kernels into a more convenient form. McKellar and Box [211] showed that the RTE is invariant if both, optical depth and phase function are scaled in a way that conserves the macroscopic transport properties. Different scaling relations were investigated in the past, and a broad consensus exists that those based on the P1-approximation of the phase function yield the best results [212–214]. The scaling is based on the conservation of the transport mean free path

$$l_{tr} = \frac{1}{\mu_s'} = \frac{1}{\mu_s(1-g)} = \frac{1}{\tilde{\mu}_s(1-\tilde{g})} \tag{3.14}$$

and the transport scattering albedo

$$\omega_{tr} = \frac{\mu_s'}{\mu_s' + \mu_a} = \frac{\tilde{\mu}_s'}{\tilde{\mu}_s' + \tilde{\mu}_a} \tag{3.15}$$

where the scaled quantities are represented by the tilde. Usually, the scaled anisotropy factor is set to zero, meaning that anisotropic scattering kernels become isotropic what makes the RTE much more convenient to solve. In this case, $\tilde{\mu}_s$ is equal to the reduced scattering coefficient. The computational benefits and accuracy of the scaling were demonstrated in steady state radiative transfer simulations in one [214] and three [213] dimensions. However, it was also demonstrated that the scaling lacks accuracy in transient simulations [215, 216].

3.3.3. Numerical methods for the RTE

3.3.3.1. Discrete Ordinate method

The discrete ordinate method (DOM) is a discretization of the RTE, firstly introduced by Chandrasekhar [217]. The method and related recent developments are comprehensively described in several monographs and reviews, e.g. [168, 206, 218]. In brief, the RTE is integrated over a control volume and the fluxes across the boundaries of each control volume are expressed in terms of the radiation intensity at nodes being located in their center. The angular discretization is obtained by considering discrete ordinates along which radiation is allowed to propagate. This discretization yields a set of differential equations being coupled via a discrete scattering kernel. Thereby, the in-scattering integral is usually replaced by different Gaussian quadrature rules [219]. It was shown that the choice of the quadra-

ture rule can cause erroneous in-scattering fluxes [220], being termed as false angular scattering [221]. More precisely, an accurate angular discretization requires that the zero$^{\text{th}}$ and first order moments of the discrete scattering phase function (see Eqs. (3.4), (3.5)) are solved exactly by applying the chosen quadrature rule. In order to ensure these conditions, different phase function normalization schemes were proposed [222–224], which will also be applied to the lattice Boltzmann model derived in this thesis (see chapter 5). Further error sources in the DOM are numerical smearing and the ray-effect [221, 225]. Since the DOM is a standard method it was also applied for the calculation of light transfer in photobioreactors, see for example [226, 227].

3.3.3.2. Monte Carlo method

An alternative method to solve the RTE is the Monte Carlo (MC) method, see for example [228–230]. The MC method is based on the idea of tracking individual photons in participating media until they are absorbed or leave the domain of interest. Thereby, the absorption and scattering probabilities per unit length are given by the optical properties of the medium. The scattering kernel in the RTE is computed by sampling the scattering angle from the integral of the scattering phase function, which represent the cumulative probability distribution for the scattering angle [231]. The radiation intensity field is obtained by calculating the spatial probability density for finding a photon at a certain location from the superimposed tracks of many photons, usually $10^6 < N_{ph} < 10^9$ [232]. Details of the algorithm can be found in the above cited monographs or references [168, 206, 232].

The MC method is often used as a reference method because no angular discretization is required, which in turn avoids the error sources mentioned in the previous section. However, the method also has some drawbacks which are the slow convergence rates at short lengths of the mean free path, noisy results due to the method's random nature and the requirement of many photon tracks to obtain smooth results in highly absorbing media. The latter might be the reason that the MC method is rarely applied for light transfer simulations in photobioreactors [233, 234]. In the context of this thesis, the Monte Carlo method is applied to generate reference solutions (see chapters 5, 6 and III).

3.3.4. 2-Flux models

A significant simplification of the RTE can be obtained by aggregating the angular fluxes into a forward and backward component. The consideration of just two fluxes of radiance also comes along with a reduction of the spatial dimensions from 3 to 1. Cornet et al. [208, 235] applied this approximation to light transfer in photobioreactors and derived an analytical solution of the RTE in one dimension under the assumption of isotropic scattering and one-sided light emission. Later, the model was ex-

tended to anisotropic scattering to reflect the scattering characteristics of microalgae cultures [209]. The analytical solution of the so-called Cornet's model is

$$\frac{I(x)}{I_0} = 2\frac{-(1-\alpha_C)\exp(-\delta_C L_0)\exp(\delta_C x) + (1+\alpha_C)\exp(\delta_C L_0)\exp(-\delta_C x)}{(1+\alpha_C)^2\exp(\delta_C L_0) - (1-\alpha_C)^2\exp(-\delta_C x)} \tag{3.16}$$

where the coefficients $\alpha_C = (\mu_a(\mu_a + 2b\mu_s)^{-1})^{0.5}$ and $\delta_C = (\mu_a(\mu_a + 2b\mu_s))^{0.5}$ are related to the radiation characteristics of the cell culture and include the backscattering fraction

$$b = \frac{1-g}{2g}\left(\frac{1+g}{\sqrt{1+g^2}} - 1\right) \tag{3.17}$$

which is a function of the anisotropy factor g. Cornet's model was widely applied for light transfer in photobioreactors with quasi one-dimensional geometry [40, 236–238] and can be considered as a good approximation of light transfer in such systems. Extensions also include the consideration of reflective boundaries [236]. However, the model considers only optically homogeneous media which might be limiting with regard to its applicability.

3.3.5. Hydrodynamic models and Diffusion Approximation

In the hydrodynamic limit, that is close to the scattering equilibrium of radiance, macroscopic formulations of the RTE can be obtained by computing the angular moments of the single terms [239]. Compared to the RTE, hydrodynamic equations are more convenient to solve, because the number of dimensions is reduced by two and no angular discretization is required. The zero$^{\text{th}}$ order integral equation

$$\int_{4\pi} \frac{\partial L}{c\partial t}\,\mathrm{d}\boldsymbol{\Omega} + \int_{4\pi} \boldsymbol{n}\nabla L\,\mathrm{d}\boldsymbol{\Omega} = \int_{4\pi} \mu_s\left(-L + \frac{1}{4\pi}\int_{4\pi} \Phi L'\mathrm{d}\boldsymbol{\Omega}'\right)\,\mathrm{d}\boldsymbol{\Omega} - \int_{4\pi} \mu_a L\,\mathrm{d}\boldsymbol{\Omega} \tag{3.18}$$

yields a balance equation for the radiation energy[6]

$$\frac{\partial I}{c\partial t} + \nabla \boldsymbol{F} = -\mu_a I \tag{3.19}$$

while the first order moment of the RTE

$$\int_{4\pi} \boldsymbol{n}\frac{\partial L}{c\partial t}\,\mathrm{d}\boldsymbol{\Omega} + \int_{4\pi} \boldsymbol{n}\boldsymbol{n}\nabla L\,\mathrm{d}\boldsymbol{\Omega} = \int_{4\pi} \boldsymbol{n}\mu_s\left(-L + \frac{1}{4\pi}\int_{4\pi} \Phi L'\mathrm{d}\boldsymbol{\Omega}'\right)\,\mathrm{d}\boldsymbol{\Omega} - \int_{4\pi} \boldsymbol{n}\mu_a L\,\mathrm{d}\boldsymbol{\Omega} \tag{3.20}$$

describes the conservation of the radiative flux.

$$\frac{\partial \boldsymbol{F}}{c\partial t} + \nabla \boldsymbol{P} = \mu_s(-\boldsymbol{F} + \boldsymbol{F}') - \mu_a \boldsymbol{F} \tag{3.21}$$

[6] the energy conservation in scattering events requires $\int_{4\pi} \mu_s\left(-L + \frac{1}{4\pi}\int_{4\pi} \Phi L' d\boldsymbol{\Omega}'\right)\,\mathrm{d}\boldsymbol{\Omega} = 0$.

Herein, $\boldsymbol{F'}$ replaces the first moment of the in-scattering term, thus,

$$\boldsymbol{F'} = \int_{4\pi} \boldsymbol{n} \left(\frac{1}{4\pi} \int_{4\pi} \Phi L' \mathrm{d}\boldsymbol{\Omega'} \right) \mathrm{d}\boldsymbol{\Omega} \tag{3.22}$$

The solution of the convolution integral in Eq. (3.22) can just be obtained a priori if scattering is isotropic ($g = 0$) , thus $\boldsymbol{F'} = 0$. Therefore, Eq. (3.21) becomes

$$\frac{\partial \boldsymbol{F}}{c\partial t} + \nabla \boldsymbol{P} = -(\mu_s + \mu_a)\boldsymbol{F} \tag{3.23}$$

In order to solve the equation system (3.19), (3.21), or respective (3.23), additional closures are required. Commonly, angular isotropy of radiance is assumed, resulting in the Eddington approximation which relates the radiation energy to the diagonal components of the pressure tensor by $P = I/3$ [240]. Plugging this relation into (3.23) and dropping the time derivatives gives an expression for the radiative flux which can be combined with (3.19) to yield the Diffusion Approximation (DA)

$$\frac{1}{3\mu_a(\mu_s + \mu_a)} \nabla(\nabla I) - I = 0 \tag{3.24}$$

Eq. (3.24) can be solved by means of different numerical schemes for parabolic equations. It should be mentioned at this point that the DA is not similar to the isotropically scaled RTE, even if similar assumptions are made. The expression $D = (\mu_a(\mu_s + \mu_a))^{-1}$ is termed the diffusion coefficient. For anisotropic scattering, the reduced scattering coefficient μ_s' is used instead of μ_s, which is related to a isotropic scaling of the anisotropic phase function to isotropic scattering (see 3.3.2). There are also alternative ways to derive the DA from the RTE (or the Boltzmann-Lorentz model, respectively), e.g. by expanding radiance in first order spherical harmonics prior to the integration [240], or replacing the scattering terms in (3.10) by the relaxation time approximation (BGK-approximation) [205]. The latter assumes that the relaxation rate to equilibrium is a linear function of the non-equilibrium parts of the distribution function and of a time constant which is related to the transport mean free path $1/\mu_s'$. The accuracy of the DA is limited by definition to situations where radiance is close to equilibrium, which requires that photons are scattered many times in the domain of interest. This condition is particularly violated near sources emitting collimated radiation [241]. A number of alternative closures and flux limiters were suggested, see e.g. [242–244], in order to extend the applicability of hydrodynamic models to the kinetic (or ballistic) conditions. However, it was shown that the accuracy or validity of these approaches is limited [240]. With regard to the utilization of the DA for predicting light transfer in microalgae cultures one should note that the assumption of radiance close to equilibrium usually does not reflect the conditions in highly absorbing media[7]. On the one hand this is because

[7] The length of the random walk is limited by the absorption length [245] so that photons might be absorbed before the information about the initial distribution is completely lost.

strong absorption counteracts the equilibration process and, moreover, the forward scattering along a short light path results in equilibration lengths in the same order as the geometrical dimensions[8]. A discussion on this topic can be found in chapter 6. Further details concerning the DA can also be found in Refs. [168, 246].

3.4. Concluding remarks

Different models for light transfer were introduced and discussed with regard to their applicability in photobioreactors. The overall light field in a photobioreactor is determined by the type and arrangement of light sources and the radiation characteristics of the cell suspension, which change in time due to biomass growth and adaption of the pigmentation (see 3.1). Due to its simplicity, Lambert's law is commonly applied to predict light fields in photobioreactors regardless of its well known weakness of neglecting scattering (see 3.2.1, 3.2.2). The Radiation Transfer Equation (RTE) is the most accurate and flexible model but its numerical solution is still challenging (see 3.3.1, 3.3.3). Since the RTE is a Boltzmann-type transport equation, a lattice-Boltzmann algorithm could be regarded as a natural choice for the discretization and solution of the RTE, what will be substantiated in chapters 5 and 6. Although all of the mentioned models were utilized for computing light distributions in photobioreactors, not much work was done concerning their systematic comparison or on the impact of uncertain model parameters on the predicted light distributions. Therefore, a further discussion of these aspects will be provided in chapter 10.

[8]The equilibration length is given by the inverse of the reduced scattering coefficient (see 3.1).

4. Lattice Boltzmann Methods

The lattice Boltzmann method (LBM) is an emerging tool for fluid dynamical simulations. In recent years several extensions of the standard lattice Boltzmann framework for fluid flows were proposed to cover the simulation of other physical transport problems. One of these is radiation transfer, which is also the focus of this chapter. First a brief review of kinetic theory is provided being the underlying physical framework of lattice Boltzmann methods. Thereafter, basic principles of the standard LBM for fluid flows will be outlined. The main part of the chapter focuses on concepts and approaches concerning the solution of the Radiation Transfer equation within the lattice Boltzmann framework.

4.1. Origin of the lattice Boltzmann method: Kinetic Theory

4.1.1. The Boltzmann model

The physical origin of lattice Boltzmann methods lies in the kinetic theory of gases. Within this concept it is assumed that fluids consist of a large number of freely moving particles which interact exclusively via elastic collisions (e.g. see [204, 209, 247]). The treatment of the particle population occurs in a statistical way, where the particle distribution function $f(\boldsymbol{x}, \boldsymbol{\xi}, t)$ is the fundamental quantity describing the distribution of the particle population in the phase space[1]. The variables t, $\boldsymbol{x}$, $\boldsymbol{\xi}$ denote for the temporal, spatial and velocity coordinates, respectively. The temporal evolution of f is governed by the Boltzmann-Equation (BE), which reads

$$\left(\frac{\partial}{\partial t} + \boldsymbol{\xi}\nabla_{\boldsymbol{x}} + \frac{\boldsymbol{F}_{ex}}{m}\nabla_{\boldsymbol{\xi}}\right) f(\boldsymbol{x}, \boldsymbol{\xi}, t) = \Omega_C[f] \tag{4.1}$$

The first two terms on the left-hand side stand for the accumulation and convective transport of particles. The acceleration (convection in $\boldsymbol{\xi}$) of particles of mass m by external forces $\boldsymbol{F}_{ex}$ is covered in the third term. On the right-hand side, $\Omega_C[f]$ is the collision operator, which depends on the distribution function itself and describes its evolution in time due to elastic interparticle collisions. A general notation of the collision operator can be obtained by balancing the losses and gains of $f(\boldsymbol{x}, \boldsymbol{\xi}, t)$ in collisions

[1] In statistical mechanics, the phase space is six-dimensional and contains the information of position $\boldsymbol{x}$ and momentum $m\boldsymbol{\xi}$ of a particle population.

with particles carrying the momentum $\boldsymbol{\xi}_1$, thus $f_1 = f(\boldsymbol{x}, \boldsymbol{\xi}_1, t)$. A mathematical description of these collision processes (see e.g. [209]) results in the collision operator

$$\Omega_C[f] = \int_{\boldsymbol{\xi}_1} \int_{\boldsymbol{\Omega}} \sigma(\boldsymbol{\xi}, \boldsymbol{\xi}_1 | \boldsymbol{\xi}', \boldsymbol{\xi}_1')(f' f_1' - f f_1) |\boldsymbol{\xi} - \boldsymbol{\xi}_1| \mathrm{d}\boldsymbol{\Omega} \mathrm{d}\boldsymbol{\xi}_1 \tag{4.2}$$

Herein, the primed quantities stand for the post-collisional states and σ for the differential collision cross-section, which defines the probability of the collision $\{\boldsymbol{\xi}, \boldsymbol{\xi}_1\} \rightarrow \{\boldsymbol{\xi}', \boldsymbol{\xi}_1'\}$ in terms of the solid angle $\boldsymbol{\Omega}$. The collision operator conserves the mass, momentum and energy of the particle population and fulfills microreversibility and the H-theorem. In the limit of low Knudsen numbers[2], thus $Kn \ll 1$, collisions dominate over convection and determine the local evolution of f. In this regime the collision operator is commonly approximated by the Bhatnagar-Groos-Krook (BGK) operator, which assumes that the relaxation of f towards a local equilibrium distribution f^{eq} is a linear function of the non-equilibrium part of f and a kinetic constant τ^{-1}. The BGK approximation reads

$$\Omega_C[f] = -\frac{1}{\tau} f^{neq} = -\frac{1}{\tau}(f - f^{eq}) \tag{4.3}$$

where the equilibrium distribution f^{eq} is given by the Maxwell-Boltzmann distribution

$$f^{eq} = \frac{\rho}{(2\pi c_s^2)^{3/2}} \exp\left(\frac{(\boldsymbol{\xi} - \boldsymbol{u})^2}{2c_s^2}\right) \tag{4.4}$$

with the speed of sound $c_s = \sqrt{RT}$ which is related to the temperature T via the fundamental gas constant R. The equilibrium depends on the local macroscopic flow field being represented by the fluid density ρ, velocity $\boldsymbol{u}$ and kinetic energy e. The particle distribution function and the equilibrium distribution are related to these quantities via the respective velocity moments

$$\rho(\boldsymbol{x}, t) = \int_{\boldsymbol{\xi}} f \mathrm{d}\boldsymbol{\xi} = \int_{\boldsymbol{\xi}} f^{eq} \mathrm{d}\boldsymbol{\xi} \tag{4.5}$$

$$\rho \boldsymbol{u}(\boldsymbol{x}, t) = \int_{\boldsymbol{\xi}} \boldsymbol{\xi} f \mathrm{d}\boldsymbol{\xi} = \int_{\boldsymbol{\xi}} \boldsymbol{\xi} f^{eq} \mathrm{d}\boldsymbol{\xi} \tag{4.6}$$

$$\rho e(\boldsymbol{x}, t) = \frac{1}{2} \int_{\boldsymbol{\xi}} |\boldsymbol{\xi} - \boldsymbol{u}|^2 f \mathrm{d}\boldsymbol{\xi} = \frac{1}{2} \int_{\boldsymbol{\xi}} |\boldsymbol{\xi} - \boldsymbol{u}|^2 f^{eq} \mathrm{d}\boldsymbol{\xi} \tag{4.7}$$

It can be shown by means of the Chapman-Enskog expansion that the solution of the Boltzmann-BGK model is similiar to the Navier-Stokes solution of the flow field if the collision frequency is properly related to the material transport coefficients. This important finding is the basis for the lattice-Boltzmann method and its capability to solve hydrodynamic flow problems.

[2]The Knudsen number relates the mean free path of the particle population l_{mfp} to a characteristic system length L_0, therefore $Kn = l_{mfp}/L_0$. The mean free path is related to the kinematic viscosity ν of the fluid by $l_{mfp} c_s = a\nu$, where c_s is the speed of sound and a a constant [247].

4.1.2. The Boltzmann-Lorentz model

The Boltzmann-Lorentz model is a linear variant of the Boltzmann model. It considers the kinetics of freely moving point-like particles interacting in elastic collisions with randomly distributed stationary particles of much higher mass [204, 209]. Collisions in this system depend on the momentum of the point particles but remain the momentum of the stationary particles unchanged. The kinetic equation for the point-like particles is called Boltzmann-Lorentz equation (BLE) and has a structure similar to the gas kinetic Boltzmann equation, Eq. (4.1). The different model representations for collisions in both systems are fully captured in their respective collision operator. In case of the Boltzmann-Lorentz model the operator just contains the pre- and post-collisional states of the light particle population while the impact of the stationary particles is covered in the collision cross-section σ. A complete derivation of the collision operator for the Boltzmann-Lorentz model is given by [209]. The final collision model reads

$$\Omega_C[f] = |\boldsymbol{\xi}| \int_{\boldsymbol{\Omega}} \sigma(\boldsymbol{\xi}|\boldsymbol{\xi}')(f' - f)\mathrm{d}\boldsymbol{\Omega}' \tag{4.8}$$

which can be rearranged to

$$\begin{aligned} \Omega_C[f] &= |\boldsymbol{\xi}| \int_{\boldsymbol{\Omega}} \sigma(\boldsymbol{\xi}|\boldsymbol{\xi}')f'\mathrm{d}\boldsymbol{\Omega}' - |\boldsymbol{\xi}| \int_{\boldsymbol{\Omega}} \sigma(\boldsymbol{\xi}|\boldsymbol{\xi}')f\mathrm{d}\boldsymbol{\Omega}' \\ &= |\boldsymbol{\xi}| \int_{\boldsymbol{\Omega}} \sigma(\boldsymbol{\xi}|\boldsymbol{\xi}')f'\mathrm{d}\boldsymbol{\Omega}' - |\boldsymbol{\xi}| f \Sigma(\boldsymbol{\xi}|\boldsymbol{\xi}') \end{aligned} \tag{4.9}$$

It can be seen that Eq. (4.9) is similar to the Radiation Transfer Equation, Eq. (3.10), if the differential cross-section and single speed particle velocity are set to $\sigma = \mu_s \Phi$ and $\boldsymbol{\xi} = c\boldsymbol{n}$, respectively and it applies that the particle distribution function is proportional to radiance, thus $f \propto L$. Indeed, a linear relation

$$f = \frac{\lambda^3}{h^4 c} L_\lambda = \zeta L_\lambda \tag{4.10}$$

between radiance at a certain wavelength and the photon distribution function exists [203], where ζ is a constant of proportionality. Thus, for the special case of particles with equal speed the RTE becomes similar to the BLE with an additional sink term for absorption.

The adoption of the Boltzmann-Lorentz model for photon kinetics involves some important aspects. First, the three-dimensional momentum space of radiance includes the one-dimensional frequency space. At constant frequency the momentum space for radiance is therefore two-dimensional and collisions only change the direction of propagation but not the particle speed or frequency. Second, because the collisions occur with static matter, the macroscopic momentum of the radiation field is not conserved. Even if the absolute momentum on the moving particles remains constant during collisions, $|c\boldsymbol{n}| = |c\boldsymbol{n}'|$, the average direction of propagation becomes increasingly isotropic. This is in accordance to the statement made in section 3.3.5 that multiple scattering drives the particle distribution function

towards an isotropic equilibrium state with zero mean velocity. The rate of relaxation is a function of the Knudsen number and complete isotropy is typically found in the limit of low Knudsen numbers. In this regime, radiation transport becomes diffusive. Finally, the transport of radiance can be ballistic at low Knudsen numbers due to the emission characteristic of the source. An example for this is the illumination of a turbid medium by laser light, where the ballistic irradiance equilibrates inside the medium but ballistic transport occurs near the source. The transition from the ballistic to the diffusive regime is therefore a typical situation in radiation transport problems.

4.2. The lattice Boltzmann method for flow problems

The lattice Boltzmann method (LBM) was originally developed as an alternative method for the solution of flow problems. The first approaches date back to the late 1980s [248] and base on the improvement of lattice gas automata [249]. Since then a huge amount of research was spent into the development of the method and several monographs [250–254] and reviews [255, 256] provide a comprehensive overview about fundamentals, recent developments and applications. The goal of this section is to briefly summarize the basic principles of the method in order to provide a methodological basis for the following sections.

The basic idea behind the LBM is to solve a discretized Boltzmann equation on a regular grid (lattice) in order to approximate the solution of a macroscopic target equation (e.g. the Navier-Stokes equations) from the velocity moments of the discrete particle distribution function. Thereby, the discretization of the Boltzmann equation includes the temporal, spatial and velocity dimensions. A possible route to achieve the discretized Boltzmann equation is to follow a two-step procedure, which consists of the discretization of the momentum space in a first step and thereafter of the spatio-temporal discretization of the discrete velocity Boltzmann equation via the method of characteristics [252, 254]. The discretization procedure can also be applied vice versa [257].

The starting point for the discretization is the Boltzmann-BGK model equation without external forces

$$\left(\frac{\partial}{\partial t} + \boldsymbol{\xi}\nabla_{\boldsymbol{x}}\right) f(\boldsymbol{x}, \boldsymbol{\xi}, t) = -\frac{1}{\tau}(f - f^{eq}) \tag{4.11}$$

To achieve the discrete velocity Boltzmann equation (DVBE), the continuous velocity variable $\boldsymbol{\xi}$ is replaced by discrete velocities $\boldsymbol{\xi_i}$ and the respective discrete particle populations $f_i = w_i f(\boldsymbol{x}, \boldsymbol{\xi_i}, t)$ are introduced. The DVBE reads

$$\left(\frac{\partial}{\partial t} + \boldsymbol{\xi}_i\nabla_{\boldsymbol{x}}\right) f_i(\boldsymbol{x}, t) = -\frac{1}{\tau}(f_i - f_i^{eq}) \tag{4.12}$$

The choice of the discrete velocities in the LBM is determined by the regular arrangement of the spatial lattice due to the restriction that the discrete particles are only allowed to move between adjacent lattice

nodes. The discrete velocity vector is thus given by $\boldsymbol{\xi_i}\Delta t = (\Delta x_i, \Delta y_i, \Delta z_i)$ and the discrete speed by $\xi_i = |\boldsymbol{\xi_i}|$. The basic idea behind the discretion procedure of the velocity space is to construct a quadrature rule which ensures that the velocity moments of the discrete particle distribution function can be computed exactly up to a certain order. For standard lattice Boltzmann models[3] the weighting coefficients w_i are given by the Gauss-Hermite quadrature and the abscissas are represented by $\boldsymbol{\xi_i}$. The combination of discrete velocities and weights is termed a velocity set. The usual nomenclature for specific sets is $DnQm$, where n denotes for the spatial dimension and m for the number of discrete populations. In this discrete representation Eqs. (4.5)-(4.7) can be re-written as

$$\rho(\boldsymbol{x}, t) = \sum_{i=1}^{m} f_i = \sum_{i=1}^{m} f_i^{eq} \tag{4.13}$$

$$\rho\boldsymbol{u}(\boldsymbol{x}, t) = \sum_{i=1}^{m} \boldsymbol{\xi_i} f_i = \sum_{i=1}^{m} \boldsymbol{\xi_i} f_i^{eq} \tag{4.14}$$

$$\rho e(\boldsymbol{x}, t) = \frac{1}{2}\sum_{i=1}^{m} |\boldsymbol{\xi_i} - \boldsymbol{u}|^2 f_i = \frac{1}{2}\sum_{i=1}^{m} |\boldsymbol{\xi_i} - \boldsymbol{u}|^2 f_i^{eq} \tag{4.15}$$

The idea of constructing a quadrature on basis of predefined abscissas to obtain exact representations of the integrals (4.5)-(4.7) is a fundamental characteristic of the LBM and differentiates the method from other discrete velocity schemes. Because the populations f_i are unknown a priori, the construction of the quadrature is based on the discrete equilibrium function f_i^{eq}. To derive f_i^{eq}, the Maxwell-Boltzmann distribution, Eq. (4.4), is taylor-expanded around $\boldsymbol{u}$ up to second order, whereby terms arise which depend on the Mach number $Ma = |\boldsymbol{u}|/c_s$ up to $\mathcal{O}(Ma^4)$. The final discrete equilibrium function is achieved by neglecting all terms with Mach number dependence higher than $\mathcal{O}(Ma^2)$ (low Mach number approximation) causing the limited applicability of the standard LBM to weakly incompressible flows. The discrete equilibrium distribution reads [255]

$$f_i^{eq} = w_i \rho \left(1 + 3(\boldsymbol{\xi}_i \cdot \boldsymbol{u}) + \frac{9}{2}(\boldsymbol{\xi}_i \cdot \boldsymbol{u})^2 - \frac{3}{2}u^2\right) \tag{4.16}$$

A more general way to achieve Eq. (4.16) is the expansion of (4.4) in Hermite Polynomials [252].

The second step of the discretization procedure is the spatio-temporal discretization of Eq. (4.12) for which the Method of Characteristics (MOC) is applied. While the left-hand side of (4.12) can be

[3]The term standard model refers here to frequently used velocity sets which share the property that only transport between adjacent lattice nodes is allowed. Higher orders can be achieved by extending the number of discrete velocity vectors and accompanying with transport over two or more layers in the lattice.

integrated exactly, the explicit first-order Euler method is used to integrate the right-hand side along a characteristic. The final lattice-Boltzmann equation reads

$$f_i(\boldsymbol{x} + \boldsymbol{\xi}_i \Delta t, t + \Delta t) - f_i(\boldsymbol{x}, t) = -\frac{\Delta t}{\tau}(f_i - f_i^{eq}) \tag{4.17}$$

Although at first glance it seems that the method is first order accurate, in fact it is second order accurate due to the diffuse scaling of the physical material transport coefficient (here the kinematic viscosity ν) in order to obtain the dimensionless relaxation time $\tilde{\tau}$. The scaling relation contains the physical time step Δt and grid spacing Δx and reads

$$\tilde{\tau}^{-1} = \frac{\Delta t}{\tau} = \frac{\nu}{\tilde{c_s}^2}\frac{\Delta t}{(\Delta x)^2} + \frac{1}{2} \tag{4.18}$$

where $\tilde{c_s} = 1/3$ is the lattice speed of sound. The definition of $\tilde{\tau}$ according to (4.18) ensures that the Navier-Stokes equations are recovered from the lattice Boltzmann Equation on the macroscopic level, what can be demonstrated by means of the Chapman-Enskog expansion technique.

A stream-and-collide algorithm is employed in order to solve the model equation (4.17). The underlying assumption is that collisions occur on the lattice nodes so that the right-hand side of (4.17) can be treated locally. In the streaming step, the post-collisional populations are shifted to the adjacent lattice nodes with their respective discrete velocities.

In summary, some major characteristics of the LBM can be identified. First, the usual introduction of the BGK collision operator restricts the applicability of the method to situations where the distribution function is close to a local equilibrium. This is usually true in the limit of low Knudsen numbers. Second, the discretization of the velocity space ensures that the properties of the macroscopic flow are exactly calculated by the velocity moments of the discrete particle density distributions f_i as given by Eqs. (4.5)-(4.7) . This requires a careful choice of the quadrature weights for abscissas given by the discrete velocity vectors. Third, a desired macroscopic behavior can be achieved by applying multiscale expansion techniques and searching for adequate relations between the collision rate and macroscopic transport coefficients for a specific equilibrium distribution. This is in accordance to the above made statement that the goal of the standard LBM is the approximation of a macroscopic target equation. Fourth, the solution of the model is obtained by an efficient stream-and collide algorithm which treats local collisions and convection separately.

4.3. Lattice Boltzmann methods for radiation transfer

4.3.1. Pioneer works

The idea behind radiation transfer lattice Boltzmann models is to use the beneficial characteristics of the LBM to solve the radiation transfer equation, Eq. (3.10), respectively the Boltzmann-Lorentz model as given by Eqs. (4.1) and (4.9), or an macroscopic asymptotic approximation of these equations. Thereby, the formulation of the standard LBM needs to be adapted to cover the Boltzmann-Lorentz collision operator or an approximation of it. The attractiveness of the lattice Boltzmann framework lies in the simple structure of the model equation, Eq. (4.17), the efficient stream-and-collide algorithm as well as its potential for parallel computation.

First works on the radiation transfer lattice Boltzmann methods (RT-LBM) were done in the field of image rendering. In 2004, Geist et al. [258] suggested a three-dimensional lattice Boltzmann model for radiation transfer calculations. The main idea is that in a discrete representation the RHS of Eq. (3.10) can be computed by a matrix multiplication,

$$-\mu_s L + \mu_s \frac{1}{4\pi} \int_{4\pi} \Phi L' \mathrm{d}\boldsymbol{\Omega}' - \mu_a L + S \approx \boldsymbol{\Theta} L_i \tag{4.19}$$

where the scattering kernel, absorption and local emission S are fully determined by the entries of an update matrix $\boldsymbol{\Theta}$ acting on the discretized radiance L_i. The discretization of the time-domain leads to the model equation of the RT-LBM

$$f_i(\boldsymbol{x} + \boldsymbol{c}_i \Delta t, t + \Delta t) = f_i(\boldsymbol{x}, t) + \boldsymbol{\Theta}_{i,\cdot} \boldsymbol{f}(\boldsymbol{x}, t) \tag{4.20}$$

for a D3Q19 discretization of the velocity space with abscissas $\boldsymbol{c}_i$ and corresponding weighting coefficients w_i. For an isotropic scattering matrix, Eq. (4.20) was shown to solve a macroscopic diffusion equation. To account for anisotropic scattering the entries of the update matrix $\boldsymbol{\Theta}$ were manipulated with coefficients $p_{i,j}$, which were determined by evaluating the Henyey-Greenstein phase function at the nodes of the angular quadrature and a subsequent normalization step ensuring energy conservation, thus

$$\boldsymbol{\Theta}_{i,j} = \mu_s w_i \frac{p_{i,j}}{\sum_{j=1}^{18} p_{i,j}} \tag{4.21}$$

with

$$p_{i,j} = \frac{1 - g^2}{(1 + g^2 - 2g\boldsymbol{n}_i \boldsymbol{n}_j)^{3/2}} \tag{4.22}$$

and $\boldsymbol{n}_i = \boldsymbol{c}_i / |c_i|$. A drawback of the model is that the achieved update matrix lacks in conserving the anisotropy of the phase function for $g > 0.4$, which can be quickly validated by a numerical evaluation (see also Eq. (3.5)). In the Discrete Ordinate Method (DOM), which can be related to the

lattice Boltzmann method [259], a similar error is known being termed as false angular scattering [221]. For non-diffusive transport, the effect of false angular scattering is reflected in the convective energy fluxes and therefore affects the spatial energy distribution. The authors did not validate their model by comparing the results to numerical data and also grid convergence was not investigated. However, the underlying concept of the model provides an innovative starting point for further developments.

Later works originated from the heat transfer community. Asinari et al. [260] suggested a 2D lattice Boltzmann model for radiation transfer in an absorbing, emitting and isotropically scattering medium in radiative equilibrium. The model equation

$$f_i(\boldsymbol{x} + \boldsymbol{c}_i \Delta t, t + \Delta t) = f_i(\boldsymbol{x}, t) - \frac{1}{\tilde{\tau}_i} \left(f_i(\boldsymbol{x}, t) - f_i^{eq}(\boldsymbol{x}, t) \right) \tag{4.23}$$

incorporates the whole radiation-matter interaction in the equilibrium function, which evenly redistributes the energy to the discrete particle populations. Although not explicitly shown by the authors, it is likely that the model solves a macroscopic diffusion equation in the limit of low Knudsen numbers. It should be noted that the formulation of the equilibrium function in their paper

$$f_i^{eq} = \sum f_i w_i \tag{4.24}$$

deviates from a standard diffusive lattice Boltzmann model, which would be $f_i^{eq} = w_i \sum f_i$ [252]. The angular discretization seems to be pretty much inspired by the DOM and stencils with up to 32 discrete velocities were proposed. The corresponding weighting coefficients were chosen somewhat randomly and are not motivated by ensuring the exact computation of the higher order velocity moments as usual for lattice Boltzmann models in fluid mechanics. This limits the extension of the model to situations were the radiation transport is non-diffusive. However, since the model is diffusive, a sufficient condition for the quadrature is energy conservation, what is ensured by the model. It should also be noted that unlike to classical LBM schemes, the collision time constant $\tilde{\tau}_i$ is direction dependent and scales with the magnitude of the respective discrete velocities and the extinction coefficient.

Ma et al. [261] presented a lattice Boltzmann model for 1D radiative transfer (D1Q2). The model equation

$$f_i(\boldsymbol{x} + \boldsymbol{c}_i \Delta t, t + \Delta t) = f_i(\boldsymbol{x}, t) - \frac{1}{\tilde{\tau}} \left(f_i(\boldsymbol{x}, t) - f_i^{eq}(\boldsymbol{x}, t) \right) + S \Delta t - \mu_a f_i(\boldsymbol{x}, t) \Delta t \tag{4.25}$$

considers the energy transport in an absorbing and emitting medium and contains a collision term although scattering is not included. The collisional relaxation towards a local equilibrium function is

designed in such a way that a diffusive behavior on the macroscopic scale is achieved. The equilibrium distribution

$$f_i^{eq} = \frac{1}{2}\left(I + \frac{c_i F}{c^2}\right) \tag{4.26}$$

is found by means of the Chapman-Enskog expansion and can be computed from the macroscopic variables of the radiation field, see Eqs. (3.11) and (3.12). The general concept behind this model differs from the previous ones in such a way that the model equation cannot be considered as a discretized version of the physical transport model. Instead, the model is explicitly designed to recover a certain macroscopic behavior of the radiative flow.

In summary, the three presented models can be classified into two groups. The mesoscopic models of Geist et al. [258] and Asinari et al. [260] are based on a direct discretization of the RTE and the solution of the numerical model by means of a stream-and-collide algorithm. This approach can be seen to be related to the Discrete Ordinate Method. Depending on the specific model and the selected equilibrium distribution, a certain macroscopic behavior is achieved which in principle can range from ballistic to diffusive transport. The approach of Ma et al. [261] differs therefrom by designing a lattice Boltzmann model in order to approximate the solution of a specific macroscopic target equation, e.g. a diffusion equation. Therefore, the applicability of a macroscopic model is limited to the regime described by the target equation. As outlined before (see 3.3.5), radiation transfer becomes diffusive in the limit of low Knudsen numbers. In contrast, there is no adequate macroscopic formulation capturing the ballistic regime or the transition to the diffusive regime. Solving radiation transfer in these regimes therefore requires the direct solution of the mesoscopic model equation. Both approaches were extended as outlined in the next sections.

Table 4.1.: Comparison of characteristic features of different lattice Boltzmann models for radiation transfer.

Author	Approach	Quadrature	Convergence	Anisotropy	Asymptotic behavior
Geist [258]	Mesoscopic	D3Q19	n.s.*	yes	diffusive
Asinari [260]	Mesoscopic	D2Q8	n.s.*	no	diffusive
		D2Q16			
		D2Q32			
Ma [261]	Macroscopic	D1Q2	n.s.*	no	diffusive

* not specified

4.3.2. Mesoscopic approaches

A systematic analysis of previous models and their extension was conducted by Bindra and Patil [262]. They extended the models of Ma [261] and Asinari [260] by approximating the scattering integral as a summation over the discrete velocity space. Essentially, this approach is equal to the update matrix

formulation of Geist et al. [258]. Moreover, anisotropic scattering was considered in terms of a linear phase function. The work was later extended by McCulloch and Bindra [263] who introduced a higher order velocity discretization and showed that the model convergence rate is of first order. Gairola and Bindra [264] applied the extended model to simulate 2D benchmark problems. They concluded that the accuracy of the achieved solutions is similar to the DOM, including the occurrence of the ray-effect (see 3.3.3).

Zhang et al. [265] extended the one-dimensional model of Ma et al. [261] to study transient radiation transfer in graded index [266] or multi-layered [267] media with diffuse or fresnel boundaries [268, 269]. Deviating from Ma's original approach of approximating diffusive radiation transport, typical features of other mesoscopic models were incorporated into the model. For example, the discretization of the scattering integral and the treatment of anisotropic scattering was adopted from Bindra and Patil [262], while the velocity discretization follows the approach of Asinari's model [260]. Additionally, an implicit time stepping scheme was proposed. Although good agreement to reference simulations was found, some key features of the model were not described adequately. These contain the specification of the quadrature weights or the convergence order of the model. A further extension of the scheme to two-dimensional domains was later proposed by Patidar et al. [270, 271] in order to simulate transient light propagation in laser-irradiated tissue phantoms. In their work, they computed the quadrature weights for the two-dimensional velocity set similarly to Asinari et al. [260]. Since they consider the transition from the ballistic to the diffusive transport regime, the arbitrary selection of the weighting coefficients in Asinari's model implies the erroneous computation of macroscopic radiation fluxes and pressure beyond the diffusive regime (see also 4.3.1). Little attention is paid to this issue throughout the literature, although the choice of a quadrature which guarantees an exact evaluation of the discrete velocity moments up to a certain order is a characteristic feature of the standard LBM [252, 257].

The above mentioned issues concerning the discretization of the velocity space also impede the derivation of mesoscopic models for three-dimensional radiative transfer. Accordingly, except from the model of Geist et al. [258] and the model being developed in this work (see chapter 5), no mesoscopic model for three-dimensional radiative transfer was published to date. This might be related to the fact that rotational invariance of the discrete velocity space is a key requirement for three-dimensional models. Considering that the quadrature weights in Asinari's model and all models based thereon are derived from the explicit computation of integrals in polar coordinates, a similar procedure in three dimensions would require the integration over the unit sphere. In spherical coordinate systems singularities exist at the poles so that rotational invariance cannot be achieved by integration over solid angles. Therefore, the discretization of the velocity space should be done in a similar procedure as in the standard LBM, namely to derive the abscissas and weights of the velocity set in order to exactly

compute higher order velocity moments. The discussion so far indicates that some of the recent models lack a fundamental theoretical background on which further developments should be build on.

4.3.3. Macroscopic approaches

Models for macroscopic radiation transfer are considered more rarely in comparison to mesoscopic formulations. Mink et al. [272] proposed a model for diffusive radiation transport in three dimensions. The underlying physical equation is the Diffusion Approximation for radiation transfer with the sink term accounting for absorption, see Eq. (3.24). The model is based on a D3Q7 velocity set which is known to be sufficient for diffusive transport problems because only the zeroth velocity moment needs to be calculated. By applying diffuse scaling of the transport coefficients the model reaches second order accuracy in space and time. Both, the discretization of the velocity space and the convergence order make this model superior to mesoscopic formulations for the computation of diffuse radiation transport. For instance, Asinari et al. [260] used stencils with up to 32 discrete velocities for diffusive radiation transport in two dimensions while the macroscopic model of Mink et al. only needs 7 discrete velocities in three dimensions. Obviously, this is related to a tremendous reduction of the computational costs. On the other hand, the model is limited to situations where the Diffusion Approximation is accurate.

In order to provide a lattice Boltzmann model for radiation transfer beyond the diffusive regime, Yi et al. [273] proposed a model which is based on the extension of the mesoscopic RTE with an artificial term accounting for diffusion. From a physical point of view, this approach is quite problematic because diffusive transport is a macroscopic phenomenon which results from collisions on the mesoscale or respective microscale [247]. Moreover, no strict distinction between mesoscopic and macroscopic transport equations is made and the relationship of both via the velocity moments (see Eqs (3.18) - (3.21)) is not taken into account. Due to these inconsistencies the model of Mink et al. [272] must be considered to be the only reliable macroscopic radiation transfer lattice Boltzmann model to date.

4.3.4. Initial and boundary conditions

The boundary conditions applied for the different radiation transfer lattice Boltzmann models include inflow, outflow and sometimes reflective boundary conditions. Generally, the complexity of inflow and reflective boundary conditions can increase significantly in the case of two or three spatial dimensions. However, due to the fact that mainly test cases were considered in the literature, not much attention has been paid to the treatment of boundary conditions.

Inflow or source boundary conditions are most often modeled to diffusively emit a certain amount of energy ρ into the domain [260–264, 272]. Mathematically, this type of boundary condition can be expressed as

$$f_i = w_i \rho(\boldsymbol{x}_B) \tag{4.27}$$

where $\rho(\boldsymbol{x}_B)$ denotes the energy density at the boundary locations $\boldsymbol{x}_B$. In the field of heat transfer $\rho(\boldsymbol{x}_B)$ is usually expressed in terms of temperature. In this context the expressions hot and cold[4] walls are frequently used. Generally, $\rho(\boldsymbol{x}_B)$ can also be a function of the time-dependent temperature $T(\boldsymbol{x}_B, t)$. A different approach was used by Mink et al. [272] who set the diffusely emitted energy density at the boundary according to the analytical solution of their test problem. In some works also non-diffusive emission is considered. For the purpose of image rendering Geist et al. [258] considered the directed illumination of the scene in their simulations. They developed an algorithm to distribute the energy of the incoming light on the discrete populations at the boundary in order to match the macroscopic light influx $\rho(\boldsymbol{x}_B)\boldsymbol{u}(\boldsymbol{x}_B)$. The special treatment is necessary because the distribution function at the boundaries can be far from the equilibrium distribution so that the well-established inflow boundary conditions in the standard LBM for flow problems cannot be applied. A different treatment of collimated inflow of energy (e.g. laser illumination of the domain of interest) is proposed in the works [265, 270, 271, 274]. Here, the radiative energy is split into a collimated and a diffusive component from which just the former is an energy source at the boundary (intensity splitting). The energy density at the boundary is constant and the propagation of the collimated component into the domain is modeled with Lambert's law. A transition from collimated to diffuse radiation in the domain occurs via the consideration of local source and sink terms. This approach is also used in the Discrete Ordinate Method to mitigate the ray effect in case of small source dimensions.

At walls, radiation either leaves the domain or is (partially) reflected. Outflow conditions without reflection are usually modeled with Dirichlet boundary conditions by simply setting $\rho(\boldsymbol{x}_B) = 0$ [258, 261–264]. As discussed in Ref. [258], the assumption of periodic boundary conditions does not match the physical nature of radiation problems. Instead, steady-state solutions of the transport problem are achieved by assuming a constant in- and outflow of energy across the boundaries of the domain. Reflective boundary conditions are rarely considered for radiation transfer lattice Boltzmann models and are mainly limited to one dimensional models [265, 267, 268]. For two- or three-dimensional models no reflective boundary conditions are reported. Similarly, the treatment of curved boundary conditions in the RT-LBM is unsolved to date.

A typical initial condition is to assume the domain as dark, meaning $\rho(\boldsymbol{x}, t_0) = 0$ [262, 264]. With open outflow boundaries the initial condition has no impact on the accuracy of the solution but can affect the computational time required to reach a stationary solution.

[4] The wall has an absolute temperature of zero.

4.4. Concluding remarks

Lattice Boltzmann methods are a quite new class of solvers for radiation or light transfer problems. The proposed models cover mesoscopic and macroscopic approaches. Predominantly, diffusive radiation transport is addressed although, also the ballistic regime can be captured in principal by mesoscopic models. However, most of the developed models lack a fundamental theory and are not in accordance with basic concepts of the lattice Boltzmann framework. This pertains particularly to the choice of the quadrature rule, which represents the discretization of the velocity space. In consequence, no mesoscopic model for three-dimensional radiation transfer has been proposed to date. In addition, the treatment of anisotropic scattering has rarely been addressed in the literature. Within the scope of this work a new lattice Boltzmann model for three-dimensional light transfer in suspensions of absorbing and anisotropic scatterers will be proposed in chapters 5, 6 and further extensions and improvements will be discussed in part III.

Part II.

Research

5. New lattice Boltzmann method for the simulation of three-dimensional radiation transfer in turbid media

The chapter describes the theoretical framework of the developed lattice Boltzmann method for light transfer. Key features like the spatio-temporal and angular discretization as well as an algorithm for the discretization of the scattering phase function are developed. Simulation results are validated by Direct Simulation Monte Carlo.

In contrast to lattice Boltzmann schemes for the simulation of fluid dynamics, the developed model aims to solve the mesoscopic Radiation Transfer Equation instead of approximating macroscropic target equations, e.g. the Navier-Stokes Equations (see also chapter 4.2). This important difference is motivated by the fact that for radiation transport often situations occur, where radiation is far from equilibrium and thus, a macroscopic description of the transport problem hardly holds. For instance, when photobioreactors are illuminated by directed light, strong absorption by microalgae cells hinders the radiance to equilibrate. Consequently, the mesoscopic kinetic description of radiation transfer governs the problem. Nevertheless, the lattice Boltzmann framework offers nice features which seem beneficial for obtaining solutions of the RTE. The discretization reduces the problem to a set of coupled linear ODEs and the whole non-linearity is included in the scattering operator. Moreover, the algorithm is completely local, which is a major benefit with regard to parallel computing.

It should be also mentioned at this point that the model has undergone several improvements since its first publication. A further discussion of the modified model is provided in chapter 9.

The chapter was published as: McHardy, C., Horneber, T., Rauh, C. (2016). New lattice Boltzmann method for the simulation of three-dimensional radiation transfer in turbid media. Optics Express, 24 (15), 16999-17017, 2016.

Research Article | Vol. 24, No. 14 | 11 Jul 2016 | OPTICS EXPRESS 16999

Optics EXPRESS

New lattice Boltzmann method for the simulation of three-dimensional radiation transfer in turbid media

CHRISTOPHER MCHARDY,* TOBIAS HORNEBER AND CORNELIA RAUH

Chair of Food Biotechnology and Food Process Engineering, Technische Universität Berlin, Berlin, 14195, Germany
*christopher.mchardy@tu-berlin.de

Abstract: Based on the kinetic theory of photons, a new lattice Boltzmann method for the simulation of 3D radiation transport is presented. The method was successfully validated with Monte Carlo simulations of radiation transport in optical thick absorbing and non-absorbing turbid media containing either isotropic or anisotropic scatterers. Moreover, for the approximation of Mie-scattering, a new iterative algebraic approach for the discretization of the scattering phase function was developed, ensuring full conservation of energy and asymmetry after discretization. It was found that the main error sources of the method are caused by linearization and ray effects and suggestions for further improvement of the method are made.

OCIS codes: (000.3860) Mathematical methods in physics; (000.4430) Numerical approximation and analysis; (010.5620) Radiative transfer; (290.7050) Turbid media; (350.5610) Radiation.

References and links

1. M. R. Hoffmann, S. T. Martin, W. Choi and D. W. Bahnemann, "Environmental applications of semiconductor photocatalysis," Chem. Rev. **95**(1), 69–96 (1995).
2. A. D. Jassby and T. Platt, "Mathematical formulation of the relationship between photosynthesis and light for phytoplankton," Limnol. Oceanogr. **21**(4), 540–547 (1976).
3. P. H. C. Eilers and J. H. C. Peters, "A model for the relationship between light intensity and the rate of photosynthesis in phytoplankton," Numer. Heat Transfer Part B **57**(2), 126–146 (2010).
4. J. Oxenius, *Kinetic Theory of Particles and Photons* (Springer, 1986).
5. R. L. Liboff, *Kinetic Theory. Classical, Quantum and Relativistic Descriptions* (Springer, 2003).
6. M. F. Modest, *Radiative Heat Transfer* (Academic, 2013).
7. E. Meinköhn, G. Kanschat, R. Rannacher and R. Wehrse, "Numerical methods for multidimensional radiative transfer," *Reactive Flows, Diffusion and Transport*, 485–526 (Springer 2007).
8. P. J. Coelho, "Advances in the discrete ordinates and finite volume methods for the solution of radiative heat transfer problems in participating media," J. Quant. Spectrosc. Radiat. Transf. **145**(16), 121–146 (2014).
9. K. Mitra and S. Kumar, "Development and comparison of models for light-pulse transport through scatteringâĂŞabsorbing media," Appl. Opt. **38**, 188–196 (1999).
10. Z. Guo and S. Kumar, "Discrete ordinates solution of short pulse laser transport in two-dimensional turbid media," Appl. Opt. **40**(19), 3156–3163 (2001).
11. Z. Guo and S. Kumar, "Three-dimensional discrete ordinates method in transient radiative transfer," J. Thermophys Heat Transfer **16**(3), 289–296 (2002).
12. J. C. Chai, H. S. Lee and S. V. Patankar, "Ray effect and false scattering in the discrete ordinate method," Numer. Heat Transfer Part B **24**(4), 373–389 (1993).
13. P. J. Coelho, "The role of ray effects and false scattering on the accuracy of the standard and modified discrete ordinates methods," J. Quant. Spectrosc. Radiat. Transf. **73**, 231–238 (2002).
14. B. Hunter and Z. Guo, "Comparison of quadrature schemes in DOM for anisotropic scattering radiative transfer analysis," Numer. Heat Transfer Part B **63**, 485–507 (2013).
15. B. Hunter and Z. Guo, "Numerical smearing, ray effect, and angular false scattering in radiation transfer computation," Int. J. Heat Mass Transfer **81**, 63–74 (2015).
16. D. Hänel, *Molekulare Gasdynamik* (Springer, 2004).
17. S. Chen, S. P. Dawson, G. D. Doolen, D. R. Janecky and A. Lawniczak, "Lattice methods and their applications to reacting systems," Comput. Chem. Eng. **19**(6–7), 617–649 (1995).
18. S. Chen and G. D. Doolen, "Lattice Boltzmann method for fluid flows," Annu. Rev. Fluid Mech. **30**, 329–364 (1998).
19. S. Succi, *The Lattice Boltzmann Equation for Fluid Dynamics and Beyond* (Oxford University, 2001).

#263298 http://dx.doi.org/10.1364/OE.24.016999
Journal © 2016 Received 18 Apr 2016; revised 15 Jun 2016; accepted 19 Jun 2016; published 19 Jul 2016

Optics EXPRESS

20. A. J. C. Ladd and R. Verberg, "Lattice Boltzmann simulation for particle fluid suspensions," J. Stat. Phys. **104** (5/6), 1191–1251 (2001).
21. D. Yu, R. Mei, L. S. Luo and W. Shyy, "Viscous flow computations with the method of lattice Boltzmann equation," Prog. Aerosp. Sci. **39**, 329–367 (2003).
22. C. K. Aidun and J. R. Clausen, "Lattice Boltzmann method for complex flows," Annu. Rev. Fluid Mech. **42**, 439–472 (2010).
23. D. Anderl, M. Bauer, C. Rauh, U. Rüde and A. Delgado, "Numerical simulation of adsorption and bubble interaction in protein foams using a lattice Boltzmann method," Food Funct. **5**, 755–763 (2014).
24. D. Anderl, S. Bogner, C. Rauh, U. Rüde and A. Delgado, "Free surface lattice Boltzmann with enhanced bubble model," Comput. Math. Appl. **67** (2), 331–339 (2014).
25. D. Anderl, M. Bauer, C. Rauh, U. Rüde and A. Delgado, "Numerical simulation of bubbles in shear flow," Proc. Appl. Math. Mech. **14** (1), 667–668 (2014).
26. D. Anderl, M. Bauer, C. Rauh, U. Rüde and A. Delgado, "Foam flow through channels with the lattice Boltzmann method," Comput. Math. Appl. (2014, submitted).
27. S. Palpacelli and S. Succi, "Quantum lattice Boltzmann simulation of expanding Bose-Einstein condensates in random potentials," Phys. Rev. E **77**, 066708 (2008).
28. A. Nabovati, D. P. Sellan and C. H. Amon, "On the lattice Boltzmann method for phonon transport," J. Comput. Phys. **230**, 5864–5876 (2011).
29. P. Asinari, S. C. Mishra and R. Borchiellini, "A lattice Boltzmann formulation to the analysis of radiative heat transfer problems in a participating medium," Numer. Heat Transfer Part B **57**(2), 126–146 (2010).
30. Y. Ma, S. K. Dong and H. P. Tan, "Lattice Boltzmann method for one-dimensional radiation transfer", Phys. Rev. E **84**, 016704 (2011).
31. A. F. DiRienzo, P. Asinari, R. Borchiellini and S. C. Mishra "Improved angular discretization and error analysis of the lattice Boltzmann method for solving radiative heat transfer in a participating medium," Int. J. Numer. Methods Heat Fluid Flow, **21**(5), 640–662 (2011).
32. H. Bindra and D.V. Patil, "Radiative or neutron transport modeling using a lattice Boltzmann equation framework," Phys. Rev. E **86**, 016706 (2012).
33. S. C. Mishra and R. R. Vernekar, "Analysis of transport of collimated radiation in a participating media using the lattice Boltzmann method," J. Quant. Spectrosc. Radiat. Transf. **113**(16), 2088–2099 (2012).
34. R. R. Vernekar and S. C. Mishra, "Analysis of transport of short-pulse radiation in a participating medium using lattice Boltzmann method," Int. J. Heat Mass Transfer **77**, 218–229 (2014).
35. Y. Zhang, H. Yi and H. Tan, "One-dimensional transient radiative transfer by lattice Boltzmann method," Opt. Express **21**(21), 24532 (2013).
36. Y. Zhang, H.-L. Yi and H.-P. Tan, "The lattice Boltzmann method for one-dimensional transient radiative transfer in graded index gray medium," J. Quant. Spectrosc. Radiat. Transf. **137**, 1–12 (2014).
37. Y. Zhang, H.-L. Yi and H.-P. Tan, "Short-pulsed laser propagation in a participating slab with Fresnel surfaces by lattice Boltzmann methods," Int. J. Heat Mass Transfer **80**, 717–726 (2015).
38. Y. Zhang, H.-L. Yi and H.-P. Tan, "Lattice Boltzmann method for short-pulsed laser transport in multi-layered medium," J. Quant. Spectrosc. Radiat. Transf. **155**, 75–89 (2015).
39. R. McCulloch and H. Bindra, "Coupled radiative and conjugate heat tranfer in participating media using lattice Boltzmann methods," Comput. Fluids (2015).
40. A. Mink, G. Thäter, H. Nirschl and M. J. Krause, "A 3D lattice Boltzmann method for light simulation in participating media," J. Comput. Sci. (2016, in press).
41. G. C. Pomraning, *Linear Kinetic Theory in Stochastic Mixtures* (World Scientific, 1991).
42. M. Jonasz and G. R. Fournier, *Light Scattering by Particles in Water* (Academic, 2007).
43. A. B. Davis and A. Marshak, "Photon propagation in heterogeneous optical media with spatial correlations: enhanced mean-free-paths and wider-than-exponential free-path distributions," J. Quant. Spectrosc. Radiat. Transf. **84**, 3–34 (2004).
44. R. Koch, W. Krebs, S. Wittig and R. Viskanta, "Discrete ordinates quadrature schemes for multidimensional radiative transfer," J. Quant. Spectrosc. Radiat. Transf. **53**(4), 353–372 (1995).
45. X. He and L. S. Luo, "Theory of the lattice Boltzmann method: From the Boltzmann equation to the lattice Boltzmann equation," Phys. Rev. E **56**, 6811–6818 (1997).
46. T. Abe, "Derivation of the lattice Boltzmann method by means of the discrete ordinate method for the Boltzmann equation," J. Comput. Phys. **131**, 241–246 (1997).
47. W. Unno and E. A. Spiegel, "The Eddington approximation in the radiative heat equation," Publ. Astron. Soc. Jap. **18**(2), 85–95 (1966).
48. V. I. Lebedev and D .N. Laikov, "A quadrature formula for the sphere of the 131st algebraic order of accuracy," Dokl. Math. **59**(3), 477–481 (1999).
49. B. Hunter and Z. Guo, "Conservation of asymmetry factor in phase function discretization for radiative transfer analysis in anisotropic scattering media," Int. J. Heat Mass Transfer **55**(5–6), 1544–1552(2012).
50. B. Hunter and Z. Guo, "Phase-function normalization in the 3-D discrete-ordinates solution of radiative transfer - Part 1: conservation of scattered energy and asymmetry factor," Numer. Heat Transfer Part B **62**, 203–222 (2012).
51. J. H. Ferziger and M. Peric, *Computational Methods for Fluid Dynamics* (Springer, 2002).

Optics EXPRESS

52. S. L. Jacques, T. Li and S. Prahl, "mcxyz.c, a 3D Monte Carlo simulation of heterogeneous tissues," http://omlc.org/software/mc/mcxyz/index.html.
53. L.-H. Wang, S. L. Jacques and L.-Q. Zheng, "MCML - Monte Carlo modeling of photon transport in multi-layered tissues," Comput. Meth. Prog. Bio. **47**, 131–146 (1995).

1. Introduction

Radiation transfer is an important issue in several fields of engineering. Typical examples are radiative heat transfer or photon transport in technical optics. In many of those applications, fluids are present and affect radiation transfer by their physical properties. In particular in turbid particle-containing media, spatial concentration gradients of particles do influence the local absorption, emission and scattering of radiation. Conversely, radiation may lead to locally varying fluid temperature, which affects temperature-dependent fluid properties, convective and diffusive transport phenomena or reaction rates within the fluid. Reaction rates might be also linked directly to irradiance, for instance in the case of photocatalytic reactions [1] or the cultivation of photosynthetic microorganisms [2, 3]. Accordingly, for accurate prediction, design and optimization of such systems, the coupling between radiation transport, flow and reaction rates has to be taken into account. Owing to the complexity and non-linearity of the arising mathematical problem, analytic solutions can be found just for very few simplified cases, necessitating the application of numerical methods.

Most commonly used for numerical calculations of radiative transfer are Monte Carlo methods (MCM), Discrete Ordinate methods (DOM) and Finite Volume methods (FVM). In case of MCM, a sample of individual photons is traced from the point of emission to the point of absorption. Since no angular discretization is required, MCM are considered to be very accurate, even if complex problems of radiation transfer must be solved. However, because of their statistical nature, MCM may lead to noisy outcomes [6]. Moreover, the size of the traced photon sample must ensure statistical certainty which leads to slow convergence, particularly if optical thick media are simulated [7]. In contrast, both, DOM and FVM, are applied frequently as a compromise between accuracy and speed of convergence [8] and enable also transient computations [9–11]. These methods are in essence similar and based on a directional discretization of the Radiative Transfer Equation (RTE) and integration by means of specific quadrature rules. Besides well-known error sources such as the ray effect or numerical smearing (also referred to as false scattering) [12, 13], angular false scattering as a third type of error was considered [14, 15]. It is caused by inaccurate discretization of the scattering phase function and becomes significant for strong anisotropic scattering.

In the recent past, as a new approach, lattice Boltzmann methods (LBM) have been developed for the simulation of radiation transport. The idea behind seems to be straightforward since the RTE as the governing equation of radiation transport can be interpreted as a Boltzmann-type transport equation for photons [4, 5]. By combining both, accuracy and simplicity, lattice Boltzmann methods were established in the past as powerful tools for the simulation of several physical problems. Originating from the kinetic theory of gases [16], these methods were primarily developed to study fluid dynamical problems. Many research was done to extend the methodological framework to complex flow problems, such as turbulence, thermohydrodyamics, multiphase, reactive or non-newtonian flows and many others [17–26]. However, the existence of LBM for applications beyond fluid dynamics, such as quantum mechanics [27] or phonon transport [28], shows the principal applicability of the lattice Boltzmann framework to a wide range of systems which can be characterized by means of statistical physics. With regard to coupled flow and radiation transport, new lattice Boltzmann methods for radiation transfer potentially allow the fast and efficient simulation of these systems by using a consistent set of numerical methods on structured grids, even in complex geometries such as porous media. In addition, it is well known that LBM show great opportunities for parallel computing, which is of special

Optics EXPRESS

importance for calculations of radiative transfer since the multidimensionality of the problem causes significant computational costs [7].

However, the development of lattice Boltzmann methods for the simulation of radiation transfer is still a new field of research. Pioneer work in this field was done by Asinari et al. [29], Ma et al. [30] and DiRienzo et al. [31] and applied to benchmark cases in one and two dimensions. While those approaches dealt with isotropic scattering media only, Bindra and Patil [32] extended the approach of [30] to anisotropic scattering media by approximating the in-scattering integral by summation over a Gaussian quadrature. Moreover, it was shown that interparticle collision of photons are negligible and modeling of absorption, emission and scattering by means of source terms is sufficient. Further work was less fundamental than rather focused on applications. In particular, the simulation of collimated radiation by means of lattice Boltzmann methods was objected. For that purpose, based on the work of Asinari et al. [29], a flux splitting approach was designed by Mishra and Vernekar [33] and applied for the transient simulation of collimated radiation in one dimension [34]. Here, the time stepping scheme was explicit. Zhang et al. [35] treated transient transfer of radiation in one dimension by using an implicit discretization for the time derivative in the RTE. The method was applied for transient simulations of radiative transfer in index graded media [36] as well as for the transient simulation of scattered collimated radiation in combination with a flux splitting scheme [37, 38]. McCulloch and Bindra [39] extended the approach given by [32] to higher order angular discretization schemes in two dimensions and applied their method for coupled radiation and convective heat transfer. Recently, further developments concerned the extension of LBM solvers for radiation transfer to three-dimensional, isotropically scattering media [40].

Although progress has been made in recent years, the development of a consistent methodological framework is still outstanding. For instance, directional weights are either constructed geometrically [29, 31] or derived from moment equations [39]. Moreover, most of the works mentioned previously did not consider radiation transfer in media containing anisotropic scatterers. To close this gap, the simulation of radiative transfer in three-dimensional domains with anisotropic scatterers by means of lattice Boltzmann methods is shown in this work for the first time. The method is derived from the kinetic theory of photons and takes fundamental differences to particle kinetics into account. For angular discretization, sets of discrete directions in three dimensions are developed ensuring the fulfillment of angular moment equations. In addition, to take scattering by Mie-scatterers into account, an innovative algebraic approach is applied to discretize the Henyey-Greenstein phase function under full conservation of energy and asymmetry. Finally, the method is applied in numerical examples to study its accuracy in comparison to Monte Carlo methods.

2. Mathematical formulation

2.1. Brief review of kinetic theory of photons

The origin of lattice Boltzmann methods lies in the kinetic theory of gases. Thus, for the calculation of radiative fields by means of LBM it is essential to consider the kinetic theory of photons and take differences to particle kinetics into account. In case of gas particles, the fundamental idea is that particle motion follows Newtonian mechanics and particles can interact via interparticle collisions [4]. On a mesoscopic scale, microkinetics of single particles are captured statistically by the Boltzmann equation, Eq. (1), which governs the kinetics of a whole particle ensemble.

$$\frac{\delta f}{\delta t} + \xi \nabla_{\mathbf{x}} f + \frac{\mathbf{F}}{m} \nabla_{\xi} f = \Gamma \tag{1}$$

Herein f is the velocity density distribution, which defines the probability of finding a gas particle in a phase space volume $\Delta\mathbf{x}\Delta\xi$ at time t, whereby $\mathbf{x}$ denotes the position vector and ξ the momentum vector. The velocity density distribution changes in time by convection, by influence

Optics EXPRESS

of external forces $\mathbf{F}$ on gas particles of mass m or due to interparticle collisions as defined by the collision operator Γ. In gas kinetic theory, a famous formulation of Γ is given by the Bhatnagar-Gross-Krook (BGK) approximation [16, 19]. It is assumed that the velocity density distribution relaxes due to interparticle collisions towards local equilibria, which are defined by the Maxwell-Boltzmann velocity distribution for gas particles of equal mass. More general, Γ can be interpreted as the difference between losses and gains of gas particles per unit time due to interactions within the phase space volume under consideration. According to this interpretation, the collision operator can be rewritten in the following way.

$$\Gamma = \frac{\delta}{\delta t}(f_G - f_L) \tag{2}$$

A kinetic equation similar to Eq. (1) can be derived for photons by replacing f by a quantity ϕ, which is known as the photon density distribution. By definition, ϕ measures the probability of finding an unpolarized photon in a phase space volume $\Delta\mathbf{x}\Delta\mathbf{p}$, where $\mathbf{p}$ is the momentum vector of photons, whose magnitude is $p = h\nu/c$ [4]. For photons, an element within the three-dimensional momentum space $\Delta\mathbf{p}$ consists of an element $\mathrm{d}\nu$ in the one-dimensional frequency space and an element in the two-dimensional directional space, represented by a solid angle $\mathrm{d}\Omega$, which contains all vectors $\mathbf{n} = \mathbf{p}/p$ for $\mathbf{p} \in \Delta\mathbf{p}$. By using this definitions, a phase space volume for photons becomes to

$$\Delta\mathbf{x}\Delta\mathbf{p} = \frac{h^3\nu^2}{c^3}\Delta\mathbf{x}\mathrm{d}\nu\mathrm{d}\Omega, \tag{3}$$

where c is the speed of light and h the Planck constant. As an important complement, according to Liouville's theorem, the photon number density in phase space is conserved in absence of collisions [5].

Radiative fields are commonly expressed in terms of the specific intensity I_ν, which is defined as the amount of energy $\mathrm{d}E$, carried by photons within a frequency band $\mathrm{d}\nu$ into a solid angle $\mathrm{d}\Omega$ per unit time $\mathrm{d}t$ and unit area $\mathrm{d}A$ [6]. The specific intensity of photons is related to the photon density distribution by the expression

$$\phi = \frac{c^2}{h^4\nu^3}I_\nu \tag{4}$$

and hence, since c and h are constants, I_ν/ν^3 can be used to derive the kinetic equation of photons [4]. Although it is known that gravity and electromagnetic forces act on the momentum of photons, in the following it is assumed that momentum of photons changes due to interaction with matter only. By using the general formulation of the collision operator as given by Eq. (2) and multiplying with ν^3, the kinetic equation for photons arises.

$$\frac{1}{c}\frac{\delta I_\nu}{\delta t} + \mathbf{n}\nabla_{\mathbf{x}} I_\nu = \frac{1}{c}\frac{\delta}{\delta t}(I_{\nu G} - I_{\nu L}) \tag{5}$$

The indexes G and L again mark gains and losses of photons within the phase space volume under consideration. Similar to Eq. (1), Eq. (5) governs the kinetics of a photon ensemble on a mesoscopic scale. However, with regard to the mechanism of collisions, fundamental differences between photons and particles exist. While particles exchange momentum due to interparticle collisions, changes in momentum of photons occur by interaction with surrounding matter. As a first mechanism, absorption and isotropic emission of photons by matter occurs. If matter is in local thermal equilibrium (LTE), the momentum distribution of photons also moves towards an equilibrium, whose frequency distribution is Plankian [41]. As a second mechanism, elastic scattering of photons occurs in turbid media [42], which affects only the directional component of the photon momentum vector while frequency stays constant [4]. By taking these

Optics EXPRESS

mechanisms of interaction into account, Eq. (5) becomes to the well known Radiation Transfer Equation (RTE), which gives a description of photon kinetics in turbid media in terms of the specific intensity.

$$\frac{1}{c}\frac{\delta I_\nu}{\delta t} + \mathbf{n}\nabla_{\mathbf{x}} I_\nu = -\beta_\nu I_\nu + \kappa_\nu I_{\nu,e} + \frac{\sigma_\nu}{4\pi}\int_{4\pi} I'_\nu \Phi(\mathbf{n}', \mathbf{n}) \mathrm{d}\Omega'. \tag{6}$$

The right-hand side of Eq. (6) capture the extinction of photons due to absorption and scattering by matter, the re-emission of photons with a specific intensity $I_{\nu,e}$ and the local in-scattering of photons into the direction of propagation $\mathbf{n}$ from directions $\mathbf{n}'$. Here, the scattering phase function Φ represents the angular distribution of scattered photons according to the scattering properties of the surrounding matter. The extinction coefficient $\beta_\nu = \kappa_\nu + \sigma_\nu$ measures the interaction of photons with matter per unit volume due to absorption and scattering, both individually expressed by the absorption (κ_ν) and scattering (σ_ν) coefficients, respectively. Thus, β_ν is related to the mean free path (MFP) l_f of photons by

$$l_f = \frac{1}{\beta_\nu}. \tag{7}$$

Eq. (7) is valid for homogeneous media only, while for non-homogeneous media both, the local MFP $l_f(\mathbf{x})$ as well as the length scale of its spatial variability, should be evaluated to avoid underestimation of free path lengths [43]. If a medium is homogeneous, the probability for collision of photons with matter along a path of length s can be shown to be $P_{coll}(s) = 1 - \exp(s/l_f)$ [6].

The local radiative field can be characterized by moment equations of the specific intensity by integration over the momentum space. A general formulation for the radiative moment M_k of order k of the specific intensity reads as

$$M_k = \int\int \psi_k(\mathbf{c}) I_\nu d\Omega d\nu, \tag{8}$$

where $\psi_k(\mathbf{c})$ is a polynomial of $\mathbf{c}$. Only the zeroth (mean intensity J), first (radiative flux) and second (radiation pressure) moments have physical meaning [6]. Nevertheless, higher order moments of the radiation field are computed for some angular discretization schemes in the DOM [44]. Since the discretization in LBM is also based on the satisfaction of several moment equations [45], it is important to take the different definitions of momentum space for particles and photons into account.

2.2. Lattice Boltzmann method

The RTE as given by Eq. (6) has to be discretized both, in time and phase space. Moreover, the scattering phase function Φ needs to be discretized to solve in-scattering integral in the discretized momentum space. For this purpose an algebraic technique will be applied to the Henyey-Greenstein phase function.

2.2.1. Time discretization

By using the substantial derivative, Eq. (6) can be reformulated as a pseudo-linear ordinary differential equation.

$$\frac{\mathrm{d}I_\nu}{\mathrm{d}t} = -c\beta_\nu (I_\nu - S_\nu) \tag{9}$$

Herein, S_ν denotes the source term

$$S_\nu = (1-\omega_\nu) I_{\nu,e} + \frac{\omega_\nu}{4\pi}\int_{4\pi} I'_\nu \Phi(\mathbf{n}', \mathbf{n}) \mathrm{d}\Omega', \tag{10}$$

Optics EXPRESS

where $\omega_\nu = \sigma_\nu/\beta_\nu$ is the scattering albedo. Making usage of the fundamental theorem of calculus, an exact expression for the left-hand side of Eq. (9) can be reached by integration over a small time intervall Δt along a characteristic line $\mathbf{c} = c\mathbf{n}$ [45]. The time integral of the right-hand side is usually approximated by a rectangular rule so that the time-discrete formulation of Eq. (9) reads as follows.

$$I_\nu(\mathbf{x}+\mathbf{c}\Delta t, \mathbf{c}, t+\Delta t) - I_\nu(\mathbf{x}, \mathbf{c}, t) = -c\beta_\nu \Delta t (I_\nu - S_\nu) \tag{11}$$

2.2.2. Discretization of phase space

In LBM, space is discretized by a structured lattice, whereby the lattice nodes represent discrete positions between which photons are able to propagate, as shown in Fig. 1. Accordingly, as a characteristic of LBM, discretization of momentum is connected to the discretization of space. An assumption in LBM is that particle or photons stream freely between the nodes of the lattice and collisions occur on the nodes [16]. This means that the grid spacing should be in the order of the MFP, as defined by Eq. (7). This local description of photon kinetics holds in the continuum limit as characterized a low Knudsen number $Kn = l_f/L$, which relates the MFP to a characteristic length of the system L. In other words, local fluctuations by collisions do not affect the mean radiation properties on a macroscopic scale, if many collisions occur.

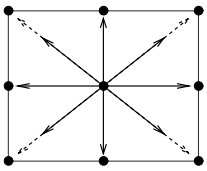

Fig. 1. 2D schematic representation of a discretized phase space in the LBM. Arrows symbolize photon propagation between lattice nodes.

As a simplification, monochromatic radiation is assumed from now on, and thus, the six-dimensional phase space reduces to five dimensions. For convenience the notation of the specific intensity is changed to I and moreover, all indexes referring to frequency-dependency are dropped. To solve the RTE on the lattice, I is discretized into discrete specific intensities I_i, which propagate with constant speed along characteristic lines $\mathbf{c}_i$. Thereby the choice of the $\mathbf{c}_i$ is constrained by the arrangement of the lattice as discussed above. On a lattice node, the macroscopic quantities of the radiative field must be evaluated by the calculation of radiative moments. Thus, also in a discretized momentum space, the exact evaluation of moment equations, Eq. (8), is required, which again necessitates the approximation of the integrals by a quadrature scheme. Assuming isotropy in radiative equilibrium, the integral is of the type $\int a\psi(x)dx$ and can be evaluated by a Gaussian quadrature, so that Eq. (8) becomes to

$$M_k = Ic \sum w_i \psi_k(\mathbf{n}_i), \tag{12}$$

where w_i are the weight coefficients, corresponding to the abscissas of the quadrature as given by a set of $\mathbf{c}_i$. It should be noted that Eq. (12) approximates the inner integral in Eq. (8), while the integration in frequency space is not considered. However, Eq. (12) represents the approximation of an integral on the surface of the unit sphere, which is in common to the calculation of radiative moments in the DOM. Since a structural similarity between both methods is known [46], design principles for the quadrature rule can be adopted from the DOM. Accordingly, the quadrature must ensure rotational invariance, symmetry and conservation of energy [44]. A common ansatz function for the polynomial $\psi_k(\mathbf{n}_i)$ is

$$\psi_k(\mathbf{n}_i) = l_i^{k1} m_i^{k2} n_i^{k3}, \tag{13}$$

Optics EXPRESS

where l_i, m_i, n_i are the direction cosines of a quadrature abscissa, which must lie on the unit sphere, so that $l_i^2 + m_i^2 + n_i^2 = 1$. The moment order k is related to the exponents by $k = k1 + k2 + k3$. By choosing $k1 = k2 = 0$ and $k3 = k$, the requested condition of energy conservation is ensured [44]. From symmetry, it follows that all odd moments become zero. For even moments a general solution was derived for the absolute value of moments of order k [47]. For the specific case of $k3 = k$, the quadrature must be able to fulfill the following conditions exactly.

$$|\mathbf{M_k}| = \begin{cases} 0 & \text{if } k \text{ is odd} \\ 4\pi \frac{1}{k+1} & \text{if } k \text{ is even} \end{cases} \tag{14}$$

For a set of given quadrature abscissas as defined by the lattice arrangement, Eqs. (12)-(14) can be reformulated in terms of a linear equation system and solved for the unknown quadrature weights.

$$\begin{pmatrix} n_1^0 & n_2^0 & \dots & n_m^0 \\ n_1^1 & n_2^1 & \dots & n_m^1 \\ \dots & & & \dots \\ n_1^k & n_2^k & \dots & n_m^k \end{pmatrix} \begin{pmatrix} w_1 \\ w_2 \\ \dots \\ w_m \end{pmatrix} = \begin{pmatrix} |\mathbf{M_0}| \\ |\mathbf{M_1}| \\ \dots \\ |\mathbf{M_k}| \end{pmatrix} \tag{15}$$

In a three-dimensional structured lattice, the solution of Eq. (15) is similar to Gaussian-type quadrature schemes as constructed by Lebedev [48] for the integration on the unit sphere. The derivation of the quadrature stands in contrast to previous approaches [29,31,39], wherefore important differences to fluid LBM shall be stressed. First, photons propagate with constant speed so that the quadrature integrates on the unit sphere. This is an important difference to common LBM, where particle velocities differentiate in direction and speed. In consequence, the weighting factors do not incorporate different lengths of photon propagation, which may be present in a cubic lattice. To address these effects in the present model, the incorporation of different propagation lengths is realized by direction-specific integration as discussed below. Second, the different equilibrium functions for particles and photons lead to different structures of the integrals which have to be calculated to evaluate the moment equations. In contrast to photons, for particles the equilibrium is Maxwellian and the integral is approximated by Gauss-Hermite quadratures, which, unlike the Lebedev quadrature, require a "zero-velocity". In a physical interpretation, this difference can be explained by the fact that photons travel with constant speed and, thus, no resting energy has to be taken into account.

As stated before, the choice of the discrete directions or quadrature abscissas is constrained by the three-dimensional lattice. Three possible arrangements are shown in Fig. 2. In accordance to the usual nomenclature, the sets of discrete directions are termed *DnQm*, where n is the dimension of the problem and m the number of discrete directions within one set.

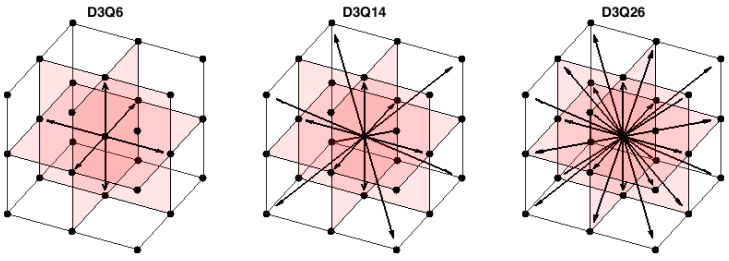

Fig. 2. Sets of discrete directions in a three-dimensional lattice. Arrows symbolize the discrete directions of photon propagation between lattice nodes.

Optics EXPRESS

By coupling the discretization of time, Eq. (11), and phase space, a fully discretizated representation of Eq. (6) can be reached. The in-scattering integral is replaced by a quadrature rule. The resulting model equation for the LBM framework reads as follows.

$$I_i(\mathbf{x}+\mathbf{c}_i\Delta t,\mathbf{c}_i,t+\Delta t)-I_i(\mathbf{x},\mathbf{c}_i,t)= \\ -c\beta\Delta t I_i+c\beta(1-\omega)\Delta t I_{e,i}+c\beta\frac{\omega\Delta t}{4\pi}w_i\sum_{j=1}^{m}I_j\Phi(i,j) \quad (16)$$

Herein, the left-hand and right-hand sides are denoted as streaming and collision terms, respectively. With regard to Fig. 2, it becomes clear that, except from the D3Q6 set, the distance between two nodes in the lattice depends on the direction of propagation. Because the distance $\Delta\mathbf{x_i}=\mathbf{c_i}\Delta t$ is included in the streaming term, Eq. (16) is valid for the D3Q6 set only. Since the speed of light is constant, streaming on a structured lattice requires direction-dependent time steps Δt_i. Because the time integration uses non-uniform time-steps, the amount of energy carried by the discrete specific intensities depends not only on scattering, emission and absorption but also on the direction dependent time-step. This numerical effect becomes important for the computation of in-scattering, since the in-scattering term couples different discrete specific intensities. As a correction, the discretized specific intensity is normalized per unit time and corrected to the specific time-step. In consequence, a limitation of the LBM is the computation of steady-state intensity fields only. With this modification, the resulting model equation becomes to the following expression.

$$I_i(\mathbf{x}+\mathbf{c}_i\Delta t_i,\mathbf{c}_i,t+\Delta t_i)-I_i(\mathbf{x},\mathbf{c}_i,t_i)= \\ -c\beta\Delta t_i I_i+c\beta(1-\omega)\Delta t_i I_{e,i}+c\beta\frac{\omega\Delta t_i}{4\pi}w_i\sum_{j=1}^{m}I_j\frac{\Delta t_i}{\Delta t_j}\Phi_{i,j} \quad (17)$$

Table 1 sums up the sets of discrete directions and resulting quadrature weights for different discretizations of momentum space for the LBM.

Table 1. Quadrature sets for different discretizations of momentum space. The quadrature abscissas result from all possible permutations and multiplication by -1 of the typical vector elements.

			weights		
no. of elements	direction	typical vector	D3Q6	D3Q14	D3Q26
6	1-6	(1,0,0)	1/6	1/15	1/21
8	7-14	$1/\sqrt{3}$ (1,1,1)	-	3/40	9/280
12	15-26	$1/\sqrt{2}$ (1,1,0)	-	-	4/105

2.2.3. Discretization of the scattering phase function

The evaluation of the in-scattering term requires a discretized representation of the phase function Φ, which represents the angular distribution of scattered photons. For media containing Mie-scatterers, the Henyey-Greenstein phase function has often been used to approximate Mie-scattering and is given by

$$\Phi(\theta)=\frac{1-g^2}{(1+g^2-2g\cos(\theta))^{3/2}}. \quad (18)$$

Herein, g is the asymmetry factor, which is equal to the mean cosine of the scattering angle θ. The asymmetry factor can take any value within the interval $[-1\leq g\leq 1]$ to represent

Optics EXPRESS

anisotropic as well as isotropic ($g = 0$) scattering. Both, the continuous as well as the discrete representation of Φ must ensure the conservation of energy and asymmetry and fulfill the following conditions.

$$1 = \frac{1}{4\pi}\int_{4\pi}\Phi(\theta)\mathrm{d}\Omega = \frac{1}{4\pi}\sum w_i\Phi_{i,j} \tag{19a}$$

$$g = \frac{1}{4\pi}\int_{4\pi}\cos(\theta)\Phi(\theta)\mathrm{d}\Omega = \frac{1}{4\pi}\sum w_i\cos(\theta_{i,j})\Phi_{i,j} \tag{19b}$$

Violation of these conditions causes inaccurate computation of the scattering kernel since either energy sources arise or the shape of the scattering phase function is not conserved in the discrete phase space. The latter error source is known from the DOM and termed as "false angular scattering" [14, 15]. To reduce the effects of inaccurate discretization, normalization methods can be applied to ensure conservation of energy or asymmetry. Recently, a normalization method was developed which conserves both, energy and asymmetry of the discretized scattering phase function [49, 50]. The idea behind this technique is that a set of discrete values $\Phi_{i,j}$, which does not fulfill the conditions as given by Eqs. (19a) and (19b), is normalized by

$$\tilde{\Phi}_{i,j} = (1 + A_{i,j})\Phi_{i,j} \tag{20}$$

so that the discrete values $\tilde{\Phi}_{i,j}$ fulfill the conservation of energy or asymmetry. The computation of the normalization factors $A_{i,j}$ leads to an under-determined linear equation system, which is solved by QR-decomposition and computation of the minimum norm of the linear equation system.

In this work, the approach of [49, 50] is adopted to discretize the scattering phase function iteratively. The basic idea behind is that the computed set of discrete $\tilde{\Phi}_{i,j}$ is more accurate after normalization, if the set of $\Phi_{i,j}$ was already a good initial solution. However, there is no solution known for $\Phi_{i,j}$ except from the isotropic case ($g = 0$), where $\Phi_{i,j} = 1$ is true for all $i, j \leq m$. Since this solution is exact, it is a good approximation for a slightly different value of $g_1 = g_{iso} + \Delta g$ and can be used as an initial solution for the normalization. The normalized solution ensures conservation of energy and asymmetry and is again a good approximation for $\tilde{\Phi}_{i,j}$ at a new slightly different $g_2 = g_1 + \Delta g$. The procedure is repeated until a desired value of g is reached and a discretized set of $\Phi_{i,j}$ is computed. Compared to the explicit calculation of $\Phi_{i,j}$ by integration of $\Phi(\theta)$ and averaging over discrete solid angles $\mathrm{d}\Omega_i$ and $\mathrm{d}\Omega_j$, an advantage of the iterative technique is that the calculation is fully algebraic and no integration bounds have to be defined on the unit sphere. To specify the step size Δg, a discretization error ε_g can be computed as [51]

$$\varepsilon_g \approx \frac{1}{m^2}\frac{||\phi_1 - \phi_2||}{r^p - 1}, \tag{21}$$

where ϕ_1 is a $m \times m$ matrix containing the values of $\Phi_{i,j}$ for a desired value of g, reached with a certain Δg and ϕ_2 is the solution for the same g, but computed with the next bigger step size. If the step size is changed by a factor r, the order of error reduction p can be computed as

$$p = \frac{\log\left(\frac{||\phi_2 - \phi_3||}{||\phi_1 - \phi_2||}\right)}{\log(r)}. \tag{22}$$

The discretization error at different step sizes is shown in Fig. 3 for the three quadrature sets as defined in table 1 and a final value of $g = 0.9$. It can be seen that the error decreases linearly with step size so that the accuracy of the iterative discretization is of first order. For a step size $\Delta g = 1\mathrm{E}{-}04$, the magnitude of the discretization error becomes 1E−06 or lower. At this step size, the required computational time for the discretization was between 2 and 34.5 seconds on

Optics EXPRESS

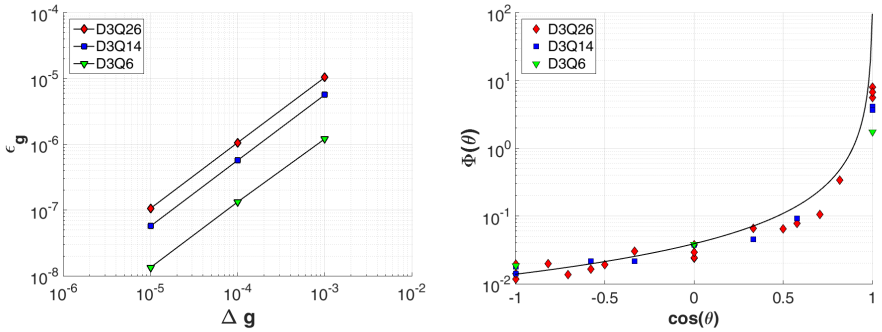

Fig. 3. Left: Discretization error with respect to the step size Δg for a final value of $g = 0.9$ (see text for details). Right: Discretized (symbols) and continuous (solid line) Henyey-Greenstein phase function for $g = 0.9$ and $\Delta g = 1\text{E}{-}04$.

a 3.4 GHz machine, depending on the number of discrete directions. Regardless of the chosen step size, the discretized phase functions fulfill the conditions as given by Eqs. (19a) and (19b) exactly within the floating-point relative accuracy.

2.2.4. Nondimensionalization

The model equation, Eq. (17), still represents physical units. Although simulations can be carried out by using physical units, it is convenient to transform the model equations into a non-dimensional representation. With regard to the RTE, an adequate choice of reference quantities would be a characteristic length L_0, a characteristic mean specific intensity J_0 and a characteristic speed, which is the speed of light c. By using these reference quantities, a set of dimensionless quantities (index D) can be defined.

$$\begin{array}{llll} \text{length} & l_D = l/L_0 & \text{mean specific intensity} & J_D = J/J_0 \\ \text{speed} & c_D = u/c & \text{extinction coefficient} & \beta_D = \beta L_0 \\ \text{time} & t_D = tc/L_0 & & \end{array} \tag{23}$$

The dimensionless extinction coefficient is also known as the optical depth τ, which needs to be equal in both, the physical and the non-dimensional representation. Since β is the inverse of the MFP, the optical depth is the inverse of the Knudsen number Kn. As a restriction, LBM are applicable for simulations at low Knudsen numbers so that $Kn \approx 1\text{E}{-}02$ [16], which corresponds to optical thick media ($\tau \gg 1$) [6]. With regard to Eq. (23) it turns out that the dimensionless speed equals unity, since photons propagate with constant speed of light. Furthermore, it holds that $l_{D,0} = 1$ and $J_{D,0} = 1$. In a discretized representation, the non-dimensional length becomes to

$$l_{D,0} = 1 = (N-1)\Delta x, \tag{24}$$

where Δx is the grid spacing and N the number of nodes in the lattice used to discretize the characteristic length. As mentioned above, the grid spacing should be in the order of the MFP. From Eqs. (23) and (24) follows that $t_D = l_D/c_D$ or $\Delta t_D = \Delta x_D/c_D$. As discussed before, with

Optics EXPRESS

the LBM the steady-state radiation field can be computed and, hence, the model becomes time-independent. In the dimensionless notation, Eq. (17) reads as

$$I_{i,D}(\mathbf{x}_D+\Delta\mathbf{x}_{i,D},\mathbf{c}_i)-I_{i,D}(\mathbf{x}_D,\mathbf{c}_i)= \\ -\tau\Delta\mathbf{x}_{i,D}\left(I_{i,D}-(1-\omega)I_{e,i,D}-\omega\frac{w_i}{4\pi}\sum_{j=1}^{m}I_{j,D}\Phi_{i,j}\frac{\Delta\mathbf{x}_{i,D}}{\Delta\mathbf{x}_{j,D}}\right) \quad (25)$$

where the dimensionless length in the lattice is $\Delta\mathbf{x}_{i,D}=(\Delta x_{i,D}^2+\Delta y_{i,D}^2+\Delta z_{i,D}^2)^{0.5}$. The dimensionless mean specific intensity can be computed as

$$J_D(\mathbf{x}_D)=\sum_{i=1}^{m}w_iI_{i,D}(\mathbf{x}_D). \quad (26)$$

2.3. Algorithm

The implementation of the LBM follows the classical lattice Boltzmann algorithms. After initialization, the following procedure is repeated until a desired degree of accuracy is reached. First, the collision of photons with matter is calculated for all discrete directions according to the right-hand side of Eq. (25). In the second step, the boundary conditions are applied, leading to an intermediate state of the specific intensity.

$$\tilde{I}_{i,D}(\mathbf{x}_D,\mathbf{c}_i)=-\tau\Delta\mathbf{x}_{i,D}\left(I_{i,D}-(1-\omega)I_{e,i,D}-\omega\frac{w_i}{4\pi}\sum_{j=1}^{m}I_{j,D}\Phi_{i,j}\frac{\Delta\mathbf{x}_{i,D}}{\Delta\mathbf{x}_{j,D}}\right) \quad (27)$$

The third step is the so-called streaming step, where the new specific intensity is calculated.

$$I_{i,D}(\mathbf{x}_D+\Delta\mathbf{x}_{i,D},\mathbf{c}_i)=I_{i,D}(\mathbf{x}_D,\mathbf{c}_i)+\tilde{I}_{i,D}(\mathbf{x}_D,\mathbf{c}_i) \quad (28)$$

The accuracy is measured in terms of the relative difference of the discretized specific intensity between two computational steps.

$$\varepsilon_i(\mathbf{x}_D)=|1-\frac{I_{i,D}(\mathbf{x}_D,\mathbf{c}_i,t+1)}{I_{i,D}(\mathbf{x}_D,\mathbf{c}_i,t)}| \quad (29)$$

2.4. Stability analysis

As a criterion for stability, the parameter settings must ensure that the specific intensity remains positive. A limiting case exists, if radiation is transported in one discrete direction and in-scattering results only from forward scattering. From Eq. (25) it follows for an absorbing, scattering and non-emitting turbid media that in that limiting case the condition

$$1-\tau\Delta\mathbf{x}_{i,D}\left(1-\omega\frac{w_i}{4\pi}\Phi_{i,i}\right)>0 \quad (30)$$

must be fulfilled to ensure positivity of specific intensity. Figure 4 shows valid parameter combinations for the D3Q26 discretization, which guarantee stable simulations. The limitation of stability was found to be caused by the direction vectors 7-14 (see table 1) for both, the D3Q14 and D3Q26 discretization. As stated before, the condition of low Knudsen numbers necessitates high optical thickness, so that in particular simulations of isotropically scattering or mainly absorbing turbid media requires fine grid spacing to ensure numerical stability. In contrast, for strong forward scattering, also simulations on coarse grids can run stable.

Optics EXPRESS

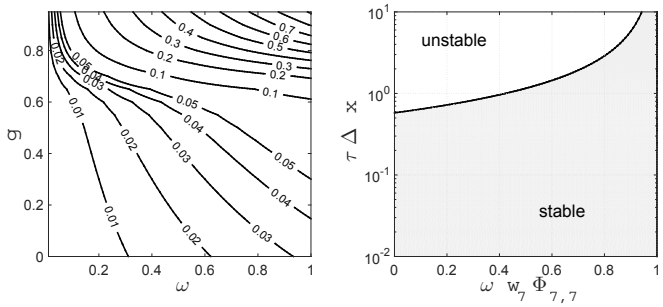

Fig. 4. Stability map for the D3Q26 discretization. Left: Contour plot of the discretized in-scattering term $\omega w_7 \Phi_{7,7}$ with respect to anisotropy g and scattering albedo ω. Right: Stable and unstable regions with respect to optical depth, grid spacing and in-scattering for the liming case (see text). The limit between the stable and unstable regions is given by Eq. (30).

3. Results and discussion

3.1. Simulation cases

To validate the LBM, simulations of radiative transfer in an absorbing, scattering and non-emitting turbid media were carried out and compared to Monte Carlo simulations. The simulation domain is a cubic enclosure with one emitting surface at which monochromatic radiation of mean intensity J_0 enters the domain. The other five surfaces are assumed to be black and cold. The domain, as sketched in Fig. 5, was assumed to initially dark. As a fist case, diffuse emission of radiation from the emitting boundary is considered. In a second case, the radiation source is modified in order to emit collimated radiation of intensity I_c. For this case, the source is changed to a square-shaped area around the origin O with an edge length of 0.2 L_0 from which the collimated radiation enters the domain normal to the emitting surface.

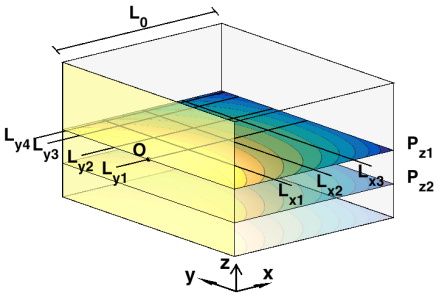

Fig. 5. Sketch of the simulated domain with evaluated lines and planes. The origin of the coordinate system is marked with O. Radiation is emitted from the wall at $x = 0$ (yellow). Lines L_y are located at y1 = 0, y2 = 0.2, y3 = 0.4 and y4 = 0.48. Lines L_x are located at x1 = 0.25, x2 = 0.50 and x3 = 0.75. Planes P_z are located at z1 = 0 and z2 = −0.25.

For the D3Q26 LBM, the spatial resolution was set to $N = 101$ nodes in each direction after a grid independence test. Steady-state was assumed to be reached if the maximum local error in the domain (see Eq. (29)) was below a threshold of 1E−06. The reference MC solutions were obtained with an Open source solver [52], which is documented elsewhere [53]. For the MC simulations, the cubic domain was splitted into 100^3 cubic voxels. In total, 1E07 photons were tracked in each simulation. The number of photons per voxel N_{vox} was normalized to the

Optics EXPRESS

incoming number of photons per surface area so that the dimensionless mean intensity becomes to

$$J_{D,MC} = \frac{N_{vox}/A_{vox}}{N_{in,tot}/A_{in,tot}}. \tag{31}$$

In total 20 different parameter combinations of optical depth, anisotropy factor and scattering albedo were simulated for both cases under consideration.

3.1.1. Diffuse emission

At the boundary, the relation between the mean intensity and the specific intensity is given by

$$J_0 = \int_{\theta>0} I(\theta)\mathrm{d}\Omega. \tag{32}$$

In the discretized momentum space of the LBM, Eq. (32) is expressed by Eq. (26) with the restriction of $I_i(\theta_i) = 0$ for $\theta_i \leq 0$. Moreover, for diffuse radiation, the specific intensity per unit solid angle is constant so that $I_i w_i = \text{const.}$ applies for all directions i with $\theta_i > 0$. The discrete specific intensities at the emitting wall can be calculated by solving the equation system that arises from the conditions as mentioned. At the cold walls, the boundary condition is $I_i(\theta_i) = 0$ for all directions. For the MCM the boundary condition at the emitting boundary is given by Eq. (32). At the cold walls, photons are fully absorbed.

3.1.2. Collimated radiation

Collimated radiation is added to the LBM model by using a flux splitting approach [33]. Here, it is distinguished between collimated and diffuse radiation, which both are connected by an one-way coupling since diffuse radiation can not be focused again by scattering. Hence, the transport of collimated radiation is affected by extinction only as given by Lambert's Law for which an analytic solution is known.

$$I_{c,D}(\mathbf{x}_D + \Delta\mathbf{x}_{c,D}, \mathbf{c}_c) = I_{c,D}(\mathbf{x}_D, \mathbf{c}_c)\exp(-\tau\Delta\mathbf{x}_{c,D}) \tag{33}$$

The extinction of collimated radiation is accompanied with an increase of the diffuse specific intensity via in-scattering. This can be included by adding a source-term $S_{c,i}$ to Eq. (25), which is

$$S_{c,i} = \omega\Delta I_{c,D}\Phi_{c,i}\frac{\Delta\mathbf{x}_{i,D}}{\Delta\mathbf{x}_{c,D}}, \tag{34}$$

where $\Delta I_{c,D} = I_{c,D}(\mathbf{x}_D + \Delta\mathbf{x}_{c,D}) - I_{c,D}(\mathbf{x}_D)$. The discrete scattering phase function is represented by a vector $\Phi_{c,i}$, which is calculated as described in section 2.2.3. The boundary condition was set to $J_D = 1$ for the LBM. For the MCM, the angle of emission was fixed to the surface normal.

3.2. Comparison with Monte Carlo simulations in scattering turbid media

Simulation results from the LBM and the MCM for the mean intensity in a scattering turbid media ($\omega = 1$) are exemplarily shown for $g = 0.85$ in Fig. 6. The predictions by the LBM are in good agreement to results obtained by the MCM, although the momentum space is discretized in the LBM with only 26 abscissas, while for the MCM no angular discretization is required. It should be noted that for the case of collimated radiation (right-hand side of Fig. 6) the intensity profiles on lines L_{y3} and L_{y4} result from scattered radiation only, which indicates that the computation of the discretized scattering phase function by the iterative method leads to accurate results. However, if the optical depth decreases, the deviation between the LBM prediction and the MCM increases, what can be particularly noticed on line L_{y1}. Results of comparable consistency to those shown in Fig. 6 were found for lower anisotropy ($g = 0.7$, $g = 0$), but, in contrast, for strong anisotropy ($g = 0.95$) the LBM was found to become less accurate.

Optics EXPRESS

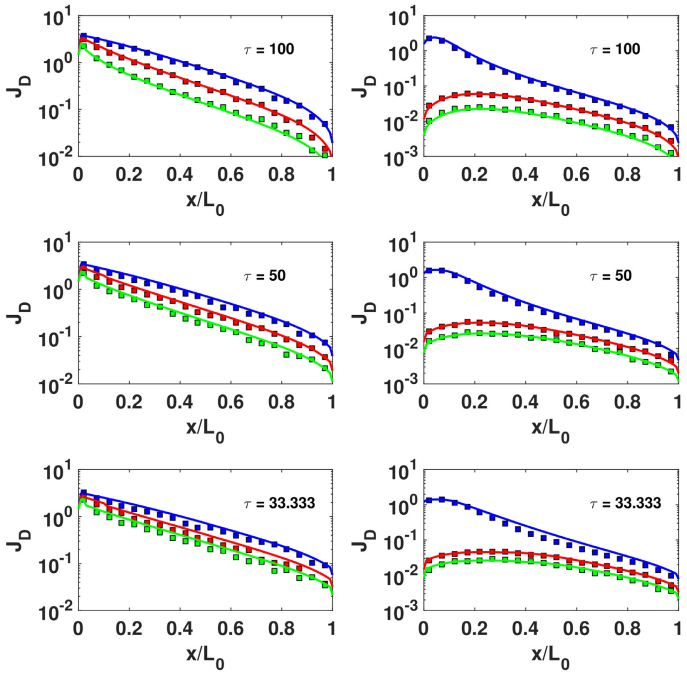

Fig. 6. Profiles of the dimensionless mean intensity J_D on plane P_{z1} along lines L_{y1} (blue), L_{y3} (red) and L_{y4} (green) for $g = 0.85$ and different optical depths in a pure scattering turbid medium ($\omega = 1$). Solid lines: lattice Boltzmann, symbols: Monte Carlo. Left: diffuse emission. Right: collimated radiation (see text for details).

A more extensive comparison of results obtained by the LBM and the MCM for the cases of diffuse and collimated radiation, different anisotropy factors and optical depths is shown in Fig. 7. For anisotropy factors $g = 0.7$ and $g = 0.85$ the data from LBM and MCM match well, independent from τ. Also for isotropic scattering, good agreement of results was achieved. For strong anisotropy ($g = 0.95$), the predicted intensity by the LBM increasingly deviates from the MCM for decreasing optical depth.

The results indicate that numerical errors depend on anisotropy and optical depth for which the following error sources are conceivable. A first error is given by the linearization of the RTE during the discretization (see section 2.2.1). It is known that intensity is decreased exponentially due to extinction. By linearization, the decay of intensity and consequently also the amount of energy being in-scattered into a certain solid angle are overestimated. In case of isotropy or weak anisotropy, the linearization error overestimates sideward scattering of radiation while for strong anisotropy, focussing of radiation due to forward scattering occurs. Hence, the extent of the linerization is basically determined by the optical depth and the grid spacing while its effect on the spatial distribution of the mean intensity is determined by anisotropy. If grid spacing or optical depth is reduced, the linearized approximation should match the exponential decay of intensity better, but, however, the results shown in Figs. 6 and 7 do not reflect the expected behavior.

To investigate this phenomenon, ray effects caused by the propagation of the specific intensity on the lattice have to be considered. For that, the assumption shall be made that specific intensity

Optics EXPRESS

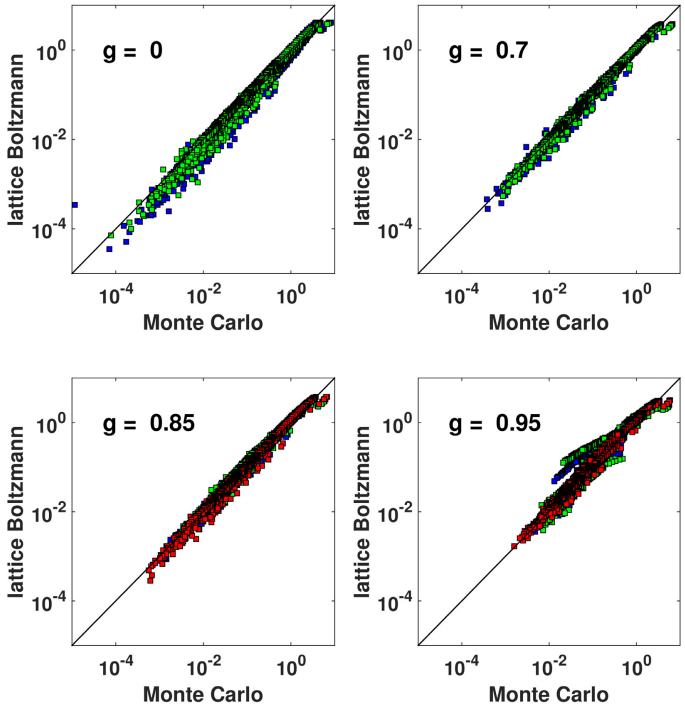

Fig. 7. Simulation data of the mean intensity obtained by the MCM and LBM for different levels of anisotropy. Data is evaluated on lines L_{y1} - L_{y4} and L_{x1} - L_{x3} of planes P_{z1} and P_{z2} for both methods. Colors symbolize different optical depths: $\tau = 100$ (red), $\tau = 50$ (blue), $\tau = 33.333$ (green). Solid line: bisector.

propagates into a solid angle $d\Omega$ and further that $\tau\Delta\mathbf{x}_D < 1$ holds between two nodes of the lattice (as it is the case here for $\tau = 50$ and $\tau = 33.333$). In that case only a portion of the specific intensity is scattered and the remaining energy propagates by free streaming. On the lattice, however, there is no difference between forward scattering and free streaming in a certain direction. In consequence, the solid angle in which the radiation propagates artificially decreases as sketched in Fig. 8, which again leads to a ray effect. From a physical point of view, the ray effect is tantamount to a violation of Liouville's theorem, which states conservation of intensity is phase space [5]. Strong anisotropic scattering pronounces the ray effect, while it is counteracted by low and medium anisotropy, high optical depth and coarse grid spacing. Another possible way to reduce ray effects is a better angular resolution and usage of higher order angular schemes [12, 15]. Similar to LBM for fluids, higher order angular schemes would also potentially allow the applicability of the method to higher Knudsen numbers [19], but at the cost of increasing computational effort.

The total numerical error, thus, results from two error sources, namely linearization error and ray effect. The extent of the total error results from an interplay of anisotropy, optical depth and grid spacing. Table 2 shows the root mean square error (RMSE) between the LBM and the MCM after outlier detection. Data was obtained by evaluation of lines L_{y1} - L_{y4} and L_{x1} - L_{x3} of planes P_{z1} and P_{z2} for both simulated cases described in section 3.1 and each data set consisted 2400 data points before elimination of outliers. Outliers were defined to be outside

Optics EXPRESS

Table 2. Root mean square error of the mean intensity obtained by the LBM compared to the MCM. Data was evaluated along lines L_{y1} - L_{y4} and L_{x1} - L_{x3} of planes P_{z1} and P_{z2} (see Fig. 5).

τ	$g = 0$	$g = 0.7$	$g = 0.85$	$g = 0.95$
33.333	0.0226	0.0268	0.0554	0.1290
50	0.0515	0.0150	0.0401	0.1072
100	-	-	0.0149	0.0590

the interval $[Q_1 - a(Q_3 - Q_1),\ Q_3 + a(Q_3 - Q_1)]$, where Q_i are the quartiles of each data set and the parameter a was set to $a = 3$.

Except from the isotropic case, decreasing the optical depth and, thus, the linearization error, did not result into more accurate prediction of the LBM. Moreover, amplification of the ray effect by strong anisotropy lead to an excessive increase of the total error, which partially is compensated by high optical depths. This results indicate that the ray effect is the dominating error source for the simulation of a scattering turbid media. Hence, to improve the accuracy of the method, future work should deal primarily with this effect. A numerical correction could be reached by implementation of artificial scattering terms, which guarantee the conservation of the specific intensity in phase space. The iterative discretization method (section 2.2.3) potentially allows to design discrete artificial scattering kernels for this purpose.

3.3. *Comparison with Monte Carlo simulations in scattering and absorbing turbid media*

The analysis made so far shall be extended to radiation transfer in a scattering, absorbing and non-emitting turbid medium. Table 3 shows the RMSE of results obtained by the LBM relative to the MCM. Similar to the simulation of radiation transfer in a non-absorbing medium, the ray effect acts as the dominant error source, even if the computation of absorption is affected by the linearization error only. This result was consistent for both simulated cases (see section 3.1).

The observation that the ray effect dominates the numerical error is plausible since for the present case, the scattering albedo was set to $\omega = 0.75$ and thus, scattering dominated over absorption. It can be assumed that for a low scattering albedo the linearization error becomes more dominant, although this was not investigated in the present study and the dependency of

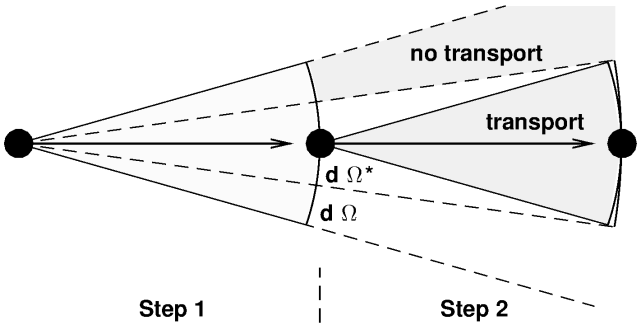

Fig. 8. Schematic representation of the ray effect. In case of free streaming of radiation, the solid angle $d\Omega$ is artificially reduced to $d\Omega^*$ while no radiation streams into the surrounding space.

Optics EXPRESS

the different numerical error on the scattering albedo is not finally clarified. By comparison of tables 2 and 3 it can be seen that the dependency of the numerical error on the optical depth is less pronounced for the non-absorbing case. Hence, it can be concluded that the error caused by the ray effect is increasingly damped by absorption the greater the optical depth becomes.

The accurate numerical calculation of absorption requires fine grid spacing or low optical depths. Alternatively, further improvement of the method could be reached by using a semi-analytic approach, similar to the modeling of collimated radiation as given by Eqs. (33) and (34). Since this approach was also used to calculate the in-scattering from collimated radiation, a semi-analytic hybrid potentially neutralizes the linearization error.

Table 3. Root mean square error of the simulated mean intensity in a scattering and absorbing turbid medium obtained by the LBM compared to the MCM. Data was evaluated along lines L_{y1} - L_{y4} of planes P_{z1} and P_{z2} (see Fig. 5).

τ	$g = 0$	$g = 0.7$	$g = 0.85$	$g = 0.95$
33.333	0.0072	0.0427	0.0496	0.1071
50	0.0096	0.0068	0.0238	0.0414
100	-	-	0.0022	0.0008

3.4. *Computational effort of the lattice Boltzmann method*

The impact of simulation parameters on the computational effort is depicted in Fig. 9. For pure scattering, the number of iterations to reach steady state increases almost linearly with increasing optical depth for all applied anisotropy factors. However, the choice of the anisotropy factor dominates the computational effort, which is the highest for isotropic scattering. This result is expectable since isotropy corresponds with the slowest propagation of intensity on macroscopic scales. In contrast, for $\omega = 0.75$ the increase of the optical depth accelerates convergence independent from anisotropy. It can be expected that this observation changes drastically in case of absorbing and emitting participating media, since isotropic emission of radiation decreases the speed of radiative transfer on macroscopic length scales.

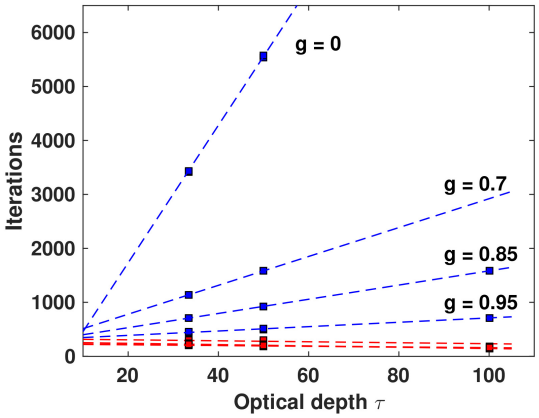

Fig. 9. Number of iterations at steady-state with respect to optical depth and anisotropy for $\omega = 1$ (blue) and $\omega = 0.75$ (red). Dashed lines: linear regression.

Optics EXPRESS

4. Conclusion

A new lattice Boltzmann method for the simulation of three-dimensional radiation transport was developed and validated with Monte Carlo simulations. The method was used for the simulation of radiation transport in turbid media containing either isotropic and anisotropic scatters, as well as absorbing particles. To the best of the authors knowledge, this is the first time that a lattice Boltzmann method was successfully applied for the simulation of anisotropic radiation transfer in three dimensions. Moreover, for the approximation of Mie-scattering, a new iterative algebraic technique for the discretization of the scattering phase function was introduced, which ensures full conservation of energy and the mean scattering angle after discretization.

It was found that the accuracy of the lattice Boltzmann method is affected by two sources of error, namely linearization error and ray effect. For the investigated simulation cases, the latter dominates the total numerical error, independently of optical properties of the turbid media. However, it can be assumed that the dominating error type depends strongly on the scattering albedo. Based on the analysis of numerical errors, the implementation of an artificial scattering kernel and semi-analytic computation of extinction was suggested to further improve the accuracy of the method.

The development of a lattice Boltzmann method for radiation transport is motivated by the interpretation of the RTE as a Boltzmann-type transport equation in the framework of statistical physics. Based on this interpretation, the RTE can be discretized analogous to the discretization of the Boltzmann equation in established lattice Boltzmann methods for fluid dynamics if characteristics of radiation, in particular the constant speed of light, are considered. The establishment of a consistent methodological set of computational methods seems to be promising for solving multiphysical problems with high accuracy in engineering applications.

Acknowledgments

The authors are grateful to Antonio Delgado and Giovanni Luzi (LSTM, FAU Erlangen-Nuremberg) for the helpful discussions and productive collaboration.

6. Spectral Simulation of Light Propagation in Participating Media by Using a Lattice Boltzmann Method for Photons

In this chapter the question of efficient integration across the visible spectrum is addressed. In photobioreactors, light is usually polychromatic so that the RTE has to be solved separately for each wavelength. To minimize the required computational cost it is important to know the required minimal spectral resolution to obtain accurate results when integrating light intensity across the spectrum.

The developed lattice Boltzmann method for light transfer is applied to compute polychromatic light intensity fields. Within the chapter, different simple integration schemes are compared with regard to their accuracy of integrating smooth spectra. Moreover, an approach was tested which aimed to use the a priori available information to minimize the number of simulations by distributing simulated wavelength.

The chapter was published as: McHardy, C., Horneber, T., Rauh, C. (2018). Spectral Simulation of Light Propagation in Participating Media by Using a Lattice Boltzmann Method for Photons. Appl. Math. Comput. 319(15), 59-70, 2018. Reprint for non-commercial use with permission of Elsevier Inc.

Applied Mathematics and Computation 319 (2018) 59–70

Contents lists available at ScienceDirect

Applied Mathematics and Computation

journal homepage: www.elsevier.com/locate/amc

Spectral simulation of light propagation in participating media by using a lattice Boltzmann method for photons

Christopher McHardy*, Tobias Horneber, Cornelia Rauh

Chair of Food Biotechnology and Food Process Engineering, Technische Universität Berlin, Berlin, Germany

ARTICLE INFO

Article history:
Available online 9 February 2017

Keywords:
Radiation transfer
Lattice Boltzmann method
Spectral simulation
Adaptive quadrature
Photobioreactor
Microalgae

ABSTRACT

A lattice Boltzmann method for radiation transfer and Newton–Cotes formulas are used in this work to compute the propagation of polychromatic light in a biosuspension of phototrophic microorganisms. The polychromatic light field is obtained from monochromatic lattice Boltzmann simulations by integration across the visible spectrum. The effects of the spectral resolution, radiation characteristics and the chosen integration rule on the accuracy of the integration are investigated. It was found that reasonable results can be achieved on equidistant spectral grids with a grid spacing of $\Delta\lambda \leq 20\,\text{nm}$, although error compensation might be a serious issue if the trapezoidal rule is applied. Based on *a priori* information about the light field, an approach for the computation of adapted spectral grids is introduced, which aims at the efficient computation of polychromatic light fields. It was found that no significant increase of accuracy can be realized by usage of adapted spectral grids for spectral integration. It is presumed that this observation is caused by the changing shape of the light spectrum along the optical path.

1. Introduction

In recent times, the cultivation of phototrophic microorganisms in photobioreactors receives increasing attention from science and industry. This interest is caused by the ability of such organisms to drive their metabolism by solar energy, and, at the same time, to accumulate huge amounts of various metabolites, making phototrophic microorganisms to be considered as a sustainable feedstock for the production of biomass, biofuels, food, feed and pharmaceuticals [1,2]. However, taking advantage of these beneficial characteristics is still limited by high costs for cultivation and processing of biomass. In particular, mixing becomes a matter of expense due to the necessity of moving cells between light and dark zones in photobioreactors since the availability of light in photobioreactors is known to be a key factor for growth and productivity [3]. Due to this importance, accurate predictions of the spatial light distribution become indispensable for design and optimization of photobioreactors and control of biomass production.

Light propagation in participating media is governed by the radiation transfer equation (RTE). Numerical solutions of the RTE can be obtained by different methods, such as Monte Carlo methods (MCM), Discrete Ordinate methods (DOM) or Finite Volume methods (FVM). All of these methods are well documented and further information can be found elsewhere [4,5]. A new class of methods to solve the RTE are lattice Boltzmann methods (LBM). The idea of using a lattice Boltzmann approach seems to be straightforward since the RTE can be interpreted as a Boltzmann-type transport equation for photons. Moreover,

* Corresponding author.
E-mail address: christopher.mchardy@tu-berlin.de (C. McHardy).

http://dx.doi.org/10.1016/j.amc.2017.01.045
0096-3003/

in addition to radiative transfer, many engineering applications also require the consideration of flows so that a consistent methodology to solve multiphysical problems seems to be beneficial. Enormous improvements have been achieved in the development of LBM for various hydrodynamic tasks [6–10], making the LBM a potential candidate for providing a powerful multiphysical simulation framework.

Originating from works of Asinari et al. [11], Ma et al. [12] and Bindra and Patil [13], a number of further developments have been made in the last years, basically dealing with radiation transfer in 1D and 2D geometries [14–18], while radiation transfer in 3D was rarely considered [19–21]. As a remarkable development, recently, the linkage of the mesoscopic lattice Boltzmann Bhatnagar–Gross–Krook (LBGK) equation and a macroscopic target equation for radiation transfer by means of Chapman–Enskog expansion was demonstrated [19,20]. This approach differs from other models in the sense that usually the target equation was the mesoscopic RTE itself [13,21], which is also true for other numerical methods, such as the DOM or the FVM. However, approximating a macroscopic target equation by solving a lattice Boltzmann equation is what is usually done in fluid dynamics, where the LBM has its origin [6].

All of the above mentioned models have in common that monochromatic radiation transfer is solved. However, radiation characteristics of participating media as well as the spectrum of radiation sources are most often characterized by wavelength-dependency. This is also relevant for photobioreactors, where spectral absorption and scattering characteristics of the microorganisms have to be taken into account and different types of light sources (sunlight, artificial sources) might be used for illumination [22–24]. Spectral-dependent radiation properties require the computation of monochromatic radiation fields and the subsequent superposition of solutions to gain polychromatic profiles of light intensity. Obviously, the accompanied increase of computational costs depends on the desired degree of spectral resolution, becoming maximum for resolving every single wavelength in the visible spectrum. A common approach to deal with polychromatic radiation transfer is to distribute a finite number of discretization points over the spectrum and compute monochromatic radiation fields at the chosen wavelengths. Afterward, the monochromatic field quantities are integrated across the spectrum by means of numerical integration rules (*e.g.*, Newton–Cotes rules) to gain the polychromatic light field. In the field of photobioreactor research, this approach as well as the comparable WSGG model (Weighted Sum of Gray Gases) have been applied with different degree of spectral resolution [25–27]. However, despite of its significant importance, the questions of minimizing the number of discretization points and their optimal placement in the spectral grid remains unanswered in the literature.

The present contribution aims at closing this gap. Effects of spectral discretization and numerical integration rules on the accuracy of polychromatic intensity profiles are investigated. Therefore, numerical solutions of the RTE are computed by means of a lattice Boltzmann method, incorporating three-dimensional scattering. Typical radiation characteristics of microalgae as well as a geometry similar to flat-panel photobioreactors and light sources which are relevant for cultivation of microalgae are assumed. In addition, an approach for the optimal placement of discretization points in the spectral grid is developed and tested. The paper is organized as follows: in Section 2, the choice of the lattice Boltzmann model is motivated by considering typical radiation characteristics of microalgae. Also the model equations and numerical quadrature rules are introduced. In Section 3, details concerning the simulation setup are specified. Results for monochromatic and polychromatic light fields are presented in Section 4, followed by the presentation and evaluation of non-uniform spectral grids for the calculation of polychromatic light fields. Finally, a discussion of the results and conclusions are given in Section 5.

2. Computational methods

2.1. Radiation transfer equation

The radiation transfer equation reads,

$$\frac{1}{c}\frac{\delta J}{\delta t} + \mathbf{n}\nabla_{\mathbf{x}} J = -\beta J + \kappa J_e + \frac{\sigma}{4\pi}\int_{4\pi} J'\Phi(\mathbf{n}', \mathbf{n})\mathrm{d}\Omega'. \tag{1}$$

Herein, J denotes the intensity of radiation, characterizing the amount of photons which propagate into direction $\mathbf{n}$ and solid angle $\mathbf{\Omega}$ with speed of light c. The extinction coefficient $\beta = \kappa + \sigma$ measures the interaction of photons with matter due to absorption and scattering, both individually expressed by absorption (κ) and scattering (σ) coefficients. Scattering re-distributes photons from directions $\mathbf{n}'$ into the direction of propagation $\mathbf{n}$ according to an angular probability density function $\Phi(g, \mathbf{n}, \mathbf{n}')$, known as the scattering phase function, where the asymmetry factor g is the cosine of the mean scattering angle. Because of its low relevance for photobioreactors, the re-emission of absorbed photons by fluorescence with intensity J_e is neglected from now on.

2.2. Lattice Boltzmann method for photons

2.2.1. Selection of the lattice Boltzmann model

In Section 1, it was mentioned that recently the linkage of the LBGK equation to a macroscopic target equation was demonstrated by [18–20]. This linkage is very beneficial from a computational point of view since it ensures convergence rates of second order in space and time. In contrast, as pointed out by Yi et al. [18], prior models are consistently characterized by first order convergence rates. However, deviating from fluid dynamics where the Navier–Stokes equations govern the fluid motion on macroscopic scales, in radiation transfer modeling the mesoscopic RTE is commonly considered as the

Table 1
Quadrature set for the D3Q26 LBM. The quadrature abscissas result from all possible permutations and multiplication by −1 of the typical vector elements.

No. of elements	Direction	Typical vector	Weights
6	1–6	(1,0,0)	1/21
8	7–14	$1/\sqrt{3}$ (1,1,1)	9/280
12	15–26	$1/\sqrt{2}$ (1,1,0)	4/105

governing equation and aimed to be solved. As discussed below, the choice of an applicable lattice Boltzmann model will also strongly depend on the radiation characteristics of the participating medium and thus, on the nature of the radiation transfer problem.

The macroscopic target equation for radiative transport in [19,20] was given by the so-called diffusion approximation. The diffusion approximation describes radiation transfer on macroscopic scales under certain conditions, namely in the limit of high optical thickness in scattering-dominated participating media. Thereby, isotropy of the local photon distribution due to multiple scattering events on small length scales is assumed [4,5]. It is clear that this situation occurs only in certain cases of radiation transfer problems. For instance, for photobioreactors one has to deal with absorbing, strongly forward scattering microorganisms [22], which are usually located in geometries with short light paths. Experimental results of Campbell et al. [28] indicate that in such situations the diffusion approximation will not give an accurate description of the light field. This is basically due to the fact that the isotropization of photons is suppressed in absorbing, non-emissive media and thus, the light field remains anisotropic with a forward peaked propagation probability for photons [29,30]. In addition, by isotropic scaling [31] the transport mean free path of photons can be estimated to be in the order of the geometric dimensions in photobioreactors, typically characterized by short light paths. Therefore, the relevant length scales of light transport in photobioreactors are smaller than the length scales on which the diffusion approximation is accurate. To investigate polychromatic light fields under these conditions, in this work a LBM is chosen which models radiation transfer on the mesoscale by direct discretization of the RTE.

2.2.2. Discretization

The lattice Boltzmann scheme applied in this work was previously published and validated [21]. The RTE is a transport equation for photons in phase space. Therefore, discretization requires both, discretization in position and momentum space. The discretized RTE is then integrated along a characteristic line in the discrete momentum space, leading to the lattice Boltzmann model equation. In the following, a brief repetition of the scheme's major characteristics is given.

Photon momentum consists of directional and frequency (or wavelength) components. For monochromatic photons of wavelength λ, the discretization of the directional component is constrained by the requirement that the exact evaluation of moments is also ensured in the discretized momentum space (see [6,21] for details). After discretization of momentum, (1) becomes

$$\frac{1}{c}\frac{\delta I_{\lambda,i}}{\delta t} + \mathbf{n_i}\nabla_{\mathbf{x}} I_{\lambda,i} = -\beta_\lambda I_{\lambda,i} + \sigma_\lambda w_i \sum_{j=1}^{m} I_{\lambda,j}\Phi_{i,j}, \tag{2}$$

where the intensity J was replaced by the monochromatic specific intensity $I_{\lambda,i}$ of photons of wavelength λ propagating into a discrete direction i. The in-scattering integral is approximated by a Gaussian quadrature, which sums up the in-scattered photons from m discrete directions. The directional weights w_i represent the solid angles $d\Omega$, associated with each discrete direction. Table 1 summarizes the parameters of the quadrature applied for the directional discretization.

For discretization of position space, the domain is represented by a cubic lattice whose nodes are centered in volume elements $\Delta\mathbf{x} = \Delta x\Delta y\Delta z$. As a special feature of LBM, the directional discretization is coupled to spatial discretization because photons are allowed to stream between adjacent nodes of the lattice only.

Eq. (2) is solved by integration along a characteristic line in the discrete momentum space. While for the left-hand side of (2) an exact expression can be obtained, the integration of the right-hand side requires approximate solutions. Applying the forward Euler method leads to the model equation of the LBM,

$$I_i(\mathbf{x_0} + \mathbf{c}_i\Delta t, \mathbf{c}_i, t + \Delta t) - I_i(\mathbf{x_0}, \mathbf{c}_i, t) = \mu_i\left[-I_{\lambda,i}(\mathbf{x_0}) + I^{eq}_{\lambda,i}\right], \tag{3}$$

where μ_i is the collision probability, defined as

$$\mu_i = \beta_\lambda|\mathbf{c_i}\Delta t|, \tag{4}$$

and $I^{eq}_{\lambda,i}$ the local equilibrium function,

$$I^{eq}_{\lambda,i} = \omega_\lambda w_i \sum_{j=1}^{m} I_{\lambda,j}(\mathbf{x_0})\Phi_{i,j}f_{i,j}. \tag{5}$$

In (5), the dimensionless scattering albedo $\omega_\lambda = \sigma_\lambda/\beta_\lambda$ was introduced. The values of $\Phi_{i,j}$ were computed by an iterative algebraic method [21]. A correction factor $f_{i,j} = \Delta t_i/\Delta t_j = \Delta x_i/\Delta x_j$ normalizes $I_{\lambda,j}$ to the direction dependent integration

time interval which results from propagation of photons with constant speed $c_i = c_j$ over direction dependent distances in the cubic lattice. Therefore, the LBM is restricted to the computation of steady-state radiation fields.

2.2.3. Macroscopic field quantities

The local macroscopic quantities of the monochromatic radiation field, namely the local mean intensity $J_\lambda(\mathbf{x})$, the radiation flux vector $\mathbf{F}_\lambda(\mathbf{x})$ and radiation pressure tensor $H_\lambda(\mathbf{x})$, are the moments of the intensity distribution and calculated by integration over the directional component of photon momentum [4]. Using the definition given in Section 2.1, the total number of photons propagating into a direction $\mathbf{n}$ is given by the intensity and the solid angle into which the photons propagate. In the discrete representation of (1), the solid angle is represented by the quadrature weight w_i and therefore the moment equations read,

$$J_\lambda(\mathbf{x}) = \sum_{i=1}^{m} w_i I_{i,\lambda}(\mathbf{x}), \tag{6a}$$

$$\mathbf{F}_\lambda(\mathbf{x}) = \sum_{i=1}^{m} w_i \xi_{i,j} I_{i,\lambda}(\mathbf{x}), \tag{6b}$$

$$H_\lambda(\mathbf{x}) = \sum_{i=1}^{m} w_i \xi_{i,j} \xi_{i,k} I_{i,\lambda}(\mathbf{x}), \tag{6c}$$

where $\boldsymbol{\xi}_{i,j}$, $\boldsymbol{\xi}_{i,k}$ denotes the direction cosines with $j,k = 1,2,3$.

Polychromatic field quantities are calculated by integrating monochromatic field quantities numerically across the spectrum. Numerical integration becomes necessary because the spectral information originates from experiments or simulations and is therefore numeric by definition. Because of their simplicity, the integrals can be easily approximated either by the composite trapezoidal rule

$$Q(\mathbf{x}) = \int_{\lambda_{min}}^{\lambda_{max}} Q_\lambda(\mathbf{x})\mathrm{d}\lambda \approx \sum_{k=1}^{N} (\lambda_{k+1} - \lambda_k) \frac{\left(Q_{\lambda_{k+1}}(\mathbf{x}) + Q_{\lambda_k}(\mathbf{x})\right)}{2}, \tag{7}$$

or by the composite Simpson's rule

$$Q(\mathbf{x}) = \int_{\lambda_{min}}^{\lambda_{max}} Q_\lambda(\mathbf{x})\mathrm{d}\lambda \approx \frac{(\lambda_N - \lambda_1)}{3(N_\lambda - 1)} \left[Q_{\lambda_1}(\mathbf{x}) + 2 \sum_{k=1}^{K/2-1} Q_{\lambda_{2k}}(\mathbf{x}) + 4 \sum_{k=1}^{K/2} Q_{\lambda_{2k-1}}(\mathbf{x}) + Q_{\lambda_N}(\mathbf{x}) \right]. \tag{8}$$

In (7) and (8), Q_λ is a monochromatic field quantity as defined in (6), N_λ is the number of discretization points in the spectral grid, $K = (N_\lambda - 1)/2$ and $\lambda_1 = \lambda_{min}$ and $\lambda_N = \lambda_{max}$. The composite trapezoidal rule approximates the integral by expressing the integrand by piecewise linear functions, given by neighboring discretization points. In contrast, for Simpson's rule the integrand is expressed by piecewise parabolic functions, specified by three adjacent discretization points. Analytical integration of the piecewise approximations finally leads to (7) and (8).

3. Case setup

3.1. Simulation parameters

A cuboid domain filled with a homogeneous suspension of phototrophic microorganisms shall be considered. The domain might be regarded as a small section of a photobioreactor and is of dimension $L_y = L_z = 2L_x$, with $L_x = 0.007$ m. A light source is located in parallel to the yz-plane and illuminates the domain from one side with parallel light, propagating in positive x-direction. All boundaries are open for photons to leave the domain. The suspension is treated as an absorbing and scattering medium, whose absorption and scattering coefficients are related to the concentration of microorganisms c_S in the suspension by

$$\sigma_\lambda = c_S A_{sca,\lambda}, \tag{9a}$$

$$\kappa_\lambda = c_S A_{abs,\lambda}, \tag{9b}$$

where $A_{abs,\lambda}$ and $A_{sca,\lambda}$ are the absorption and scattering cross-sections of the biomass. Both, light source and the radiation properties of the suspension are characterized by spectral dependency. Fig. 1 depicts the normalized emission spectra of the light sources under consideration as well as absorption and scattering spectra of the biomass. Mie-scattering of microorganisms is approximated by the Henyey–Greenstein phase function with a constant anisotropy factor $g = 0.98$ [22].

For a discrete representation of the spectral radiation characteristics, in total $N_\lambda = 33$ discretization points across the spectrum are chosen (Fig. 1). The discretization points of the spectral grid are equidistantly distributed between wavelengths $\lambda_{min} = 400$ nm and $\lambda_{max} = 700$ nm. For each discretization point a monochromatic light field is computed by means of the LBM described above. The criterion of reaching steady-state in monochromatic simulations is given by the relative

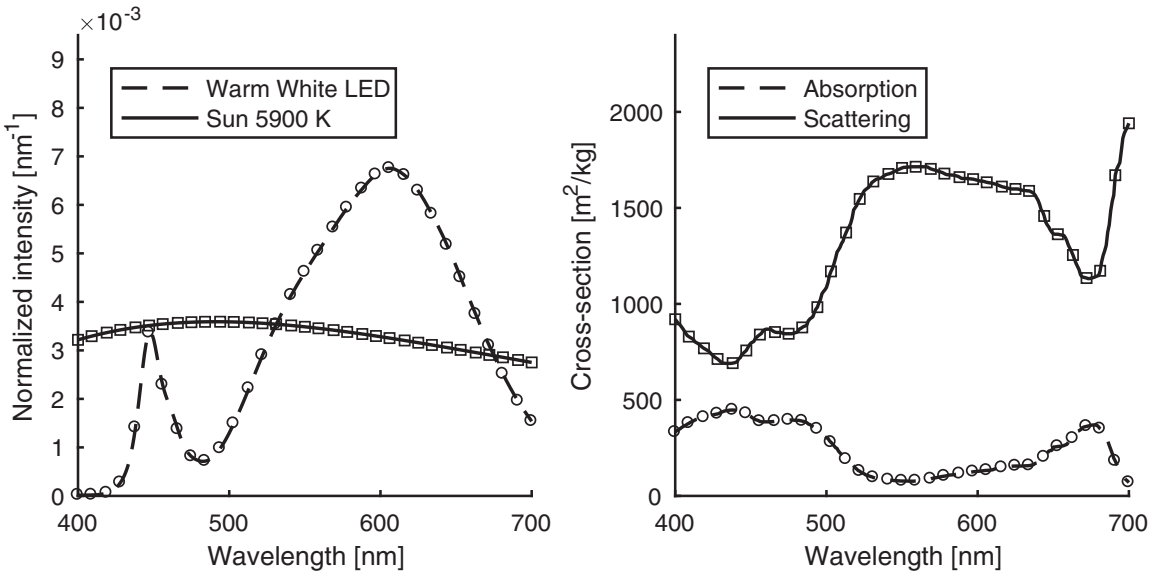

Fig. 1. Left: emission spectra of light sources. Right: absorption and scattering spectra of biomass (data taken from [22]). Symbols illustrate discrete representations of the spectra.

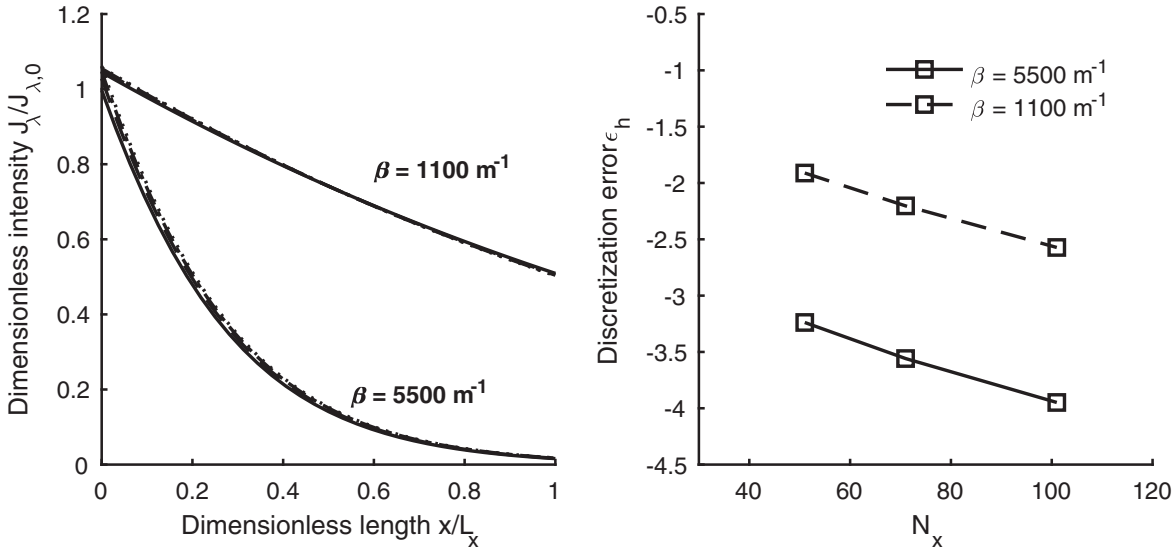

Fig. 2. Grid independence study on equidistant grids with $N_x = 35$ (——), $N_x = 51$ (– –), $N_x = 71$ (– · –), $N_x = 101$ (· · · ·) nodes in x-direction and scattering albedo $\omega = 10/11$. Left: dimensionless intensity. Right: discretization error (log-scale) with respect to spatial resolution.

error ϵ_r

$$\epsilon_r = \left| \frac{I^t_{i,\lambda}(\mathbf{x}) - I^{t-1}_{i,\lambda}(\mathbf{x})}{I^t_{i,\lambda}(\mathbf{x})} \right| \leq 1\mathrm{E}-06, \tag{10}$$

where t is the recent iteration. To investigate the effect of the spectral resolution on the polychromatic light field, a varying number of points are removed from the spectral grid for the computation of polychromatic field quantities according to (7) and (8).

3.2. Spatial grid independence

To estimate the grid independence of the solution and the rate of convergence, solutions of (3) were computed for participating media with different extinction coefficients, a scattering albedo close to unity and $g = 0.98$. The case of scattering dominant media is considered to become limiting for the accuracy of the solution since (3) can be solved analytically for pure absorption.

Fig. 2 shows the computed solutions of (3) on different equidistant grids and the corresponding discretization errors. The profiles of the mean intensity were estimated along the x-axis at the centerline of the domain. The discretization error was

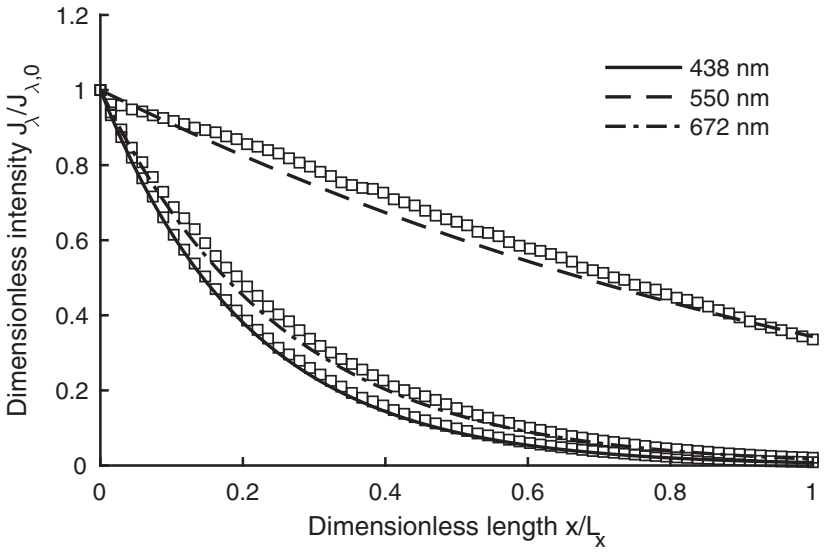

Fig. 3. Monochromatic intensity profiles at wavelengths 438, 550 and 672 nm, computed with the LBM (lines) and MCM (symbols).

quantified according to [32],

$$\epsilon_h = \frac{\phi_h - \phi_{rh}}{r^p - 1}, \tag{11}$$

where $\phi_h = 1 - J_{min}/J_{max}$ was computed from a light intensity profile obtained with spatial grid spacing h, as depicted in Fig. 2. The rate of convergence p was estimated from

$$p = \frac{\log\left(\frac{\phi_{rh} - \phi_{r^2h}}{\phi_h - \phi_{rh}}\right)}{\log(r)}, \tag{12}$$

with a grid refinement ratio $r = 1.41$. The rate of convergence of the LBM was found as $p = 1.0806$ and $p = 0.8451$ for $\beta = 1100\ \mathrm{m}^{-1}$ and $\beta = 5500\ \mathrm{m}^{-1}$, respectively. From Fig. 2 it can be seen that a grid with $N_x = 71$ nodes ensures that the error for the extinction along L_x becomes less than 1%. Therefore, this resolution was chosen for all simulations.

4. Results

4.1. Monochromatic intensity profiles

Fig. 3 shows profiles of the monochromatic mean intensity at the symmetry axis of the domain, computed with the LBM for wavelengths 438, 550 and 672 nm and normalized to J_{max}. For comparison, results obtained by MCM simulations are also depicted. MCM simulations were performed with the same spatial resolution as for the LBM. In total, 1E + 08 photons were traced in each MCM simulation. It can be seen that both methods agree well for different values of β_λ and ω_λ so that the results generated by the LBM can be expected to be reliable.

4.2. Polychromatic intensity on equidistant spectral grids

To study the effect of the spectral discretization on the prediction of the polychromatic light intensity, monochromatic intensity profiles were computed for several test cases. Thereby, different light sources (LED, Sun 5900 K, Fig. 1), as well as different extinction coefficients were considered. The extinction coefficients were computed by means of (9) for two different biomass concentrations (1.5 kg/m^3 and 4.5 kg/m^3), typical for conditions in photobioreactors. The polychromatic light intensity was computed by integration across the spectrum on different equidistant spectral grids. Therefore, the initial spectral grid with discretization points at 400, 550 and 700 nm was gradually refined by adding additional discretization points mid-way between existing points.

Fig. 4 depicts polychromatic intensity profiles with respect to the resolution of the spectral grid, calculated from monochromatic profiles by means of (7) and (8). It can be seen that the application of both integration rules leads to quite similar results if the spectrum is discretized by $N_\lambda \geq 17$ discretization points and further grid refinement has little effect on the shape of the polychromatic profile. Comparable results were found for all cases under consideration. Hence, as a first conclusion, it can be stated that for light predictions in photobioreactors an accurate discretization in the visible spectrum is obtained by choosing wavelength intervals $\Delta\lambda \leq 20$ nm. This finding underlines the necessity for spectral grid

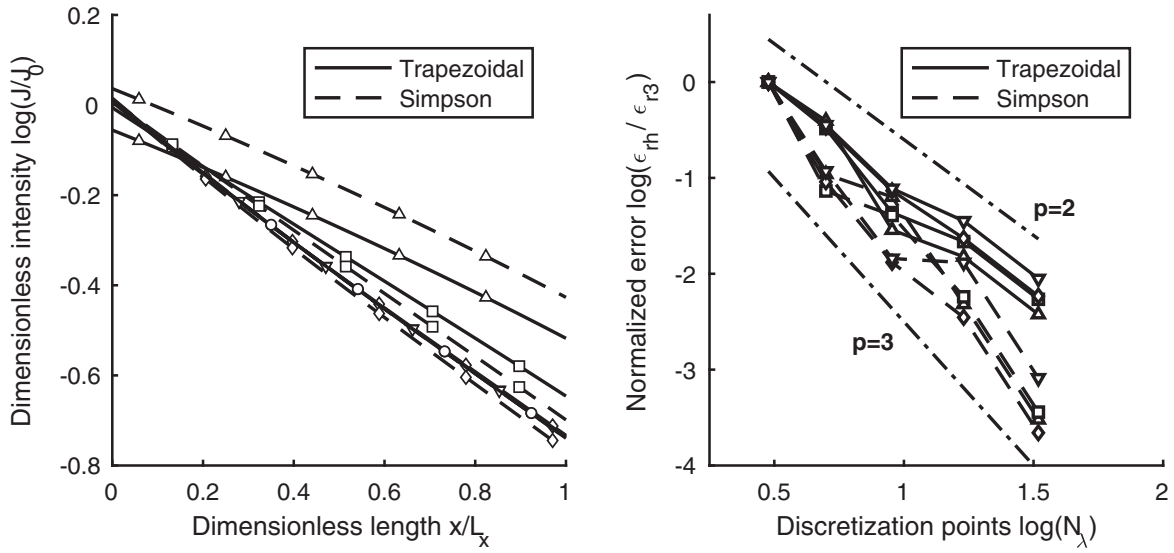

Fig. 4. Effect of spectral discretization and applied integration rule on polychromatic intensity profiles for the case of $c_S = 1.5$ kg/m^3 and illumination by warmwhite LED. Left: profiles computed on different spectral grids. Symbols represent grid resolution: $N_\lambda = 3$ (△), 5 (□), 9 (◇), 17 (▽), 33 (○) discretization points. Right: convergence plot for Newton–Cotes formulas. Symbols represent different cases under consideration: LED, $c_S = 1.5$ (△), LED, $c_S = 4.5$ (□), Sun, $c_S = 1.5$ (◇), Sun, $c_S = 4.5$ (▽).

Table 2
Total relative error, expressed as Euclidian norm of local errors of polychromatic intensity profiles with respect to spectral discretization, integration rule, light source and biomass concentration. Reference solutions were computed by means of Richardson extrapolation.

	Trapezoidal rule				Simpson's rule			
	LED		Sun		LED		Sun	
	1.5	4.5	1.5	4.5	1.5	4.5	1.5	4.5
3	3.0243	10.9606	5.8605	16.4154	5.3188	14.9757	7.2964	19.2120
5	1.1920	3.5848	1.9806	5.8468	0.5816	1.0937	0.6640	2.2605
9	0.0866	0.4762	0.4305	1.2713	0.3365	0.6084	0.0959	0.2772
17	0.0455	0.2375	0.1371	0.5837	0.0256	0.0861	0.0256	0.2514
33	0.0114	0.0594	0.0343	0.1459	0.0016	0.0054	0.0016	0.0157

convergence studies, in particular with regard to previous computations of polychromatic light profiles in photobioreactors at much lower spectral resolutions [25].

Table 2 summarizes the total relative error for all cases under consideration. The respective reference solutions ϕ_{ext} were calculated by extrapolating the solutions on the two finest spectral grids ($N_\lambda = 17, 33$) for every case by means of Richardson extrapolation [33],

$$\phi_{ext} = \phi_f + \frac{\phi_f - \phi_c}{r^p - 1}. \tag{13}$$

Herein, the indices denote coarse (c) and fine (f), $r = 2$ denotes the ratio of the spectral band widths $\Delta\lambda_c/\Delta\lambda_f$ and p is the theoretical rate of convergence of each integration rule, which is $p = 2$ for the trapezoidal rule and $p = 4$ for Simpson's rule. The total relative error ϵ_{rh} was estimated as

$$\epsilon_{rh} = \| 1 - \frac{J_h(x)}{J_{ext}(x)} \|, \tag{14}$$

where J_{ext} is the extrapolated polychromatic intensity profile and J_h the polychromatic intensity profile at spectral grid spacing h.

For spectral grids with wavelength intervals $\Delta\lambda \leq 20$ nm, the total error takes values in an acceptable order of magnitude (the mean relative error is approximately two orders of magnitude below, so less than 1%). Irrespective of the applied integration rule, errors generally increase with increasing extinction coefficient, which indicates that changes of the spectral distribution along the light path have markable effects on the accuracy of spectral integration. Moreover, an effect of the emission spectrum of light sources becomes visible by comparison of results for LED and sunlight. From Fig. 4, the experimental order of convergence for the spectral integration can be obtained. For comparability, ϵ_{rh} was normalized to the error at the lowest spectral resolution. The experimental order of convergence was found to be approximately $p = 2$ for the trapezoidal rule and $p = 3$ for Simpson's rule for all cases under consideration. In conclusion, application of Simpson's

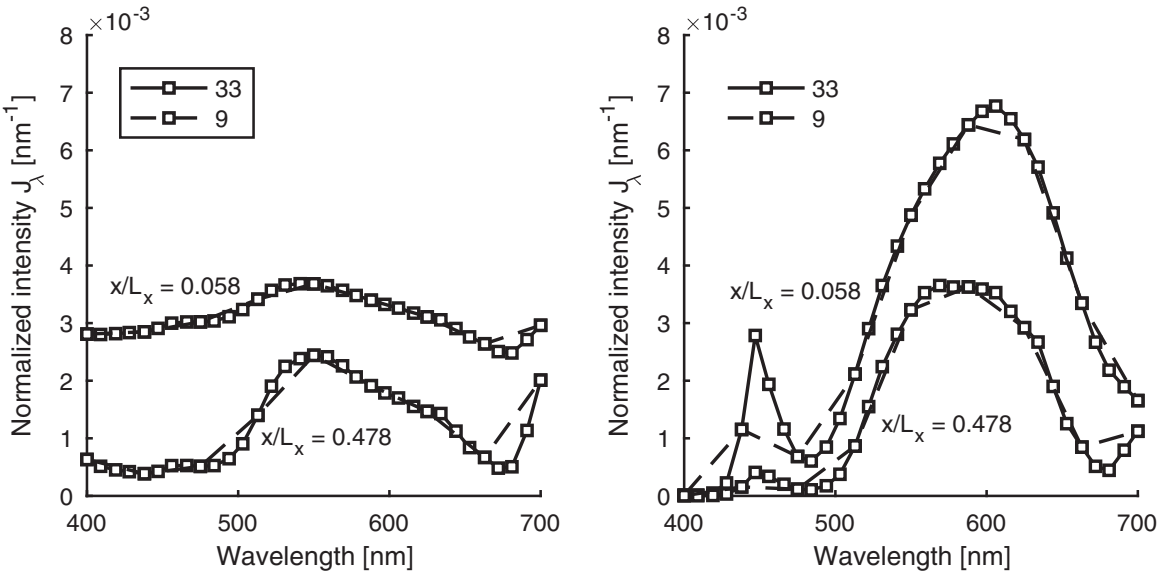

Fig. 5. Piecewise linearized spectral distribution at different spectral resolutions for sunlight (left) and LED (right) at two positions x/L_x along the light path for $c_S = 1.5$ kg/m^3.

rule for spectral integration enhances the speed of convergence and leads to more accurate polychromatic profiles of light intensity for similar resolutions of the spectral grid (the error decreases approximately by an order of magnitude, Table 2). It is therefore recommended to apply Simpson's rule instead of the trapezoidal rule for the integration across the spectrum.

Interestingly, solutions for LED illumination computed with the trapezoidal rule and $N_\lambda = 9$ show at a first glance higher accuracy than results computed with Simpson's rule at similar spectral resolution (Table 2). For a closer examination of this effect, the spectral information from which the integrals are computed should be regarded. Fig. 5 shows the development of the piecewise linearized spectral light distribution along the light path for sunlight and LED illumination and $N_\lambda = 9,\ 33$ discretization points. In the blue region of the spectrum, for sunlight the results are more or less in good agreement at coarse and fine spectral resolutions. The opposite is true in case of LED illumination, where the emission peak of the LED is not resolved accurately for $N_\lambda = 9$, leading to an incorrect prediction of the spectral distribution between 400 and 500 nm. In the green region between 500 and 600 nm, for both cases little errors occur due to a coarse spectral resolution. In contrast, the intensity in the red region between 600 and 700 nm is generally overestimated in case of a coarse spectral resolution because the absorption maximum of biomass remains unresolved.

This observation suggests that at low resolution of the spectral grid and application of the trapezoidal rule, additional errors occur due to the piecewise linear approximation of the spectrum. These errors compensate each other in varying magnitude along the light path, leading to an overestimation of accuracy. Error compensation may lead to misinterpretation of results from spectral grid refinement studies, or wrong calculations of absorbed energy by biomass, which is a key factor for the design of photobioreactors. The analysis supports the suggestion to carry out spectral integration by means of Simpson's rule. However, with regard to a minimal computational effort for calculation of polychromatic intensity profiles with high accuracy, a strategy for optimizing spectral grids could consist of local grid refinement for precise resolution of peaks in the emission and absorption characteristics.

4.3. Local refinement strategy for spectral grids

From the analysis in Section 4.2 the question remains, how discretization points can be placed in the spectral grid to achieve high accuracy while keeping the number of monochromatic simulations moderate at the same time. Thereby, the spectral grid should cover emission characteristics of the source, as well as scattering and absorption characteristics of the turbid suspension. An approach to design such a spectral grid could consist of two steps: first, a characteristic function is built, capturing the available *a priori* knowledge of the light field, which is given by the spectral radiation characteristics of light sources and biomass. Second, the characteristic function is integrated across the spectrum by an adaptive quadrature with a desired degree of accuracy. The discretization points used in the adaptive quadrature are used as points of the final spectral grid.

In an absorbing and mainly forward scattering suspension, a fair approximation for the spatial profile of the specific intensity J_λ is given by an exponential function, known as Lambert–Beer's law. If the specific intensity J_λ is a measure for finding a photon at some point in space, then the extinction probability of photons p_λ is exponentially distributed,

$$p_\lambda(x) = J_{\lambda,0}\left(1 - \exp(-\beta'_\lambda x)\right). \tag{15}$$

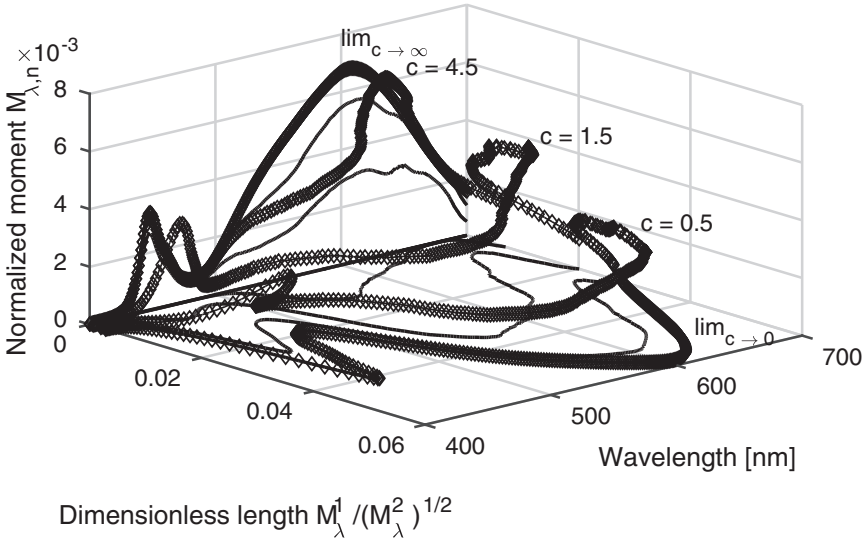

Fig. 6. Characteristic functions for different biomass concentrations $c\,[\mathrm{kg/m^3}]$ and LED illumination along a scaled light path.

In (15), the extinction coefficient $\beta'_\lambda = (\alpha_\lambda + \sigma'_\lambda)$ and the reduced scattering coefficient $\sigma'_\lambda = (1-g)\sigma_\lambda$ were introduced. The characteristic function of $p_\lambda(x)$ is $\phi_\lambda(t) = \int_0^{L_x} \mathrm{e}^{(\mathrm{i}tx)} p_\lambda(x)\mathrm{d}x$ in the interval $[0, L_x]$. The solution of the integral is

$$\phi_\lambda(t) = J_{\lambda,0}\frac{\beta'_\lambda}{\mathrm{i}t - \beta'_\lambda}\left(e^{(\mathrm{i}tL-\tau)} - 1\right), \tag{16}$$

where t is the variable of the characteristic function and $\tau = \beta'_\lambda L_x$. The kth moment M^k of p_λ can be computed from the kth derivative of ϕ_λ, so that ϕ_λ can be Taylor-expanded around $t = 0$ into a series of M^k. Thus, the characteristic function contains the spatial characteristics of the monochromatic intensity field. At $t = 0$ the first three moments are given by the expressions:

$$M^0_\lambda = J_{\lambda,0}(1 - \exp(-\tau_\lambda)), \tag{17a}$$

$$M^1_\lambda = J_{\lambda,0}\frac{-(\tau_\lambda + 1)}{\beta_\lambda}\exp(-\tau_\lambda), \tag{17b}$$

$$M^2_\lambda = J_{\lambda,0}\frac{-(\tau^2_\lambda + 2\tau_\lambda + 2)(\tau_\lambda - 1)}{\beta'^2_\lambda}\exp(-\tau_\lambda). \tag{17c}$$

The physical meaning of (17) is that M^0_λ is the cumulated extinction probability of photons at the monochromatic expected value M^1_λ. Hence, the intensity is $J_\lambda = J_{\lambda,0}(1 - M^0_\lambda)$. The square root of the second moment M^2_λ is a measure for the length scale on which the intensity varies. At $t = 0$ it is valid that $\phi_\lambda = M^0_\lambda$, so that the spectrum of zeroth moments can be interpreted as a characteristic spectrum that represents *a priori* information of the polychromatic light field. Fig. 6 shows the relationship between the spatial light distribution and the moments of the distribution. If the extinction coefficient is high, the shape of the light source becomes important because the variation of the light field occurs close to the source while further away the light field is dominated by a flat spectrum. The lower the extinction coefficient becomes, the more important become modifications of the spectrum along the light path so that the radiation characteristics of the suspension become more important for the shape of the characteristic function.

Coming back to the design of the spectral grid, in a second step an adaptive Simpson's rule is applied to integrate the normalized quantities $M^0_{\lambda,n} = M^0_\lambda/|M^0_\lambda|$ and $J_{\lambda,n} = (J_{\lambda,0} - M^0_\lambda)/J_{\lambda,0}$ across the spectrum. The resulting two adapted grids are superimposed to receive the spectral grid for the LBM. In the adaptive Simpson's rule, integration over spectral intervals is carried out similar to conventional Simpson's rule. The algorithm refines a local integration interval into two subintervals until the increase of accuracy by refining the spectral grid is below a certain threshold ϵ_1. Following [34], the criterion for refinement of a spectral interval $\Delta\lambda = \lambda_u - \lambda_l$ is

$$\epsilon_1 \le \frac{1}{15}\left[\int_{\lambda_l}^{\lambda_l+\Delta\lambda/2} Q_{\lambda,n}\mathrm{d}\lambda + \int_{\lambda_l+\Delta\lambda/2}^{\lambda_u} Q_{\lambda,n}\mathrm{d}\lambda - \int_{\lambda_l}^{\lambda_u} Q_{\lambda,n}\mathrm{d}\lambda\right], \tag{18}$$

where $Q_{\lambda,n}$ is the normalized integrand and the integrals are approximated by Simpson's rule. The refinement strategy lead to good results, however it might fail locally due to error compensation in subintervals. In particular, resolving the blue emission peak of the LED was found to be problematic. To capture the shape of the curve and prevent error compensation, an additional criterion for refinement is established. Simpson's rule approximates the distribution piecewise by parabolas

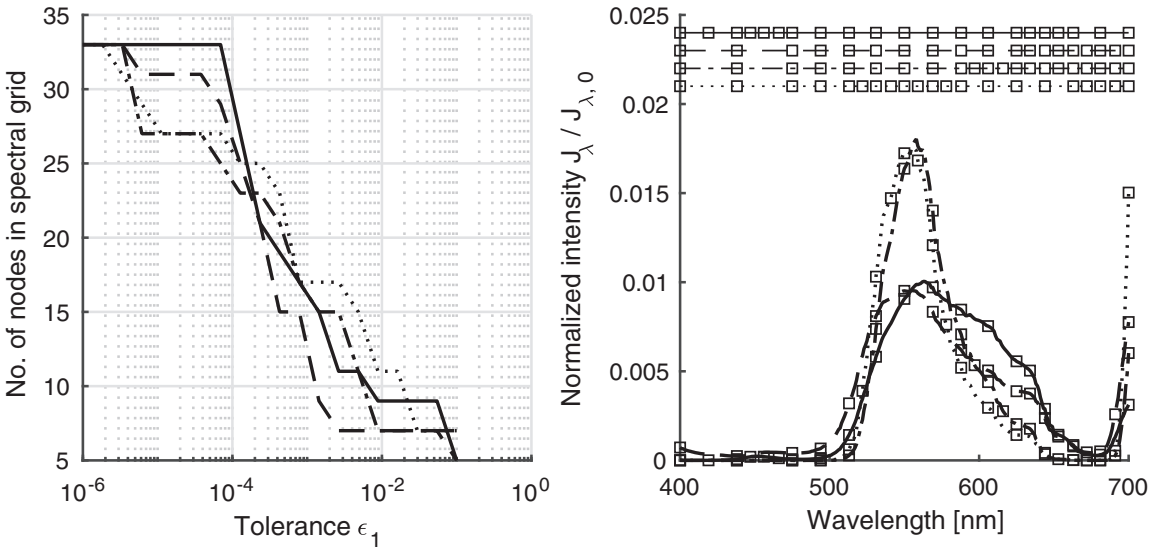

Fig. 7. Adaptive grid generation for different illumination and biomass concentrations: LED 1.5 kg/m^3 (——), Sun 1.5 kg/m^3 (– –), LED 4.5 kg/m^3 (– · –), Sun 4.5 kg/m^3 (. . . .). Left: number of discretization points with respect to threshold ϵ_1. Right: Adapted spectral grids for different cases and $\epsilon_1 = 51\text{E}-04$. Profiles show the quantity $(J_{\lambda,0} - M^0_\lambda)/J_{\lambda,0}$. For clarity, spectral grids are additionally shown at the top of the figure.

Table 3
Total relative error, expressed as Euclidian norm of local errors of polychromatic intensity profiles on adapted spectral grids. Reference solutions were computed by means of Richardson extrapolation.

	LED		Sun	
	1.5	4.5	1.5	4.5
Discretization points	21	21	19	21
Error $_{N_\lambda \text{ adapted}}$	0.0347	0.0294	0.0324	0.0353
Error $_{N_\lambda=17}$	0.0256	0.0861	0.0256	0.2514
Error $_{N_\lambda=33}$	0.0016	0.0054	0.0016	0.0157

so that the coarse grid approximation can be evaluated at discretization points of the refined spectral grid and compared to the values of the real spectrum. If the deviation is large, it indicates that the shape of the spectrum is not well covered. Thus, the second refinement criterion is

$$\epsilon_2 \leq |Q^{app}_{\lambda,n}(\lambda') - Q_{\lambda,n}(\lambda')|, \tag{19}$$

where $\lambda' = \lambda_l + \Delta\lambda/4$ or $\lambda' = \lambda_u - \Delta\lambda/4$. In addition, the maximum degree of local refinement is limited by definition of a maximum resolution of $N_\lambda = 33$ discretization points across the spectrum. Fig. 7 shows the dependence of the spectral grid on ϵ_1. The value of ϵ_2 was set to $\epsilon_2 = 51\text{E}-04$ ($c_S = 1.5$ kg/m^3) and $\epsilon_2 = 11\text{E}-03$ ($c_S = 4.5$ kg/m^3), respectively. Setting the thresholds to this values ensures that all spectral grids have about 20 discretization points. The adapted spectral grids are shown on the right-hand side of Fig. 7.

4.4. Polychromatic intensity on locally refined spectral grids

To verify the applicability of the adapted spectral grids, the integrals across the spectrum were computed for all cases and compared to the reference solution, which is extrapolated from the two finest equidistant spectral grids by means of (13). Table 3 shows the computed errors and sizes of the optimized spectral grids. For comparison, the errors from equidistant spectral grids are shown as well. It can be seen that the errors decrease for high biomass concentrations ($c_S = 4.5$ kg/m^3) compared to the results for $N_\lambda = 17$ discretization points. Since the number of discretization points is slightly increased, also the effect of adaption must be considered to be moderate and equidistant spectral grids seem to be an applicable choice for integration across the spectrum. In case of low biomass concentrations $c_S = 1.5$ kg/m^3, no decrease of the errors could be estimated. The results indicate that equidistant spectral grids are a proper choice for the integration as long as the grid spacing $\Delta\lambda$ is fine enough. From the different cases under consideration in this study it was found that, as a rule of thumb, the choice of $\Delta\lambda \approx 15...20$ nm ensures accurate results.

5. Discussion and conclusions

In this study a lattice Boltzmann method for photon propagation was applied for computation of monochromatic light fields. Subsequently, the monochromatic light fields were integrated across the spectrum by means of Newton–Cotes formulas to study the effects of the integration rule and spectral resolution on the computation of polychromatic light fields.

The application of lattice Boltzmann methods for radiation transport problems is quite new. In analogy to fluid dynamics, the linkage of the LBGK equation to a macroscopic target equation was recently introduced [20]. In contrast, in this work a direct discretization of the radiation transfer equation was applied and therefore a mesoscopic target equation was solved. Although the method shows only first order convergence rates in space, it allows the computation of light fields near sources and in strongly absorbing and anisotropic participating media, which was demonstrated in a huge number of numerical experiments [21]. With regard to a more general theory, it has to be stated that the application of LBM for radiation transfer has still not been investigated in depth and a consistent LBM framework for radiation transfer is outstanding. In particular, a remaining question concerns the target equations to be solved. In a couple of contributions, the LBM was applied to solve mesoscopic target equations as the RTE, regardless of postulating target equations on macroscopic scales [13,21,35]. Since incorporation of macroscopic diffusion into the LBM enables second order convergence in space and time [6], the coupling to macroscopic target equations seems to be a favorable goal. However, macroscopic target equations on a physical base which enable the simulation of radiation transport beyond the diffusion regime were not introduced to LBM, yet.

Simulation based design of photobioreactors became quite popular in recent times. Thereby, the calculation of light fields becomes limiting because the light field may change dynamically due to the motion of cells or gas bubbles inside the reactor. In extreme cases this means that a full polychromatic simulation of the light field must be carried out for every time step of the fluid dynamics simulation. It becomes clear that efficient integration across the spectrum might significantly reduce the costs accompanied with the computation of the polychromatic light field. In this work, Newton–Cotes formulas were applied to obtain polychromatic light intensity profiles. For conditions typical for photobioreactors, it was found that reasonable accuracy could be obtained by using Simpson's rule on equidistant spectral grids with grid spacing $\Delta\lambda < 20\,\text{nm}$. It also turned out that error compensation leads to over-prediction of the accuracy in case of integration by means of the trapezoidal rule, whose usage is therefore not recommended.

To further increase the efficiency of computing polychromatic light fields, an approach based on the usage of available *a priori* information of the light field and an adaptive Simpson's rule was developed and tested. In general, the described integration task is similar to numerical integration of any discrete density distribution. For instance, this kind of integration is reported for determining pest insect population sizes from spatially distributed field data [36]. Consistent to the results shown in Section 4.4, [36] found that adaptive quadrature schemes were not able to improve the accuracy of integration, which was explained by missing *a priori* information about the spatio-temporal distribution of the integrands. In contrast, for photons such *a priori* information is available in terms of the radiation characteristics of light sources and the turbid suspension. However, application of the method developed in Section 4.3 did not further increase the accuracy of the spectral integration. Thereby, it can be presumed that the changing shape of the light spectrum along the optical path is the major difficulty for the design of optimized spectral grids.

In the context of constructing adapted spectral grids, a characteristic function was introduced. Applying this function to photobioreactors might offer new possibilities in analyzing light fields for future research. In future works, discrete simulation data could be used instead of an exponential ansatz to compute the characteristic function of the light field and obtain moments of the spatial light distribution. In particular, this could be of interest to estimate characteristic length scales of the light field and couple this information to the length and time scales of cell motion and mixing in the photobioreactor. Further research should address the applicability of this approach to establish scaling laws for photobioreactors, whose absence is still a major concern for the implementation of the technology.

References

[1] O. Pulz, W. Gross, Valuable products from biotechnology of microalgae, Appl. Microbiol. Biotechnol. 65 (6) (2004) 635–648.
[2] M.A. Borowitzka, High-value products from microalgae—their development and commercialisation, J. Appl. Phycol. 25 (3) (2013) 743–756.
[3] A.P. Carvalho, S.O. Silva, J.M. Baptista, F.X. Malcata, Light requirements in microalgal photobioreactors: an overview of biophotonic aspects, Appl. Microbiol. Biotechnol. 89 (5) (2011) 1275–1288.
[4] M.F. Modest, Radiative Heat Transfer, Academic Press, 2013.
[5] J.R. Howell, M.P. Menguc, R. Siegel, Thermal Radiation Heat Transfer, CRC Press, 2015.
[6] S. Succi, The Lattice Boltzmann Equation: For Fluid Dynamics and Beyond, Oxford University Press, 2001.
[7] A. Ladd, R. Verberg, Lattice-Boltzmann simulations of particle–fluid suspensions, J. Stat. Phys. 104 (5–6) (2001) 1191–1251.
[8] C.K. Aidun, J.R. Clausen, Lattice-Boltzmann method for complex flows, Annu. Rev. Fluid Mech. 42 (2010) 439–472.
[9] D. Anderl, S. Bogner, C. Rauh, U. Rüde, A. Delgado, Free surface lattice Boltzmann with enhanced bubble model, Comput. Math. Appl. 67 (2) (2014) 331–339.
[10] D. Anderl, M. Bauer, C. Rauh, U. Rüde, A. Delgado, Numerical simulation of adsorption and bubble interaction in protein foams using a lattice Boltzmann method, Food Funct. 5 (4) (2014) 755–763.
[11] P. Asinari, S.C. Mishra, R. Borchiellini, A lattice Boltzmann formulation for the analysis of radiative heat transfer problems in a participating medium, Numer. Heat Transfer Part B: Fundam. 57 (2) (2010) 126–146.
[12] Y. Ma, S. Dong, H. Tan, Lattice Boltzmann method for one-dimensional radiation transfer, Phys. Rev. E 84 (1) (2011) 016704.
[13] H. Bindra, D. Patil, Radiative or neutron transport modeling using a lattice Boltzmann equation framework, Phys. Rev. E 86 (1) (2012) 016706.
[14] S.C. Mishra, R.R. Vernekar, Analysis of transport of collimated radiation in a participating media using the lattice Boltzmann method, J. Quant. Spectrosc. Radiative Transfer 113 (16) (2012) 2088–2099.
[15] Y. Zhang, H. Yi, H. Tan, One-dimensional transient radiative transfer by lattice Boltzmann method, Optics Express 21 (21) (2013) 24532–24549.

[16] Y. Zhang, H.-L. Yi, H.-P. Tan, Lattice Boltzmann method for short-pulsed laser transport in a multi-layered medium, J. Quant. Spectrosc. Radiative Transfer 155 (2015) 75–89.
[17] R. McCulloch, H. Bindra, Coupled radiative and conjugate heat transfer in participating media using lattice Boltzmann methods, Comput. Fluids 124 (2016) 261–269.
[18] H.-L. Yi, F.-J. Yao, H.-P. Tan, Lattice Boltzmann model for a steady radiative transfer equation, Phys. Rev. E 94 (2) (2016) 023312.
[19] R. Geist, K. Rasche, J. Westall, R. Schalkoff, Lattice-Boltzmann lighting, in: A. Keller, H.W. Jensen (Eds.), Eurographics Workshop on Rendering, The Eurographics Association, 2004.
[20] A. Mink, G. Thäter, H. Nirschl, M.J. Krause, A 3D lattice Boltzmann method for light simulation in participating media, J. Comput. Sci. 17 (Part 2) (2016) 431–437.
[21] C. McHardy, T. Horneber, C. Rauh, New lattice Boltzmann method for the simulation of three-dimensional radiation transfer in turbid media, Optics Express 24 (15) (2016) 16999–17017.
[22] R. Kandilian, J. Pruvost, A. Artu, C. Lemasson, J. Legrand, L. Pilon, Comparison of experimentally and theoretically determined radiation characteristics of photosynthetic microorganisms, J. Quant. Spectrosc. Radiative Transfer 175 (2016) 30–45.
[23] H. Berberoglu, L. Pilon, A. Melis, Radiation characteristics of *Chlamydomonas reinhardtii* cc125 and its truncated chlorophyll antenna transformants tla1, tlax and tla1-cw+, Int. J. Hydrogen Energy 33 (22) (2008) 6467–6483.
[24] L. Pilon, H. Berberoğlu, R. Kandilian, Radiation transfer in photobiological carbon dioxide fixation and fuel production by microalgae, J. Quant. Spectrosc. Radiative Transfer 112 (17) (2011) 2639–2660.
[25] H. Berberoglu, J. Yin, L. Pilon, Light transfer in bubble sparged photobioreactors for H_2 production and CO_2 mitigation, Int. J. Hydrogen Energy 32 (13) (2007) 2273–2285.
[26] B. Kong, R.D. Vigil, Simulation of photosynthetically active radiation distribution in algal photobioreactors using a multidimensional spectral radiation model, Bioresour. Technol. 158 (2014) 141–148.
[27] W. Blanken, P.R. Postma, L. de Winter, R.H. Wijffels, M. Janssen, Predicting microalgae growth, Algal Res. 14 (2016) 28–38.
[28] S. Campbell, A. O'Connell, S. Menon, Q. Su, R. Grobe, Light scattering regimes along the optical axis in turbid media, Phys. Rev. E 74 (6) (2006) 061909.
[29] E. Gorodnichev, A. Kuzovlev, D. Rogozkin, Propagation of circularly polarized light in media with large-scale inhomogeneities, J. Exp. Theor. Phys. 88 (3) (1999) 421–432.
[30] E. Gorodnichev, A. Kuzovlev, D. Rogozkin, Multiple scattering of polarized light in a turbid medium, J. Exp. Theor. Phys. 104 (2) (2007) 319–341.
[31] V. Ntziachristos, Going deeper than microscopy: the optical imaging frontier in biology, Nat. Methods 7 (8) (2010) 603–614.
[32] J.H. Ferziger, M. Peric, Computational Methods for Fluid Dynamics, Springer Science & Business Media, 2012.
[33] C.J. Freitas, The issue of numerical uncertainty, Appl. Math. Model. 26 (2) (2002) 237–248.
[34] J.N. Lyness, Notes on the adaptive Simpson quadrature routine, J. ACM 16 (3) (1969) 483–495.
[35] A. Gairola, H. Bindra, Lattice Boltzmann method for solving non-equilibrium radiative transport problems, Ann. Nuclear Energy 99 (2017) 151–156.
[36] N.L. Embleton, Handling Sparse Spatial Data in Ecological Applications Ph.D. thesis, The University of Birmingham, School of Mathematics, 2014.

7. Numerical Analysis of the Effects of Air on Light Distribution in a Bubble Column Photobioreactor

Air bubbles are frequently mentioned to affect the light intensity field in photobioreactors in a positive way by contributing to a more homogeneous illumination [108–110]. At a fixed gas hold-up the effect of air on the light field must be a function of the cell concentration and wavelength since both determine the radiation characteristics of a cell suspensions as outlined in chapter 3. It is clear that an impact of the gaseous phase on the light distribution can not be static and depends on the operating point of the PBR. However, these relations are rarely considered in the literature so that incorrect conclusions might arise.

In this chapter, a hybrid simulation framework is developed in order to include the local concentrations of the gaseous phase in the computation of the light distribution. The numerical hybrid consists of an Euler-Euler model for the dynamic multiphase flow and the proposed lattice Boltzmann solver for the Radiation transfer equation. The overall goal of the chapter is the quantification of the impact of air on the light field and its effect on the prediction of microalgae growth.

The chapter was published as: McHardy, C., Luzi, G., Lindenberger, C., Agudo, J.R., Delgado, A., Rauh, C. (2018). Numerical Analysis of the Effects of Air on Light Distribution in a Bubble Column Photobioreactor. Algal Research, 31, 311-325, 2018. Reprint for non-commercial use with permission of Elsevier Inc.

Algal Research 31 (2018) 311–325

Contents lists available at ScienceDirect

Algal Research

journal homepage: www.elsevier.com/locate/algal

Numerical analysis of the effects of air on light distribution in a bubble column photobioreactor

Christopher McHardy[a,*], Giovanni Luzi[b], Christoph Lindenberger[b], Jose R. Agudo[b], Antonio Delgado[b,c], Cornelia Rauh[a,b,c]

[a] Technische Universität Berlin, Fachgebiet Lebensmittelbiotechnologie und –prozesstechnik, Königin-Luise Str. 22, 14195 Berlin, Germany
[b] Universität Erlangen-Nürnberg, FAU-Campus Busan, 46-742, Republic of Korea
[c] Universität Erlangen-Nürnberg, Lehrstuhl für Strömungsmechanik, Cauerstr. 4, D-91058 Erlangen, Germany

ARTICLE INFO

Keywords:
Bubble column photobioreactor
Numerical simulation
Light distribution
Gas bubbles

ABSTRACT

Light distribution inside photobioreactors (PBR) is a crucial parameter for the determination of growth of phototropic microorganisms and reactor productivity. In order to compute the light propagation inside PBR, scattering due to the presence of microorganisms is often neglected, since it is difficult to measure experimentally and it is not trivial to handle numerically. Moreover, absorption is usually assumed constant, but it is affected by the concentration of microorganisms and the presence of gas bubbles. In the present contribution we study how the flow hydrodynamics and local gas fractions inside a bubble column PBR affect the light distribution. First, we perform numerical simulations of a bubble column flow at different gas superficial velocities. Afterwards, we use instantaneous air volume fractions to calculate the effective scattering and absorption coefficient of the mixture, as well as the effective scattering phase function. Finally, we compute the polychromatic light distribution inside the PBR by means of a Lattice-Boltzmann solver. On the one hand, we find that gas bubbles affect both spatial distribution and magnitude of the light intensity field and their impact increases at higher gas superficial velocity. On the other hand, we also observe that the biomass counteracts these effects already at concentrations less than 1 kg/m^3 so that the role of the gas phase on light fields seems to be of minor importance in PBR.

1. Introduction

Bubble column photobioreactors are common installations for the cultivation of microalgae. Their application covers a wide range of different scales, spanning from laboratory to large scale cultivation [1–5]. Thereby, illumination may occur either by sunlight or artificially, either from external or internal sources. The frequent usage of bubble columns is due to their beneficial characteristics, including simple design and low investment costs [5], easy mode of operation, possibility to cultivate under low shear conditions [6–8], as well as excellent mass transfer characteristics particularly with regard to carbon dioxide supply and oxygen removal [9,10]. Moreover, due to several applications of bubble column reactors in different industries, existing scaling laws [11,12] provide indicators regarding important and still unsolved upscaling issues, which arise for instance from the sensitivity of hydrodynamic mixing and gas-liquid mass transfer efficiency with respect to the geometric aspect ratio or pneumatic power input. Mastering these issues is a necessity for an economic feasible large scale production of microalgae biomass and intracellular metabolites.

Recently, multiphysics simulations of phototrophic cell cultivation in PBR have become more popular [13–21], since they represent a valid alternative to time consuming and costly experimental investigations. Simulations can also be coupled to mathematical optimization algorithms [22], in order to find optimal geometrical designs or process conditions (e.g. the intensity or spectrum of the light source, air mass flow) to achieve a desired process outcome such as a maximum biomass concentration. Therefore, the simulation of phototrophic cultivation processes requires a proper modeling of the physical environment inside the reactor, and/or kinetic modeling of the cells metabolic response to environmental stimuli. An example of this is the modeling of the cellular energy metabolism to predict the specific growth rate with respect to light intensity. Important physical fields that have to be determined in this context are the fluid flow field as well as the spatial distribution of light. While the latter determines the overall supply of energy for phototrophic growth, the former affects gas liquid mass

* Corresponding author.
E-mail address: christopher.mchardy@tu-berlin.de (C. McHardy).

https://doi.org/10.1016/j.algal.2018.02.016
Received 5 October 2017; Received in revised form 17 January 2018; Accepted 14 February 2018
Available online 27 February 2018

transfer, mixing of cells and therefore, growth conditions of individual microorganisms.

However, modeling of physical phenomena in PBR is not trivial, and an adequate modeling of gas-liquid multiphase flows requires the correct determination of momentum transfer between both phases. Thereby, two-dimensional numerical simulations of bubble column flow require a significantly lower computational time compared to three-dimensional ones. Therefore, they have been extensively used to test different flow models, like for instance, the classic Euler-Euler approach [23], the Algebraic Slip Mixture Model (ASMM) [24], a modified Euler-Euler model for the liquid phase [25], according to the formulation of Zhang and Prosperetti [26,27], and the Eulerian-Lagrangian approach [28], among others. Although it is reported that they compare favorably with experiments in terms of time average gas-holdup [23], liquid velocity and turbulent kinetic energy [24], two-dimensional simulations ignore the three-dimensional nature of turbulence [29]. They are also seen to predict a frozen plume that does not oscillate, due a too high turbulent viscosity [29,30]. In addition to, they are found to be highly grid dependent [29]. Therefore, three-dimensional simulations are necessary to obtain a correct determination of the flow field, although they are computationally much more expensive. Three-dimensional simulations have been carried out for different reactor geometries, like for instance, an empty cylindrical bubble column [31], a cylinder with internal solid plates to increase the gas holdup and mixing time [32], and a square bubble column [33], among others. Comparing numerical results with the experiments of Deen and Solberg [34], Masood *et al.* [35] performed a comprehensive analysis and comparison of different turbulence closure models for the liquid phase, as well as for different drag force correlations. Additionally, they examined the influence of interphase forces such as lift, virtual mass, wall lubrication and turbulent dispersion forces on the flow field. Other researchers focus on the heterogeneous regime, considering also bubble coalescence and break-up effects. Chen *et al.* [36] carried out two-dimensional axis symmetric simulations implementing a bubble population balance equation (BPBE) together with bubble break-up and coalescence models. They reported that the BPBE improves the predictions compared to a single bubble group model in the churn-turbulent flow regime. Diaz *et al.* [37] validated their numerical results with experiments, comparing both single and multiple size group model. They concluded that at sufficiently high values of gas superficial velocity, computations with the multiple size group result in better agreement with experiments.

Concerning the modeling of light propagation, most commonly researchers choose analytic expressions, such as Beer's law [19,20,38–40], Cornet's model [41,42] or regression models to fit experimental or numerical data [15]. All of these models are one-dimensional, but they differentiate in their degree of accuracy. While Beer's law considers only the light absorbed by the cell culture, Cornet's model is based on a two-flux approximation and distinguishes between anisotropic forward and backward scattering in its advanced formulation [42]. A more detailed approach is to take the three-dimensional nature of scattering into account by solving the governing equation of light transport, which is the Radiation Transfer Equation (RTE). This approach is increasingly chosen by researchers, using different numerical methods [13,14,43–47]. However, major difficulties in the computation of light distribution are the determination of absorption and scattering characteristics of cell suspensions, emission characteristics of light sources and internal reflectivity [48]. These difficulties lie on challenging experimental measurements [49,50] and model uncertainties [50,51]. Moreover, non-uniform spectral distribution of radiation characteristics, and their temporal variation due to cell growth and photoacclimation add further complications. The situation is even more complex in cultivation systems where the radiation characteristics of suspensions are affected by the presence of a gas phase. In contrast to the extensive numbers of investigations dealing with the effects of the gas phase on liquid flow, little work was done concerning the effects of gas bubbles on light fields. Lee and Palson [52] state without experimental evidence that gas sparging increases the light penetration depth. Miron *et al.* [1] experimentally investigated light fields in a bubble column PBR and found a higher light dispersion inside the column due to reflections on gas bubble surfaces. However, the study fully neglects the presence of microalgae cells, which clearly affect the light field by absorption and scattering. More recently, Berberoglu *et al.* [45] included the effect of gas bubbles in a 1D light propagation model for a plane-parallel PBR. In their model, they considered different air volume fractions (up to approx. 0.075 m^3/m^3, not clearly specified) and relatively low biomass concentrations (up to 0.35 kg dry matter/m^3). They found significant backscattering of light under these conditions. Therefore, the overall amount of energy in the system increased, thus leading to higher local light intensities. However, they assume the void fraction to be randomly distributed in space so that a potential error source arises. For example, in case of dip tube spargers, the gas is expected to be concentrated in the center of the reactor. Therefore, its effect on the light distribution should be weak, since light energy is mostly absorbed near the reactor walls. In contrast to the findings of [1,45], the results of Wheaton and Krishnamoorthy [43] indicate that the presence of air bubbles has little effects on the light distribution. The authors combined a fluid-dynamical model for bubbly flows with computations of radiation transport in order to investigate the effects of micro-bubbles, air mass flow rate and algae concentration. They conclude that at higher biomass concentrations the effect of air on light distribution is weaker. However, results regarding the computed flow fields are not reported and scattering by algae is not considered although is it well established that true light intensity profiles in PBR deviate from predictions which assume a purely absorbing suspension [14,53].

With regard to the contradictory results concerning the impact of the gas phase on light distribution in air-sparged PBR, the aim of this work is to contribute with clarifying information into this debate. We hypothesize that the presence of a gas phase lowers light attenuation and therefore increases the local light intensity; however we expect the effect to become less important if the culture density increases. Although this presumption seems to be *a priori* obvious, it is not clear to what extent the increase of light availability due to the presence of a gas phase affects the specific rate of cell growth. Thus, to put it simply, the key question to be answered is whether the presence of a gas phase has to be considered for accurate predictions of cell growth or not.

To answer this question, we perform full 3D simulations of the flow field in a benchtop scale bubble column PBR, determining the local gas distributions under different operating conditions. Extending the work of McHardy *et al.* [47], we consider local scattering of light caused by gas bubbles and algae cells and investigate their effects on the polychromatic light distribution in the bubble column at different gas superficial velocities. Thereby, instead of treating the air as homogeneously distributed in the PBR [45], the spatial characteristics of bubble localization are considered. The effect of the gas phase on cell growth is examined by coupling the computed light fields to the Aiba growth model and compared to simulations which take only the presence of microalgae cells into account.

The paper is organized as follows: first, the underlying modeling approach is presented in Section 2. The calculated flow field and the corresponding spatial distribution of radiation characteristics are presented in Section 3. In addition, in this section we quantify the effects of gas superficial velocity and biomass concentration on the light fields and specific cell growth rates in the PBR. Finally, we discuss our findings with regard to prior experimental and numerical results in Section 4.

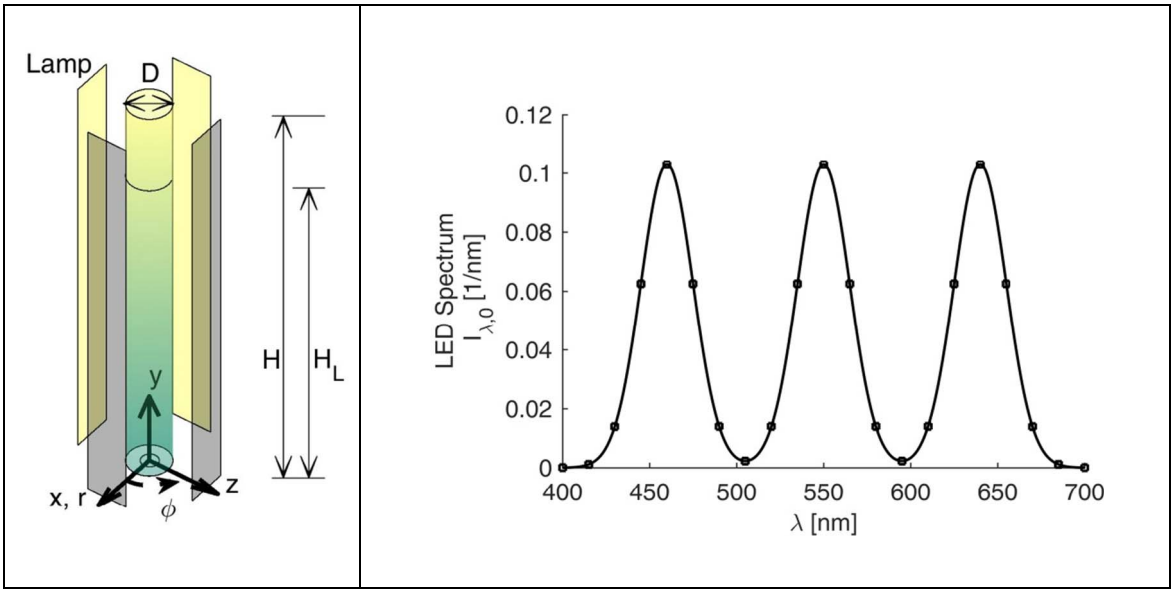

Fig. 1. Left: sketch of the simulated PBR system with Cartesian and Cylindrical coordinate system. Right: spectrum of the LED lamps. Symbols show the simulated wavelengths.

2. Modeling and numerical methods

2.1. Photobioreactor

In this study, we consider a cylindrical bubble column PBR filled with a suspension of microalgae *Chlamydomonas reinhardtii* at concentration X, measured in kg dry matter/m^3. The diameter of the PBR is $D = 5$ cm, its height is $H = 50$ cm whereby the liquid height is $H_L = 40$ cm. The inlet where air is introduced is located at the center of one of the two reactor bases. Its diameter is $d = 1$ cm, and the distributed air bubbles have a constant mean diameter $d_b = 7$ mm.

Illumination of the PBR occurs from 4 LED light sources, each of them emitting polychromatic RGB light with intensity I_0 in parallel to both, the x and z coordinate axis. The normalized spectrum of the light sources is approximated by superimposing three Gaussians with maximum emission at 460 (R), 550 (G), 640 (B) nm and standard deviation of 15 nm. Reflections on the reactor surface and refraction due to mismatching refractive indices of the reactor material, algae suspension and surrounding air are not considered. The simulated PBR system is sketched in Fig. 1.

2.2. Flow model

The multiphase flow in the bubble column is modelled with a classic Eulerian-Eulerian formulation, which treats the single phases as interpenetrating continua. The flow field is governed by the conservation equations of mass and momentum for each phase. The mass conservation equations read

$$\frac{\partial}{\partial t}(\rho_k \alpha_k) + \nabla\cdot(\rho_k \alpha_k \boldsymbol{u}_k) = 0 \tag{1}$$

where the subscripts $k = L, G$ stand for liquid and gas respectively. The other symbols u_k, α_k and ρ_k represent the velocity vector, volume fraction and density of each phase respectively. The momentum equations are

$$\frac{\partial}{\partial t}(\rho_k \alpha_k \boldsymbol{u}_k) + \nabla\cdot(\rho_k \alpha_k \boldsymbol{u}_k \boldsymbol{u}_k) = -\alpha_k \nabla p + \nabla\cdot(\alpha_k \boldsymbol{\tau}_k) + \rho_k \alpha_k \boldsymbol{g} + \boldsymbol{M}_{s,k} \tag{2}$$

where $s = L, G$. The left-hand side of Eq. (2) describes the temporal and the inertial convective acceleration, while the right-hand side contains terms accounting for the pressure gradient, the divergence of the stress tensor as well as the gravitational and the interphase forces. In the Eulerian-Eulerian formulation, both phases share the same pressure field. The stress tensor is defined as

$$\boldsymbol{\tau}_k = \mu_{k,eff}\left[\nabla \boldsymbol{u}_k + (\nabla \boldsymbol{u}_k)^T - \frac{2}{3} I(\nabla\cdot \boldsymbol{u}_k)\right] \tag{3}$$

where $\mu_{k,\ eff}$ is the effective viscosity of each phase. The effective viscosity results from the contribution of the molecular $\mu_{k,\ Lam}$ and the turbulent one $\mu_{k,\ Turb}$

$$\mu_{k,eff} = \mu_{k,Lam} + \mu_{k,Turb} \tag{4}$$

where $\mu_{L,\ Turb}$ is calculated according to the Shear Stress Transport (SST) model [54], and $\mu_{G,\ Turb}$ is computed by means of an algebraic equation [Ansys CFX –Solver Theory Guide]. The last term of Eq. (2) represents the so called interphase forces, that is

$$\boldsymbol{M}_{s,k} = \boldsymbol{M}_{L,G} = -M_{G,L} = \sum_A \boldsymbol{F}^A_{L,G} = \boldsymbol{F}^D_{L,G} + \boldsymbol{F}^L_{L,G} + \boldsymbol{F}^{VM}_{L,G} + \boldsymbol{F}^{WL}_{L,G} + \boldsymbol{F}^{TD}_{L,G} \tag{5}$$

The terms on the right hand-side of Eq. (5) indicate the drag, lift, virtual mass, wall lubrication and turbulent dispersion forces. The drag force is

$$\boldsymbol{F}^D_{L,G} = \frac{3}{4}\alpha_G \rho_L \frac{C_D}{d_B}|\boldsymbol{u}_G - \boldsymbol{u}_L|(\boldsymbol{u}_G - \boldsymbol{u}_L) \tag{6}$$

where C_D is the drag coefficient. We compute it by a power law

$$C_D = \alpha_L^f C_{D\infty} \tag{7}$$

where $C_{D\infty}$ is the drag coefficient of a single bubble calculated with the Grace correlation, for the values of gas superficial velocities $u_G = 4.25$ mm/s and $u_G = 8.5$ mm/s, and $f = 2$ is a correction factor. For the case $u_G = 1.28$ cm/s, we calculate the drag coefficient with the Ishii Zuber correlation

$$C_D(sphere) = \frac{24}{Re_m}(1 + 0.15 Re_m^{0.687}) \tag{8a}$$

$$C_D(ellipse) = E(\alpha_G)\frac{2}{3} Eo^{(1/2)} \tag{8b}$$

$$C_D(cap) = \alpha_L^2 \frac{8}{3} \tag{8c}$$

which differentiates among the spherical $C_D(sphere)$, distorted $C_D(ellipse)$ and spherical cap $C_D(cap)$ regime. Re_m is a mixture Reynolds

Table 1
Values of the absorption and scattering cross-sections of *Chlamydomonas reinhardtii* with respect to wavelength.

λ [nm]	400	415	430	445	460	475	490	505	520	535	550
A_{abs} [m^2/kg]	331	401	434	436	386	395	367	261	140	87	77
A_{sca} [m^2/kg]	920	794	699	743	868	845	927	1209	1512	1653	1708

λ [nm]	565	580	595	610	625	640	655	670	685	700
A_{abs} [m^2/kg]	82	106	123	136	156	176	259	358	311	70
A_{sca} [m^2/kg]	1714	1673	1651	1628	1599	1538	1360	1139	1305	1941

number, based on the velocity difference between the continuous and the disperse phase and on a mixture viscosity, and *Eo* is the Eötvös number [Ansys CFX–Solver Theory Guide]. The lift force reads

$$\boldsymbol{F}_{L,G}^{L} = \alpha_G \rho_L C_L (\boldsymbol{u}_G - \boldsymbol{u}_L) \times \nabla \times \boldsymbol{u}_L \tag{9}$$

where the lift force coefficient C_L is computed according to the Legendre-Magnaudet model [55], which takes into account the contribution of the flow at both low and high Reynolds numbers. The virtual mass force

$$\boldsymbol{F}_{L,G}^{VM} = \alpha_G \rho_L C_{VM} \left(\frac{D\boldsymbol{u}_G}{Dt} - \frac{D\boldsymbol{u}_L}{Dt} \right) \tag{10}$$

accounts for the additional inertia gas bubbles possess since they displace a certain amount of volume of the surrounding liquid. We fix the value of the virtual mass coefficient to $C_{VM} = 0.5$. The wall lubrication force

$$\boldsymbol{F}_{L,G}^{WL} = -\alpha_G \rho_L C_{WL} \ |\boldsymbol{u}_L - \boldsymbol{u}_G|^2 \hat{\mathbf{n}}_W \tag{11}$$

prevents the gas phase from touching the reactor walls and push it away from them, producing a void fraction peak. Here, $\hat{\boldsymbol{n}}_W$ is the unit vector normal to a reactor surface, and the wall lubrication coefficient C_{WL} has been evaluated using the Frank correlation [56]. Finally, the effect of the turbulent dispersion forces

$$\boldsymbol{F}_{L,G}^{TD} = C_{TD} C_{CD} \frac{\nu_{L.Turb}}{\sigma_{L.Turb}} \left(\frac{\nabla \alpha_L}{\alpha_L} - \frac{\nabla \alpha_G}{\alpha_G} \right) \tag{12}$$

has been evaluated according to the Favre averaged model [57]. In Eq. (12) $\sigma_{L,\ Turb}$ is the turbulent Schmidt number of the continuous phase, $C_{TD} = 1$ is a constant multiplier and C_{CD} is a momentum transfer coefficient related to the drag force [Ansys CFX –Solver Theory Guide].

2.3. Light distribution model in the multiphase suspension

The governing equation of light distribution is the Radiation Transfer Equation (RTE), which reads

$$\frac{\partial L_\lambda(\boldsymbol{x}, t, \hat{\mathbf{n}})}{c\ \partial t} + \hat{\mathbf{n}} \cdot \nabla L_\lambda(\boldsymbol{x}, t, \hat{\mathbf{n}}) = -\beta_\lambda L_\lambda + \frac{\sigma_\lambda}{4\pi} \int_{4\pi} \Phi(\hat{\mathbf{n}}\ ,\ \hat{\mathbf{n}}') L_\lambda'(\boldsymbol{x}, t, \hat{\mathbf{n}}')\, d\Omega \tag{13}$$

Here, L_λ is the radiance at wavelength λ propagating with the speed of light c along the direction $\hat{\mathbf{n}}$ into the solid angle $d\Omega$. The extinction coefficient $\beta_\lambda = \kappa_\lambda + \sigma_\lambda$ considers the change of L_λ by absorption (κ_λ) and scattering (σ_λ) per unit length. The index λ denotes wavelength-dependency of the indexed quantities. The second term on the right-hand side is the scattering integral, which takes into account the in-scattering of L_λ' along $\hat{\mathbf{n}}$ with a probability given by the scattering phase function $\Phi(\hat{\mathbf{n}}\ ,\ \hat{\mathbf{n}}')$. Moreover $\boldsymbol{x}$ indicates the position vector.

L_λ is related to the photon directional distribution. Since the quantity of interest is the local specific light intensity I_λ, one needs to take the zeroth angular moment of L_λ

$$I_\lambda(\boldsymbol{x}, t) = \int_{4\pi} L_\lambda(\boldsymbol{x}, t, \hat{\mathbf{n}})\, d\Omega \tag{14}$$

from which the polychromatic light intensity I can be calculated by integration across the spectrum

$$I(\boldsymbol{x}, t) = \int I_\lambda(\boldsymbol{x}, t)\, d\lambda \tag{15}$$

Generally, the effective radiation characteristics of a turbid suspension reflect the properties of the single components contained. In case of microalgae, the scattering and absorption coefficients can be obtained from

$$\sigma_{A,\lambda}(t) = A_{sca,.\lambda}\, X(t) \tag{16a}$$

$$\kappa_{A,\lambda}(t) = A_{abs,\lambda}\, X(t) \tag{16b}$$

where $X(t)$ is the dry biomass concentration at time t. For the biomass-specific scattering and absorption cross-sections A_{sca} and A_{abs} of *Chlamydomonas reinhardtii*, we use the values measured by Kandilian [50], see Table 1. Gas bubbles are assumed to be non-absorbent, therefore $\kappa_B = 0$. However, the gas bubble scattering coefficient can be calculated similarly to Eq. (16a) from the scattering cross section of a single bubble and the number density of gas bubbles, which is related to the air volume fraction in a PBR. In the present study, we resolve the air volume fraction locally and temporally, therefore the bubble scattering coefficient becomes a quantity depending on both, space and time. It reads

$$\sigma_B(\boldsymbol{x}, t) = \alpha_G(\boldsymbol{x}, t) Q_{sca} \frac{A_B}{V_B} \tag{17}$$

where $Q_{sca} = 1$ is the scattering efficiency of a single bubble, and A_B and V_B denote the geometrical cross-section and volume of a gas bubble, respectively. In Eq. (17) we assume that σ_B has no wavelength-dependency. The effective absorption and scattering coefficients of the mixture can be obtained by superimposing those of the single components [45,49]. Thus, the effective scattering and absorption coefficients become

$$\sigma_\lambda(\boldsymbol{x}, t) = \sigma_{A,\lambda}(t)(1 - \alpha_G(\boldsymbol{x}, t)) + \sigma_B(\boldsymbol{x}, t) \tag{18a}$$

$$\kappa_\lambda(\boldsymbol{x}, t) = \kappa_{A,\lambda}(t)(1 - \alpha_G(\boldsymbol{x}, t)) \tag{18b}$$

Eqs. (18a) and (18b) consider the local reduction of the liquid volume by the presence of air and thus, a reduced biomass concentration. According to Pilon *et al.* [49], the effective scattering phase function can also be computed by superimposing those of the gas bubbles and microalgae cells, using their individual scattering coefficients as weights

$$\Phi(\mathbf{x}, t) = \frac{\sigma_{A,\lambda}(t)(1 - \alpha_G(\mathbf{x}, t))\Phi_A + \sigma_B(\mathbf{x}, t)\Phi_B}{\sigma_{A,\lambda}(t)(1 - \alpha_G(\mathbf{x}, t)) + \sigma_B(\mathbf{x}, t)} \tag{19}$$

For both gas bubbles and microalgae cells, we utilize the Henyey-Greenstein phase function with anisotropy factors $g_A = 0.98$ and $g_B = 0.86$, respectively. We retain the usual assumption that light propagation is much faster than any other process in the system, dropping the time-dependence in the computation of light propagation and focusing on short system states.

2.4. Simulation strategy

We cover the whole volume with a structured grid obtained by employing two O-grids that have been generated with the commercial software ANSYS ICEM® 15.0. We select a mesh with 54201 volumes

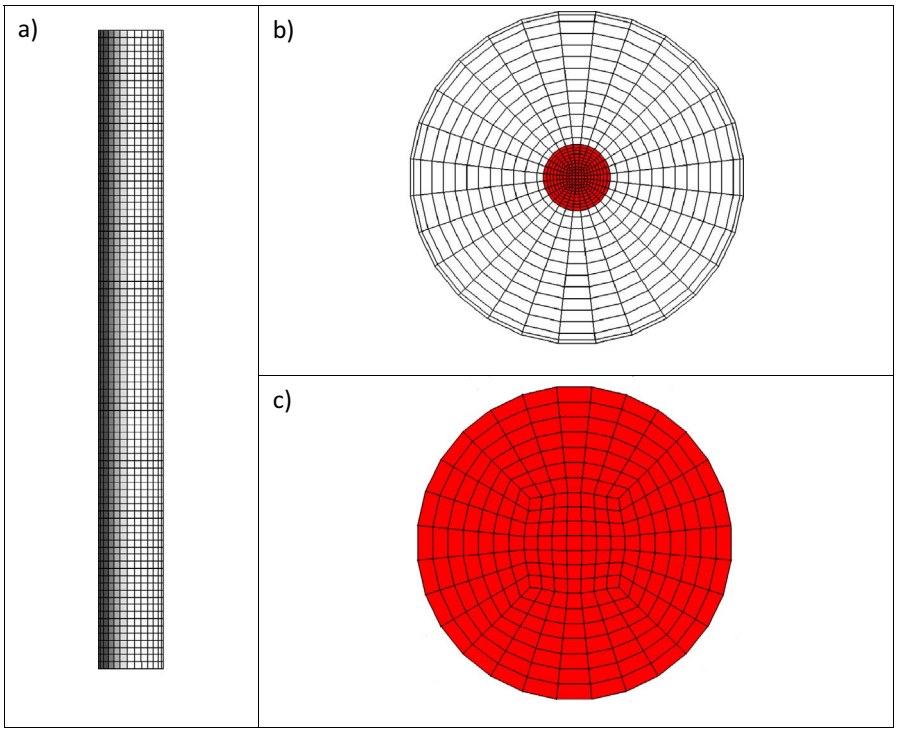

Fig. 2. Structured mesh of the PBR with hexahedral elements a) side view, b) view of the bottom face and c) zoom on the inlet part.

after performing a grid sensitivity study, see Section 3.2. In Fig. 2 we show some details of the mesh used in the simulations. The inner O-grid creates a central square with 7 × 7 cells and four additional rim parts of 7 × 7 cells each, encompassing one-quarter of a circle between the inlet boundary and the central grid square. The cross-section between the inlet and the reactor boundary has 364 cells arranged circularly, and the length of the main axis of the cylinder has been subdivided into 89 equally spaced parts. We use the commercial software ANSYS CFX® 15.0, which is a node-centered finite volume solver, to perform all the numerical computations. We specify the value of the air mass flow rate at the inlet and we set an opening boundary condition at the outlet. By doing so, the computed pressure is either the total or the static one, depending on the flow direction. We set a no-slip condition for the velocity of both fluids and zero gradient for the pressure at all the other surfaces.

We run the simulations with three different values of gas superficial velocity, i.e. u_G = 4.25 mm/s, u_G = 8.5 mm/s and u_G = 1.28 cm/s. The gas superficial velocity is defined as the gas flow rate divided by the cross-sectional area of the PBR. The three values of gas superficial velocity used in our numerical computations correspond to typical range of volume flow rates commonly used in PBR [1,58]. In case of the lowest value of gas superficial velocity, we set an adaptive time step to initialize the simulations, ranging from a minimum $\Delta t = 5{\cdot}10^{-4}$ s until a maximum $\Delta t = 1.25{\cdot}10^{-3}$ s. The maximum number of inner iterations after which the time step is decreased is 30, while the minimum number of inner iterations before which the time step is increased is 15. The increasing factor is 2, while the decreasing factor is 0.5. In case of u_G = 8.5 mm/s, we use a fixed time-step $\Delta t = 1.25{\cdot}10^{-3}$ s, while for the case of the highest value of gas superficial velocity we employ first $\Delta t = 6.25{\cdot}10^{-4}$ s and subsequently we increase it up to $\Delta t = 8.75{\cdot}10^{-4}$ s.

For each of the three values of the gas superficial velocity, we run the simulations for 100 s, advancing the solution in time using an implicit second-order backward Euler scheme. We keep the bubble diameter d_B = 7 mm constant in all the numerical computations, neglecting bubble coalescence and break-up effects, since our values of gas superficial velocities are small [35,59,60]. The convergence criteria is achieved when the root mean square (RMS) value of the residuals of velocity and pressure drop below 10^{-4} at each time steps. From the computed flow field, we extract the air volume fractions at a specific time instant, in order to compute the local radiation characteristics of the mixture by means of Eqs. (18a)–(19), assuming a certain biomass concentration X. We consider three biomass concentrations, X = 0.25 kg/m^3, X = 0.50 kg/m^3 and X = 1.00 kg/m^3, which can be considered to be representative of early and medium stages of the batch cultivation of *Chlamydomonas reinhardtii* in a bubble column reactor [61], similar to the one considered in this work. Finally, the monochromatic RTE is solved on a structured lattice with 1.16x1E07 nodes by means of a lattice Boltzmann solver [62]. The selected grid (lattice) has been chosen after a grid independence study. Integration across the spectrum was performed by means of the Simpson's rule with 21 spectral discretization points, which was previously shown to produce accurate results [46].

2.5. Data processing

For further evaluation, the computed light intensity $I(\boldsymbol{x},t)$ was interpolated on a grid in cylindrical coordinates $I(r,\phi,y,t)$ and averaged over the angular coordinate. The corresponding standard deviations were computed from the variance $s^2_{I\phi}$.

$$I_\phi(r,y,t) = \frac{1}{N_\phi}\sum I(r,\phi,y,t) \tag{20}$$

$$s^2_{I\phi}(r,y,t) = \frac{1}{N_\phi}\sum \left(I(r,\phi,y,t) - I_\phi(r,y,t)\right)^2 \tag{21}$$

The cylindrical grid is composed of N_ϕ = 360 points (angular coordinate), N_r = 51 points (radial coordinate) and N_y = 1020 points (y coordinate). Thereby, the number of points along the reactor radius $R = D/2$ and in y-direction equals the discretization in Cartesian coordinates. From the radial profiles of an angular averaged quantity $Y_\phi(r,y)$, the volumetric average in the PBR can be computed (see Appendix A for details)

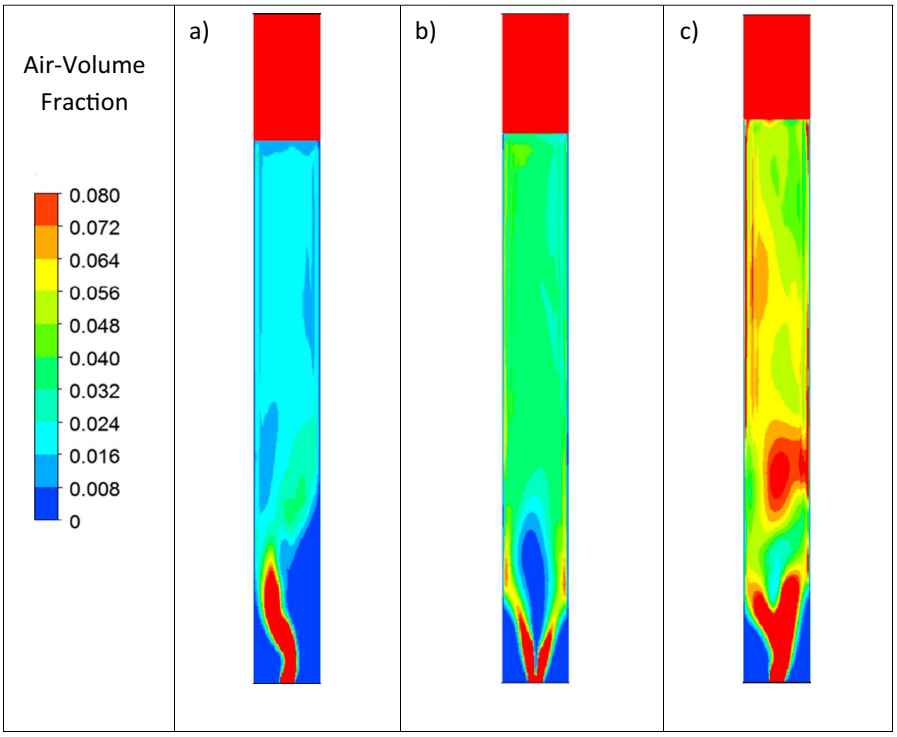

Fig. 3. Air-volume fraction contours at different time instants for each of the three values of the gas superficial velocity, a) $t = 88.8$ s and $u_G = 4.25$ mm/s, b) $t = 136.95$ s and $u_G = 8.5$ mm/s and c) $t = 286.02$ s and $u_G = 1.28$ cm/s.

$$\overline{Y} = \frac{1}{V}\int_0^H\int_0^{2\pi}\int_0^R Y_\phi(r,y)\, r\, \mathrm{d}r\, \mathrm{d}\phi\, \mathrm{d}y \approx \frac{1}{N_y R^2}\sum_{i=1}^{N_y}\left[\sum_{j=2}^{N_r-1} 2r_j \Delta r Y_\phi(r_j,y_i) + \frac{\Delta r^2}{4}Y_\phi(r_1,y_i) + \left(R\Delta r - \frac{\Delta r^2}{4}\right)Y_\phi(r_{N_r},y_i)\right] \quad (22)$$

3. Results

3.1. Flow field

Fig. 3 shows contours of instantaneous air-volume fractions used to compute the radiation properties of the mixture. For a better visualization, they are displayed on a cross-sectional (x-y) plane located at $z = 0$. They have been computed with different values of gas superficial velocities, i.e. $u_G = 4.25$ mm/s, $u_G = 8.5$ mm/s, and $u_G = 1.28$ cm/s, see Fig. 3a, b and c respectively. The gas hold-up achieves higher values as the gas superficial velocity increases, and the gas phase shows a highly dynamic motion with a randomly oscillating plume, see Fig. 3a, b and c. The movement of the plume induces chaotic three-dimensional vortical structures in the liquid phase, typical of the bubble column hydrodynamics. The wave motion of a central plume creates large vortices in the liquid phase on the bottom part of the reactor, thus resulting in an intense recirculation region. Moving towards the top of the reactor, the plume spreads across the column due to the interphase forces. It results in a more defined flow structure with an ascending liquid region in the central part of the column, and a descending flow region close to the reactor walls. A minor vortical-spiral flow region is also noticeable between the central part of the column and the walls.

3.2. Grid study and spatiotemporal variation of radiation characteristics

We examine the effects of grid size comparing the time averaged scattering coefficient obtained with three different grids. The coarse, medium and fine grid have 33575, 54201 and 81675 hexahedral cells, respectively. We utilize the value of gas superficial velocity $u_G = 4.25$ mm/s and run the simulations up to 150 s. Afterwards, we start the time averaging and we continue running the simulations up to a final value of 300 s. Therefore, the total averaging time is 150 s, the same reported by Masood *et al.* [35]. We compute the time averaged scattering coefficient profiles on a (x-y) plane at $z = 0$ at three different heights in the PBR, i.e. at $y = 0.025$ m, $y = 0.1$ m and $y = 0.3$ m, using time averaged air volume fraction profiles in Eq. (18a). We consider a biomass concentration $X = 0.5$ kg/m^3 and a scattering cross-section $A_{sca} = 1139$ m^2/kg at $\lambda = 670$ nm. Moreover, we also calculate the extrapolated solution σ_{ext}^{21}

$$\sigma_{ext}^{21} = \frac{(r_{21}^{p'_{ave}}\sigma_1 - \sigma_2)}{(r_{21}^{p'_{ave}} - 1)} \quad (23)$$

where σ_1 and σ_2 are the values of the scattering coefficient computed at each point of the profile with the fine and the medium grid, respectively. r_{21} is the refinement factor, which is the ratio between the representative cell sizes of the medium and the fine grid [63]. A representative cell size for three dimensional simulations is defined as

$$h_j = \left[\frac{1}{N_j}\sum_{i=1}^{N_j}(\Delta V_i)\right]^{\frac{1}{3}} \quad (24)$$

where ΔV_i is the volume of the ith cell composing the total volume and N_j is the total number of cells of the j grid [63]. Here $j = 1, 2, 3$ correspond to the fine, medium and coarse grid, respectively. In our case, the refinement factor is constant, that is, $r_{21} = r_{32}$ where r_{32} is the ratio of the representative cell sizes between the coarse and the medium grid. p_{ave}' is the average of the local apparent order of the method p'

$$p' = \frac{1}{ln(r_{21})}\left|ln\left[\frac{\varepsilon_{32}}{\varepsilon_{21}}\right]\right| \quad (25)$$

where $\varepsilon_{32} = \sigma_3 - \sigma_2$ and $\varepsilon_{21} = \sigma_2 - \sigma_1$. σ_3 is the local value of the

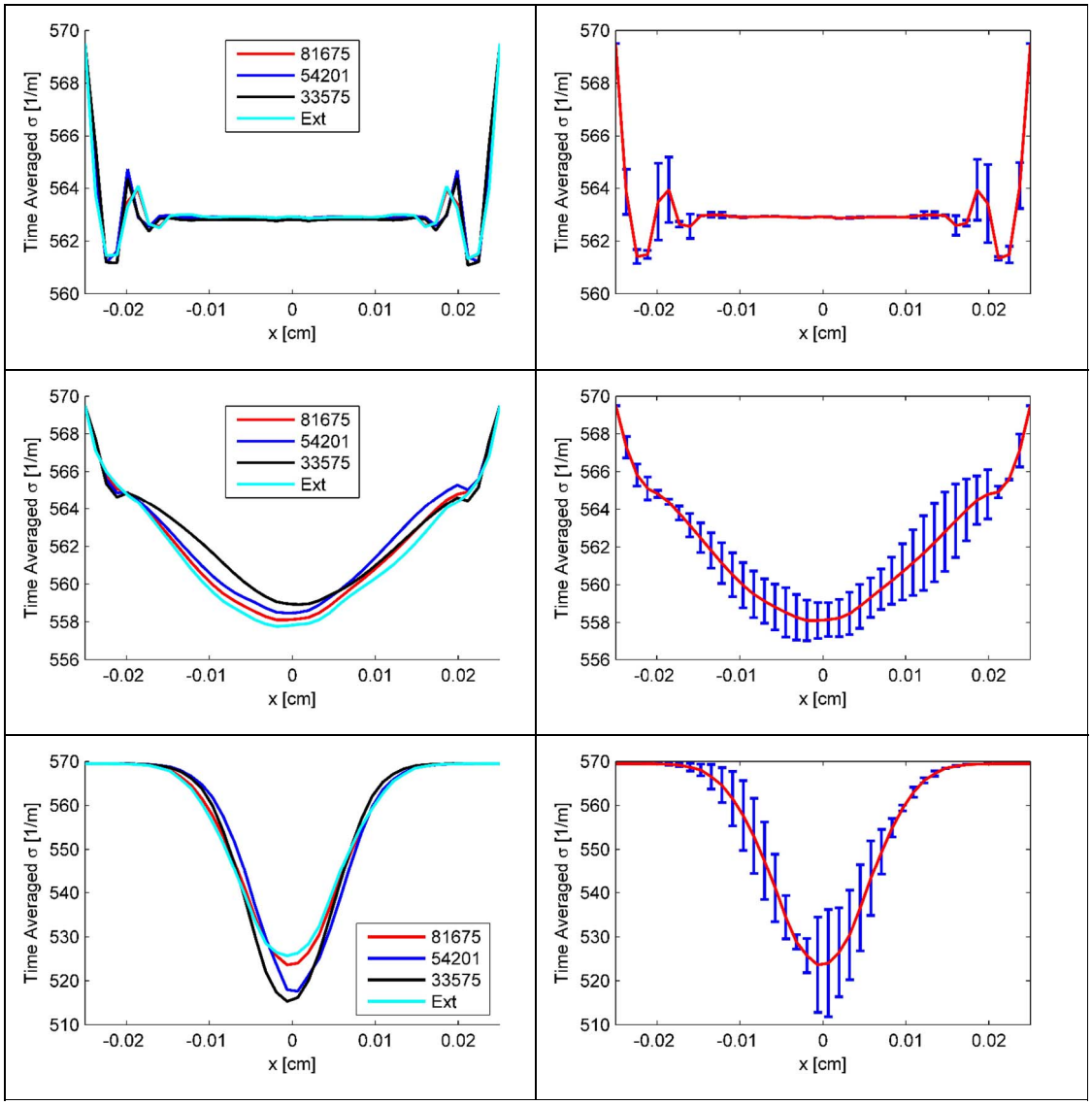

Fig. 4. Left: time averaged scattering coefficient profiles on a (x-y) plane at $z = 0$ at three different heights, i.e., $y = 0.3$ m (top), $y = 0.2$ m (center) and $y = 0.025$ m (bottom). The profiles have been computed with three meshes, increasing the number of cells. The numbers in the legend represent the number of hexahedral cells each grid has. "Ext" means the extrapolated numerical profile according to Eq. (23). Right: the profile obtained on the fine grid is reported along with the error bars calculated with Eq. (26).

scattering coefficient computed with the coarse mesh. Finally, we estimate the numerical uncertainty

$$U_{GCI} = 1.25P\frac{|\varepsilon_{21}|}{r_{21}^{p_{ave}^{'}} - 1} \tag{26}$$

where $P = p_{ave}^{'}/p_{th}$ and p_{th} is the theoretical order of accuracy of the numerical method. The factor P improves the uncertainty estimate in Eq. (26) [64].

The profiles of the time averaged scattering coefficient are symmetric with respect to the x-axis, see Fig. 4 top, center and bottom left. At the location $y = 0.025$ m, the maximum relative difference between the values of σ_1 and σ_2 is approximately 1.2%, while between the values of σ_2 and σ_3 is approximately 1.5%. At the location $y = 0.1$ m the maximum relative difference decreases, being approximately 0.14% between σ_1 and σ_2 and 0.22% between σ_2 and σ_3. Finally, at $y = 0.3$ m the maximum relative difference is approximately 0.22% between σ_1 and σ_2, and 0.18% between σ_2 and σ_3. We also report the numerical uncertainties, computed with Eq. (26), in form of error bars along with the fine grid solution, see Fig. 4 top, center and bottom right. The maximum uncertainty is approximately 2.33% at the location $y = 0.025$ m which corresponds to $\pm$ 12.2 m^{-1}. Going towards the top of the PBR the maximum uncertainty decreases, being approximately 0.37% and 0.26% at the locations $y = 0.1$ m, and $y = 0.3$ m, respectively. This corresponds to values of approximately $\pm$ 2.1 m^{-1} at $y = 0.1$ m, and $\pm$ 1.48 m^{-1} at $y = 0.3$ m, see Fig. 4 top, center and bottom right. For reasons of computational efficiency, we select the mesh with 54201 hexahedral cells.

3.3. Effect of gas superficial velocity and biomass concentration on spatial distribution of light

In the following we investigate the effects of spatially distributed radiation characteristics on the light distribution in the PBR at certain time increments.

Fig. 5 shows contours of the polychromatic light intensity on the (x-z) plane at $y = 0.025$ m for different biomass concentrations. It can be clearly seen that the light field is not symmetric due to the three-dimensional motion of the bubble plume. However, the effect mainly takes place in the reactor center where light intensity reaches the lowest value. In contrast, close to the walls the shape of the contour becomes

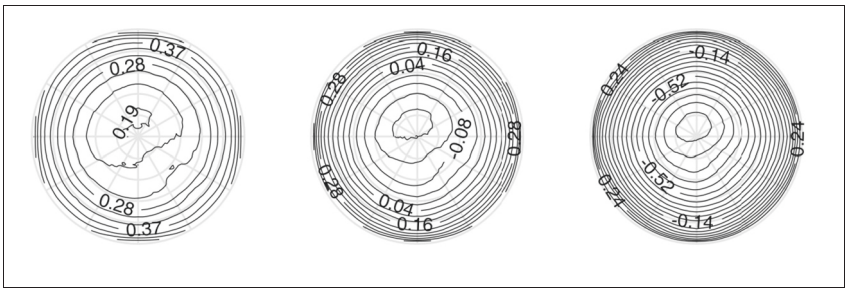

Fig. 5. Effect of biomass concentration X on the contour of the light field in the (x-z) plane at $y = 0.025$ m for gas superficial velocity $u_g = 1.28$ cm/s. Left: $X = 0.25$ kg/m^3. Center: $X = 0.50$ kg/m^3. Right: $X = 1.0$ kg/m^3. Contour labels indicate the logarithmised polychromatic light intensity I/I_0.

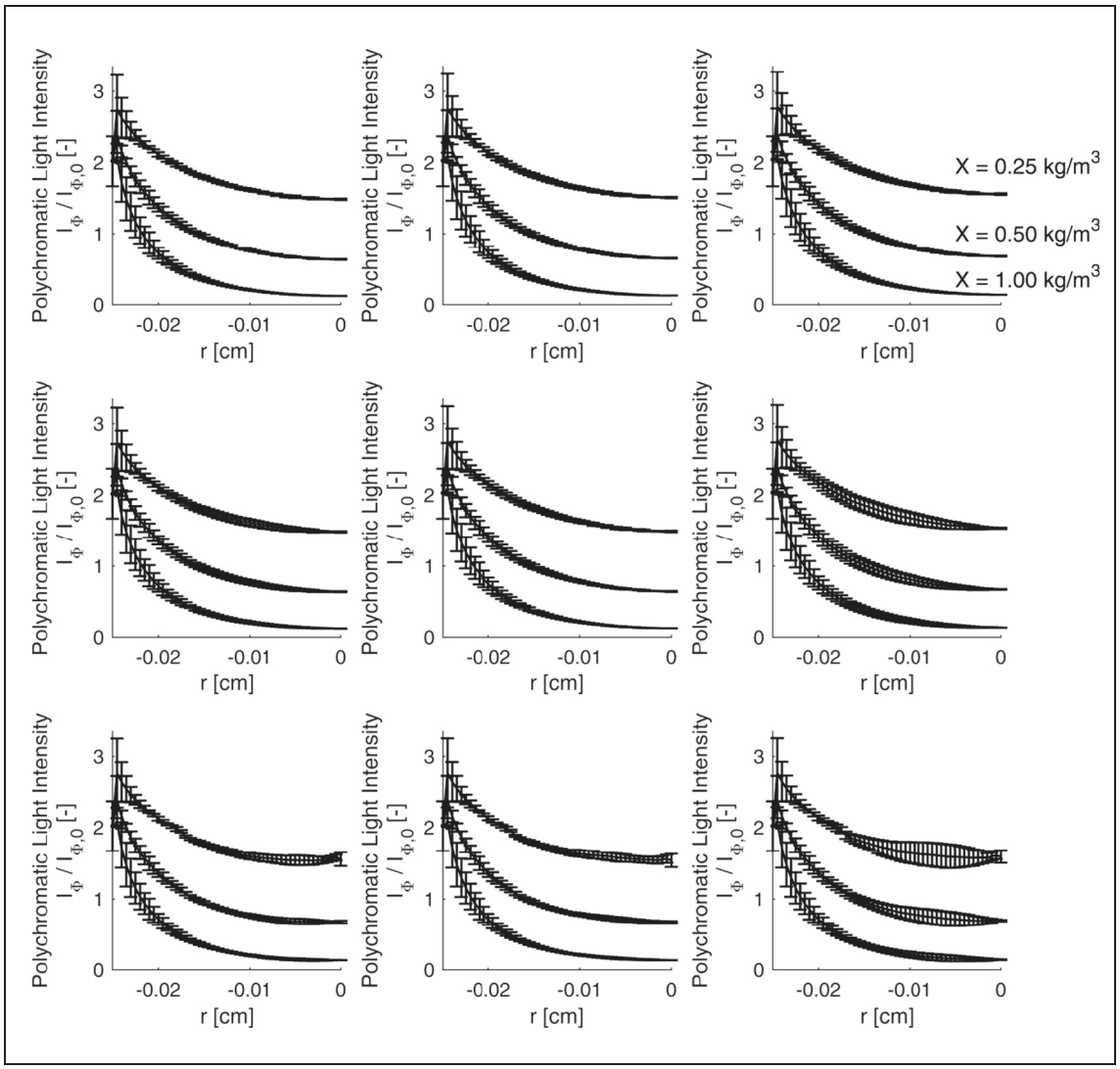

Fig. 6. Profiles of polychromatic light intensity at different biomass concentrations, gas superficial velocities and heights in the PBR. Top row: $y = 0.3$ m. Center row: $y = 0.1$ m. Bottom row: $y = 0.025$ m. Left Column: $u_G = 4.25$ mm/s, center column: $u_G = 8.5$ mm/s, right column: $u_G = 1.28$ cm/s. Error bars indicate 3 angular standard deviations. The average value at the boundary is 2.019 for all cases with 1 being the intensity emitted by a single LED lamp.

almost symmetric. At higher biomass concentrations the location of the lowest light intensity shifts towards the reactor center.

Fig. 6 depicts profiles of the angularly averaged polychromatic light intensity I_ϕ along the radial coordinate with respect to biomass concentration and gas superficial velocity at different heights ($y = 0.025$ m, $y = 0.1$ m and $y = 0.3$ m) of the PBR. The variability of the light intensity with respect to ϕ at a given radial position is indicated by the error bars.

The decay of the polychromatic intensity profiles is not exponential which can easily be proven by linear regression of the logarithmised profiles. As expected, higher biomass concentrations cause a faster attenuation of light intensity. The averaged intensity at the boundary is 2.019 and for some cases we observe higher light intensities close to the walls due to backscattering effects. As already indicated, close to the gas inlet the minimum averaged intensity is not located in the reactor center for low biomass concentrations, meaning that the light

distribution in the PBR is eccentric due to the high local concentration of gas bubbles. In case of higher biomass concentrations the averaged intensity minimum moves towards the reactor center, so that the effect of biomass absorption dominates over the effects of gas. As indicated by the error bars, the clear decrease in angular variability at higher biomass concentration supports this observation.

An increase of the gas superficial velocity has two visible effects. First, the angular variability of light intensity clearly correlates with the gas superficial velocity. In addition to, a slight increase of the averaged light intensity can be noted at higher air mass flow rates, which we will address in the next section. With regard to the axial position in the PBR we observe that the variability of light intensity in the angular coordinate is lower far from the gas inlet. This is plausible with respect to the results shown in Fig. 4, which indicate almost spatially independent radiation characteristics in the top region of the PBR. However, in the top region we observe slightly lower light intensities in the reactor center as compared to the region close to the gas inlet which is explained by the higher concentrated gas fraction near the sparger and thus, lower local absorption coefficients.

For all cases under investigation a high angular variability of light intensity can be noted near the reactor walls, although the gas volume fractions can be expected to be minimal at these locations. This observation is caused by the non-circular arrangement of light sources around the PBR. A different degree of light superposition at different locations close to the reactor wall occurs due to the parallel emission to the coordinate x and z axes. The plausibility of this explanation is supported by the fact that the variability close to the reactor walls is independent from the gas volume fraction which was checked by Levene's statistical test for similarity of variances. For the computation of the test statistic, the statistics toolbox in Matlab 2016b was used.

The results shown in this section allow the major conclusion that the presence of gas affects both, symmetry and magnitude of the light distribution. The effect of gas bubbles on the light field can particularly be observed close to the sparger where the gas is highly concentrated. In contrast, far away from it the light field becomes approximately concentric since the air disperses in the reactor. Thereby, increasing the biomass concentration counteracts the effect of the gas phase on the symmetry of the light field so that asymmetry becomes less important at higher biomass concentrations. A remaining question is the quantification of the effects of air on the magnitude of light intensity and if it must be considered at all in computations of light distribution. We address this question in the following section.

3.4. Effect of gas superficial velocity on the magnitude of light intensity and cell growth

To quantify the effect of gas bubbles on the magnitude of polychromatic light intensity, we compute as a reference additional intensity profiles with radiation characteristics according to Eqs. (16a)–(19) and a gas volume fraction $\alpha_G = 0$.

Fig. 7 shows the evolution of the light spectrum along the radial coordinate close to the sparger ($y = 0.025$ m) for a biomass concentration $X = 0.25$ kg/m^3 and gas superficial velocity $u_G = 1.28$ cm/s. At these conditions, a strong effect of the gas phase on the polychromatic light field was estimated (see Fig. 5, left and Fig. 6, bottom right). For comparison, simulations of the light spectrum which do not take the gas phase into account ($u_G = 0$ mm/s) are also depicted in Fig. 7. It can be observed that the difference between the curves is most prominent in the green part of the spectrum where the absorption cross-section of the cells has its minimum and scattering becomes more important. On the contrary, in the red and blue parts of the spectrum, the curves are almost identical. However, close to the center of the PBR, it also can be observed that the presence of the gas phase has increasing effect on the red and blue parts of the spectrum and the deviation from the simulations without considering the gas phase increase.

To explain these observations, we recall Eqs. (18a) and (18b), which

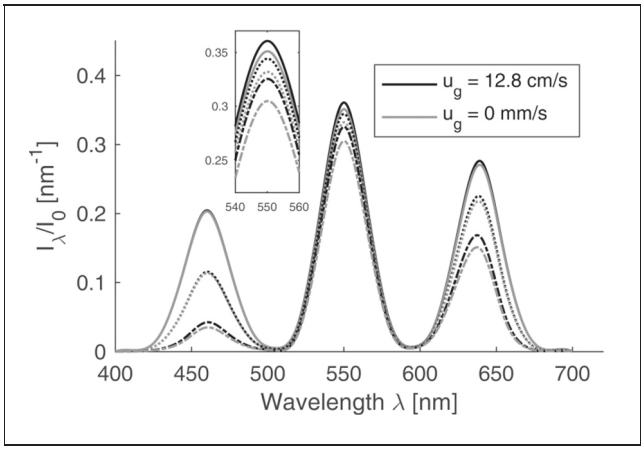

Fig. 7. Light spectrum inside the PBR at different radial positions $r = 0.0245$ m (solid line), $r = 0.02$ m (dotted line), $r = 0$ m (dash-dotted line). The height coordinate is $y = 0.025$ m and the biomass concentration is $X = 0.25$ kg/m^3. The spectra are normalized to the emitted light intensity I_0. The inset shows the peaks in the green part of the spectrum.

show that the presence of the gas phase acts on both, scattering and absorption coefficients. Thereby the right-hand side of Eq. (18a) takes two effects into account, namely the replacement of the cell suspension by the gas phase (first term) and the contribution of the gas phase to the scattering coefficient of the mixture (second term). It becomes clear that if the cell's scattering cross-section $\sigma_{A,\lambda}$ is much higher than the bubble scattering cross-section σ_B, the second term of Eq. (18a) becomes less significant in comparison to the first one, meaning that the bubble scattering itself is not dominating the effective scattering coefficient. As this is the case for the green part of the spectrum it is likely that the scattering of gas bubbles is not the dominant reason for the increase of light intensity. The observed behavior can rather be explained by the effect of gas bubbles on the absorption coefficient. To substantiate this presumption, we take into account that the light penetration depth $l_{p,\lambda} \approx \kappa_\lambda^{-1}$ is approximately inversely proportional to the absorption coefficient. Calculating the derivative of $l_{p,\lambda}$ with respect to κ_λ, which is $\mathrm{d}l_{p,\lambda}/\mathrm{d}\kappa_\lambda = -\kappa_\lambda^{-2}$, allows to evaluate how a change of κ_λ, caused for instance by the presence of the gas phase, affects the light penetration depth and therefore the local light intensity. From the computed derivative it becomes clear that the impact of the gas phase on the light penetration depth must become most prominent when κ is small. This is true in the green part of the spectrum where the absorption of light by the cells is weak, while in the red and blue parts the absorption cross-section is much higher due to the absorption maximum of the chlorophyll. As this qualitative analysis of the model equations is consistent to the observed results, we make the conclusion that lowering the mixture absorption coefficient is probably a more important effect on the light field than additional backscattering caused by gas bubbles.

In practical applications of photobioreactor engineering, most often the total energy available for microalgal growth is of interest, for which the average polychromatic intensity is a measure. Therefore, we estimate the difference in the volumetric average of light intensity for the cases with and without a gas phase, which is

$$\Delta I_\phi = \frac{(\overline{I}_\phi - \overline{I}_{\phi,ref})}{I_0} \tag{27}$$

where the average values $\overline{I}_\phi$ and $\overline{I}_{\phi,ref}$ were computed by means of Eq. (22).

Fig. 8 shows the estimated difference in average light intensity with respect to biomass concentration and gas superficial velocity. In accordance with the results shown in the previous section, at higher gas superficial velocities the deviation from the reference solution

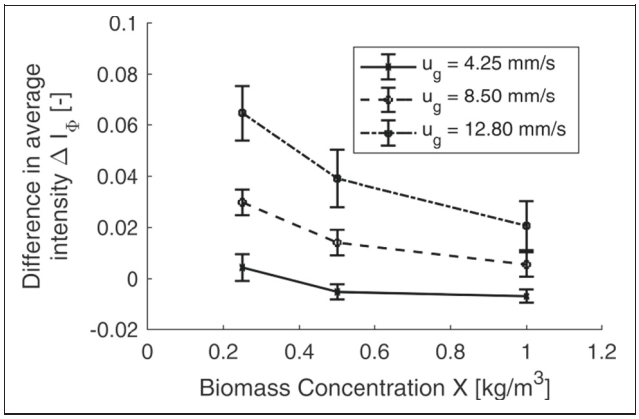

Fig. 8. Effect of gas superficial velocity on the average light intensity in the PBR. Symbols represent the difference between the cases with and without consideration of the gas phase according to Eq. (27). Positive values indicate that the gas phase increases the average light intensity in comparison to the case without the consideration of the gas phase. Error bars indicate the standard deviation of the difference over the reactor height.

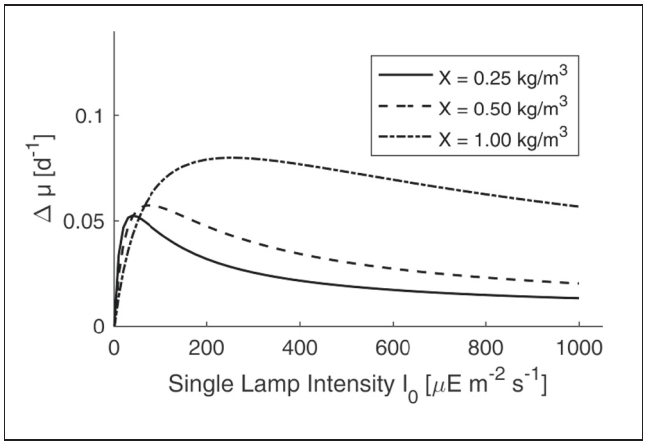

Fig. 9. Effect of the gas phase on the prediction of the average specific growth rate with respect to biomass concentration X and single lamp intensity I_o. The y-axis depicts the difference $\Delta\mu = \overline{\mu} - \overline{\mu}_{ref}$ of the average specific growth rates, where the reference is computed without taking the presence of the gaseous phase into account (see text). The gas superficial velocity is $u_g = 1.28$ cm/s.

increases. This result is expected since the gas superficial velocity is correlated with the gas hold-up. However, if the biomass concentration increases, the influence of the gas phase on the light field becomes smaller. The absolute deviation in physical units can be achieved by multiplying ΔI_ϕ by the single lamp intensity I_0 [μE m^{-2}s^{-1}]. For instance, in comparison to the reference solution, we find for $X = 0.25$ kg/m^3 a maximum difference in the average light intensity of about 6.5 μE m^{-2}s^{-1} for a single lamp intensity of $I_0 = 100$ μE m^{-2}s^{-1}, which reduces to 2 μE m^{-2}s^{-1} with increasing biomass concentration. Interestingly, we also find cases where the deviation of the average light intensity is negative, meaning that less light is available on average if gas is present. Such a situation can occur at low gas superficial velocities, if gas bubbles pronounce backscattering but at the same time do not reduce the absorption coefficient of the mixture too much. These findings are in conflict to the often made statement that the presence of gas bubbles improves illumination, although we indeed observed higher light intensity in the majority of the investigated cases.

Keeping in mind that the interest in light intensity fields in photobioreactors is mainly driven by the request of predicting cell growth, the key question arises whether and to what extent the presence of a gaseous phase affects the outcome of growth models. Obviously, photoautotrophic growth of microalgae depends on local light availability, which again is also affected by the amount of light energy supplied across the reactor surface as well as by the biomass concentration inside the PBR as it significantly influences the light intensity field. Therefore, the importance of considering the gas phase for cell growth predictions will also potentially depend on these parameters.

To quantify these effects, we use a kinetic growth model for *Chlamydomonas reinhardtii* and compute the average specific growth rate in the reactor for both cases with and without gas. Thereby, we assume three different biomass concentrations, being representative for different stages of the batch cultivation process and similar to the ones assumed before. Following Pruvost *et al.* [65], the specific growth rate of *Chlamydomonas reinhardtii* with respect to light intensity can be computed from the Aiba model

$$\mu(I) = \mu_m \frac{I}{I + k_1 + \left(\frac{k_2}{I}\right)^2} - \mu_s \tag{28}$$

where the estimated parameters are $\mu_m = 0.2479$ h^{-1}, $k_1 = 69.75\frac{\mu E}{m^2 s}$, $k_2 = 2509.66\frac{\mu E}{m^2 s}$ and $\mu_s = 0.0531$ h^{-1} [65]. Assuming certain single lamp intensity I_0, local values for the specific growth rate $\mu(I_\phi(r,y))$ can be estimated from the computed radial intensity profiles and Eq. (28). Subsequently, the average specific growth rate for the whole PBR $\overline{\mu}$ can be calculated from the local information by means of Eq. (22).

Fig. 9 shows the difference $\Delta\mu = \overline{\mu} - \overline{\mu}_{ref}$ of the average specific growth rates $\overline{\mu}$ at $u_G = 1.28$ cm/s and the reference solution $\overline{\mu}_{ref}$ which does not take the effect of the gas phase on light intensity into account ($u_G = 0$ mm/s).

Generally, we observe that at increasing single lamp intensity the difference of the two model outcomes decreases. This observation can be easily explained by considering that higher light intensity shifts the cells towards the light saturated state where growth occurs at its maximum rate and is less sensitive to variations of light intensity. Thus, the effect of the gas phase on the growth prediction becomes less important in such a situation. A second observation is that the effect of gas bubbles on the mean specific growth rate becomes more important if the biomass concentration increases. Both, low light intensity and high biomass concentrations correspond to a situation where the availability of light is limiting cell growth and the kinetic model outcome reacts most sensitive with respect to light intensity.

The question remains whether it is necessary to consider the presence of a gaseous phase for predictions of cell growth at all. As shown before, the absolute effect of gas bubbles on light intensity is relatively small, which is also reflected in the deviation $\Delta\mu$ of the average specific growth rates. From Fig. 8 it can be seen that all the values of $\Delta\mu$ are less than 0.1 d^{-1}, which is about 2% of the maximum specific growth rate of *Chlamydomonas reinhardtii*. For lower gas superficial velocities, the estimated values of $\Delta\mu$ were even smaller. Considering the fact that due to several simplifications the outcome of growth models can be erroneous at least in a similar order of magnitude [38], it seems to be acceptable to ignore the gaseous phase for predicting cell growth in PBR.

Although the magnitude of the effect might be not important for practical purposes, it should also kept in mind if effects of mixing in bubble column PBR are investigated. Thereby, cell growth is often correlated with gas superficial velocity [7,66] and increasing growth rates are explained by mixing while cell death is related to shear stress. However, our results show that gas bubbles increase the average light intensity which means that higher gas superficial velocities can additionally promote cell growth and may lead to erroneous conclusions concerning mixing effects, especially if one cultivates species with high sensitivity to changes of light intensity under low light conditions.

4. Discussion

The results shown in this work indicate that the presence of gas affects both symmetry and magnitude of the light distribution in PBR. This is caused by the three-dimensional motion of the bubble plume, leading to non-homogeneous radiation characteristics of the cell

suspension. The magnitude of the light intensity slightly increases in most of the investigated cases, although backscattering by gas bubbles at low biomass concentrations may decrease the overall amount of energy within the reactor volume. The effect on the symmetry of the light field is most prominent close to the gas sparger. However, it seems only to be important at low biomass concentrations and almost vanishes already at biomass concentrations of 1 kg/m^3. In many cultivation systems it is possible to reach significantly higher biomass concentrations up to 10 kg/m^3 and therefore asymmetry of the light field can be expected to play a minor role in most gassed PBR.

Although this study assumed a specific geometry of the column, we expect similar results also in other geometries if the bubble size differs not too much. If the column diameter is small, the gas phase tends to spread across the column and is almost homogeneously distributed along the radial coordinate. In cases where the column diameter is larger, the gas phase might be more concentrated in the center, but at the same time light attenuation is higher due to longer light paths. Thus, low light intensity can be expected in the core region with a small effect on the overall light field and cell growth. Moreover, the effect of the gas phase on the light field becomes more important in air-lift systems with central downcomer, where the gas phase is mainly located near the reactor walls. It is unclear however, if such a configuration is beneficial with respect to illumination because the backscattering fraction of gas bubbles is much higher as compared to microalgae cells. Thus, one may expect a lower input of light energy into a PBR, especially in case of small bubbles with more isotropic scattering characteristics.

Our results indicate that the effect of the gas phase on the light field is mostly due to the decrease of the effective absorption coefficient in the PBR in consequence to the local replacement of algae cells by gas bubbles. The effect was found to be most prominent when the absorption coefficient is low. These findings allow a qualitative discussion of some other aspects important for microalgae cultivation in PBR. One of these aspects is the emission spectrum of the light source. As the light penetration depth in our simulations was basically affected in the green part of the spectrum, one option for increasing the homogeneity of the light field could lie in pronouncing the green spectral part. Baer *et al.* [67] have recently investigated the dependence of bio-productivity of *Chlamydomonas reinhardtii* on light quality in an air-sparged PBR illuminated with RGB light. However, they found no beneficial effect for cell productivity by pronouncing the green part of the spectrum. Possibly, the observed increase of light intensity due to the presence of the gas phase is a little bit more pronounced if other light sources are used. Since the narrow peaks of RGB light cause low light intensities in many parts of the spectrum (see Fig. 7), these parts contribute just marginally to the polychromatic light intensity. If a light source with a more uniform emission spectrum is used instead (e.g. sunlight), the proportion of the mainly affected green part of the spectrum to the whole spectrum might be higher and leads to an increase of the overall effect. However, with regard to future research we think that model-based optimization of light emission spectra could be an important step to increase reactor productivities, being more promising than increasing light intensity by means of gas sparging. Combining simulation models with optimization algorithms can help to design tailored light sources, for instance made of differently colored LEDs. As LED lamps provide the option of manipulating their individual emission intensity and thus, the overall emission spectrum during the cultivation process, also dynamic adaption of the emission spectrum in dependence of the process state (e.g. biomass concentration, pigmentation) might be possible. We plan to address this approach in future works.

Another important phenomenon occurring in PBR is photoacclimation, which means that cells adapt their intracellular pigment content in response to environmental stimuli such as high or low availability of light [68]. Accordingly, photoacclimation corresponds to a change of the cell's absorption cross-section. Since the absorption coefficient is defined as the product $\kappa = A_{abs}X$, the effect of a changing biomass concentration on the absorption coefficient is in a first approximation comparable to the effect of a changing absorption cross-section due to photoacclimation. In principle, both, up- and down-regulation of the photosynthetic pigment content is possible for microalgae, termed low-light adaption and high-light adaption, respectively. If high-light adapted cells are considered, the intracellular pigment content and the absorption coefficient decreases and therefore high-light adaption should pronounce the effect of the gas bubbles on light intensity. This conclusion is supported by the findings of Berberoglu *et al.* [45] who state that the gas phase needs to be considered for light predictions when genetically modified organisms with artificially downregulated photosynthetic apparatus are cultivated. For both, high-light adapted and genetically manipulated cells one can expect that the light penetration depth of the red and blue parts will increase due to the presence of gas bubbles. However, with respect to the specific growth rate of the cells, high-light adaption implies that growth is not light limited by light availability and thus, the increase of light intensity due to the presence of gas bubbles seems not important to consider with regard to cell growth. This conclusion is also implied by Fig. 9, as discussed in the previous section. It is clear that an excess of light weakens the impact of the gas phase on cell growth, because the speed of growth is close to its maximum under these conditions. On the contrary, for genetically modified microalgae an increase of the light penetration depth may also occur in situations where light is limiting cell growth. Under these conditions possibly a positive effect of the gas phase on cell growth occurs, although deeper investigations are necessary to confirm this presumption.

As recently shown by Yarold *et al.* [69], in cultivation systems with a large dark volume, cells must be expected to be in their low-light adapted state, even when intense mixing causes rapid light/dark fluctuations. As low-light adapted pigmentation is accompanied with an increase of the absorption coefficient, this form of photoacclimation should suppress the effect of gas bubbles on the light field, similar to the shown effect of increasing biomass concentrations. However, in such a situation the predicted cell growth rate is also sensible to slightly increased light intensity, although the overall effect remains small as indicated by Fig. 9.

Concerning the prediction of cell growth we observed that the model outcome is sensitive to the effect of the gas phase on the magnitude of light intensity, especially under light limiting conditions. Thereby, the importance of considering the presence of air in the computation of light fields and growth predictions will depend on the cultivated species. As shown in the previous section, for *Chlamydomonas reinhardtii* we estimated an impact of the gas phase on the prediction of cell growth up to 2% of the maximum specific growth rate. Since this outcome is based on specific growth kinetics, the magnitude of the effect can be expected to vary between species. A possible indicator for the sensitivity of the photosynthetic response to deviations in light intensity is the initial slope of the PI curve, which determines the photosynthetic response to increasing light availability under low light conditions. However, we like to stress that a detailed comparison of the effects of gas bubbles on growth predictions for different species would be necessary to manifest the relation to the initial slope of the PI curve.

From the discussion so far it becomes clear that making general statements on the impact of the gas phase on light fields is not straightforward due to the different effects and their interactions. However, as also indicated by a recent study [43], the role of the gas phase seems to be of minor importance for light distribution and cell growth, contradictory to the frequently made assumption that the gas phase remarkably enhances the light penetration length. Regarding the relationship of computational costs and gained information, the additional computation time due to the consideration of inhomogeneous radiation characteristics is not justified, although this conclusion might be different for conditions deviating from those as the investigated ones (e.g. other algae species or very high gas superficial velocities). If the integration of the gas phase in a radiation model is desired, the

approach of Berberoglu *et al.* [45], which utilizes the gas hold-up instead of local air volume fractions, might be an option because the gas hold-up is a good accessible parameter and multiple correlations are present in literature. Our results, however, state that this is not required, at least under the investigated conditions and even more at high biomass concentrations. Based on our results, we think that future research in the field of bubble column PBR should focus on the hydrodynamic effects caused by gas sparging rather than its impact on magnitude and quality of light. For instance, variation of air mass flow rate and sparger design are well known to affect mixing and gas-liquid mass transfer [12], which is still an issue in large production systems. Besides, many low cost cultivation systems such as plastic bag PBR operate under mostly undefined conditions with regard to mixing and mass transfer. Future research should address these questions more in depth to further optimize air-sparged PBR.

5. Conclusions

The impact of gas bubbles on light distribution in a bubble column PBR has been investigated in this work. On the one hand, we found that the presence and the spatial distribution of gas bubbles affect both symmetry and magnitude of the light intensity field, and their impact increases at higher gas superficial velocities. On the other hand we also observe that biomass concentration suppresses these effects already at concentrations less than 1 kg/m^3, so that role of the gas phase on light fields seems to be of minor importance for light penetration and cell growth.

List of Symbols

Parameter	Unit	Explanation
Latin Symbols		
$A_{abs,\,\lambda}$	m^2/kg	Absorption cross-section of microalgae cells at wavelength λ
$A_{sca,\,\lambda}$	m^2/kg	Scattering cross-section of microalgae cells at wavelength λ
A_B	m^2	Geometrical cross-section of a single bubble
c	m/s	Speed of light
C_{CD}	kg/(m^3·s)	Momentum transfer coefficient in the Favre average model of the turbulent dispersion forces
C_D		Drag coefficient
$C_{D\infty}$		Drag coefficient of a single bubble
C_L		Lift force coefficient
C_{TD}		Constant multiplier in the Favre average model of the turbulent dispersion forces
C_{VM}	1/m	Wall lubrication force coefficient
d	m	Inlet diameter of the PBR
d_B	m	Mean bubble diameter
D	m	PBR diameter
$\frac{D}{Dt}$	1/s	Material or substantial derivative
E		Correlation for the computation of the drag coefficient in the distorted regime of the Ishii-Zuber drag force model.
Eo		Eötvös number
f		Correction factor in the Grace correlation
$\boldsymbol{F}_{L,\,G}{}^{D}$	N/m^3	Drag force per unit volume
$\boldsymbol{F}_{L,\,G}{}^{L}$	N/m^3	Lift force per unit volume
$\boldsymbol{F}_{L,\,G}{}^{VM}$	N/m^3	Virtual mass force per unit volume
$\boldsymbol{F}_{L,\,G}{}^{WL}$	N/m^3	Wall lubrication force per unit volume
$\boldsymbol{F}_{L,\,G}{}^{TD}$	N/m^3	Turbulent dispersion force per unit volume
$\boldsymbol{g}$	m/s^2	Gravitational acceleration vector
g_A		Anisotropy factor of microalgae cells
g_B		Anisotropy factor of gas bubbles
G		Gas phase
h_j	m	Representative cell size of the j grid
H	m	PBR height
I	μE/(m^{2}s)	Polychromatic light intensity
I_λ	μE/(m^{2}s)	Local specific light intensity at wavelength λ
I_Φ	μE/(m^{2}s)	Light intensity averaged over the angular coordinate
k		Subscript index indicating the gas or the liquid phase
k_1	μE/(m^{2}s)	Light saturation coefficient for cell growth
k_2	μE/(m^{2}s)	Light prohibition coefficient for cell growth
l_p	m	Light penetration depth
L		Liquid phase
L_λ	μE/(m^{2}s·sr)	Radiance at wavelength λ
$\boldsymbol{M}_{s,\,k}$	N/m^3	Interphase forces vector
$\hat{\boldsymbol{n}}$		Unit vector indicating the direction into which light is propagated
$\hat{\boldsymbol{n}}_{\boldsymbol{W}}$		Unit vector normal to a reactor surface
N_j		Total number of cells of the j grid
N_Φ		Number of points along the angular coordinate of the cylindrical grid
N_r		Number of points along the radial coordinate of the cylindrical grid
N_y		Number of points along the y coordinate of the cylindrical grid
p	N/m^2	Pressure field shared by both fluids
p'		Local apparent order of the numerical method
p_{ave}'		Average value of the local apparent order of the numerical method
P		Ratio between the average local apparent order of the numerical method and the theoretical order of accuracy of the numerical method
p_{th}		Theoretical order of accuracy of the numerical method
Q_{SCA}		Scattering efficiency of a single bubble
r	m	Radial coordinate
r_{21}		Ratio between the representative cell sizes of the medium and the fine grid
r_{32}		Ratio between the representative cell sizes of the coarse and the medium grid
Re_m		Mixture Reynolds number
s		Subscript index indicating the gas or the liquid phase
$s_{I\phi}$	μE/(m^{2}s)	Standard deviation of light intensity over the angular coordinate
t	s	Time
Δt	s	Time step
u_G	m/s	Gas superficial velocity
$\boldsymbol{u}_k$	m/s	Velocity vector of the phase k
U_{GCI}	1/m	Numerical uncertainty of the effective scattering coefficient
V_B	m^3	Volume of a gas bubble
ΔV_i	m^3	Volume of the ith cell of the total volume
x	m	Abscissa of the Cartesian reference system
X	kg dry mass/m^3	Microalgae concentration
y	m	Ordinate of the Cartesian reference system
Y_Φ		Angularly averaged quantity
z	m	Applicate of the Cartesian reference system
$\boldsymbol{x}$	m	Position vector

Greek Symbols

α_k		Volume fraction of the phase k
β_λ	1/m	Effective extinction coefficient at wavelength λ
ε_{21}	1/m	Difference between the local value of the scattering coefficient computed with the medium grid and the one computed with the fine grid
ε_{32}	1/m	Difference between the local value of the scattering coefficient computed with the coarse grid and the one computed with the medium grid
$\kappa_{A,\,\lambda}$	1/m	Absorption coefficient of microalgae cells at wavelength λ
κ_λ	1/m	Effective absorption coefficient at wavelength λ
λ	nm	Wavelength
μ	1/h	Specific growth rate
$\mu_{k,\,eff}$	Pa·s	Effective viscosity of the phase *k*
$\mu_{k,\,Lam}$	Pa·s	Laminar contribution of the viscosity of the phase *k*
$\mu_{k,\,Turb}$	Pa·s	Turbulent contribution of the viscosity of the phase *k*
μ_m	1/h	Maximum specific growth rate
μ_s	1/h	Specific death rate
$\nu_{k,\,eff}$	m^2/s	Effective kinematic viscosity of the phase *k*
ρ_k	kg/m^3	Density of the phase *k*
$\sigma_{A,\,\lambda}$	1/m	Scattering coefficient of microalgae cells at wavelength λ
σ_λ	1/m	Effective scattering coefficient at wavelength λ
σ_B	1/m	Bubble scattering coefficient
$\sigma_{L,\,Turb}$		Turbulent Schmidt number of the continuous liquid phase
σ_1	1/m	Effective scattering coefficient computed with the fine grid
σ_2	1/m	Effective scattering coefficient computed with the medium grid
σ_3	1/m	Effective scattering coefficient computed with the coarse grid
τ_k	N/m^2	Stress tensor of the phase *k*
ϕ		Angular coordinate
Φ		Scattering phase function
$d\Omega$	sr	Solid angle

Other symbols

∇	1/m	Vector derivative with respect to axial position

Acknowledgements

This work was funded in parts by the German Federal Ministry of Education and Research (BMBF 03SF0457). The authors gratefully acknowledge the support.

Declaration of authors' contribution

CM and GL designed the study and wrote the manuscript. GL and JRA developed the multiphase flow model, performed flow simulations and related data analysis. CM developed the flow-radiation coupling and performed simulations of radiation transfer including subsequent evaluation and analysis of light fields. CM and CL contributed with the evaluation of cell growth and the discussion of biological aspects. AD and CR took response for the integrity of the study as a whole, from inception to the final article, and supervised the scientific work. Funding was obtained by AD. All authors have read and approved the final manuscript.

Declaration of conflict of interests

The authors declare no conflict of interests.

Statement of informed consent, human/animal rights

No conflicts, informed consent, human or animal rights applicable.

Appendix A

A.1. Derivation of Eq. (22)

The volumetric average of quantity $Y_\phi(r,y)$ in cylindrical coordinates is given by its integral along the radial, polar and height coordinates.

$$\overline{Y} = \frac{1}{V}\int_0^H\int_0^{2\pi}\int_0^R Y_\phi(r,y)\, r\, \mathrm{d}r\, \mathrm{d}\phi\, \mathrm{d}y$$

The volume of the cylinder is $V = \pi R^2 H$. The quantity Y_ϕ represents an average in the angular coordinate (see Eq. (20)) and on a discrete grid we assume $Y_\phi(r_j,y_i)$ to be constant in a partial volume $\Delta V = \int_0^{\Delta y}\int_0^{2\pi}\int_{r_1}^{r_2} r\, \mathrm{d}r\, \mathrm{d}\phi\, \mathrm{d}y = 2\pi\frac{\Delta y}{2}(r_2^2 - r_1^2)$, where $r_1$and r_2 are the upper and lower bounds of the integration. Because $Y_\phi(r_j,y_i)$ is a local constant, the integration over the whole reactor volume can be replaced by the sum of integrals over all partial volumes ΔV. With the above given definition of ΔV we have $N = N_y N_r$ partial volumes, where N_y and N_r are the number of grid points along the *y* and *r* coordinates, respectively.

$$\overline{Y} = \frac{1}{V}\sum_{i=1}^{N_y}\sum_{j=1}^{N_r}\int_0^{\Delta V} Y_\phi(r_j,y_i)dV = \frac{\pi\,\Delta y}{V}\sum_{i=1}^{N_y}\sum_{j=1}^{N_r} Y_\phi(r_j,y_i)(r_2^2 - r_1^2)$$

To obtain Eq. (22), the values of the integration boundaries $r_1$and r_2 on the discrete grid need to be considered. In case of a location r_j within the volume, the radial integration boundaries of the partial volume are $r_{1,2} = r_j \pm \frac{\Delta r}{2}$. A different situation occurs for the center node, where the volume has boundaries at $r_1 = 0$ and $r_2 = \frac{\Delta r}{2}$, and the reactor wall, where $r_1 = R - \frac{\Delta r}{2}$ and $r_2 = R$. Inserting these boundaries in the summation above and using $V = \pi R^2 H$ with $H = N_y \Delta y$, we obtain Eq. (22)

$$\overline{Y} \approx \frac{1}{N_y R^2}\sum_{i=1}^{N_y}\left[\sum_{j=2}^{N_r-1} 2r_j\Delta r Y_\phi(r_j,y_i) + \frac{\Delta r^2}{4}Y_\phi(r_1,y_i) + \left(R\Delta r - \frac{\Delta r^2}{4}\right)Y_\phi(r_{N_r},y_i)\right]$$

where the last two terms in the inner summation account for the special case at $r_1 = 0$ and $r_{N_r} = R$.

References

[1] A.S. Mirón, A.C. Gómez, F.G. Camacho, E.M. Grima, Y. Chisti, Comparative evaluation of compact photobioreactors for large-scale monoculture of microalgae, Prog. Ind. Microbiol. 35 (C) (1999) 249–270.

[2] A.S. Mirón, M.C.C. Garcia, F. García-Camacho, E.M. Grima, Y. Chisti, Growth and characterization of microalgal biomass produced in bubble column and airlift photobioreactors: studies in fed-batch culture, Enzym. Microb. Technol. 31 (2002) 1015–1023.

[3] C.G. Khoo, M.K. Lam, K.T. Lee, Pilot-scale semi-continuous cultivation of microalgae *Chlorella vulgaris* in bubble column photobioreactor (BC-PBR): hydrodynamics and gas-liquid mass transfer study, Algal Res. 15 (2016) 65–76.

[4] K. Kumar, D. Das, Growth characteristics of *Chlorella sorokiniana* in airlift and bubble column photobioreactors, Bioresour. Technol. 116 (2012) 307–313.

[5] C.U. Ugwu, H. Aoyagi, H. Uchiyama, Photobioreactors for mass cultivation of algae, Bioresour. Technol. 99 (10) (2008) 4021–4028.

[6] L. López-Rosales, F. García-Camacho, A. Sánchez-Mirón, A. Contreras-Gómez, E. Molina-Grima, An optimisation approach for culturing shear-sensitive dinoflagellate microalgae in bench-scale bubble column photobioreactors, Bioresour. Technol. 197 (2015) 375–382.

[7] J. Vega-Estrada, M.C. Montes-Horcasitas, A.R. Domínguez-Bocanegra, R.O. Cañizares-Villanueva, *Haematococcus pluvialis* cultivation in split-cylinder internal-loop airlift photobioreactor under aeration conditions avoiding cell damage, Appl. Microbiol. Biotechnol. 68 (1) (2005) 31–35.

[8] M.J. Barbosa, Hadiyanto, R.H. Wijffels, Overcoming shear stress of microalgae cultures in sparged photobioreactors, Biotechnol. Bioeng. 85 (1) (2004) 78–85.

[9] N.T. Eriksen, The technology of microalgal culturing, Biotechnol. Lett. 30 (9) (2008) 1525–1536.

[10] B. Wang, C.Q. Lan, M. Horsman, Closed photobioreactors for production of microalgal biomasses, Biotechnol. Adv. 30 (4) (2012) 904–912.

[11] A. Shaikh, M. Al-Dahhan, Scale-up of bubble column reactors: a review of current state-of-the-art, Ind. Eng. Chem. Res. 52 (24) (2013) 8091–8108.

[12] N. Kantarci, F. Borak, K.O. Ulgen, Bubble column reactors, Process Biochem. 40 (7) (2005) 2263–2283.

[13] F. Krujatz, R. Illing, T. Krautwer, J. Liao, K. Helbig, K. Goy, J. Opitz, G. Cuniberti, T. Bley, J. Weber, Light-field-characterization in a continuous hydrogen-producing photobioreactor by optical simulation and computational fluid dynamics, Biotechnol. Bioeng. 112 (12) (2015) 2439–2449.

[14] B. Kong, R.D. Vigil, Simulation of photosynthetically active radiation distribution in algal photobioreactors using a multidimensional spectral radiation model, Bioresour. Technol. 158 (2014) 141–148.

[15] X. Gao, B. Kong, R.D. Vigil, Comprehensive computational model for combining fluid hydrodynamics, light transport and biomass growth in a Taylor vortex algal photobioreactor: Lagrangian approach, Bioresour. Technol. 224 (2017) 523–530.

[16] E.K. Nauha, V. Alopaeus, Modeling method for combining fluid dynamics and algal growth in a bubble column photobioreactor, Chem. Eng. J. 229 (2013) 559–568.

[17] E.K. Nauha, V. Alopaeus, Modeling outdoors algal cultivation with compartmental approach, Chem. Eng. J. 259 (2015) 945–960.

[18] J.P. Bitog, I.-B. Lee, C.-G. Lee, K.-S. Kim, H.-S. Hwang, S.-W. Hong, I.-H. Seo, K.-S. Kwon, E. Mostafa, Application of computational fluid dynamics for modeling and designing photobioreactors for microalgae production: a review, Comput. Electron. Agric. 76 (2) (2011) 131–147.

[19] J.S. Marshall, K. Sala, A stochastic Lagrangian approach for simulating the effect of turbulent mixing on algae growth rate in a photobioreactor, Chem. Eng. Sci. 66 (3) (2011) 384–392.

[20] G. Olivieri, L. Gargiulo, P. Lettieri, L. Mazzei, P. Salatino, A. Marzocchella, Photobioreactors for microalgal cultures: a Lagrangian model coupling hydrodynamics and kinetics, Biotechnol. Prog. 31 (5) (2015) 1259–1272.

[21] J. Huang, X. Qu, M. Wan, J. Ying, Y. Li, F. Zhu, J. Wang, G. Shen, J. Chen, W. Li, Investigation on the performance of raceway ponds with internal structures by the means of CFD simulations and experiments, Algal Res. 10 (2015) 64–71.

[22] J. Krauss, Ö. Ertunç, C. Rauh, A. Delgado, Novel, multi-objective optimization of pulsed electric field processing for liquid food treatment, in: K. Knoerzer, P. Juliano, P. Roupas, C. Versteeg (Eds.), Innovative Food Processing Technologies: Advances in Multiphysics Simulation, Blackwell Publishing Ltd, Oxford, UK, 2011, pp. 209–231.

[23] D. Law, F. Battaglia, T.J. Heindel, Numerical Simulations of Gas-Liquid Flow Dynamics in Bubble Columns, (2006), pp. 1–8.

[24] J. Sanyal, S. Vásquez, S. Roy, M.P. Dudukovic, Numerical simulation of gas–liquid dynamics in cylindrical bubble column reactors, Chem. Eng. Sci. 54 (21) (1999) 5071–5083.

[25] Y. Pan, M.P. Dudukovic, M. Chang, Numerical investigation of gas-driven flow in 2-D bubble columns, AICHE J. 46 (3) (2000) 434–449.

[26] D.Z. Zhang, A. Prosperetti, Ensemble phase-averaged equations for bubbly flows, Phys. Fluids 6 (9) (1994) 2956–2970.

[27] D. Zhang, A. Prosperetti, Momentum and energy equations for disperse two-phase flows and their closure for dilute suspensions, Int. J. Multiphase Flow 23 (3) (1997) 425–453.

[28] E. Delnoij, F.A. Lammers, J.A.M. Kuipers, W.P.M. van Swaaij, Dynamic simulation of dispersed gas-liquid two-phase flow using a discrete bubble model, Chem. Eng. Sci. 52 (9) (1997) 1429–1458.

[29] K. Bech, Dynamic simulation of a 2D bubble column, Chem. Eng. Sci. 60 (19) (2005) 5294–5304.

[30] R.F. Mudde, O. Simonin, Two- and three-dimensional simulations of a bubble plume using a two-fluid model, Chem. Eng. Sci. 54 (21) (1999) 5061–5069.

[31] D. Pfleger, S. Becker, Modelling and simulation of the dynamic flow behaviour in a bubble column, Chem. Eng. Sci. 56 (4) (2001) 1737–1747.

[32] H.F. Lobatón, C.A. Suárez, A. Molina, CFD-facilitated flow field analysis of bubble columns with concentric plates for biological applications, Chem. Eng. Technol. 34 (9) (2011) 1490–1496.

[33] N.G. Deen, T. Solberg, B.H. Hjertager, Large eddy simulation of the gas–liquid flow in a square cross-sectioned bubble column, Chem. Eng. Sci. 56 (21–22) (2001) 6341–6349.

[34] N.G. Deen, T. Solberg, Comparison of PIV and LDA measurement methods applied to the gas-liquid flow in a bubble column, 10th Int. Symp. Appl. Laser Tech. to Fluid Mech, 2000, pp. 1–12.

[35] R.M.A. Masood, A. Delgado, Numerical investigation of the interphase forces and turbulence closure in 3D square bubble columns, Chem. Eng. Sci. 108 (2014) 154–168.

[36] P. Chen, J. Sanyal, M.P. Duduković, Numerical simulation of bubble columns flows: effect of different breakup and coalescence closures, Chem. Eng. Sci. 60 (4) (2005) 1085–1101.

[37] M.E. Díaz, A. Iranzo, D. Cuadra, R. Barbero, F.J. Montes, M.A. Galán, Numerical simulation of the gas–liquid flow in a laboratory scale bubble column, Chem. Eng. J. 139 (2) (2008) 363–379.

[38] W. Blanken, P.R. Postma, L. de Winter, R.H. Wijffels, M. Janssen, Predicting microalgae growth, Algal Res. 14 (2016) 28–38.

[39] M.H. Huesemann, J. Van Wagenen, T. Miller, A. Chavis, S. Hobbs, B. Crowe, A screening model to predict microalgae biomass growth in photobioreactors and raceway ponds, Biotechnol. Bioeng. 110 (6) (2013) 1583–1594.

[40] F.G.A. Fernández, F.G. Camacho, J.A.S. Pérez, J.M.F. Sevilla, E.M. Grima, A model for light distribution and average solar irradiance inside outdoor tubular photobioreactors for the microalgal mass culture, Biotechnol. Bioeng. 55 (5) (1997) 701–714.

[41] J.F. Cornet, C.G. Dussap, G. Dubertret, A structured model for simulation of cultures of the cyanobacterium *Spirulina platensis* in photobioreactors: I. Coupling between light transfer and growth kinetics, Biotechnol. Bioeng. 40 (7) (1992) 817–825.

[42] L. Pottier, J. Pruvost, J. Deremetz, J.-F. Cornet, J. Legrand, C.G. Dussap, A fully predictive model for one-dimensional light attenuation by *Chlamydomonas reinhardtii* in a torus photobioreactor, Biotechnol. Bioeng. 91 (5) (2005) 569–582.

[43] Z.C. Wheaton, G. Krishnamoorthy, Modeling radiative transfer in photobioreactors for algal growth, Comput. Electron. Agric. 87 (2012) 64–73.

[44] J.M. Heinrich, I. Niizawa, F.A. Botta, A.R. Trombert, H.A. Irazoqui, Analysis and design of photobioreactors for microalgae production I: method and parameters for radiation field simulation, Photochem. Photobiol. 88 (4) (2012) 938–951.

[45] H. Berberoglu, J. Yin, L. Pilon, Light transfer in bubble sparged photobioreactors for H2 production and CO2 mitigation, Int. J. Hydrog. Energy 32 (13) (2007) 2273–2285.

[46] C. McHardy, T. Horneber, C. Rauh, Spectral simulation of light propagation in participating media by using a lattice Boltzmann method for photons, Appl. Math. Comput. 319 (2018) 59–70.

[47] C. McHardy, G. Luzi, J.R. Agudo, A. Delgado, C. Rauh, Hybrid numerical simulation of fluid flow and light distribution in a bubble column photobioreactor, *Proceedings of the 5th International Conference on Photonics, Optics and Laser Technology*, Photoptics, 2017, pp. 304–311.

[48] G. Marotta, J. Pruvost, F. Scargiali, G. Caputo, A. Brucato, Reflection-refraction effects on light distribution inside tubular photobioreactors, Can. J. Chem. Eng. 95 (9) (2017) 1646–1651.

[49] L. Pilon, H. Berberoğlu, R. Kandilian, Radiation transfer in photobiological carbon dioxide fixation and fuel production by microalgae, J. Quant. Spectrosc. Radiat. Transf. 112 (17) (2011) 2639–2660.

[50] R. Kandilian, J. Pruvost, A. Artu, C. Lemasson, J. Legrand, L. Pilon, Comparison of experimentally and theoretically determined radiation characteristics of photosynthetic microorganisms, J. Quant. Spectrosc. Radiat. Transf. 175 (2016) 30–45.

[51] J. Dauchet, S. Blanco, J.-F. Cornet, R. Fournier, Calculation of the radiative properties of photosynthetic microorganisms, J. Quant. Spectrosc. Radiat. Transf. 161 (2015) 60–84.

[52] C.-G. Lee, B. Palsson, High-density algal photobioreactors using light-emitting diodes, Biotechnol. Bioeng. 44 (10) (Nov. 1994) 1161–1167.

[53] M.D. Ooms, P.J. Graham, B. Nguyen, E.H. Sargent, D. Sinton, Light dilution via wavelength management for efficient high-density photobioreactors, Biotechnol. Bioeng. 114 (6) (2017) 1160–1169.

[54] F.R. Menter, 2-equation eddy-visocity turbulence models for engineering applications, AIAA J. 32 (8) (1994) 1598–1605.

[55] D. Legendre, J. Magnaudet, The lift force on a spherical bubble in a viscous linear shear flow, J. Fluid Mech. 368 (1998) 81–126, 1998.

[56] T. Frank, P.J. Zwart, E. Krepper, H.-M. Prasser, D. Lucas, Validation of CFD models for mono- and polydisperse air–water two-phase flows in pipes, Nucl. Eng. Des. 238 (3) (2008) 647–659.

[57] A.D. Burns, T. Frank, I. Hamill, J.M. Shi, The Favre averaged drag model for turbulent dispersion in Eulerian multi-phase flows, *5th Int. Conf. Multiph. Flow*, no. 392, 2004, pp. 1–17.

[58] Q. Huang, F. Jiang, L. Wang, C. Yang, Design of photobioreactors for mass cultivation of photosynthetic organisms, Engineering 3 (3) (2017) 318–329.

[59] Y.T. Shah, B.G. Kelkar, S.P. Godbole, W.-D. Deckwer, Design parameters estimations for bubble column reactors, AICHE J. 28 (3) (1982) 353–379.

[60] S.M. Monahan, V.S. Vitankar, R.O. Fox, CFD predictions for flow-regime transitions in bubble columns, AICHE J. 51 (7) (2005) 1897–1923.

[61] M. Heining, A. Sutor, S.C. Stute, C.P. Lindenberger, R. Buchholz, Internal

illumination of photobioreactors via wireless light emitters: a proof of concept, J. Appl. Phycol. 27 (1) (2015) 59–66.
[62] C. McHardy, T. Horneber, C. Rauh, New lattice Boltzmann method for the simulation of three-dimensional radiation transfer in turbid media, Opt. Express 24 (15) (2016).
[63] I.B. Celik, U. Ghia, P.J. Roache, C.J. Freitas, H. Coleman, P.E. Raad, Procedure for estimation and reporting of uncertainty due to discretization in CFD applications, *J. Fluids Eng.* 130 (7) (2008) 78001.
[64] T. Xing, F. Stern, Factors of safety for richardson extrapolation, *J. Fluids Eng.* 132 (6) (2010) 61403.
[65] J. Pruvost, J.-F. Cornet, J. Legrand, Hydrodynamics influence on light conversion in photobioreactors: an energetically consistent analysis, Chem. Eng. Sci. 63 (14) (2008) 3679–3694.
[66] A.S. Mirón, M.C.C. Garcia, A.C. Gómez, F.G. Camacho, E.M. Grima, Y. Chisti, Shear stress tolerance and biochemical characterization of *Phaeodactylum tricornutum* in quasi steady-state continuous culture in outdoor photobioreactors, Biochem. Eng. J. 16 (3) (2003) 287–297.
[67] S. Baer, M. Heining, P. Schwerna, R. Buchholz, H. Hübner, Optimization of spectral light quality for growth and product formation in different microalgae using a continuous photobioreactor, Algal Res. 14 (2016) 109–115.
[68] R.J. Geider, H.L. Maclntyre, T.M. Kana, A dynamic regulatory model of phytoplanktonic acclimation to light, nutrients, and temperature, Limnol. Oceanogr. 43 (4) (1998) 679–694.
[69] J. Yarnold, I.L. Ross, B. Hankamer, Photoacclimation and productivity of *Chlamydomonas reinhardtii* grown in fluctuating light regimes which simulate outdoor algal culture conditions, Algal Res. 13 (2016) 182–194.

8. Comparison between different strategies for the realization of flashing-light effects - pneumatic mixing and flashing illumination

It was outlined in chapter 2 that the productivity of photobioreactors can be increased by operating them in such a way that the FLE takes place. In the literature it is often mentioned that mixing of the culture is an adequate way to create sufficient light/dark fluctuations on the single cell level. Another possibility to realize the FLE is to decouple the light exposure of single cells from hydrodynamic mixing. This can be achieved by providing pulsed illumination to the PBR. It is clear that also for pulsed illumination light intensity gradients exist which affect the overall light exposure so that the numerical investigation of both strategies must include light propagation, mixing and reaction kinetics.

The goal of the chapter is to compare the effects of gas-induced mixing and pulsed illumination on the kinetics of photosynthesis in a bubble column photobioreactor. Therefore, a comprehensive numerical model is built, including the hydrodynamics of the gas-liquid flow, transport of single cells therein, light transfer and photosynthetic reaction kinetics.

The chapter was published as: Luzi, G., McHardy, C., Lindenberger, C., Rauh, C., Delgado, A. (2019). Comparison between different strategies for the realization of flashing-light effects - pneumatic mixing and flashing illumination. Algal Research, 101404, 2019. Reprint for non-commercial use with permission of Elsevier Inc.

Algal Research 38 (2019) 101404

Contents lists available at ScienceDirect

Algal Research

journal homepage: www.elsevier.com/locate/algal

Comparison between different strategies for the realization of flashing-light effects – Pneumatic mixing and flashing illumination

Giovanni Luzi[a,*], Christopher McHardy[b], Christoph Lindenberger[d], Cornelia Rauh[a,b], Antonio Delgado[a,c]

[a] FAU Busan Campus, University of Erlangen-Nuremberg, 46742 Busan, Republic of Korea
[b] Technische Universität Berlin, Fachgebiet Lebensmittelbiotechnologie und-prozesstechnik, Königin-Luise Str. 22, 14195 Berlin, Germany
[c] Friedrich-Alexander Universität Erlangen-Nürnberg, Lehrstuhl für Strömungsmechanik, Cauerstraße 4, 91058 Erlangen, Germany
[d] OTH Amberg-Weiden, Department of Mechanical Engineering and Environmental Engineering, Kaiser-Wilhelm-Ring 3, 92241 Amberg, Germany

ARTICLE INFO

Keywords:
Photobioreactor
Flashing light
Mixing
Bubble column
Numerical simulation

ABSTRACT

A major limitation for the phototrophic cultivation of microalgae in photobioreactors is the low culture density which results in expensive harvesting and downstream processes. It is often mentioned that intensive mixing of the culture can improve the efficiency of light utilization by realizing flashing-light effects which enhance the growth of cell cultures. Alternatively, flashing light sources could provide a way to realize this effect without the need of supplying additional energy for fast mixing. While the effects of mixing have been investigated at various reactor scales, experiments with flashing illumination have been mostly conducted in small geometries. In addition, few studies have been conducted for photobioreactors with larger light paths, being characteristic for the production scale. By means of numerical simulations, we evaluate pneumatic mixing and flashing illumination with regard to their ability to realize flashing-light effects in a 5 cm diameter bubble column filled with a suspension of *Chlamydomonas reinhardtii*. To the best of our knowledge, a numerical comparison between the effects of flashing illumination and pneumatic mixing on the culture growth has not been reported in literature.

A thorough comparison of the two methods requires a robust numerical tool which integrates the computation of the fluid flow and the light field, as well as the growth kinetics of algal cells. In the present work, we compute the three-dimensional flow field in a bubble column photobioreactor tracking also micrometer particles in order to simulate the movement of algae. The spectral light field is computed by solving the three-dimensional Radiation Transfer Equation (RTE) at different wavelengths and biomass concentrations. The coupling of the flow and light fields enables the computation of the spatio-temporal light exposure of individual algae cells, which is used to estimate the respective dynamic photosynthesis reaction rates under different operating conditions of the bubble column reactor.

We found, numerically, that the contribution of pneumatic mixing alone is negligible in comparison to flashing-light effects, for the investigated operating conditions. In contrast, illumination with flashing LED leads to an increase of the growth rate up to a factor of 2.5 at flashing frequencies higher than 50 Hz in a PBR with industrially relevant operating conditions. Thereby, a proper selection of the duty cycle is not only needed to prevent photoinhibition but also to maximize the effects of flashing light at the same time. According to these results, the utilization of flashing LED sources can provide a mostly unused way to improve photobioreactor productivity in the future.

1. Introduction

The growth of world population and the related increasing demand for food and energy resources is one of the major challenges of the 21st century. Microalgae are often considered to be a potential sustainable feedstock to contribute to overcome these challenges. These organisms are usually cultivated in open or closed photobioreactors (PBR) and use light energy for growth and maintenance. Typical values of reachable culture densities in PBR are restricted to few grams per liter, entailing expensive harvesting and downstream processes. Among the main factors that affect the growth of microalgae, light availability, temperature, pH, salinity and nutrients are the most important ones [1,2].

* Corresponding author.
E-mail address: giovanni.luzi@fau.de (G. Luzi).

https://doi.org/10.1016/j.algal.2018.101404
Received 30 July 2018; Received in revised form 5 November 2018; Accepted 25 December 2018

In addition, the exposure of single cells to alternating light intensities is known to enhance the overall efficiency of light utilization and consequently enable higher culture growth rates. Ideally, the experience of such a flashing-light regime results in full light integration, which means that the rate of photosynthesis of a cell is similar to the one under continuous illumination [3]. Small-scale experiments under flashing light show that light/dark (L/D) frequencies of the order of 10^1–10^2 Hz are required to reach full light integration for different species [3–5]. Even at suboptimal L/D frequencies partial light integration can be induced and contribute to a significant improvement of the PBR productivity [4,6–10].

It is often mentioned that intensive mixing of the culture realizes this effect by shuttling algae between regions of different irradiance levels. Thereby, the cycling frequency and the time averaged rate of energy absorption must match the time scales of the light and dark reactions of photosynthesis to improve the overall cell growth [11–13]. It is also known that the biomass concentration has a great impact on the realization of partial light integration as it determines the ratio of light and dark parts in the reactor, as well as the steepness of the light intensity gradient [6,14]. However, according to some researchers the enhancement of PBR productivity due to mixing-induced L/D cycling is not a relevant phenomenon in practice [15,16]. Moreover, intensive mixing is accompanied with high shear stress on single algae which may cause cell damage and reduced viability [17–20]. Accordingly, there is still a vital debate in the scientific community about the relevance of mixing-induced flashing-light effects in common reactor types. Therefore, additional research is needed to improve the reactor designs at scales being relevant for production [21].

Another way to create flashing light conditions in PBR is to modify the type of illumination [22]. This approach has the important benefit that the light regime is decoupled from the flow field. Many experiments have been conducted in special chambers with pulsed illumination for the purpose of determining the respective reaction kinetics [3,4]. Some researchers also employed pulsed illumination to study the growth of cell cultures, mainly in reactors with ultra-short light paths. For example, Sforza et al. [5] used a reactor with 8 mm light path to study the effects of flashing illumination on biomass growth. For the same purpose, Park and Lee [23] conducted experiments in a reactor with light path of 7 mm while Lunka and Bayless [24] utilized a reactor with a light path of 6.4 mm. However, typical light paths of reactors at the production scale are in the order of few centimeters so that the obtained results are not necessarily representative for the production scale. Although both mixing-induced and illumination-induced flashing light effects have been studied separately in experiments and simulations, no comparable study considering the enhancement of culture growth by comparing pulsed illumination of photobioreactors and mixing was conducted before. However, a direct comparison is important since different experimental conditions or simulation setups can affect the results and make the comparison hard or even impossible. Moreover, to benefit from the effects of flashing light exposure at the production scale, a careful examination of the right strategy is necessary, which is the major goal of the present paper.

Some PBR configurations lead to distinctive degrees of light integration due to the L/D frequencies reached under the conditions they were operated [14,25,26]. However, these systems are mainly in the prototype stage and it is unclear whether the same effects can be reached at larger scales. Among the common PBR types, bubble columns represent a good choice for microalgae cultivation because of their simple construction and ease mode of operation. In order to shed more light on the possibilities for realizing flashing-light effects in bubble columns, we investigate numerically how pneumatic mixing and different illumination strategies, i.e. continuous and pulsed illumination, can enhance cell growth.

Numerical simulations are highly requested and desirable since they have the potential to offer a valid predictive tool compared to expensive experiments. They can also provide information about the time-resolved conditions experienced by individual cells which are hard to determine experimentally [27], but fundamental to characterize the impact of operating conditions on the dynamics of photosynthesis. Therefore, a robust and complete predictive model that incorporates Computational Fluid Dynamics (CFD), light distribution and growth kinetics of algal cells would be highly beneficial. However, the accurate modeling of these phenomena and their coupling is far from being trivial. Examples of numerical models which attempt to simulate light/dark cycles date back from Wu and Merchuk [20], who assumed a typical cell trajectory with a cosine function to simulate light/dark cycles. Nevertheless, this so-called circulation approach is empirical and not realistic. Later on, Marshall et al. [28] employed a Lagrangian particle-cloud method in order to compute the algae cell trajectories. More recently, Olivieri et al. [14] utilized a stochastic Lagrangian approach based on superficial liquid velocity and eddy diffusivity to describe cells paths. However, they did not consider the real case of a bubble column PBR where the liquid movement is generated by the oscillations of a bubble plume. Moreover, the eddy diffusivity is not a constant rather than being a spatially distributed quantity [29].

Since the modeling of the flow field greatly impacts the resulting light regime single cells are exposed to, this task should be done with great care. It is well-established that in order to achieve realistic results, models for multiphase flow should include the complete set of interface forces, containing drag, lift, wall lubrication, virtual mass and turbulent dispersion forces. In addition, it should be taken into account that although two-dimensional simulations of fluid flow may be a good option to save computational time, the three-dimensionality of the flow should not be neglected in order to avoid an over-predicted eddy viscosity which in turn could lead to the unphysical result of a non-oscillating plume [30,31]. Moreover, two-dimensional simulations are able only in part to correctly reproduce the complex flow patterns which are typical of bubble columns [32,33]. All of the mentioned issues may be critical for the correct determination of trajectories and light histories of individual cells and thus, for the numerical investigation of the flashing-light effect in pneumatically mixed reactors.

As far as the modeling of light propagation concerns, several authors confirm the necessity of using the complete Radiative Transfer Equation (RTE) rather than the commonly employed Beer-Lambert law, which fully neglects the effects of scattering by algae cells [34,35]. Moreover, effective solution algorithms for solving the RTE are nowadays available [36,37] and remove former limitations due to the computational power. Additionally, the presence of algae cells affects the light spectrum along the light path. For species with peak absorption in the red and blue parts of the spectrum, the contribution of the green fraction to the overall light intensity increases along the light path. Consequently, the relative fraction of light energy being absorbed deep in the culture is also lower compared with locations near the reactor walls. It is clear that a varying light spectrum must impact on what a cell percepts as dark and thus, on the L/D cycles itself. Therefore, besides the intensity of light, the spectral nature of light should be considered in numerical investigations on effects of flashing-light, but is rarely done.

Examples of dynamic photosynthesis models date back to early 2000 and most of them are based on the photosynthetic factory model developed by Eilers and Peeters [38]. The model of Eilers and Peeters [38] uses the concept of photosynthetic units (PSU) and assumes three possible states, e.g. resting, acting and damaged, considering also the effects of photo-saturation and photo-inhibition. Later on, Wu and Merchuk [39] included a maintenance term to take into account the possibility of cell death due to energy limitation. A more sophisticated model has been proposed by Rubio et al. [40] and later refined by Garcia-Camacho et al. [41], which is also able to describe photo-acclimation. In general, it is accepted that models based on the photosynthetic factory approach are able to predict the flashing-light effect [42], which is not true for simple PI-relationships. Therefore, we choose a photosynthetic factory model to study the effects of flashing light on

photosynthesis. Nevertheless, numerical difficulties arise when pulsed light is considered because the reaction rates can change drastically over very short times, thereby affecting the stability of the numerical solver. Thus, it is important to carefully review the computed results, in order to prevent their misinterpretation in consequence of numerical artefacts.

In the present contribution we combine CFD, light distribution and photosynthetic reaction kinetics into an integrated model in order to compare different strategies to realize flashing light effects in a bubble column PBR, employing state-of-the-art models for the considered biological and physical phenomena. Based on the results of our previous paper [43], we neglect here the presence of the void fraction in the computation of the light field, since it has a negligible effect. As a benefit, the computational time needed to solve the RTE drastically reduces. The main goal of the present paper is to compare two strategies for the growth enhancement under conditions which are relevant to production scale: pneumatic mixing under continuous illumination at different light spectra and intensities as well as illumination of the reactor with pulsed light. To the best of our knowledge, this is the first study which combines the simulation of flow field, light distribution and microalgae growth under pulsed illumination in a photobioreactor. Our model also takes into account the presence of spatial gradients of light intensity and light spectrum as well as the movement of individual cells.

2. Materials and methods

2.1. Photobioreactor geometry

In this study we consider a cylindrical bubble column PBR, filled with a suspension of microalgae *Chlamydomonas reinhardtii*. The setting is similar to the one described in our previous paper [43]. Briefly, the reactor is characterized by its internal diameter $D = 0.05$ m and total height $H = 0.5$ m. The liquid level is fixed to $H_L = 0.4$ m. Air is injected from a circular inlet with diameter $d = 0.01$ m being located at the bottom of the PBR. The reactor is illuminated from four sides by LED, each emitting RGB light with intensity I_0. The light is assumed to enter the reactor in normal direction to the light sources. Refraction and reflection of light due to the mismatching refractive indices of the surrounding air, the transparent reactor material and the culture suspension are neglected. This is justified by the superposition of the single light sources, which largely compensates the index mismatching.

2.2. Fluid flow model

2.2.1. Governing equations

We choose the Eulerian-Eulerian formulation to model the multiphase fluid flow in the bioreactor. The dispersed gaseous phase is regarded as a second continuous phase interacting with the continuous liquid one. Therefore, each phase is treated separately, each with its own set of governing equations. Mass transfer phenomena are not taken into account and the flow is considered isothermal, therefore the energy equation does not need to be solved. Additionally, both phases are assumed to be incompressible. The mass conservation equations of each phase read

$$\frac{\partial}{\partial t}(\rho_k \alpha_k) + \nabla\cdot(\rho_k \alpha_k \boldsymbol{u}_k) = 0 \tag{1}$$

Herein, the subscript $k = L, G$. L refers to the liquid phase, while G indicates the gas one. The quantities $\boldsymbol{u}_k$, α_k and ρ_k correspond to the velocity vector, volume fraction and density of each phase. The momentum equations of each phase are

$$\frac{\partial}{\partial t}(\rho_k \alpha_k \boldsymbol{u}_k) + \nabla\cdot(\rho_k \alpha_k \boldsymbol{u}_k \boldsymbol{u}_k) = -\alpha_k \nabla \mathrm{p} + \nabla\cdot(\alpha_k \boldsymbol{\tau}_k) + \rho_k \alpha_k \boldsymbol{g} + \boldsymbol{M}_{s,k} \tag{2}$$

where the subscript $s = L, G$ too. The terms on the right-hand side of Eq. (2) represent the gradient of the pressure field shared between both phases, the divergence of the viscous stress tensor, the gravitational force and the interphase forces acting between the continuous and the disperse phase. We included this term in the momentum equations since Deen et al. [44] reported that if the interphase forces in air-water system are neglected, results strongly deviate from experimental observations because the central bubble plume does not spread across the column.

On the left-hand side of Eq. (2), the first term is the temporal acceleration while the second one is the inertial convective acceleration of each phase. The stress tensor reads

$$\boldsymbol{\tau}_k = \mu_k \left[\nabla \boldsymbol{u}_k + (\nabla \boldsymbol{u}_k)^T - \frac{2}{3}\boldsymbol{I}(\nabla \boldsymbol{u}_k) \right] \tag{3}$$

where $\mu_{k,\ eff}$ is the effective viscosity of each phase. It is defined as

$$\mu_{k,eff} = \mu_{k,Lam} + \mu_{k,Turb} \tag{4}$$

where $\mu_{k,\ Lam}$ and $\mu_{k,\ Turb}$ are the molecular and the turbulent viscosity of each phase. More details about the modeling of the eddy viscosity are given in the next section. The last term of Eq. (2) consists of five forces which are the drag, lift, virtual mass, wall lubrication and turbulent dispersion forces. It reads

$$\boldsymbol{M}_{s,k} = \boldsymbol{M}_{G,L} = -\boldsymbol{M}_{L,G} = \sum\nolimits_A \boldsymbol{F}^A_{L,G} = \boldsymbol{F}^D_{L,G} + \boldsymbol{F}^L_{L,G} + \boldsymbol{F}^{VM}_{L,G} + \boldsymbol{F}^{WL}_{L,G} + \boldsymbol{F}^{TD}_{L,G} \tag{5}$$

A detailed description of the interphase forces of Eq. (5) can be found in our previous contributions [43,45,46]. Thereby, we summarize the equations in Table 1.

2.2.2. Turbulence models

We opt for the SST two-equation model [52] to compute the turbulent viscosity of the continuous phase, and a one equation model to compute the turbulent viscosity of the disperse phase. Concerning the continuous phase, the turbulent viscosity reads

$$\mu_{L,Turb} = \rho_L \frac{k_L}{\omega_L} \tag{6}$$

where k_L is the turbulent kinetic energy and ω_L is the specific rate of dissipation. According to the Shear Stress Transport (SST) model, these two quantities are here computed by solving two independent scalar equations for k_L

$$\frac{\partial}{\partial t}(\rho_L \alpha_L k_L) + \nabla\cdot(\rho_L \alpha_L \boldsymbol{u}_L \mathrm{k}_L) = \nabla\cdot(\alpha_L(\mu_{L,Lam} + \sigma_{k3}\mu_{L,Turb})\nabla k_L) + \alpha_L P_k - \alpha_L \beta' \rho_L k_L \omega_L \tag{7}$$

Table 1
Interphase force correlations between the gas and the liquid phase.

Drag force: Correlation of Clift et al. [47] in case of $u_G = 4.25$ mm/s and $u_G = 8.5$ mm/s and Ishii and Zuber [48] in case of $u_G = 1.28$ cm/s for C_D

$\boldsymbol{F}^D_{L,G} = \frac{3}{4}\alpha_G \rho_L \frac{C_D}{d_B} |\boldsymbol{u}_G - \boldsymbol{u}_L|(\boldsymbol{u}_G - \boldsymbol{u}_L)$

Lift force: Model of Legendre-Magnaudet [49] for C_L

$\boldsymbol{F}^L_{L,G} = \alpha_G \rho_L C_L (\boldsymbol{u}_G - \boldsymbol{u}_L) \times \nabla \times \boldsymbol{u}_L$

Virtual mass force: $C_{VM} = 0.5$

$\boldsymbol{F}^{VM}_{L,G} = \alpha_G \rho_L C_{VM} \left(\frac{D\boldsymbol{u}_G}{Dt} - \frac{D\boldsymbol{u}_L}{Dt} \right)$

Wall lubrication force: Correlation of Frank et al. [50] for C_{WL}

$\boldsymbol{F}^{WL}_{L,G} = -\alpha_G \rho_L C_{WL} |\boldsymbol{u}_L - \boldsymbol{u}_G|^2 \hat{\boldsymbol{n}}_W$

Turbulent dispersion force: Model of Burns et al. [51]

$\boldsymbol{F}^{TD}_{L,G} = C_{TD} C_{CD} \frac{\nu_{L.Turb}}{\sigma_{L.Turb}} \left(\frac{\nabla \alpha_G}{\alpha_G} - \frac{\nabla \alpha_L}{\alpha_L} \right)$

and ω_L

$$\frac{\partial}{\partial t}(\rho_L \alpha_L \omega_L) + \nabla\cdot(\rho_L \alpha_L \boldsymbol{u}_L \omega_L) = \nabla\cdot(\alpha_L(\mu_{L,Lam} + \sigma_{\omega 3}\mu_{L,Turb})\nabla\omega_L) + 2(1 - F_1)\rho_L \sigma_{\omega 2}\frac{\alpha_L}{\omega_L}(\nabla k_L\cdot\nabla\omega_L) + \alpha_3 \alpha_L \frac{\omega_L}{k_L}P_k - \alpha_L \beta_3 \rho_L \omega_L^2 \quad (8)$$

where $\sigma_{\omega 2}$ and β' are constants, while α_3, β_3, $\sigma_{\omega 3}$ and σ_{k3} are functions that depend linearly on the blending function F_1. The latter is equal to one close to the wall region and zero far away from it. The limiter of the eddy viscosity

$$\nu_{L,Turb} = \frac{\alpha_1 k_L}{max(\alpha_1 \omega_L; \Omega F_2)} \quad (9)$$

allows to properly take into account the transport of the principal turbulent shear stress. In Eq. (9) a_1 is a constant, F_2 is another blending function and Ω is the absolute value of the vorticity [52]. We choose a zero equation turbulence model for the gas phase

$$\mu_{G,Turb} = \frac{\rho_G}{\rho_L}\frac{\mu_{L,Turb}}{\sigma_{LP,Turb}} \quad (10)$$

where σ_{LP} is the turbulent Prandtl number.

2.2.3. Particle tracking

We inject and track small solid particles inside the PBR in order to simulate the motion of algae cells. The particle displacement $\boldsymbol{x}_p$ is related to particle velocity $\boldsymbol{u}_p$ via the usual equation,

$$\frac{d\boldsymbol{x}_p}{dt} = \boldsymbol{u}_p \quad (11)$$

By integrating numerically Eq. (11) by means of an explicit Euler method [53], the particle position is computed as

$$\boldsymbol{x}_P^n = \boldsymbol{x}_P^0 + \boldsymbol{u}_P^0 \Delta t \quad (12)$$

where the superscripts n and 0 refer to the current and the previous time step, respectively. The particle velocity $\boldsymbol{u}_p$ is computed by solving Newton's second law

$$m_P \frac{d\boldsymbol{u}_p}{dt} = \boldsymbol{F}_{TOT} \quad (13)$$

where m_P is the particle mass and $\boldsymbol{F}_{TOT}$ is the sum of all the forces acting on a discrete particle, that is,

$$\boldsymbol{F}_{TOT} = \boldsymbol{F}_D + \boldsymbol{F}_B \quad (14)$$

where $\boldsymbol{F}_D$ is the drag force and $\boldsymbol{F}_B$ is the buoyancy force (see Table 2). Since in our case the Stokes number $St \ll 1$ due to the very small particle size, we select the option one-way coupling in ANSYS CFX®. In this way, the fluid flow influences particle trajectories, but particles do not affect fluid flow motion. The main benefit is that the computational time is strongly reduced with compared to the fully coupled option.

2.2.4. Grid generation and CFD simulation settings

We generated both the geometry and the structured mesh by using the software ANSYS ICEM® 15.0, while the commercial CFD software ANSYS CFX® 15.0 was used to perform all the numerical simulations. The bubble diameter is kept constant to $d_B = 7$ mm, since coalescence and break-up phenomena can be regarded as negligible for the considered values of the gas superficial velocity [55]. The grid used in the simulations has 54201 hexahedral cells, and it has been chosen after a grid independence study similar to the one described by McHardy et al. [43]. In the present contribution, the time averaged water velocity profile has been chosen as a target parameter. Additional details of the mesh and the simulation settings have already been reported [43,45,46], and they will not be repeated here. For the three cases of $u_G = 4.25$ mm/s, $u_G = 8.5$ mm/s and $u_G = 1.28$ cm/s we track particles for approximately 12 s, which is of the same order of magnitude of the mixing time measured experimentally [56]. Particles are injected from four point cones inside the reactor, and their positions, particle mass flow and number rate are summarized in Table 3. The number of representative particles which assume the role of certain amount of real particles is the particle number rate. We set a maximum particle diameter to $d_P = 10$ μm and a minimum one to $d_P = 1$ μm.

Table 2
Interphase forces between particles and the liquid phase.

Drag force: Correlation of Schiller and Naumann [54] for C_D
$\boldsymbol{F}_D = \frac{1}{2}A\rho_L C_D \lvert\boldsymbol{u}_L - \boldsymbol{u}_P\rvert(\boldsymbol{u}_L - \boldsymbol{u}_P)$
Buoyancy force
$\boldsymbol{F}_B = \frac{\pi}{6}d_P^3(\rho_P - \rho_L)\boldsymbol{g}$

Table 3
Positions, mass flow rate and particle number rate of the four injectors.

	x [m]	y [m]	z [m]	Mass flow rate [kg/s]	Particle number rate [1/s]
Injector 1	0.01	0	0.005	$9.85 * 10^{-6}$	20
Injector 2	−0.01	0.05	0.007	$9.85 * 10^{-6}$	20
Injector 3	0.005	0.1	−0.015	$9.85 * 10^{-6}$	300
Injector 4	0.004	0.13	0.01	$9.85 * 10^{-6}$	300

2.3. Light model

2.3.1. Physical model

The governing equation of light propagation is the Radiation Transfer Equation (RTE), which describes the change of the radiance L in a medium due to the interaction with the surrounding matter. Assuming the matter to be a suspension of microalgae and neglecting the emission of energy within the medium, e.g. by fluorescence, the monochromatic RTE reads

$$\frac{\partial L_\lambda}{c\ \partial t} + \nabla L_\lambda = -\mu_{a,\lambda}L_\lambda - \mu_{s,\lambda}\left(L_\lambda - \frac{\omega_\lambda}{4\pi}\int_{4\pi}\Phi(\boldsymbol{n}\boldsymbol{n}')L_\lambda' d\boldsymbol{\Omega}'\right) \quad (15)$$

The zeroth angular moment of the radiance

$$I_\lambda(\boldsymbol{x}) = \int_{4\pi} L(\boldsymbol{x})d\boldsymbol{\Omega} \quad (16)$$

equals the intensity of monochromatic light I_λ from which the intensity of polychromatic light I can be obtained by integration across the spectrum, thus

$$I(\boldsymbol{x}) = \int_{\lambda_1}^{\lambda_2} I_\lambda(\boldsymbol{x})d\lambda \quad (17)$$

The absorption and scattering coefficients in Eq. (15) are related to the absorption and scattering cross-sections of the microalgae cells via the concentration of dry biomass.

$$\mu_a = A_{abs}X \quad (18)$$

$$\mu_s = A_{sca}X \quad (19)$$

The spectral absorption and scattering cross-sections of *Chlamydomonas reinhardtii* are extracted from measurements of Kandilian et al. [57] and are given in Table 4. In accordance to these measurements, we further assume that the scattering phase function $\Phi(\boldsymbol{n}, \boldsymbol{n}')$ is given by the Henyey-Greenstein phase function with the asymmetry factor $g = 0.98$. Under the considered operating conditions of the bubble column PBR it was shown that the effect of the gas phase on the light intensity is weak [43] and therefore it is not further taken into account.

Table 4
Absorption and scattering cross-sections of *Chlamydomonas reinhardtii* with respect to wavelength.

λ [nm]	400	415	430	445	460	475	490	505	520	535	550
A_{abs} [m^2/kg]	331	401	434	436	386	395	367	261	140	87	77
A_{sca} [m^2/kg]	920	794	699	743	868	845	927	1209	1512	1653	1708

λ [nm]	565	580	595	610	625	640	655	670	685	700
A_{abs} [m^2/kg]	82	106	123	136	156	176	259	358	311	70
A_{sca} [m^2/kg]	1714	1673	1651	1628	1599	1538	1360	1139	1305	1941

2.3.2. Numerical model

The PAR spectrum of light was discretized into 21 equally spaced discretization points ($\Delta\lambda = 15$ nm), each representing a certain wavelength between $\lambda_1 = 400$ and $\lambda_2 = 700$ nm. It was previously shown that this resolution is sufficient for an accurate integration across the spectrum [37].

Eq. (15) is discretized on a regular grid (lattice) with grid spacing $\Delta x = 0.333$ mm in three spatial dimensions and solved for each wavelength by means of a Radiation Transfer lattice Boltzmann method (RT-LBM). Further details of the numerical method can be found elsewhere [36,37]. The spatial grid resolution was selected by means of a grid independence study. The solution of the integral in Eq. (16) is obtained by replacing it with a Gaussian quadrature rule which is related to the angular discretization of the lattice Boltzmann model. The solution of the integral in Eq. (17) is computed by means of Simpson's rule using the discretization points given by the discretization of the spectrum.

2.4. Photosynthesis model

In order to model the dynamics of photosynthesis we utilize the model proposed by Garcia-Camacho et al. [41], which is based on the assumption that the thylakoids contain resting photosynthetic units (PSU) which can be activated by the absorption of light. In brief, activated PSUs either relax again towards the resting state by liberating the absorbed energy via photochemical quenching or are damaged if light is absorbed in excess. In its original formulation the model includes photoacclimation which we neglect in this paper because the time-scale of the biological response to changes in light intensity is much larger than the considered particle tracks. Instead, cells are assumed to have a constant total number of PSUs a_{tot} and consequently constant radiation properties. This assumption is also consistent to the computation of the light fields. The dynamics of photosynthesis are governed by the mass balances for the fractions of activated PSUs ($x_1 = a_{act}/a_{tot}$)

$$\frac{dx_1}{dt} = \frac{x_3}{\eta a_{tot}} \int \zeta_\lambda I_\lambda(\boldsymbol{x}t) d\lambda - \frac{r_m}{a_{tot}} \frac{x_1}{\kappa + x_1} - k_i x_1 \int \zeta_\lambda I_\lambda(\boldsymbol{x}t) d\lambda \tag{20}$$

which can be reformulated to

$$\frac{dx_1}{dt} = \beta \left[\frac{x_3}{\eta r_m} \int \zeta_\lambda I_\lambda(\boldsymbol{x}t) d\lambda - \frac{x_1}{\kappa + x_1} \right] - k_i x_1 \int \zeta_\lambda I_\lambda(\boldsymbol{x}t) d\lambda \tag{21}$$

by introducing the characteristic frequency $\beta = r_m/a_{tot}$ [41], and that of the fraction of damaged PSUs ($x_2 = a_{dam}/a_{tot}$)

$$\frac{dx_2}{dt} = k_i x_1 \int \zeta_\lambda I_\lambda(\boldsymbol{x}t) d\lambda - \frac{k_r x_2}{\kappa_2 + x_2} \tag{22}$$

The fraction of resting PSUs is $x_3 = 1 - x_1 - x_2$. The first term on the RHS of Eq. (20) accounts for the absorption of light by resting PSUs. Deviating from the original model we include the integration of the wavelength specific quantities to account for that the absorption rate depends on the available light spectrum. The cell specific spectral absorption cross-section ζ_λ can be related to the dry mass specific absorption cross-section $A_{Abs,\lambda} = \zeta_\lambda m_c$ where m_c denotes for the mass of a single cell. From the data set of Kandilian et al. [57] we calculate m_c by using the provided cell properties d_P, w_c, and ρ_X (see Table 5 for details) and find the spectral average of ζ_λ in the same order of magnitude as specified in the original model. The parameter η is the excitation requirement of a PSU. The second term accounts for photochemical quenching which is enzyme-mediated and assumed to follow Monod kinetics. The parameters r_m and κ account for the maximum rate of photochemical quenching and the half-saturation constant of the enzymatic reaction. The third term accounts for the transition of an activated to a damaged PSU, which is determined by a rate constant k_i and the amount of absorbed light. On the opposite, the second term in Eq. (22) describes the recovery of damaged PSU and their transition to the resting state in an enzymatic reaction which is governed by the constants k_r and κ_2.The reaction rates of photodamage and repair are net rates which also include the dissipation of energy due to non-photochemical quenching, being discussed in detail in Ref. [41]. The saturation intensity is given in the original model by a parameter $\alpha = r_m\eta/\zeta$ which we reformulate to

$$\alpha = r_m \eta \frac{\int I_\lambda d\lambda}{\int \zeta_\lambda I_\lambda d\lambda} \tag{23}$$

in order to take the wavelength-dependency of ζ_λ and the available light spectrum into account. The observable rate of photosynthesis μ is related to the rate of enzymatic photochemical quenching and furthermore determined by the energy demand for maintenance. Accordingly,

$$\mu_i(t) = \left(\frac{P_{max} x_1}{\kappa + x_1} - m \right) (1 + c_r)^{-1} \tag{24}$$

where P_{max} is the maximum rate, m accounts for the maintenance and c_r takes into account the energetic costs of biomass synthesis.

In order to parametrize the model, parameters were either calculated from published data (ζ, m) or directly taken from literature (a_{tot}, η, c_r). $P_{max}$was approximated based on the maximum growth rate of *Chlamydomonas*, which is about $\mu_{max} \approx 0.13\,h^{-1}$. The remaining parameters (β, κ, κ_2, k_i, k_r) were estimated by fitting the steady-state solution of the model to the experimental PI-curve of Takache et al. [58], see Fig. 7 therein. For the fitting procedure, the *fminsearch* subroutine of Matlab 2015 was used and most of the fitted parameters agreed on their order of magnitude to the estimations of Garcia-Camacho. Taking into account that the original model was calibrated for a different species and that the fitting yielded a reasonable agreement with Takache's data, we accept the estimated parameter set. All model parameters including their values are summarized in Table 5.

Extending our previous work [46], we use the temporal light exposure $I_\lambda(\boldsymbol{x}(t))$ of N_C simulated cells as input of the dynamic model, which can be computed by tracing cells through the simulated spatial light intensity distribution. Eqs. (21) and (22) are solved numerically by means of a third-order Runge-Kutta method with the time step set to $\Delta t = 0.1$ ms. The average growth rate of the whole cell population can be obtained by first averaging the individual growth rates $\mu_i(t)$ (see Eq.

Table 5
Parameters of the metabolic model.

	Value		Comment	Ref.
a_{tot}	96.000	[PSU/cell]	Taken from Ref.	[59]
ζ_λ	$A_{abs,\ \lambda} m_c$	[m^2/cell]	Calculated from A_{abs} (Table 4) and $m_c = \frac{\pi}{6} d_P{}^3 \rho_{X,wet}(1 - w_c)$	[57]
w_c	0.78	[kg/kg]	Taken from Ref.	[57]
d_c	4.2	[μm]	Taken from Ref.	[57]
$\rho_{X,\ wet}$	1088	[kg m^{-3}]	$\rho_{X,\ wet} = \rho_X(1 - w_c) + \rho_L w_c$ $\rho_X = 1400$ kg m^{-3}	[57]
η	4·1E06	[μE/mol PSU]	Taken from Ref.	[41]
β	504	[s^{-1}]	Fitted to experimental PI-curve. In original model $\beta = 1$ kHz at $a_{tot} = 88.000$ PSU/cell	[58]
κ	0.0275	[−]	Fitted to experimental PI-curve. In original model $\kappa = 0.0055$ at $a_{tot} = 88.000$ PSU/cell.	[58]
κ_2	0.0497	[−]	Fitted to experimental PI-curve. In original model $\kappa_2 = 0.0398$ at $a_{tot} = 88.000$ PSU/cell	[58]
k_i	3.7·1E07	[cell/μE]	Fitted to experimental PI-curve. In original model $k_i = 1.2 \cdot 1E07$	[58]
k_r	0.00389	[s^{-1}]	Fitted to experimental PI-curve. In original model $k_r = 0.00048 s^{-1}$.	[58]
P_{max}	0.16	[h^{-1}]	Set according to maximum growth rate $\mu_{max} \approx 0.13$ h^{-1}	[58]
m_s	$0.048 P_{max}$	[h^{-1}]	Estimated from the published data of oxygen evolution and used model coefficients.	[6]
c_r	0.162	[−]	Taken from Ref.	[6]

(24)) of all cells over time and then averaging over the population in a second step.

$$\mu_{av}(t) = \frac{1}{N_C} \sum_{N_C} \bar{\mu}_i \tag{25}$$

3. Results and discussion

3.1. Flow and particle mixing

3.1.1. Flow field at different gas superficial velocities

Fig. 1a depicts the contour of air-volume fractions at a time instant in a cross-sectional plane located at $z = 0$ m. The value of the gas superficial velocity is $u_G = 8.5$ mm/s. A meandering plume can be clearly observed and it oscillates randomly inside the reactor, spreading all over the cross-section after a short distance from the gas sparger due to the action of the turbulent dispersion forces. The resulting radial gas hold-up profile determines a pressure profile which attains its maximum and minimum values near the walls and close to the center, respectively. The time averaged results show a liquid upward motion in the central region as well as a downward motion of the liquid close to the walls. Moreover, the uneven gas distribution determines a circulation of the liquid phase with consequent formation of eddies, concentrated mostly in the bottom part of the reactor, see Fig. 1b, which depicts the streamlines of the liquid velocity for the case of gas

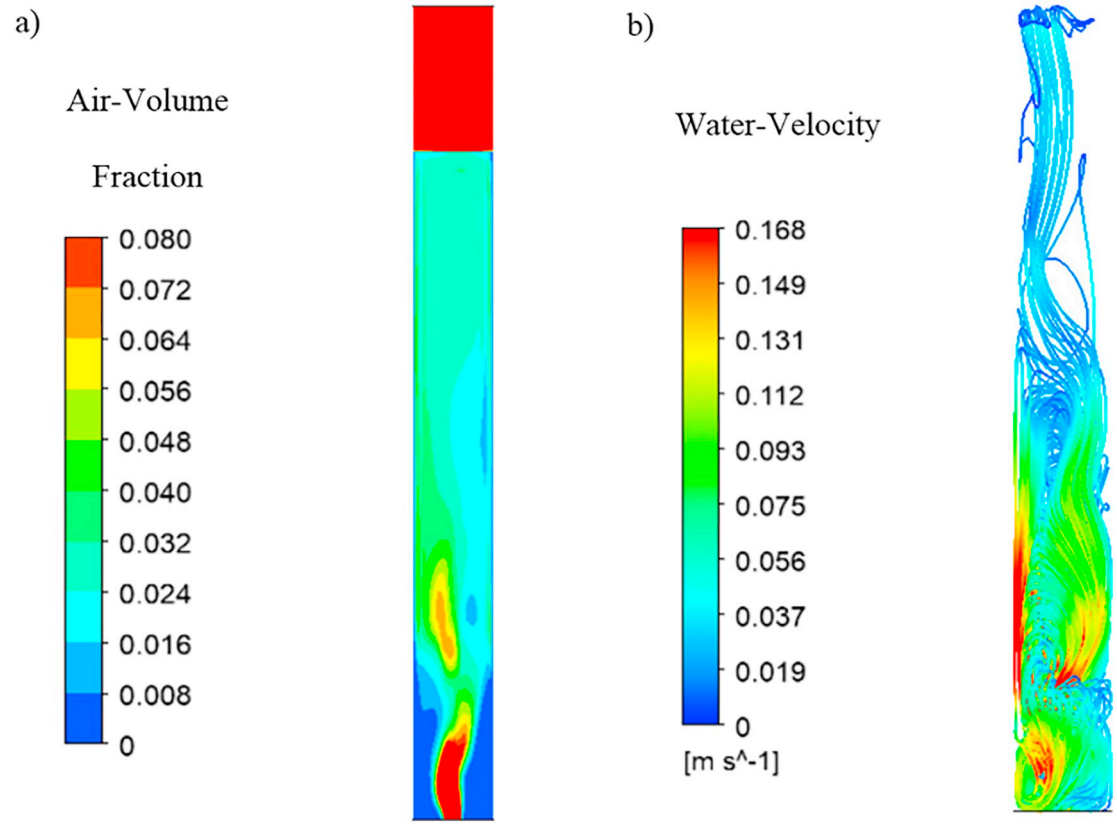

Fig. 1. Flow field. a) Air-volume fraction distribution in a cross-sectional plane at $z = 0$ m and b) streamlines of liquid at $t = 166.95$ s. The gas superficial velocity is $u_G = 8.5$ mm/s.

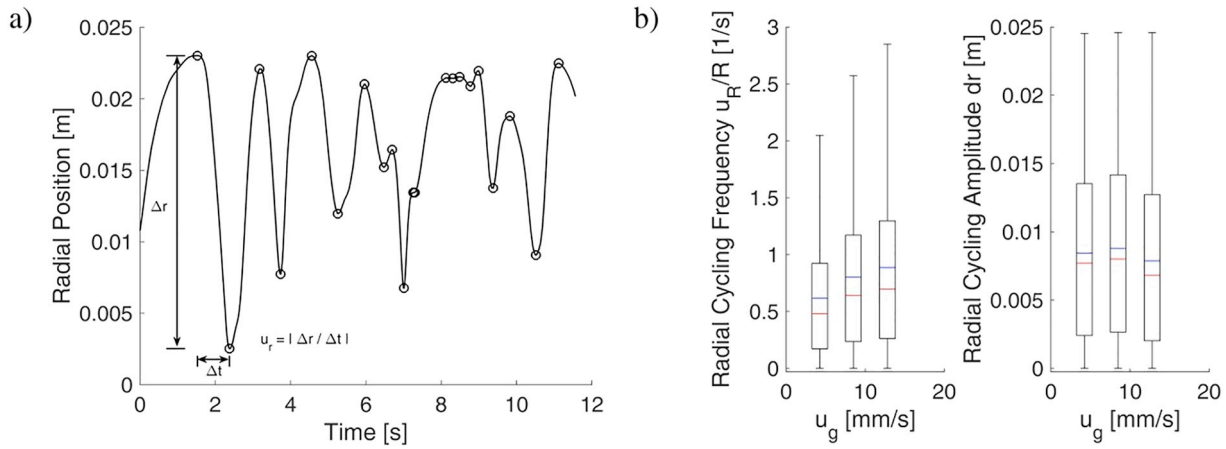

Fig. 2. Particle trajectory statistics. a) Particle trajectory of a randomly chosen particle at u_G = 8.5 mm/s with definition of the radial cycling velocity. The distance Δr is the distance between two consecutive turning points and the time interval Δt denotes the time a particle travels in one direction. b) Boxplots showing the distributions of radial cycling frequency and amplitude with respect to the gas superficial velocity within a population of 1000 particles. Horizontal lines indicate the respective median (red) and arithmetic mean (blue). (For interpretation of the references to color in this figure legend, the reader is referred to the web version of this article.)

superficial velocity u_G = 8.5 mm/s. By increasing the gas superficial velocity, the liquid recirculation results more vigorous leading to bigger and stronger eddies. The opposite happens for the case of the lowest value of gas superficial velocity, i.e. u_G = 4.25 mm/s. The presence and the strength of eddies affect the motion of algae inside and outside of the photic zone, thereby influencing L/D cycles. Higher gas superficial velocities promote an increase of the frequency of L/D cycles by shortening the cycle duration as it will be described in the next section.

3.1.2. Particle trajectories and mixing statistics

It is frequently mentioned that the realization of light integration requires the fast radial motion of algae cells. To investigate the effect of the gas superficial velocity on the radial particle motion, we compute from the trajectories of individual particles radial velocities $u_r = dr/dt$ as indicated in Fig. 2a. The length and time increments dr and dt respectively are chosen from the turning points of the radial particle motion. Fig. 2b compares the distributions of radial velocities computed from 1000 particle tracks at different gas superficial velocities. It can be seen that the radial cycling frequency correlates with u_G while the amplitudes of the radial motion are unaffected. With regard to flashing-light effects these results indicate the possibility of their occurrence since some researchers state that low frequency L/D-cycling might be sufficient for this purpose (see Section 1). However, assessing the potential of pneumatic mixing to enhance cell growth necessitates considering the temporal light exposure cells undergo and its impact on the growth kinetics. These results will be shown in Section 3.3.

3.2. Polychromatic light intensity field and spectra

Fig. 3a shows the computed polychromatic light intensities in the bubble column along the column radius for different biomass concentrations. Thereby, the effective light intensity is affected by the superposition of photons emitted from the four sources. As expected, a higher biomass concentration causes a steeper decay of the light intensity. Intensities higher than the incoming light intensity are found near the reactor wall due to backscattering. The decay of the polychromatic light intensity is clearly non-exponential, which is caused by light scattering but primarily due to the changing spectral composition along the light path. The latter is related to a less effective absorption of green light and thus, to the flattening of the polychromatic light intensity profile. The evolution of the light spectrum towards the reactor center is depicted in Fig. 3b. It can be seen that backscattering particularly affects the green part of the spectrum, which is plausible considering that in this part of the spectrum scattering is most prominent while the absorption of light is weakest (see Table 4). Particularly at high biomass concentration just green light is present in the center of

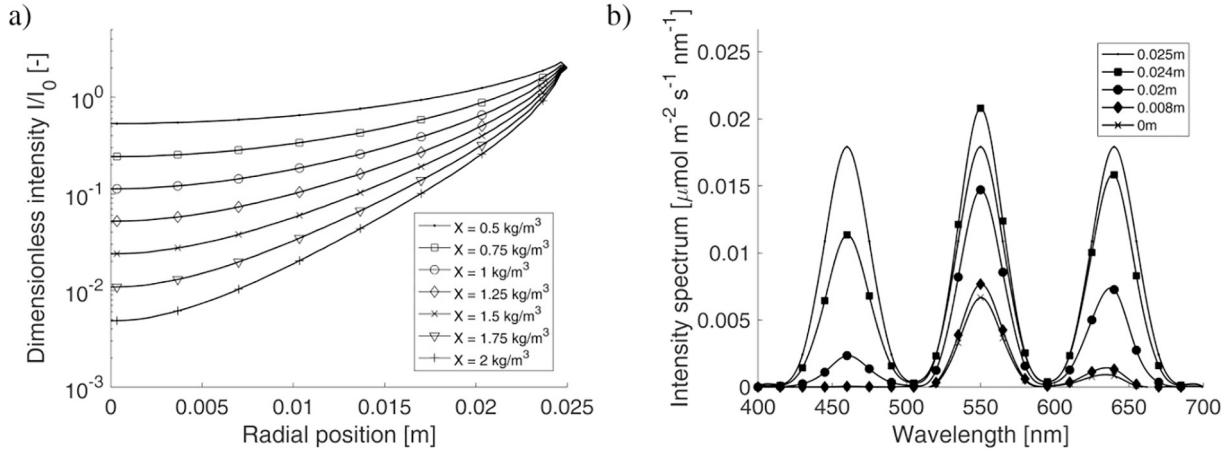

Fig. 3. Distribution of RGB light in the bubble column. a) Non-dimensional polychromatic light intensity profiles with respect to radial position and biomass concentration. b) Spatial evolution of the emitted light spectrum at biomass concentration X = 0.75 kg m^{-3}.

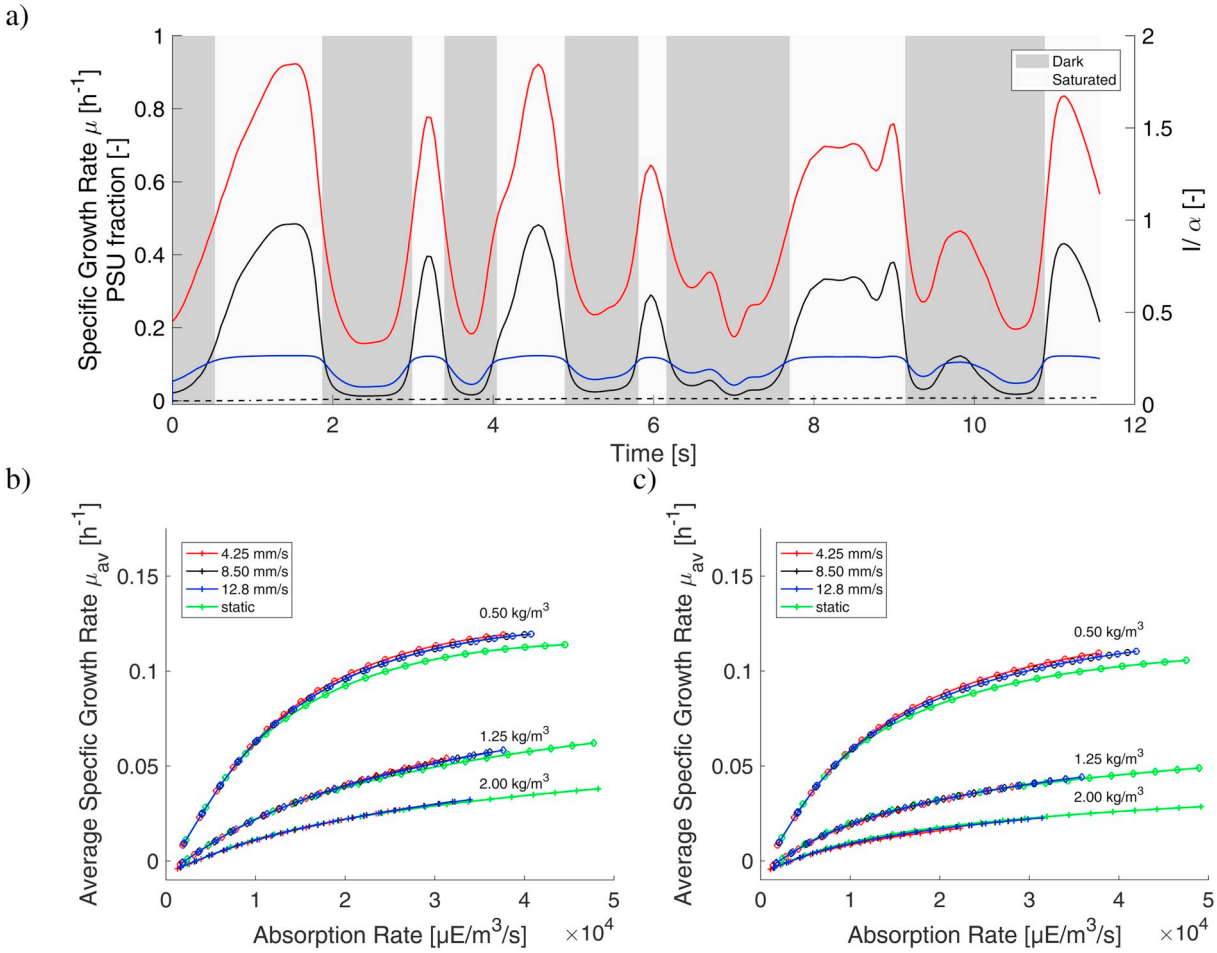

Fig. 4. Dynamics of photosynthesis under continuous illumination. a) Time resolved response of a randomly chosen particle at gas superficial velocity u_G = 8.5 mm/s, biomass concentration X = 2 kg m^{-3} and single lamp intensity I_0 = 200 μE s^{-1} m^{-2}. Line colors encode received dimensionless light intensity (red), specific growth rate (blue), activated PSUs (black) and damaged PSUs (black dashed). b) Time-averaged growth rate of the cell population under RGB light with respect to volumetric light absorption and gas superficial velocity. c) Time-averaged growth rate of a cell population under RB light with respect to volumetric light absorption and gas superficial velocity. (For interpretation of the references to color in this figure legend, the reader is referred to the web version of this article.)

the reactor. Green light is absorbed only weakly so that the reactor is dark in the center.

3.3. Evaluation of strategies to realize flashing-light effects

3.3.1. Photosynthetic response of a single cell moving in continuous light

Fig. 4a shows the metabolic response over the course of the tracking time of the same cell whose trajectory was shown in Fig. 2a. The conditions in the reactor are: gas superficial velocity $u_G = 8.5\,\mathrm{mm/s}$, biomass concentration $X = 2\,\mathrm{kg\,m^{-3}}$ and single lamp intensity $I_0 = 200\,\mu\mathrm{E\,m^{-2}\,s^{-1}}$. Due to its motion the cell is exposed to fluctuating light intensities between low values when the cell is located near the reactor center and much higher values when it is close to the reactor wall. Note that the received light intensity is non-dimensionalized by relating it to the saturation intensity α (see Eq. (23)), thus, the cell is in a light saturated regime at times when $I/\alpha > 1$. The amount of activated PSUs in this cell closely follows the time course of the received light intensity and also the light history has no significant effect on the activated PSUs under these conditions. This observation is plausible if one recalls that the characteristic frequency $\beta = r_m/a_{tot}$ measures the maximum rate at which activated PSUs are recovered in the enzymatic dark reaction. In our simulations $\beta = 504\,\mathrm{s^{-1}}$ is much higher than the radial cycling frequency (Fig. 2b), indicating that the relaxation of activated PSUs is too fast to bridge periods during which the cell is located in the dark. However, it should be noted that the rate of cell growth is not linearly proportional to the amount of activated PSUs (see Eq. (24)) and growth occurs at maximum as long $x_1 \geq 0.15$.

3.3.2. Pneumatic mixing of a cell culture under continuous light

In order to investigate if similar observations can be made on the scale of the cell culture, we evaluate the trajectories of 1000 cells under different operating conditions, namely cell concentration, gas superficial velocity and single lamp intensity of the LED. Fig. 4b depicts the average population growth rate under continuous RGB light with respect to these variables. Note that the culture growth rate is plotted over the time averaged volumetric light absorption rate $1/N_C \Sigma m_c/(T_i X) \int \int \zeta_\lambda I_\lambda(t) d\lambda dt$, where T_i is the duration of a particle track. This quantity increases at higher single lamp intensity. It can be seen that different levels of the gas superficial velocity have almost no impact on the growth rate under RGB illumination. Moreover, the predicted growth rate is very similar to the prediction of the steady-state in a static culture, where cells were assumed to stay at constant positions. Since under these conditions no mixing and thus no flashing-light effect occur, it follows that flashing-light effects are also not realized by pneumatic mixing. On the contrary, if the pneumatic mixing would be sufficient to improve flashing-light effects, the efficiency of light utilization should increase at higher gas superficial velocity, resulting in faster growth at same volumetric light absorption rate. For a culture illuminated with Red Blue (RB) LED light we observe similar results as for RGB illumination, see Fig. 4c. However, the overall growth of the

culture is lower in comparison to RGB illumination, which is due to a less homogeneous light distribution.

The results underline that flashing-light effects can be hardly realized by means of pneumatic mixing. The radial cycling at different gas superficial velocities is much slower than the relaxation of activated PSUs and therefore no benefit can be taken from radial motion and L/D cycling. Thus, pneumatic mixing cannot be considered as a promising strategy to improve cell growth by generating flashing-light effects, at least for the investigated geometry and operating conditions. At this point it should be emphasized that the gas superficial velocities chosen in this study are typical for operating conditions of bubble column PBR. It is important to keep in mind that these results are only valid for the investigated organism and different results might be obtained for organisms where β is in the same order as u_R/R. This might also be an explanation for the scattering of reported results concerning growth enhancement as a consequence of L/D cycling [6,8,15,16]. One option to overcome the limitations of pneumatic mixing could be to include an additional degree of freedom into the illumination regime by utilizing flashing LED illumination, as suggested by Schulze et al. [22]. Flashing LED allow modifying the temporal light exposure of a moving cell from a relation $I(\boldsymbol{x}(t))$ to a relation $I(t,\boldsymbol{x}(t))$ and therefore to tune the frequency of L/D cycles to the same order as the characteristic frequency β.

3.3.3. Photosynthesis of the cell culture under flashing LED illumination

In order to investigate the effect of flashing LED light on the cell growth rate, we include time-dependency of the light field by modifying the received intensity in Eqs. (20)–(23) to $I_\lambda'(t,\boldsymbol{x}(t)) = I_\lambda(\boldsymbol{x}(t))f(t)$ where $f(t)$ is a time-dependent rectangular pulse function being characterized by its duty cycle $\tau = t_l/(t_l + t_d)$, frequency $\nu = 1/(t_l + t_d)$ and amplitude $f_0 = 1/\tau$. The times t_l and t_d are the flash and dark times of the LED. The choice of the amplitude ensures that the time-averaged emission power of the LED source is equal to continuous illumination and thus, the overall supply of light energy remains constant. This simple modification is valid since the time scale of light propagation in our reactor ($\sim 10^{-10}$ s) is much smaller than the time scales of mixing (~ 1 s) or the light ($\sim 10^{-6}$ s) and dark ($\sim 10^{-3}$ s) reactions.

Fig. 5a depicts the received light intensity and specific growth rate of a single cell under flashing LED light with $\nu = 10$ Hz and $\tau = 0.5$. The light flashes clearly overlay the slow movement of the cells along the light gradient which is also reflected in the time course of the specific growth rate. Fig. 5b illustrates the dynamics of the activated PSU fraction under light flashes of 10 Hz and 500 Hz. The duty cycle in this simulation is set to $\tau = 0.5$. At 10 Hz all activated PSUs relax to the ground state quickly after the end of the flash. In contrast, at 500 Hz one observes that the dark period is too short for relaxing all activated PSUs. Therefore, activated PSUs are also available during the dark period and allow the dark reaction to proceed. Fig. 5c depicts the impact of the flash frequency and duty cycle on the average population growth rate at $X = 1.5\,\mathrm{kg\,m^{-3}}$, single light intensity $I_0 = 200\ \mu\mathrm{E\,m^{-2}\,s^{-1}}$ and gas superficial velocity $u_G = 8.5$ mm/s in comparison to the respective growth rates under continuous illumination (see Fig. 4b). At frequencies up to 50 Hz the flash frequency does not affect the growth rate which is due to a complete relaxation of activated PSUs during the dark period as discussed above. However, we observe that even at low frequencies the population growth is already higher in comparison to continuous light for $\tau = 0.5$ while for lower duty cycles continuous light enables faster growth. At frequencies above 50 Hz, we observe a significant increase of the population growth rate at all duty cycles. This is consistent with the observation that under these conditions the dark period is too short for relaxing all activated PSUs. Similar effects were also observed at other single lamp intensities up to $500\ \mu\mathrm{E\,m^{-2}\,s^{-1}}$. The simulation also shows that the duty cycle plays a minor role at very high flash frequencies. Fig. 5d shows the effect of the flash frequency and the biomass concentration on the relative population growth rate in the reactor for single light intensity $I_0 = 200\ \mu\mathrm{E\,m^{-2}\,s^{-1}}$, duty cycle $\tau = 0.2$ and gas superficial velocity $u_g = 8.5$ mm/s. It can be seen that the enhancement of the culture growth correlates with the biomass concentration. Recalling the inverse relation of flash amplitude and duty cycle, this effect is probably related to the increased light penetration depth during the flashes in comparison to continuous illumination. However, in order to prevent confusion it should be emphasized that this is a relative effect and the absolute growth is faster at low biomass concentration when no light limitation exists.

Our simulations show that the strategy of supplying light in high-frequent flashes seems to be superior over pneumatic mixing to achieve flashing-light effects in bubble columns. The required L/D frequencies can hardly be reached by pneumatic mixing so that it makes sense to decouple the temporal light exposure from the pneumatic power input. The supplied energy is concentrated during the flash which increases also the light penetration depth. Moreover, the application of light flashes provides additional degrees of freedom to match the supply of light energy and the requirements of photosynthesis. In the simulated setup, the specific growth rate of the cell population increased up to a factor of 2.5 if the flashing conditions are chosen properly. The simulations also confirm the presumptions of Schulze et al. [22], namely that high frequency light flashes act twofold on the kinetics of photosynthesis: firstly by preventing the complete relaxation of activated PSUs and secondly due to the concentration of light energy during the flash by supplying light energy to cells which would be located in the dark under continuous illumination.

3.4. Discussion

The results of this work are valid only for the simulated setup and under the presumption that the parametrized growth model is valid for *Chlamydomonas*. With regard to the results presented in Section 3.3.2 (see Fig. 4), we like to mention that the simulated maximum gas superficial velocity ($u_G = 1.28$ cm/s) corresponds to a gas flow rate of 1.925 vvm which is already high for several species of microalgae in air-agitated cultures. In addition, the column diameter is only 5 cm, so that our results can be considered to include a best-case scenario for a cylindrical PBR. This makes clear that the realization of flashing-light effects by pneumatic mixing is far from reality. Further increase of the pneumatic power input will increase the operation costs while at the same time it may cause additional problems as it is known that several algae species are sensitive to shear stress [19]. Therefore it is questionable if flow induced cycling between the light and dark region of the reactor is a realistic strategy to improve photobioreactor operation, at least for organisms whose kinetics of photosynthesis are comparable to our simulations. In contrast, for some species it is reported that significant improvement of growth was observed under conditions where just low frequency L/D cycles can be expected [17]. In experiments, however, it is hard to consider all the impacts of the pneumatic power input on other growth determinants like mass transfer of carbon dioxide and oxygen, shear stress, cell sedimentation or the attachment of cells to the reactor walls. One of the major benefits of numerical simulations is that single effects can be isolated, while it is not easy in experiments. Therefore, a direct and non-biased comparison of pneumatic mixing and pulsed light with respect to their ability to enhance photosynthesis via the flashing-light effect becomes possible.

Therefore, the determination of the kinetics of photosynthesis for different species and the utilization of model-based process design might be a key for further improvement of photobioreactor operation. The photosynthetic factory models provide an accepted framework for this purpose although also other models are available [6]. The illumination of a PBR with flashing light sources might be an option to realize flashing-light effects and to overcome the limitations accompanied with pneumatic mixing. At this point we emphasize that all results were based on the evaluation of single cells moving through the flashing light field, thus, under consideration of a light gradient being present in

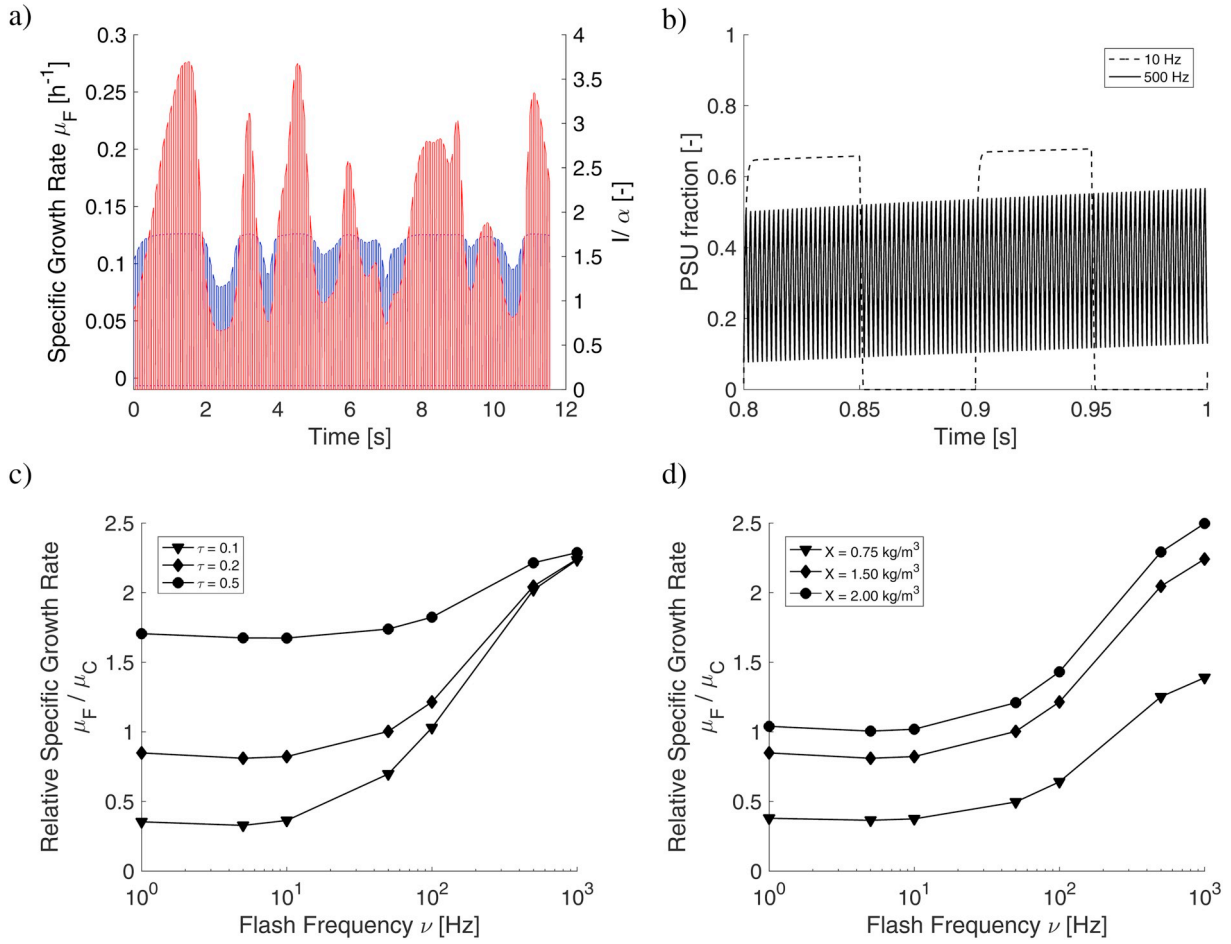

Fig. 5. Dynamics of photosynthesis under flashing illumination at u_G = 8.5 mm/s, X = 2 kg m^{-3}, I_0 = 200 μE s^{-1} m^{-2}. a) Time course of the received dimensionless light intensity (red) and specific growth rate (blue) of a randomly chosen particle at ν = 10 Hz, τ = 0.5. b) Effect of the flash frequency on the amount of activated PSU in a cell moving along a similar trajectory. The duty cycle is set to τ = 0.5. c) Effect of flash frequency and duty cycle on the relative population average growth rate. Indices denote flashing (F) and continuous (C). d) Effect of flash frequency and biomass concentration on the population average growth rate. (For interpretation of the references to color in this figure legend, the reader is referred to the web version of this article.)

every PBR. Our results are in principal agreement with other researchers who predicted significant improvement of cell growth under high-frequency light fluctuations [7,11]. Flow induced mixing is often considered to realize these conditions in PBR whereas the application of flashing LED light is a new and promising concept. However, its applicability to microalgae cultivation requires further research including to overcome technical hurdles as pointed out by Schulze et al. [22].

Interestingly, we found that longer duty cycles were more beneficial in comparison to very short ones, although in some papers the opposite is reported [4]. We like to emphasize that in this study the effect of flashing LED illumination was investigated under constant supply of light energy, leading to an inverse relation of light intensity and duty cycle. Therefore, at short duty cycles very high light intensities are provided which in turn may pronounce photoinhibition [5]. To underline this, Fig. 6 shows the simulated amount of damaged PSUs with respect to the duty cycle. Clearly at short duty cycle photoinhibition is stronger which in turn lowers the overall growth rate. It can also be seen that the amount of damaged PSUs becomes minimal and independent from the duty cycle at highest flash frequencies. This is in accordance to the observation that under high frequency flashes the growth enhancement is not much affected by the duty cycle as it is depicted in Fig. 5b. Thus, photoinhibition seems to be an important aspect which needs to be considered when operating flashing light sources. On the contrary, short duty cycles may be beneficial when flashing light is applied for light integration, meaning that the rate of photosynthesis under flashing light is similar as under continuous illumination of the *same* light intensity, as in the work of Vejrazka et al. [4]. This slight but important difference illustrates that a careful

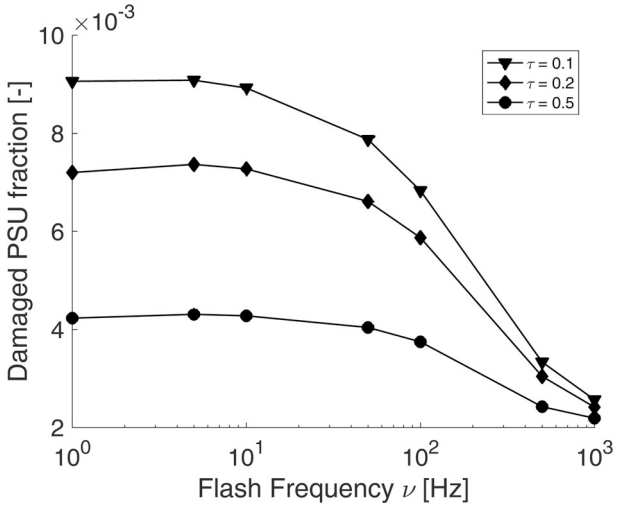

Fig. 6. Effect of frequency and duty cycle on photoinhibition under flashing illumination. Operating conditions are u_G = 8.5 mm/s, X = 1.75 kg m^{-3}, I_0 = 200 μE s^{-1} m^{-2}.

interpretation of experimental outcomes is required in order to design flashing illumination sources properly.

4. Conclusions

In this study the suitability of pneumatic mixing and flashing LED illumination to realize flashing-light effects in a bubble column PBR was evaluated by means of numerical simulations. For this purpose, a robust numerical tool was built based on state-of-the art models for multiphase flow, light propagation and reaction kinetics. The comprehensive numerical model enabled the simulation of photobioreactor operation under flashing illumination and the direct comparison of the enhancement of culture growth by pulsed illumination and pneumatic mixing.

The results showed that pneumatic mixing at different usual gas superficial velocities did not enhance the observed cell growth at all, which is due to the fast relaxation of activated PSUs. In contrast, illumination with flashing LED might be a good and flexible option to enhance the PBR productivity. Thereby, the operating conditions of the flashing light sources should be carefully chosen to prevent photoinhibition which counteracts the benefits of light flashes.

Acknowledgements

This work was funded by the Federal Ministry of Education and Research [BMBF 03SF0457]. The authors gratefully acknowledge the support.

Declaration of authors' contribution

GL and CM designed the study and wrote the manuscript. GL developed the multiphase flow model, performed flow simulations and related data analysis. CM performed simulations of light transfer and cell growth kinetics, realized the coupling of all models and performed the subsequent data analysis of flashing light effects. CL, CR and AD critically revised the manuscript and improved the intellectual content. Funding was obtained by AD. All authors have read and approved the final manuscript.

Declaration of conflict of interests

The authors declare no conflict of interests.

Statement of informed consent, human/animal rights

No conflicts, informed consent, human or animal rights applicable.

References

[1] L. Fatemeh, D. Mohsen, Effects of environmental factors on the growth, optical density and biomass of the green algae *Chlorella Vulgaris* in outdoor conditions, J. Appl. Sci. Environ. Manag. 20 (2016) 133.
[2] A. Juneja, R. Ceballos, G. Murthy, Effects of environmental factors and nutrient availability on the biochemical composition of algae for biofuels production: a review, Energies 6 (2013) 4607–4638.
[3] K.L. Terry, Photosynthesis in modulated light: quantitative dependence of photosynthetic enhancement on flashing rate, Biotechnol. Bioeng. 28 (1986) 988–995.
[4] C. Vejrazka, M. Janssen, G. Benvenuti, M. Streefland, R.H. Wijffels, Photosynthetic efficiency and oxygen evolution of *Chlamydomonas reinhardtii* under continuous and flashing light, Appl. Microbiol. Biotechnol. 97 (2013) 1523–1532.
[5] E. Sforza, D. Simionato, G.M. Giacometti, A. Bertucco, T. Morosinotto, Adjusted light and dark cycles can optimize photosynthetic efficiency in algae growing in photobioreactors, PLoS One 7 (2012) e38975.
[6] C. Vejrazka, M. Streefland, R.H. Wijffels, M. Janssen, The role of an electron pool in algal photosynthesis during sub-second light–dark cycling, Algal Res. 12 (2015) 43–51.
[7] P. Hartmann, Effect of Hydrodynamics on Light Utilization in Large Scale Cultures of Microalgae, (2015).
[8] M. Cuaresma, M. Janssen, C. Vílchez, R.H. Wijffels, Productivity of *Chlorella sorokiniana* in a short light-path (SLP) panel photobioreactor under high irradiance, Biotechnol. Bioeng. 104 (2009) 352–359.
[9] H. Qiang, Y. Zarmi, A. Richmond, Combined effects of light intensity, light-path and culture density on output rate of *Spirulina platensis* (cyanobacteria), Eur. J. Phycol. 33 (1998) 165–171.
[10] M. Janssen, P. Slenders, J. Tramper, L.R. Mur, R. Wijffels, Photosynthetic efficiency of *Dunaliella tertiolecta* under short light/dark cycles, Enzym. Microb. Technol. 29 (2001) 298–305.
[11] E. Greenwald, J.M. Gordon, Y. Zarmi, Physics of ultra-high bioproductivity in algal photobioreactors, Appl. Phys. Lett. 100 (2012) 143703.
[12] Y. Zarmi, G. Bel, C. Aflalo, Theoretical analysis of culture growth in flat-plate bioreactors: the essential role of timescales, Handb. Microalgal Cult, John Wiley & Sons, Ltd, Oxford, UK, 2013, pp. 205–224.
[13] Z. Dubinsky, P.G. Falkowski, K. Wyman, Light harvesting and utilization by phytoplankton, Plant Cell Physiol. 27 (1986) 1335–1349.
[14] G. Olivieri, L. Gargiulo, P. Lettieri, L. Mazzei, P. Salatino, A. Marzocchella, Photobioreactors for microalgal cultures: a Lagrangian model coupling hydrodynamics and kinetics, Biotechnol. Prog. 31 (2015) 1259–1272.
[15] A.M.J. Kliphuis, L. de Winter, C. Vejrazka, D.E. Martens, M. Janssen, R.H. Wijffels, Photosynthetic efficiency of *Chlorella sorokiniana* in a turbulently mixed short light-path photobioreactor, Biotechnol. Prog. 26 (2010) 687–696.
[16] J.-W.F. Zijffers, K.J. Schippers, K. Zheng, M. Janssen, J. Tramper, R.H. Wijffels, Maximum photosynthetic yield of green microalgae in photobioreactors, Mar. Biotechnol. 12 (2010) 708–718.
[17] A.S. Mirón, M.C.C. García, A.C. Gómez, F.G. Camacho, E.M. Grima, Y. Chisti, Shear stress tolerance and biochemical characterization of *Phaeodactylum tricornutum* in quasi steady-state continuous culture in outdoor photobioreactors, Biochem. Eng. J. 16 (2003) 287–297.
[18] X. Gao, B. Kong, R.D. Vigil, Multiphysics simulation of algal growth in an airlift photobioreactor: effects of fluid mixing and shear stress, Bioresour. Technol. 251 (2018) 75–83.
[19] M.H.A. Michels, A.J. van der Goot, M.H. Vermuë, R.H. Wijffels, Cultivation of shear stress sensitive and tolerant microalgal species in a tubular photobioreactor equipped with a centrifugal pump, J. Appl. Phycol. 28 (2016) 53–62.
[20] X. Wu, J.C. Merchuk, Simulation of algae growth in a bench-scale bubble column reactor, Biotechnol. Bioeng. 80 (2002) 156–168.
[21] S. Abu-Ghosh, D. Fixler, Z. Dubinsky, D. Iluz, Flashing light in microalgae biotechnology, Bioresour. Technol. 203 (2016) 357–363.
[22] P.S.C. Schulze, R. Guerra, H. Pereira, L.M. Schüler, J.C.S. Varela, Flashing LEDs for microalgal production, Trends Biotechnol. 35 (2017) 1088–1101.
[23] K.-H. Park, C.-G. Lee, Optimization of algal photobioreactors using flashing lights, Biotechnol. Bioprocess Eng. 5 (2000) 186–190.
[24] A.A. Lunka, D.J. Bayless, Effects of flashing light-emitting diodes on algal biomass productivity, J. Appl. Phycol. 25 (2013) 1679–1685.
[25] F. Krujatz, R. Illing, T. Krautwer, J. Liao, K. Helbig, K. Goy, J. Opitz, G. Cuniberti, T. Bley, J. Weber, Light-field-characterization in a continuous hydrogen-producing photobioreactor by optical simulation and computational fluid dynamics, Biotechnol. Bioeng. 112 (2015) 2439–2449.
[26] I. Perner-Nochta, C. Posten, Simulations of light intensity variation in photobioreactors, J. Biotechnol. 131 (2007) 276–285.
[27] H.-P. Luo, A. Kemoun, M.H. Al-Dahhan, J.M.F. Sevilla, J.L.G. Sánchez, F.G. Camacho, E.M. Grima, Analysis of photobioreactors for culturing high-value microalgae and cyanobacteria via an advanced diagnostic technique: CARPT, Chem. Eng. Sci. 58 (2003) 2519–2527.
[28] J.S. Marshall, K. Sala, A stochastic Lagrangian approach for simulating the effect of turbulent mixing on algae growth rate in a photobioreactor, Chem. Eng. Sci. 66 (2011) 384–392.
[29] A.A. Kulkarni, J.B. Joshi, Measurement of eddy diffusivity in bubble column and validation based on the intermittency models, Chem. Eng. Sci. 60 (2005) 6146–6159.
[30] R.F. Mudde, O. Simonin, Two- and three-dimensional simulations of a bubble plume using a two-fluid model, Chem. Eng. Sci. 54 (1999) 5061–5069.
[31] D. Pfleger, S. Gomes, N. Gilbert, H. Wagner, Hydrodynamic simulations of laboratory scale bubble columns fundamental studies of the Eulerian} Eulerian modelling approach, Chem. Eng. Sci. 54 (1999) 5091–5099.
[32] E. Delnoij, F.A. Lammers, J.A.M. Kuipers, W.P.M. van Swaaij, Dynamic simulation of dispersed gas-liquid two-phase flow using a discrete bubble model, Chem. Eng. Sci. 52 (1997) 1429–1458.
[33] A. Sokolichin, G. Eigenberger, Applicability of the standard k–ε turbulence model to the dynamic simulation of bubble columns: part I. detailed numerical simulations, Chem. Eng. Sci. 54 (1999) 2273–2284.
[34] M.D. Ooms, P.J. Graham, B. Nguyen, E.H. Sargent, D. Sinton, Light dilution via wavelength management for efficient high-density photobioreactors, Biotechnol. Bioeng. 114 (2017) 1160–1169.
[35] B. Kong, R.D. Vigil, Simulation of photosynthetically active radiation distribution in algal photobioreactors using a multidimensional spectral radiation model, Bioresour. Technol. 158 (2014) 141–148.
[36] C. McHardy, T. Horneber, C. Rauh, New lattice Boltzmann method for the simulation of three-dimensional radiation transfer in turbid media, Opt. Express 24 (2016).
[37] C. McHardy, T. Horneber, C. Rauh, Spectral simulation of light propagation in participating media by using a lattice Boltzmann method for photons, Appl. Math. Comput. 319 (2018) 59–70.
[38] P.H.C. Eilers, J.C.H. Peeters, A model for the relationship between light intensity and the rate of photosynthesis in phytoplankton, Ecol. Model. 42 (1988) 199–215.
[39] X. Wu, J.C. Merchuk, A model integrating fluid dynamics in photosynthesis and photoinhibition processes, Chem. Eng. Sci. 56 (2001) 3527–3538.
[40] F.C. Rubio, F.G. Camacho, J.M.F. Sevilla, Y. Chisti, E.M. Grima, A mechanistic

model of photosynthesis in microalgae, Biotechnol. Bioeng. 81 (2003) 459–473.
[41] F. García-Camacho, A. Sánchez-Mirón, E. Molina-Grima, F. Camacho-Rubio, J.C. Merchuck, A mechanistic model of photosynthesis in microalgae including photoacclimation dynamics, J. Theor. Biol. 304 (2012) 1–15.
[42] Q. Béchet, A. Shilton, B. Guieysse, Modeling the effects of light and temperature on algae growth: state of the art and critical assessment for productivity prediction during outdoor cultivation, Biotechnol. Adv. 31 (2013) 1648–1663.
[43] C. McHardy, G. Luzi, C. Lindenberger, J.R. Agudo, A. Delgado, C. Rauh, Numerical analysis of the effects of air on light distribution in a bubble column photobioreactor, Algal Res. 31 (2018) 311–325.
[44] N.G. Deen, T. Solberg, B.H. Hjertager, Large eddy simulation of the gas–liquid flow in a square cross-sectioned bubble column, Chem. Eng. Sci. 56 (2001) 6341–6349.
[45] C. McHardy, G. Luzi, J.R. Agudo, A. Delgado, C. Rauh, Hybrid numerical simulation of fluid flow and light distribution in a bubble column photobioreactor, Proc. 5th Int. Conf. Photonics, Opt. Laser Technol. 2017, pp. 304–311.
[46] G. Luzi, C. McHardy, J.R. Agudo, C. Rauh, Influence of fluid flow and light distribution on single cells in a bubble column photobioreactor, Proc. 14th Int. Conf. Multiph. Flow Ind. Plants, Desenzano, 2017.
[47] R. Clift, J.R. Grace, M.E. Weber, Bubbles, Drops, and Particles, (1978).
[48] M. Ishii, N. Zuber, Drag coefficient and relative velocity in bubbly, droplet or particulate flows, AICHE J. 25 (1979) 843–855.
[49] D. Legendre, J. Magnaudet, The lift force on a spherical bubble in a viscous linear shear flow, J. Fluid Mech. 368 (1998) 81–126.
[50] T. Frank, P.J. Zwart, E. Krepper, H.-M. Prasser, D. Lucas, Validation of CFD models for mono- and polydisperse air–water two-phase flows in pipes, Nucl. Eng. Des. 238 (2008) 647–659.
[51] A.D. Burns, T. Frank, I. Hamill, J.M. Shi, The Favre averaged drag model for turbulent dispersion in Eulerian multi-phase flows, 5th Int. Conf. Multiph. Flow, 2004, pp. 1–17.
[52] F.R. Menter, 2-Equation eddy-visocity turbulence models for engineering applications, AIAA J. 32 (1994) 1598–1605.
[53] ANSYS CFX-solver theory guide, ANSYS CFX Release. 15317, (2009), pp. 724–746.
[54] L. Schiller, A.Z. Naumann, Über die grundlegenden Berechnungen bei der Schwerkraftaufbereitung, Ver. Dtsch. Ing. 77 (1933) 318–320.
[55] Y.T. Shah, B.G. Kelkar, S.P. Godbole, W.-D. Deckwer, Design parameters estimations for bubble column reactors, AICHE J. 28 (1982) 353–379.
[56] S. Jung, J. Hahm, G. Luzi, R. Buchholz, C. Lindenberger, Prediction method of scale-dependent growth characteristics of *A. platensis*, Theor. Appl. Chem. Eng. 23 (2017) 2505–2508.
[57] R. Kandilian, J. Pruvost, A. Artu, C. Lemasson, J. Legrand, L. Pilon, Comparison of experimentally and theoretically determined radiation characteristics of photosynthetic microorganisms, J. Quant. Spectrosc. Radiat. Transf. 175 (2016) 30–45.
[58] H. Takache, J. Pruvost, J.-F. Cornet, Kinetic modeling of the photosynthetic growth of *Chlamydomonas reinhardtii* in a photobioreactor, Biotechnol. Prog. 28 (2012) 681–692.
[59] P.J. Graham, B. Nguyen, T. Burdyny, D. Sinton, A penalty on photosynthetic growth in fluctuating light, Sci. Rep. 7 (2017) 12513.

Part III.

Discussion and Conclusions

9. Discussion of the lattice Boltzmann model for light transfer

Since the first publication of the developed lattice Boltzmann model for light transfer (see chapter 5), several adjustments and extensions of the model have been developed in order to improve its numerical accuracy. These improvements have been steadily applied to the subsequent model applications (chapters 6 - 8), though, in consideration of the respective target readership not all numerical details were explicitly mentioned whereas a comprehensive picture of the numerical method shall be drawn in this work. Therefore, the undergone improvements will be outlined in this section followed by a brief discussion on outstanding issues and research needs.

9.1. Model features and improvements

9.1.1. Revised derivation of the lattice Boltzmann model

In order to provide a basis for the discussion of the lattice Boltzmann model, first a brief revision of its derivation is outlined. The starting point is the Radiation transfer equation, Eq. (3.10), which is repeated here for the readers convenience.

$$\frac{\partial L}{c\partial t} + \boldsymbol{n}\nabla L = \mu_s \left(-L + \frac{1}{4\pi} \int_{4\pi} \Phi L' \mathrm{d}\boldsymbol{\Omega'} \right) - \mu_a L \tag{9.1}$$

Introducing the discrete photon density distribution $f_i = w_i L(\boldsymbol{x}, \boldsymbol{n}_i, t)$ with the corresponding weighting coefficient w_i yields the discrete velocity radiation transfer equation.

$$\frac{\partial f_i}{c\partial t} + \boldsymbol{n}_i \nabla f_i = \mu_s \left(-f_i + w_i \sum_{j=1}^{Q} \Phi_{i,j} f_j \right) - \mu_a f_i \tag{9.2}$$

In order to account for the connectivities in a cubic lattice, the discrete vectors $\boldsymbol{n}_i$ are chosen in such a way that they point from one node into the direction of its adjacent nodes. Since photons can be considered as point-like particles with similar speed c (see 4.1.2), the endpoints of the discrete velocity vectors $c\boldsymbol{n}_i$ are located on a spherical shell. As outlined in chapter 5, the Lebedev quadrature ensures the exact integration of the discrete velocity moments for such a set of abscissas. Applying the Method

of Characteristics for the integration of Eq. (9.2) along a characteristic $c\boldsymbol{n}_i$ results in a fully discretized phase space, in which the model equation reads

$$f_i(\boldsymbol{x}, \boldsymbol{x} + c\boldsymbol{n}_i\Delta t, t + \Delta t) - f_i(\boldsymbol{x}, t) = c\mu_s\Delta t \left(-f_i + w_i \sum_{j=1}^{Q} \Phi_{i,j} f_j \right) - c\mu_a \Delta t f_i \tag{9.3}$$

While the left-hand side is exact, the first order forward Euler scheme was utilized for the time integration of the right-hand side. This formulation is equal to Eq. (16) in chapter 5. However, deviating from the derivation of Eq. (17) therein, the improved lattice Boltzmann model is outlined now.

According to Eq. (9.3), the spherical shell on which the discrete particles are located after a time interval Δt has a radius of $c\Delta t$. A general relation between the shell radius and the grid spacing Δx is

$$c\Delta t = C\Delta x \tag{9.4}$$

where C is a dimensionless parameter known as the Courant number. Without loss of generality, figure 9.1 shows a simplified two-dimensional representation of three possible cases for relation (9.4) being $C = 1$, $C < 1$ and $C > 1$. In case of $C = 1$, discrete photons which propagate along the major coordinate axis are located on a lattice node at time $t + \Delta t$, while particles propagating in other directions do not reach the next lattice node. Because the perfect shift of discrete particles from nodes to their neighbors is a major characteristic of the lattice Boltzmann method, an additional extrapolation step is required to shift the off-lattice populations to the nearest node of the lattice. Similarly, this applies for all discrete photon populations in case of $C < 1$, see figure 9.1. On the contrary, in case of $C > 1$ some or all of the discrete particles are shifted to locations further away from their origin as the nearest lattice node. In order to map these discrete particles on the lattice, an additional interpolation step is required. Therefore, interpolation or extrapolation is required for any value of C to map some or all of the discrete particle populations to the lattice. In the following, it will be shown that both, the interpolation and extrapolation lead to a similar model equation.

It is important to recall that the radiation transfer equation is a linear variant of the Boltzmann equation without interaction of radiance. Accordingly, the propagation of radiation is not affected by its surrounding and one dimensional linear interpolation along the discrete characteristic is possible. A more general formulation of (9.3) is

$$f_i(\boldsymbol{x}, \boldsymbol{x} + c\boldsymbol{n}_i\Delta t, t + \Delta t) = f_i(\boldsymbol{x}, t) + k_i c\Delta t \tag{9.5}$$

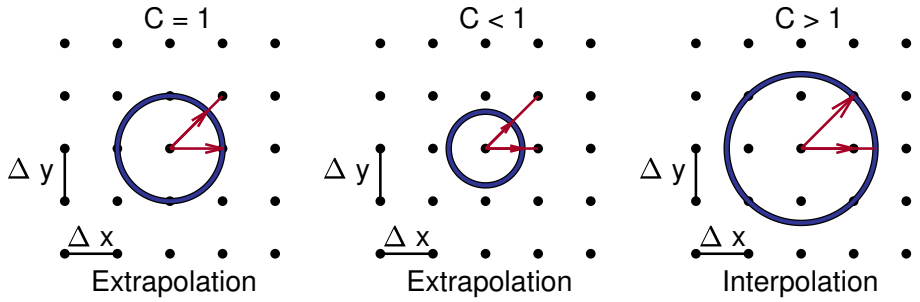

Figure 9.1.: Schematic definition of the Courant number C in the lattice Boltzmann model. The distance $c\Delta t$ which photons propagate within one time step is indicated by the circular shell being centered at the origin of propagation. The red arrows indicate the discrete velocity vectors. An interpolation or extrapolation step is required to map the off-lattice photon populations to the next lattice node depending on the chosen Courant number.

where the slope k_i is given by

$$k_i = \mu_s \left(-f_i(\boldsymbol{x}, t) + w_i \sum_{j=1}^{Q} \Phi_{i,j} f_j(\boldsymbol{x}, t) \right) - \mu_a f_i(\boldsymbol{x}, t) \tag{9.6}$$

Introducing the lattice speed $c_i = (\Delta x_i^2 + \Delta y_i^2 + \Delta z_i^2)^{0.5} \Delta t^{-1}$ for each discrete particle population enables to perform the linear extrapolation the spherical shell to the next lattice node. Eq. (9.5) becomes thus

$$f_i(\boldsymbol{x}, \boldsymbol{x} + c_i \boldsymbol{n}_i \Delta t, t + \Delta t) = f_i(\boldsymbol{x}, t) + k_i c \Delta t \frac{c_i}{c} = f_i(\boldsymbol{x}, t) + k_i c_i \Delta t \tag{9.7}$$

The linear interpolation step can be carried out in a similar way and leads to the same result. With the new discrete velocity $\boldsymbol{c_i} = c_i \boldsymbol{n_i}$, the final lattice Boltzmann model equation for radiation transfer reads

$$f_i(\boldsymbol{x}, \boldsymbol{x} + \boldsymbol{c}_i \Delta t, t + \Delta t) - f_i(\boldsymbol{x}, t) = c_i \mu_s \Delta t \left(-f_i + w_i \sum_{j=1}^{Q} \Phi_{i,j} f_j \right) - c_i \mu_a \Delta t f_i \tag{9.8}$$

The model gives stable results if $f_i(\boldsymbol{x}, \boldsymbol{x} + \boldsymbol{c}_i \Delta t, t + \Delta t) > 0$. To get the stability condition Eq. (9.8) can be rearranged to the expression

$$f_i(\boldsymbol{x}, \boldsymbol{x} + \boldsymbol{c}_i \Delta t, t + \Delta t) = f_i \left(1 - c_i \Delta t (\mu_s + \mu_a)\right) + w_i \sum_{j=1}^{Q} \Phi_{i,j} f_j \tag{9.9}$$

The in-scattering term is always positive as long $f_j > 0$ so that the stability is determined by the first term of the RHS. The limiting case for the $D3Q26$ model is given by $c_{i,max} = \sqrt{3} \Delta x \Delta t^{-1}$ so that the method is always stable if the condition

$$\Delta x (\mu_s + \mu_a) \leq \frac{1}{\sqrt{3}} \tag{9.10}$$

Table 9.1.: Radiation characteristics of participating media in terms of physical transport coefficients, optical depth τ and single scattering albedo ω. The characteristic length of the domain is $L_0 = 1$ m and the Knudsen number is defined as $Kn = l_{tr}/L_0 = (\mu_s' L_0)^{-1}$.

Medium	μ_a [m^{-1}]	μ_s [m^{-1}]	g [-]	τ [-]	ω [-]	Kn [-]
1	0	10	0	10	1	0.100
2	3	7	0	10	0.7	0.143
3	0	30	0	30	1	0.033
4	10	20	0	30	0.667	0.050

is fulfilled. Therefore, the stability of the model is determined by the grid resolution for a given set of transport coefficients.

In order to test the revised model, radiation transfer in a cubic domain with collimated illumination is considered. The test case is similar to the one studied in chapter 5, see figure 5 therein. For the test of the model, four different participating media with radiation characteristics as listed in table 9.1 are defined. As a reference, Monte Carlo simulations are performed similarly to chapter 5, each with $N_{ph} = 10^8$ photon tracks in total. Figure 9.2 reports the results obtained by lattice Boltzmann simulations in comparison to the respective Monte Carlo solution. In the purely scattering media 1 and 3, the transport regime is mainly diffusive ($Kn \ll 1$, see table 9.1). It can be seen that the agreement between both methods is fairly well in these cases, also in parts of the domain where the illumination occurs only indirectly by scattering (see lines L_{y2}, L_{y3} and L_{y4}). This conclusions is also supported by the contours of light intensity as depicted in figure 9.3.

Regarding the results in medium 2, one observes good agreement between both methods for the intensity profile along the center line (L_{y1}). In other parts of the domain, the lattice Boltzmann solution has the correct order of magnitude but discontinuities can be observed along lines L_{y3} and L_{y4}. Under the conditions of medium 2, the equilibration of radiance is counteracted by absorption (see 3.3.5) so that the radiative flux remains mainly directed. This means that radiance propagates preferentially along rays and the angular discretization affects the solution more significantly. The issue becomes visible in figure 9.3 depicting contours of the simulated intensity in medium 1 and 2. In medium 2 one clearly observes rays in the solution at angles $\pi/4$ and $\pi/2$ measured from the surface normal. These angles correspond to the discrete velocities in the depicted plane. It is therefore likely that the observed artifacts result from the relatively coarse velocity discretization in lattice Boltzmann method with just 26 abscissas[1]. The effect becomes predominantly visible when the distribution of radiation in the domain occurs indirectly by scattering as for the here considered small light source. In case of larger sources, the artifact is compensated by the superposition of emitted light.

In medium 4 one observes also slight discontinuities in the solution but to a less extend as in medium 2, which is due to the higher level of scattering. However, the agreement between the lattice Boltzmann

[1] In the Discrete Ordinate method angular quadratures with more than 1000 abscissas are known [218].

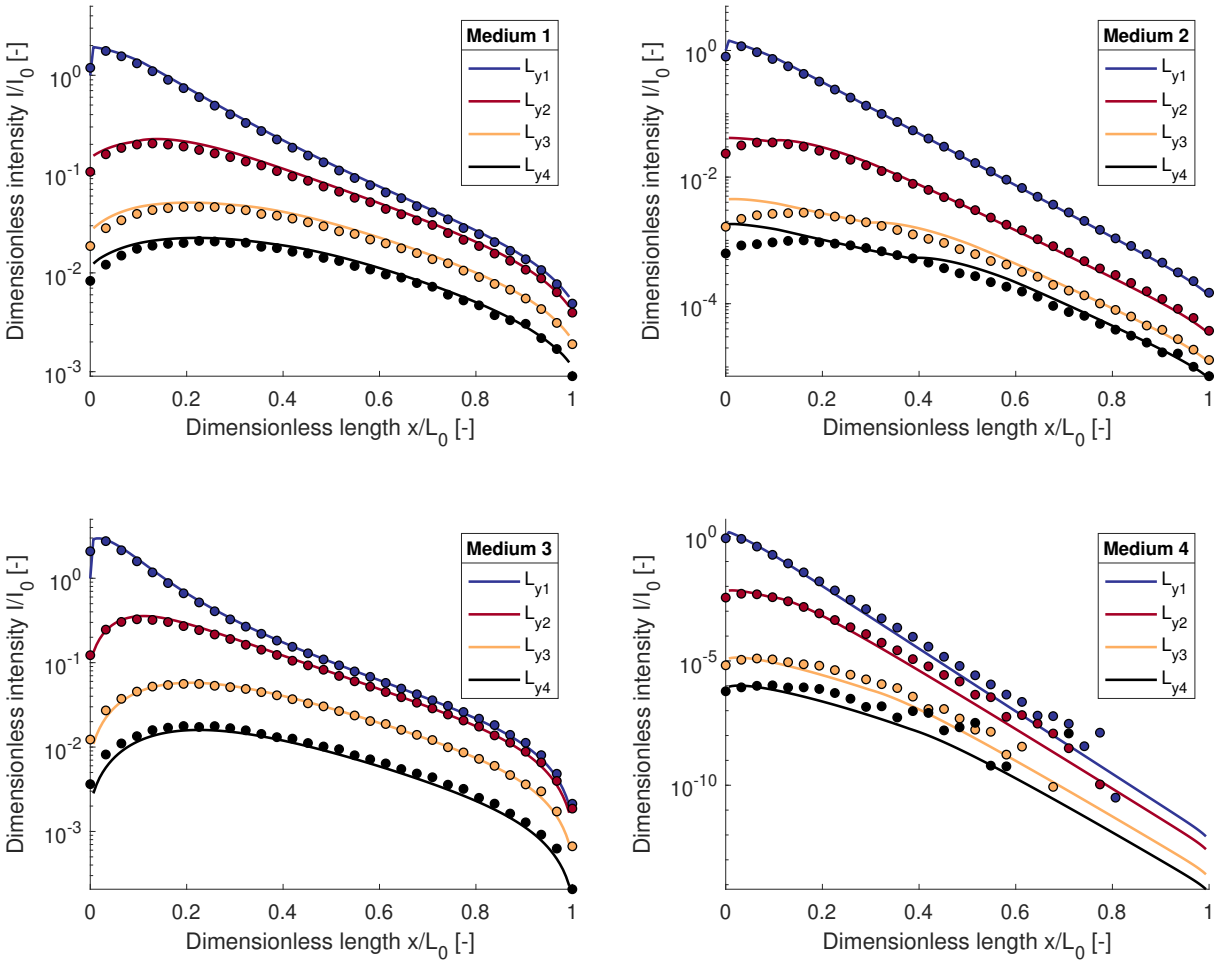

Figure 9.2.: Comparison of lattice Boltzmann (lines) and Monte Carlo (symbols) simulations in different participating test media as defined in table 9.1. The grid for the lattice Boltzmann simulation is composed of $N = 155^3$ nodes for all test cases. For the Monte Carlo simulations 10^8 photons were traced. Top left: medium 1; top right: medium 2; bottom left: medium 3; bottom right: medium 4. Note the different scaling of the respective y-axis.

and the Monte Carlo solution is not perfect, even at the center line L_{y1}. It should be noticed that the reliability of Monte Carlo results is no longer given for intensities $I/I_0 < 10^{-7}$ where the results become noisy. However, it can be seen that the lattice Boltzmann method underestimates the intensity, or in other words overestimates absorption, what is related to the utilization of the first order forward Euler scheme for the discretization of Eq. (9.3). This conclusion is substantiated by simulations on different grid refinement levels which show that very fine grid resolutions are required to obtain correct results in strongly absorbing media.

In conclusion, the revised lattice Boltzmann model is able to provide similar solutions as the Monte Carlo method in the diffusive regime. This also includes the transition from ballistic to diffusive transport as it occurs in the present test cases. In absorbing media the discretization of the velocity space affects the solution in case of small light sources. However, with regard to the results in chapters 6 - 8 it should be stated that the error due to the velocity discretization is compensated by the superposition of

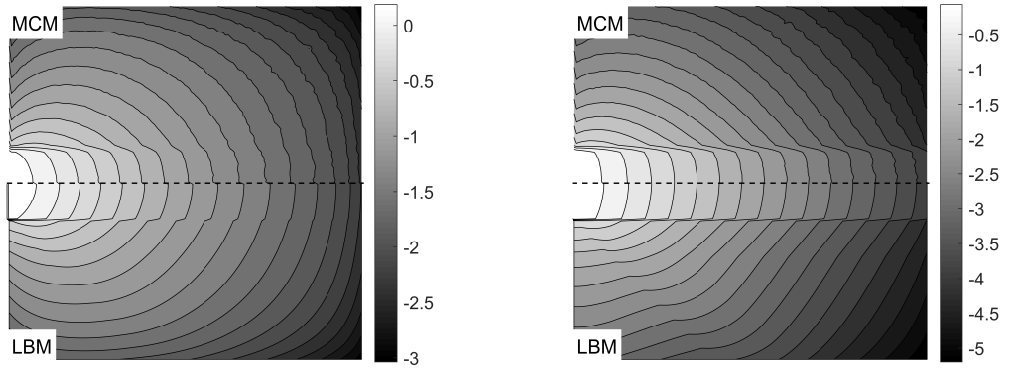

Figure 9.3.: Contour plots of the radiative intensity on plane P_{z1} (see chapter 5, figure 5) for medium 1 (left) and medium 2 (right) obtained with the lattice Boltzmann method (LBM) and the Monte Carlo method (MCM). The greyscale denotes for the logarithmic intensity value.

light emitted from different sources. Regarding the required spatial discretization it can be concluded that scattering can be accurately resolved on coarser grids, while absorption needs a finer resolution due to the utilized time integration scheme. An approach to improve this issue will be presented in the next section. Another potential improvement of the method lies in the adjustment of the transport coefficients, which will be discussed in section 9.1.3.

9.1.2. Time integration and improved convergence

In chapter 6 it was shown that the lattice Boltzmann model converges at a rate of first order, see section 3.2 therein. Moreover, in the previous section it turned out that the resolution of the absorption term requires fine numerical grids, which was also discussed in chapter 5. In contrast, classical lattice Boltzmann schemes and also Mink's macroscopic model for radiative transfer [272] are characterized by second order convergence rates due to the diffuse scaling of the transport coefficients, see Eq. (4.18) in section 4.2 and section 4.3.3.

Differing from usual lattice Boltzmann models, the target equation for the present method is mesoscopic. Due to the acoustic scaling of the transport coefficients, the convergence rate is determined by the forward Euler scheme, which is combined with the Method of Characteristics to solve the initial value problem given by the time integration of Eq. (9.2), see 9.1.1. A promising approach to improve the accuracy and convergence of the lattice Boltzmann model is to combine the Method of Characteristics with a higher order scheme for the time integration. Higher order extensions of the Euler scheme are known as Runge-Kutta methods. The basic concept behind these schemes is to construct a quadrature with one or more fix points within the time interval Δt at which the integrand is additionally evaluated. The integral with bounds t and $t+\Delta t$ is then approximated as the sum of the weighted function evaluations at these fix points by what the numerical representation of the integral becomes more

accurate [275]. With regard to Eq. (9.5) this procedure corresponds to a more accurate approximation of the slope coefficients k_i.

The simplest extension of the forward Euler scheme is Heun's method, where the integral of interest is approximated by the trapezoidal rule. The scheme requires two evaluations of any function y at times t and $t + \Delta t$ respectively, from which the slope coefficients k_i are computed. In the present model, the function y represents Eq. (9.6). The Heun scheme reads

$$\begin{aligned} k_i^I &= y(t, f_i^0) \\ k_i^{II} &= y(t + \Delta t, f_i^0 + k_i^I c_i \Delta t) \\ k_i &= \frac{1}{2}\left(k_i^I + k_i^{II}\right) \end{aligned} \tag{9.11}$$

and its implementation leads to the following modified collision step of the lattice Boltzmann model:

- compute the slope coefficients k_i^I from $f_i(\boldsymbol{x}, t)$ by means of Eq. (9.6)
- compute the intermediate populations $f_i^I(\boldsymbol{x}, t + \Delta t)$ by means of (9.3) and k_i^I
- compute the slope coefficients k_i^{II} from $f_i^I(\boldsymbol{x}, t + \Delta t)$ by means of Eq. (9.6)
- compute the slope coefficients k_i from k_i^I and k_i^{II}
- compute the new populations $f_i(\boldsymbol{x}, t + \Delta t)$ by means of (9.3) and k_i

Schemes of higher order can be achieved by additional evaluations of the function y at intermediate points in time. The most common scheme is the classical fourth order Runge-Kutta (RK) scheme, which reads

$$\begin{aligned} k_i^I &= y(t, f_i^0) \\ k_i^{II} &= y(t + \Delta t/2, f_i^0 + k_i^I c_i \Delta t/2) \\ k_i^{III} &= y(t + \Delta t/2, f_i^0 + k_i^{II} c_i \Delta t/2) \\ k_i^{IV} &= y(t + \Delta t, f_i^0 + k_i^{III} c_i \Delta t) \\ k_i &= \frac{1}{6}\left(k_i^I + 2k_i^{II} + 2k_i^{III} + k_i^{IV}\right) \end{aligned} \tag{9.12}$$

The implementation of this scheme leads to a modified collision step, similar to the one for the Heun scheme, but computationally more costly because of the additional evaluations of y.

Table 9.2 compares the results for different time integration schemes in test medium 4 (see table 9.1), evaluated on plane P_{z1} (see chapter 5, figure 5). Based on the results of the previous section, medium

Table 9.2.: Simulation results for different time integration schemes in medium 4.

Euler	$N = 55^3$	$N = 76^3$	$N = 110^3$	$N = 156^3$	$N = 220^3$
Steps until convergence	155	205	279	384	530
Av. time per step [s]	0.377	1.093	3.081	8.879	22.169
Total time [s]	58.431	224.017	859.643	3409.472	11749.37
RMSE	0.029	0.026	0.018	0.020	0.017
MAPE	0.893	0.780	0.663	0.501	0.414
Heun	$N = 55^3$	$N = 76^3$	$N = 110^3$	$N = 156^3$	$N = 220^3$
Steps until convergence	137	193	269	376	523
Av. time per step [s]	0.586	1.674	4.712	13.471	63.550
Total time [s]	80.288	323.132	1267.644	5065.260	33236.73
RMSE	0.025	0.025	0.019	0.021	0.018
MAPE	0.790	0.474	0.317	0.323	0.273
Runge-Kutta	$N = 55^3$	$N = 76^3$	$N = 110^3$	$N = 156^3$	$N = 220^3$
Steps until convergence	141	195	270	377	523
Av. time per step [s]	1.006	2.865	8.025	22.867	119.539
Total time [s]	141.791	558.659	2166.671	8620.560	62518.88
RMSE	0.025	0.025	0.019	0.021	0.018
MAPE	0.367	0.336	0.281	0.298	0.265

4 was chosen for a primary comparison because of the high absorption coefficient. The complete data set for all test media is provided in Appendix A. The RMSE in table 9.2 is defined as

$$RMSE = \sqrt{\frac{1}{N}\sum_{i=1}^{N}\left(I_{LBM}(\boldsymbol{x_i}) - I_{MC}(\boldsymbol{x_i})\right)^2} \tag{9.13}$$

and the MAPE was computed as

$$MAPE = \sqrt{\frac{1}{N}\sum_{i=1}^{N}\left(\frac{I_{LBM}(\boldsymbol{x_i}) - I_{MC}(\boldsymbol{x_i})}{I_{MC}(\boldsymbol{x_i})}\right)^2} \tag{9.14}$$

The Monte Carlo solution was taken as a reference to prove that convergence is towards an independent solution. In order to take the uncertainty of the Monte Carlo solution at low intensities into account, just such locations $\boldsymbol{x_i}$ were considered for the error computation where the local dimensionless intensity exceeds a value of 10^{-7}.

It can be seen from table 9.2 that the RMSE is not much affected by the choice of the time integration method, which is due to the fact that the solution for highly absorbing media varies by several orders of magnitude (see figures 9.2 and 9.3) so that a large part of the domain contributes marginally to this error measure. In contrast, the MAPE can be significantly reduced by utilizing the Heun or RK time integration method. More precisely, it can be seen that the MAPE for the RK scheme at the lowest grid resolution is already significantly lower than for the Euler scheme at highest grid resolution, which is a remarkable improvement of the method for the simulation of highly absorbing media. The

benefit of higher order time integration schemes becomes clear by a closer evaluation of the total computation times. According to the presented results, the computation time until convergence can be reduced by more than 98 % in comparison to the reference model and at the same time, a more accurate result is achieved. However, for purely scattering media no such effect is observed (see tables A.1 and A.3 in Appendix A) and the Euler time integration yields the same results as the higher order methods. Accordingly, it can be concluded that the Euler scheme is sufficient for the discretization of the scattering term while the accuracy of the absorption term can be improved by higher order time integration methods. The convergence rate of the lattice Boltzmann method must therefore be a function of the scattering albedo ω with first order convergence in purely scattering media ($\omega = 1$).

Figure 9.4 illustrates the grid dependency and convergence behavior of the conventional and the improved lattice Boltzmann method. The error measure is the MAPE according to Eq. (9.14) with the difference that the reference solution Σ_R was calculated by means of Richardson extrapolation [276]

$$\Sigma_R = \Sigma_1 + \frac{\Sigma_1 - \Sigma_2}{r^p - 1} \tag{9.15}$$

where Σ_1 and Σ_2 stand for the obtained solutions on the grids with 220^3 and 110^3 nodes. Accordingly, the grid refinement factor is $r = 2$. The grid convergence order p was calculated separately for each test medium from the obtained solutions on the grids with 220^3, 110^3 and 55^3 nodes by means of the equation

$$p = \frac{\log\left(\frac{\phi_{23}}{\phi_{12}}\right)}{\log(r)} \tag{9.16}$$

where ϕ_{23} is the MAPE of the coarsest grid with the medium grid as a reference. In a similar way, the quantity ϕ_{12} relates the solutions on the medium grid and the finest grid. It can be seen from figure 9.4 that the model converges approximately at first order with respect to the grid spacing. As indicated by the beforehand presented results, in purely scattering media the higher order time integration scheme neither affects the magnitude of the error nor the convergence order. In contrast, if the participating medium is absorbing, the application of the higher order time stepping schemes significantly reduces the error (medium 2 and 4) and improves the convergence order (medium 4). It should be emphasized at this point that the convergence order of the improved method is still approximately one, even if the RK scheme is well known for fourth order convergence. It is likely that fourth order convergence can be reached in the limit of a purely absorbing medium since the RTE reduces to an ordinary differential equation in this case. However, the presented results show that the computation of the scattering kernel limits the order of convergence in the investigated parameter range. Therefore, a complete characterization of the convergence behavior in terms of the scattering albedo and the optical depth must be part of future work. A hypothesis is that mixed convergences will be found in consequence of fourth

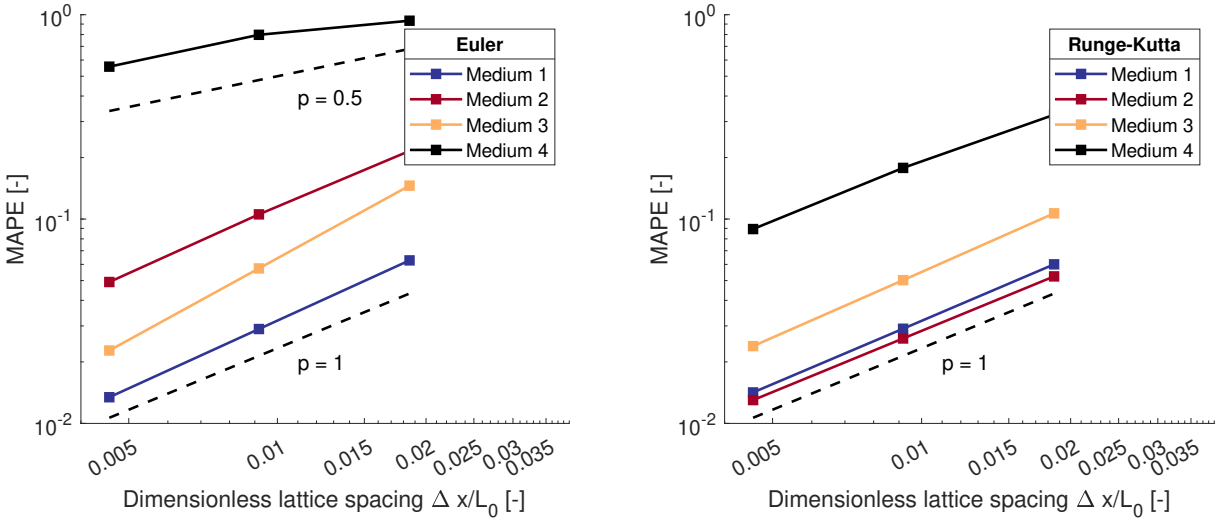

Figure 9.4.: Impact of the time integration scheme on the convergence order and the discretization error for the simulated test case in different participating test media. The radiation characteristics of the test media are defined in table 9.1. The error is measured as defined in Eq. (9.14) with the reference solution according to Eqs. (9.15) and (9.16).

order convergence of the absorption term and first order convergence of the scattering term. Mixed convergence was also observed in multistep schemes for the standard LBM [277].

9.1.3. Scaling of transport coefficients

The speed of light is a constant in the model and therefore the time step Δt is linearly related to the grid spacing Δx. This means that in consequence of a grid refinement, the degree of light-matter interaction decreases, and for infinite small grid spacing it holds that

$$\lim_{\Delta x \to 0} c_i \mu_s \Delta t = 0. \tag{9.17}$$

This behavior of the model is a potential source of inaccuracy since it is known from the standard lattice Boltzmann model for fluid flows that the value of the collision frequency should be in the same order of magnitude as the numerical time step [252]. Applied to the present model, this means that the expression $c_i \mu_s \Delta t$ should be of order 1 for all grid sizes so that a significant fraction of the discrete particle populations collide within each time step. In order to fulfill this condition, the physical scattering and absorption coefficients need to be rescaled. In this section a framework for this purpose will the introduced, tested and discussed.

The basis for the scaling of the transport coefficients is provided by the similarity relations of radiative transfer (see section 3.3.2). A prerequisite is thereby that the physical transport problem remains unchanged by the scaling procedure. In the standard LBM for flow problems, this is ensured by keeping the Reynolds number of the scaled problem similar to the one of the physical problem. The similarity

relations for radiation transfer are based on the conservation of the transport mean free path and the transport scattering albedo, see Eqs. (3.14) and (3.15). These relations will be employed for the scaling of the transport coefficients in the light transfer LBM.

The conservation of the transport mean free path or rather the reduced scattering coefficient $\mu_s' = \mu_s(1-g)$ allows the free choice of different combinations of the parameters μ_s and g. If one defines a desired degree of radiation-matter interaction per grid spacing

$$(\tilde{\mu}_s + \tilde{\mu}_a)\Delta x = \kappa \tag{9.18}$$

one obtains from Eqs. (3.14) and (3.15) the following grid-related scaling relations [278]:

$$\tilde{\mu}_a = \mu_a \tag{9.19}$$

$$\tilde{\mu}_s = \frac{\kappa}{\Delta x} - \tilde{\mu}_a \tag{9.20}$$

$$\tilde{g} = 1 - \frac{\mu_s'}{\tilde{\mu}_s} \tag{9.21}$$

In (9.18) - (9.21) the tilde marks the grid-scaled transport coefficients. The parameter κ can be freely chosen in principal but should be of order 1 to ensure that a significant fraction of the f_i collide in each step. It should be also mentioned at this point that application of the higher order time integration schemes is fully applicable also with scaled transport coefficients.

To obtain the stability conditions for the model with scaled coefficients, the scaling relations (9.19) - (9.21) can be plugged into Eq. (9.8), which becomes

$$\begin{aligned} f_i(\boldsymbol{x}, \boldsymbol{x} + \boldsymbol{c}_i\Delta t, t + \Delta t) &= f_i(\boldsymbol{x}, t) + c_i\tilde{\mu_s}\Delta t \left(-f_i + w_i \sum_{j=1}^{Q} \tilde{\Phi}_{i,j} f_j \right) - c_i\tilde{\mu_a}\Delta t f_i \\ &= f_i(\boldsymbol{x}, t) + c_i \left(\frac{\kappa}{\Delta x} - \tilde{\mu}_a \right) \Delta t \left(-f_i + w_i \sum_{j=1}^{Q} \tilde{\Phi}_{i,j} f_j \right) - c_i\tilde{\mu}_a\Delta t f_i \\ &= \left(1 - \frac{c_i\kappa\Delta t}{\Delta x} \right) f_i + (\kappa - \tilde{\mu}_a\Delta x) \frac{c_i\Delta t w_i}{\Delta x} \sum_{j=1}^{Q} \tilde{\Phi}_{i,j} f_j \end{aligned} \tag{9.22}$$

By using $c = \Delta x \Delta t^{-1}$ Eq. (9.22) can be rewritten as

$$f_i(\boldsymbol{x}, \boldsymbol{x} + \boldsymbol{c}_i\Delta t, t + \Delta t) = (1 - \kappa c_{i,LU})\, f_i + c_{i,LU}\, (\kappa - \tilde{\mu}_{a,LU})\, w_i \sum_{j=1}^{Q} \tilde{\Phi}_{i,j} f_j \tag{9.23}$$

where the quantities $c_{i,LU} = c_i/c$ and $\tilde{\mu}_{a,LU} = \tilde{\mu}_a\Delta x$ are the non-dimensional lattice speed and lattice absorption coefficient. The correct capture of scattering is ensured by the scaling of the asymmetry

factor g (see Eq. (9.21)) and the computation of the scattering matrix $\tilde{\boldsymbol{\Phi}}$ by means of the algorithm described in chapter 5. Similar as for the reference model, the stability criterion is

$$f_i(\boldsymbol{x}, \boldsymbol{x} + \boldsymbol{c}_i \Delta t, t + \Delta t) > 0 \tag{9.24}$$

which is fulfilled, if

$$1 - \kappa c_{i,LU} \geq 0 \tag{9.25}$$

and

$$\kappa - \tilde{\mu}_{a,LU} > 0. \tag{9.26}$$

The maximum lattice velocity for the D3Q26 velocity set is $c_{i,LU,max} = \sqrt{3}$ so that (9.25) is always fulfilled if $0 < \kappa \leq 1/\sqrt{3}$. Thus, for non-absorbing media the choice $0 < \kappa \leq 1/\sqrt{3}$ ensures that the model is always stable. In case of absorbing media, a coarse mesh resolution and strong absorption can cause the algorithm to become unstable. According to Eq. (9.26), for a given level of κ the stability can be improved by refining the mesh and consequently decreasing the magnitude of the lattice absorption coefficient $\tilde{\mu}_{a,LU}$.

To test the scaling procedure, a setting similar to the one in the previous sections is considered. The chosen simulation parameters and scaled transport coefficients of the different test media are listed in table 9.3. The scaled scattering coefficients vary with respect to the grid size and the phase function becomes increasingly anisotropic for small grid spacing. Figure 9.5 shows line profiles of the radiation intensity in all media with respect to number of grid nodes. For comparison, results obtained by Monte Carlo simulations are also shown. For the highly scattering medium 3 an excellent agreement between the scaled LBM and the Monte Carlo simulation is obtained and the scaled radiation problem converges towards the reference for $\Delta x \to 0$. In case of the other tested media convergence is also achieved but the converged solutions differ from the reference, particularly in the absorbing test media 2 and 4.

Additional Monte Carlo simulations were conducted for the test media 2 and 4 in order to investigate whether the observed mismatch is due to a non-perfect scaling relationship or due to a failure of the lattice Boltzmann model itself, for example by an inaccurately computed scattering matrix. In these simulations the transport coefficients were set to the same values as for the scaled lattice Boltzmann

Table 9.3.: Characteristics of participating media and simulation parameters.

					$\Delta x = 1/54$		$\Delta x = 1/77$		$\Delta x = 1/109$		$\Delta x = 1/155$	
Medium	μ_a	μ_s'	κ	$\tilde{\mu}_a$	$\tilde{\mu}_s$	$\tilde{g}$	$\tilde{\mu}_s$	$\tilde{g}$	$\tilde{\mu}_s$	$\tilde{g}$	$\tilde{\mu}_s$	$\tilde{g}$
1	0	10	$1/\sqrt{3}$	0	31.177	0.6792	44.456	0.7751	62.931	0.8411	89.489	0.8883
2	3	7	$1/\sqrt{3}$	3	28.177	0.7516	41.456	0.8311	59.931	0.8832	86.489	0.9191
3	0	30	$1/\sqrt{3}$	0	31.177	0.0377	44.456	0.3253	62.932	0.5233	89.489	0.6648
4	10	20	$1/\sqrt{3}$	10	21.177	0.0556	34.456	0.4195	52.931	0.6222	79.489	0.7484

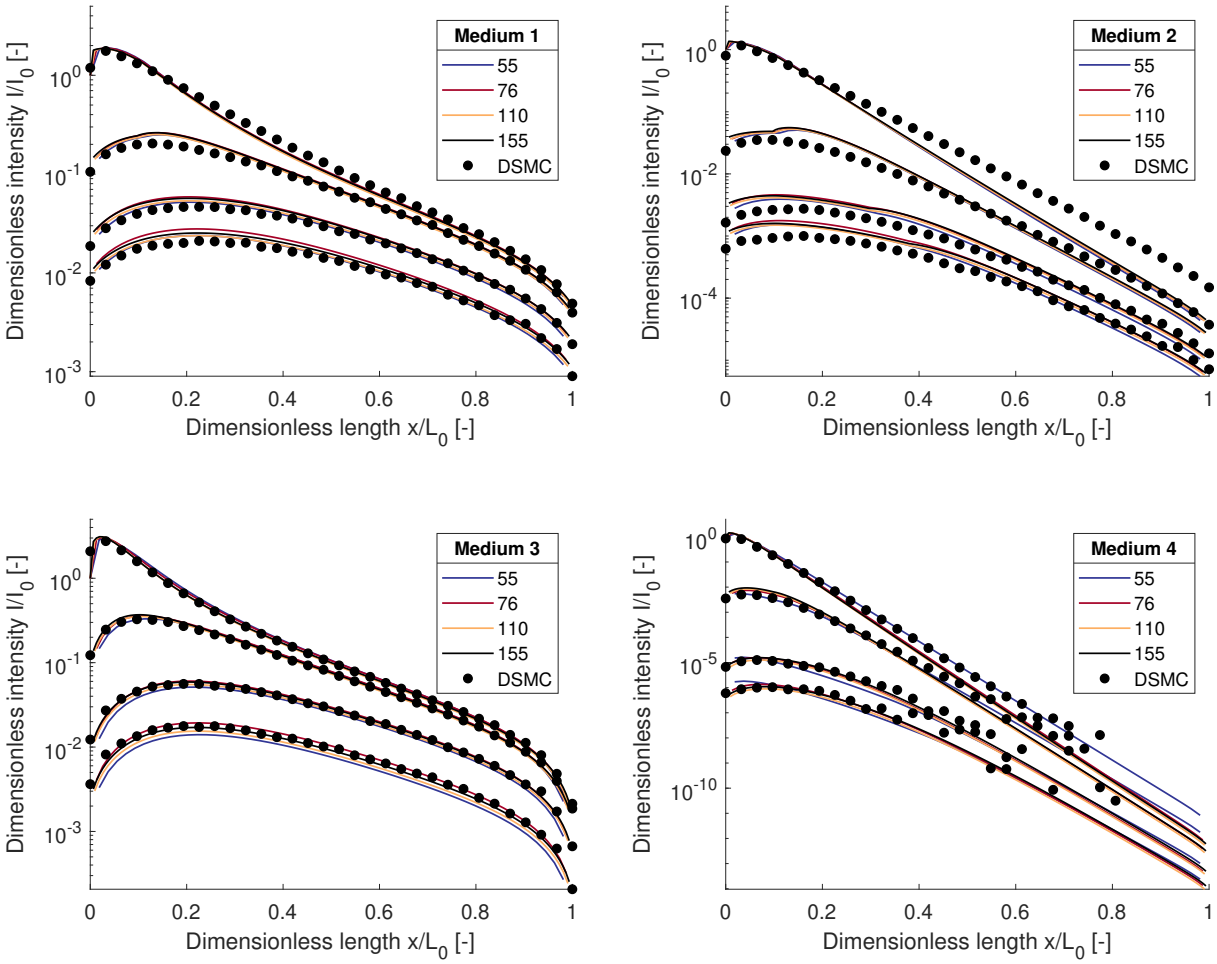

Figure 9.5.: Comparison of scaled lattice Boltzmann (lines) and Monte Carlo (symbols) simulations in different participating test media with respect to the number of lattice nodes (indicated by colors). The radiation properties of the participating media are defined in table 9.3. The free parameter κ is set to $\kappa = 1/\sqrt{3}$ and the Runge-Kutta time integration scheme is applied. Settings for the Monte Carlo simulations are similar as for figure 9.2. Top left: medium 1; top right: medium 2; bottom left: medium 3; bottom right: medium 4. Note the different scaling of the respective y-axis.

method for the grids with $N = 55^3$ and $N = 155^3$ nodes (see table 9.3). As depicted in figure 9.6, the results of the Monte Carlo simulations in medium 4 agree very well with the results obtained by the lattice Boltzmann method as soon as the transport coefficients are identical for both methods. The picture is somewhat different in medium 2, where the LBM predicts slightly higher intensities than the MCM (see also the inset in figure 9.6). The degree of scattering in medium 2 is relatively low, which means that the angular spreading of the energy occurs on larger distances. It is likely that under the conditions of medium 2 an accurate capture of the energy redistribution process requires a fine angular discretization while the LBM operates with a relatively coarse angular quadrature. Thus, the mismatch of intensity in medium 2 can be explained by the observation that to much energy is propagated in forward direction due to the small number of abscissas used in the LBM. However, with regard to the results in medium 4, the numerical experiment supports also the conclusion that the similarity relations

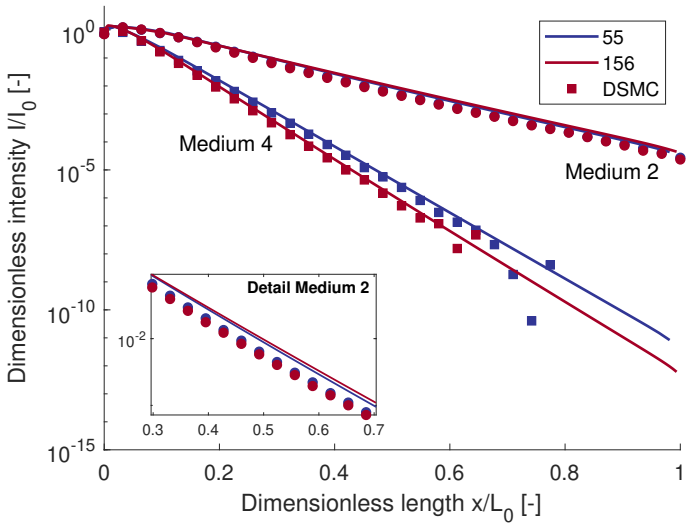

Figure 9.6.: Comparison of intensity profiles along line L_{y1} (see chapter 5, figure 5) computed by means of the Monte Carlo method and the lattice Boltzmann method with scaled transport coefficients and anisotropic scattering matrix. The simulated test media were equal for both methods and defined by the grid-scaled radiation characteristics listed in table 9.3. Colors indicate the grid size and symbols the corresponding Monte Carlo simulation with anisotropic scattering. The free parameter κ of the lattice Boltzmann model is set to $\kappa = 1/\sqrt{3}$ and the Runge-Kutta time integration scheme is applied.

are not perfectly suited to scale the transport coefficients. This result is also in accordance to previous investigations, where erroneous results have been reported for scaled radiation transfer problems with collimated irradiance in 1D [279]. More precisely, the accuracy of the similarity relations was found to be a function of the scattering albedo with the highest error around $\omega \approx 0.5$ and increased with the optical depth. In another work on diffusive radiative transfer it was found that the intensity profiles in absorbing media differ for same values of μ_s' but different anisotropy factors [280], similar to the observations in this work. The numerical test also shows that the lattice Boltzmann method gives accurate results for the case of anisotropic scattering, which was not demonstrated in the previous sections where isotropic scattering was assumed (see table 9.1). The results therefore underline the accuracy of the discrete scattering matrix and the developed algorithm for the discretization of the scattering phase function.

9.1.4. Discrete scattering matrix and scattering kernel

The discrete scattering phase function $\boldsymbol{\Phi}$ is a major ingredient for the proposed lattice Boltzmann model since it defines the redistribution of the discrete populations f_i during the collision step. Accordingly, it is of crucial importance that the discretization algorithm provides accurate results. As mentioned in section 2.2.3 of chapter 5, the proposed algorithm conserves the zero$^{\text{th}}$ and first angular moments of $\boldsymbol{\Phi}$ within the floating-point relative accuracy of the machine so that the requirement of a precisely

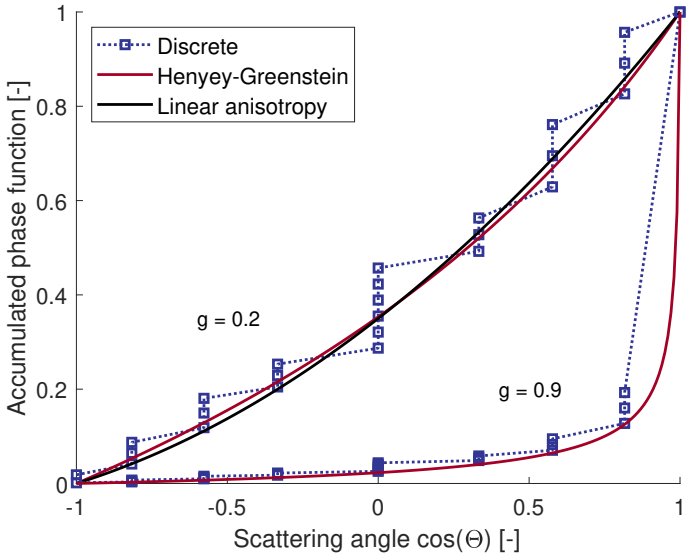

Figure 9.7.: Comparison of discrete and analytical phase functions for different values of the asymmetry factor. The phase functions are depicted as their accumulated distributions $\int_{-1}^{\cos(\Theta)} \Phi \, \mathrm{d}\cos(\Theta)$ with the scattering angle $\cos(\Theta) \in (-1, 1)$.

computed scattering matrix is fulfilled. As depicted in figure 9.7, a sufficient discrete representation of the Henyey-Greenstein phase function (see Eq. (3.6)) can be reached.

However, it should also be mentioned that the description of scattering is restricted to the first two moments in the current implementation. To underline this, the linear anisotropic phase function

$$\Phi_l = \frac{1}{4\pi} \left(1 + w\cos(\Theta)\right) \tag{9.27}$$

is considered for which the mean scattering angle[2] is given by $g = w/3$. It can be seen from figure 9.7 that also the linear phase function is well represented by the discrete phase function. In contrast, features of more complex phase shaped functions like the Mie phase function cannot be reproduced. Accordingly, the algorithm is able to reproduce scattering phase functions as long as they are adequately defined by the zero$^{\text{th}}$ and first angular moments. In principal, the proposed discretization procedure can be extended by higher moments of the phase functions to include additional features. However, pre-tests have shown that the discrete scattering matrix may contain unphysical negative entries for the extended algorithm. Alternatively, two or more separate scattering matrices can be superimposed as it was done in chapter 7. The first moment of the received scattering matrix is given by the weighted average of the single asymmetry factors[3], although the achieved scattering matrix itself differs from a matrix which is directly computed with the average asymmetry factor.

[2] It is required that $w \in (-1, 1)$ so that $g \in (-1/3, 1/3)$ for the linear phase function.

[3] Consider two matrices $\boldsymbol{\Phi}^I$ and $\boldsymbol{\Phi}^{II}$ with their first moments $g^n = \sum_{j=1}^{Q} w_j c_j \Phi_{i,j}^n$ and $n = I, II$, which are superimposed so that $\boldsymbol{\Phi} = a\boldsymbol{\Phi}^I + b\boldsymbol{\Phi}^{II}$ with $a+b = 1$. It shall be proven that the asymmetry factor g of the new matrix is $g = ag^I + bg^{II}$. Thus, $g = a\sum_{j=1}^{Q} w_j c_j \Phi_{i,j}^I + b\sum_{j=1}^{Q} w_j c_j \Phi_{i,j}^{II} = \sum_{j=1}^{Q} w_j c_j (a\Phi_{i,j}^I + b\Phi_{i,j}^{II}) = \sum_{j=1}^{Q} w_j c_j \Phi_{i,j}$.

9.2. Limitations of the lattice Boltzmann model

9.2.1. Light transfer beyond the low Knudsen regime

A key element of all lattice Boltzmann methods are collisions as they account for the spatial redistribution of the discrete particle populations f_i what ensures the complete occupation of the available space. The Knudsen number Kn is a measure for the importance of collisions for transport and relates the mean free path to a macroscopic length L_0, see 4.1.1. For light transfer, $Kn = (\mu_s' L_0)^{-1}$ can be defined in terms of the reduced scattering coefficient μ_s' and increases as μ_s' becomes smaller.

Beyond the low Knudsen regime, collisions are rare or absent and the f_i propagate in straight lines along the discrete velocity vectors. Consequently, the relatively coarse discretization of the velocity space becomes visible in the solution. This issue was already mentioned during the discussion of figure 9.3 in section 9.1.1. Similar problems are known from lattice Boltzmann simulations of rarefied gas flows or microflows and special treatments like artificial collision terms [281] or improved expressions for the relaxation time [282] were developed to enable simulations of the non-hydrodynamic regime within the lattice Boltzmann framework. It is important to state at this point that in contrast to fluid dynamical simulations, a lack of collisions is not a problem per se in simulations of radiative transfer[4]. If a source with geometrical dimensions in the order of the domain boundaries is considered, the energy from the source nodes superimposes and the error due to the angular discretization is mainly compensated. This statement is supported by the results presented in sections 9.1.2 and 9.1.3, where it was shown that the developed method is accurate, even if just a minor part of the discrete particles collide within one time step. Thus, the limitation of the developed method exists primarily when domains with small sources and media beyond the low Knudsen regime are simulated, what does not apply for the photobioreactor setups in chapters 6-8.

However, regarding a setup with a small radiation source, a similar error occurs in the Discrete Ordinate method, which is known as the ray effect [218, 221, 283]. A common strategy to reduce this error is to increase the number of discrete ordinates at the cost of extra computational time [218]. The strategy of including additional abscissas was also adopted by some authors for lattice Boltzmann simulations of radiative transfer in 2D ($D2Q16$, $D2Q32$, see e.g. [260, 274]), even though some obvious difficulties are related to the utilization of so-called multispeed velocity sets[5]. First, it can be expected that the computational costs increase dramatically in three-dimensional simulations due to the increasing number of discrete populations. Also, special treatments at the boundary nodes might become necessary in order to deal with the fact that the discrete particles do not necessarily terminate the streaming step at a boundary node (see for example [284]).

[4] In the complete absence of collisions, the RTE reduces to the differential formulation of Lambert's law which also can be solved numerically by the lattice Boltzmann model.

[5] Multispeed velocity sets are characterized by a larger number of abscissas than neighboring nodes. Consequently, a fraction of the discrete particle population propagates over two belts in the lattice.

The limits for the application of the developed lattice Boltzmann method in terms of Kn are not specified yet and the exact evaluation of the discussed errors source are evaluated in ongoing research. Monte Carlo simulations can provide a suitable reference as they cover in principal the whole range of Kn regimes from the hydrodynamic to the ballistic limit.

9.2.2. Diffuse radiation sources

Closely related to the discussion in the previous section is the issue of resolving small diffuse sources like the test case of an isotropic point source, which was investigated by Mink et al. [272]. The source is characterized by an even emission of energy into all directions. Although the boundary condition given by Eq. (4.27) is exact for this problem at the boundary nodes, in weakly scattering media the emitted radiation propagates radially along the discrete velocities and consequently, unphysical bumps occur in the solution after a short distance as depicted in figure 9.8.

A possible treatment to solve this issue is inspired by the modified DOM (MDOM), where the emitted source radiation is treated separately until the occurrence of the first scattering event and thereafter converted to diffuse radiation within the medium by means of an internal source term (see also section 4.3.4). Thus, source and medium radiation exist in parallel and contribute both to the total intensity[6] [206, 225]. This approach was applied in radiation transfer lattice Boltzmann simulations by some researchers [265, 270, 271, 274] and is easy to implement for isotropic scattering. In case of anisotropic scattering an additional difficulty is caused by the fact that the angular distribution of scattered particles must be computed separately for every node in the domain because it depends on the relative angle between the source ray and the set of discrete velocities considered for the diffuse medium radiation. A benefit of this approach in comparison with the utilization of multispeed models is that the calculation has to be carried out only once per simulation.

9.2.3. Boundary conditions

As mentioned in section 4.3.4, the treatment of reflection and refraction at the domain boundaries is a challenging task in three dimensions concerning both, sources and wall boundary conditions. In the recent state of the developed lattice Boltzmann model it is possible to account for open or diffusive boundaries with variable degree of reflection. Also inflow conditions in parallel to the discrete velocity vectors can easily be implemented and were applied for boundary modeling in chapters 5-8. In contrast, boundary conditions accounting for Fresnel reflection or source emission in directions other than the discrete velocities have not been realized yet.

The algorithm developed by Geist et al. [258] for the consideration of inflow boundary conditions with any desired radiation flux (see 4.3.4) should also be applicable to the developed lattice Boltzmann

[6] So-called intensity splitting.

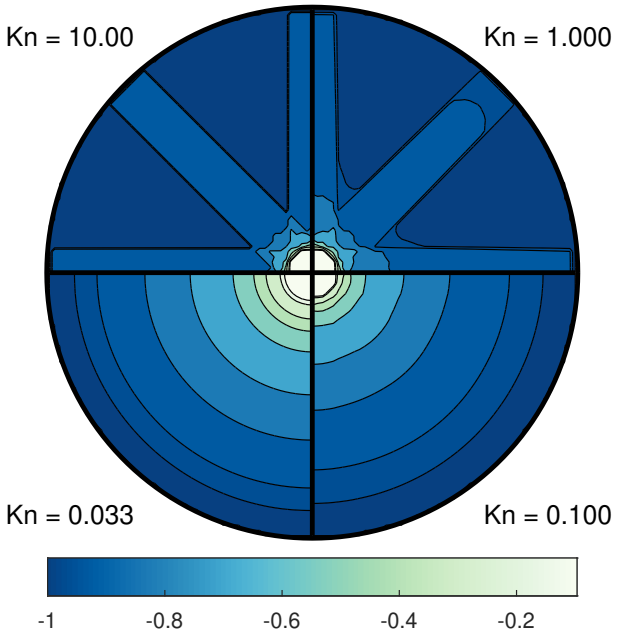

Figure 9.8.: Contours of the dimensionless radiation intensity (log scale) around an isotropic point source. The setup and boundary conditions are is similar as described in Ref. [272]. The physical diameter of the spherical domain is $D_0 = 0.001$ m and the grid size is $\Delta x = 10^{-5}$ m. The participating media are defined by the radiation characteristics $\mu_a = 0$ m^{-1}, $g = 0$. Top left: $\mu_s = 100$ m^{-1}, $Kn = 10$. Top right: $\mu_s = 1000$ m^{-1}, $Kn = 1$. Bottom right: $\mu_s = 10000$ m^{-1}, $Kn = 0.1$. Bottom left: $\mu_s = 30000$ m^{-1}, $Kn = 0.033$.

model since a structural similarity of both approaches exists. Its implementation could therefore further improve the capabilities of the model. On the other hand, the algorithm developed for the computation of the scattering matrix also delivers a discrete distribution of particles for any desired macroscopic radiation flux and could be a basis for the modeling of inflow boundary conditions. Similarly, it is thinkable to compute the reflection of particles by means of matrices similar to the scattering matrix for macroscopic fluxes which result from the first angular moments of the Fresnel equations. The improved modeling of boundary conditions is definitively one of the major issues to be solved in future research. This concerns all known lattice Boltzmann models of radiative transfer as it was also stated in 4.3.4.

9.3. A one-dimensional model variant

In many situations radiation or light transfer can be simplified as quasi one-dimensional, particularly if the extend of the radiation source in the domain of interest is much larger than the light path. Under such conditions, the out-scattered energy is compensated by similar scattering events in the immediate vicinity so that it is suitable to assume aggregated forward and backward fluxes. The assumption of quasi one-dimensionality is also often adopted in the context of photobioreactors, see sections 3.2.1, 3.2.2 and 3.3.4.

It is straightforward to design a one-dimensional variant of the proposed lattice Boltzmann model, what will be shown in the following. Although analytical solutions for the related two-flux models exist (see 3.3.4), a fast numerical scheme may provide additional flexibility, for instance for the simulation of radiation transfer in non-homogeneous participating media. The derivation of the one-dimensional model is similar to the one of the three-dimensional model so that Eq. (9.3) is the discrete model equation. For the convenience of the reader, it is re-written here.

$$f_i(\boldsymbol{x}, \boldsymbol{x} + c\boldsymbol{n}_i\Delta t, t + \Delta t) - f_i(\boldsymbol{x}, t) = c\mu_s\Delta t \left(-f_i + w_i \sum_{j=1}^{Q} \Phi_{i,j} f_j \right) - c\mu_a \Delta t f_i \tag{9.28}$$

The difference to the three-dimensional model lies in the chosen quadrature, defined by the abscissas $\boldsymbol{n}_i$ and weights w_i as well as the discrete scattering matrix $\boldsymbol{\Phi}$. Since the model is one-dimensional just two abscissas exist ($D1Q2$), thus $\boldsymbol{n}_1 = 1$ and $\boldsymbol{n}_2 = -1$. Energy conservation and symmetry requirements yield $w_1 = w_2 = 0.5$. The discrete scattering matrix is of dimension $Q \times Q$. Similar as in three dimensions, the zero[th] and first moments of $\boldsymbol{\Phi}$ shall be represented in the discrete case. The requirement of microreversibility of scattering causes that the matrix is fully defined by computing just two entries. Thus, the solution of the equation system

$$\begin{bmatrix} 1 \\ g \end{bmatrix} = \begin{bmatrix} w_1 & w_2 \\ w_1 \cos(\Theta_{1,1}) & w_2 \cos(\Theta_{1,2}) \end{bmatrix} \times \begin{bmatrix} \Phi_{1,1} \\ \Phi_{1,2} \end{bmatrix} \tag{9.29}$$

defines $\boldsymbol{\Phi}$ since $\Phi_{1,1} = \Phi_{2,2}$ and $\Phi_{1,2} = \Phi_{2,1}$. Further, it applies that $\cos(\Theta_{1,1}) = \boldsymbol{n}_1 \times \boldsymbol{n}_1 = 1$ and $\cos(\Theta_{1,2}) = \boldsymbol{n}_1 \times \boldsymbol{n}_2 = -1$. Alternatively, the scattering matrix can be defined by means of the backscattering fraction b of the Henyey-Greenstein phase function as given by Eq. (3.17). In that case, the numerical values of the matrix entries are defined as $\Phi_{1,1} = \Phi_{2,2} = 2(1-b)$ and $\Phi_{1,2} = \Phi_{2,1} = 2b$ and differ from those obtained by solving Eq. (9.29) due to the non-linearity covered in b. In both cases, the resulting model can be solved by the standard stream-and-collide algorithm. The beforehand discussed application of higher time-stepping schemes is also applicable for the one-dimensional model variant.

Figure 9.9 shows a comparison of Cornet's 2-Flux model, given by Eq. (3.16), and the one-dimensional lattice Boltzmann model with the scattering matrix being defined in terms of the backscattering fraction b of the Henyey-Greenstein phase function. The domain is illuminated from one side with intensity I_0 while the opposite boundary is transparent. It can be seen that the numerical scheme matches the analytical solution perfectly for different values of the anisotropy factor. The computational time required to achieve the lattice Boltzmann solution on a mesh with 10^3 nodes is about 0.02 seconds for 3000 iterations. In principle it is possible to extend the method by the implementation of additional features like spatially varying radiation characteristics, reflective boundaries or transient

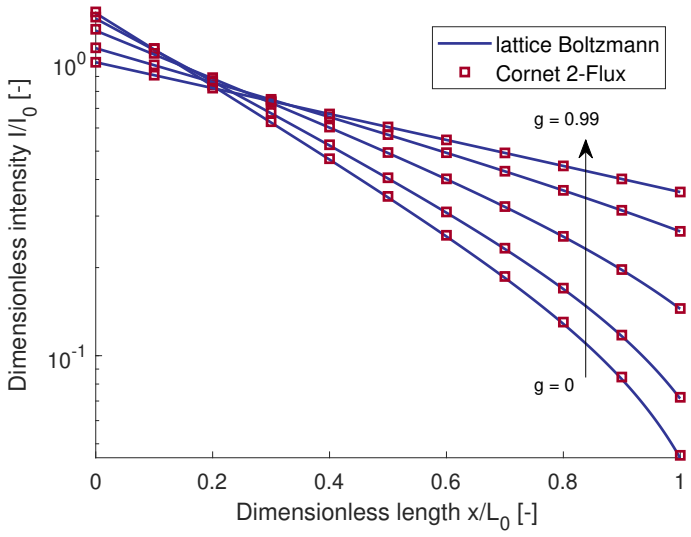

Figure 9.9.: Comparison between Cornet's 2-Flux model and the one dimensional variant of the lattice Boltzmann model for different values of the asymmetry factor g. The medium characteristics are $\mu_a L_0 = 1$, $\mu_s L_0 = 7$ and $g = (0, 0.2, 0.5, 0.9, 0.99)$.

radiation transfer. As discussed in section 4.3.2, some of these objectives were studied by means of one-dimensional lattice Boltzmann simulations [261, 265–269].

9.4. Comparison to experiments

For a comparison of the lattice Boltzmann model with experimental data, fiber optical measurements of the spectral light distribution in a rectangular-shaped bubble column filled with polystyrene suspensions were conducted in the laboratory of innoFSPEC in Potsdam, Germany.

9.4.1. Experimental setup

The inner dimensions of the bubble column are given by the width $W_0 = 51$ mm and length $L_0 = 28$ mm and the total volume $V_{tot} = 400$ ml. Gassing took place from the bottom via an inlet having a diameter of approximately 3 mm. The illumination of the column occurred from one side by fluorescent lamps. The whole setup was darkened during the experiment to prevent disturbances through environmental factors. The experiment is visualized in figure 9.10.

9.4.2. Polystyrene suspension

The polystyrene suspensions were made out of two aqueous stock solutions with known mass fraction, each containing particles with diameter[7] $d_{p1} = 555$ nm or $d_{p2} = 95$ nm, respectively. By means of electron microscopy it was found that the particles were spherical and by dynamic light scattering that they were monomodal. Between the experimental runs, the concentration of the polystyrene suspension

[7] Determined by dynamic light scattering (DLS).

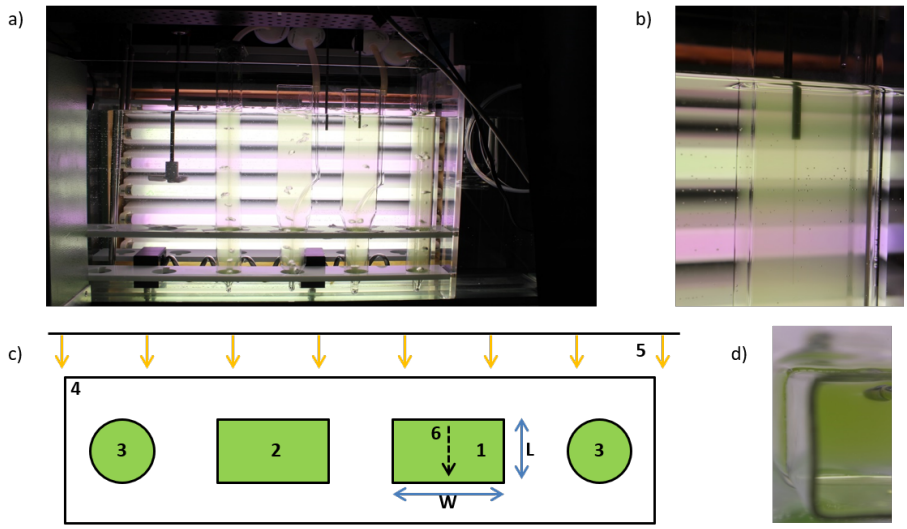

Figure 9.10.: Pictures and sketch of the experimental setup. a) Illuminated bubble columns in the water tank. b) Optical fiber in the suspension. c) Sketch of the experimental setup (top view): (1) measurement column, (2) control column, (3) dummy columns, (4) water tank, (5) fluorescent lamps, (6) measurement path of the moving optical fiber. d) Top view of the measurement column with optical fiber at its initial position near the reactor wall. All pictures show a dilute microalgae culture in the column, though the setup was similar for measurements in polystyrene suspensions.

was steadily increased by repeated dosage of polystyrene stock solution into the bubble column. After each addition, the volume fraction ϕ_v of polystyrene in the bubble column was calculated as

$$\phi_v = \frac{c_m}{\rho_{PS}} \frac{V_{PS}}{(V_{PS} + V_{tot})} \tag{9.30}$$

where c_m is the mass fraction of the polystyrene stock solution, ρ_{PS} the mass density of polystyrene and V_{PS} the accumulated amount of added stock solution.

For the calculation of the radiation properties of the suspensions it was assumed that absorption of polystyrene and water is very small, thus $\mu_{a,\lambda} = 0$ for the all λ. The wavelength-dependent scattering coefficients and asymmetry factors were computed from Mie theory by means of a code provided by Mätzler [285]. The computation requires information about the particle diameter d, the particle volume fraction in the suspension ϕ_v and the wavelength-dependent refractive index of the suspension n. The latter was computed by means of a mixing rule [286], which reads

$$n = \sqrt{\phi_v n_{PS}^2 + (1 - \phi_v) n_W^2} \tag{9.31}$$

The spectra of the refractive indexes of polystyrene n_{PS} and water n_W were measured at innoFSPEC and depicted in Appendix B together with the computed scattering coefficients and asymmetry factors.

9.4.3. Fiber optical measurements and signal processing

A movable optical fiber attached to a spectrometer and inserted in a metal cannula for mechanical stability was dipped into the bubble column about 8 cm below the liquid surface. The fiber was automatically displaced in steps of 1 mm over 21 positions along the length l by means of a motorized table. At each position, the spectrometer measured counts[8] $j_{\lambda,i}(x,t)$ in the range from 300 to 1100 nm. The displacement of the fiber and the data recording were controlled by a LabView routine. In order to account for the different signal amplitudes at different wavelengths, the measurements were performed with various integration times τ_{int} (50, 100, 300, 500, 700, 1000 ms), each in 10-fold repetition per position. After measuring spectra at all positions, the fiber was automatically moved to its initial position and the measurement cycle restarted. A whole measurement cycle took about 13 minutes.

The measured counts $j_{\lambda,i}(x,t)$ were corrected by the noise value $j_{\lambda,0}(t)$, which was recorded in darkness on a separate channel of the spectrometer. The indexes denote for wavelength-dependency (λ) and repetitions (i). From the 10-fold repeated measurements at each time and position, the arithmetic mean and variance were computed by means of pre-built Matlab functions. Subsequently, the averaged counts were scaled to the respective integration time, giving the respective count rate which is proportional to spectral light intensity I_λ, thus

$$I_{\lambda,\tau_{int}}(x,t) \propto \frac{j_{\lambda,i}(x,t) - j_{\lambda,0}(t)}{\tau_{int}} \tag{9.32}$$

At the peak wavelengths of the lamp, signal saturation occurred at long integration times, while the signal was equal to the noise level at low intensities and short integration times. To obtain an optimal data base, an average signal $I_\lambda(x,t)$ was computed from the $I_{\lambda,\tau_{int}}(x,t)$ without considering the respective saturated and unresolved parts.

An uncertainty for the comparison of simulated and measured data lies in the not precisely known distance between the first measurement position x_0 and the column wall. Therefore, x_0 was fitted for each measuring sequence to the simulation data $I_{\lambda,sim}$ by minimizing the error

$$\epsilon = \sum \left(I_\lambda(x_i) - aI_{\lambda,sim}(x_i)\right)^2 \tag{9.33}$$

at the measuring points x_i. Thereafter, the most likely value for x_0 was chosen and kept constant for the evaluation of the whole sequence. As a constraint, the diameter of the sensor probe $d_s \approx 1$ mm and the length of the measuring path $l = 20$ mm limit the minimum and maximum values for the distance to the wall so that $x_0 \in (d_s/2, L_0 - l - d_s/2)$. The constant a scales the non-dimensional simulation data to the measured data and deceased with increasing scattering coefficient according to a power law.

[8] The number of counts at each wavelength is proportional to the number of photons impinging the fiber within the integration time.

This might be explained by the change of the refractive index with ϕ_v, see Eq. (9.30), and consequently a higher reflectivity at the wall and a lower energy flux into the column.

9.4.4. Simulation setup and boundary conditions

The geometry of the bubble column is abstracted as a rectangular box with dimensions similar to the physical ones as defined in section 9.4.1. The simulation of the light distribution is carried out in three dimensions by the lattice Boltzmann model with Euler time integration. This model is chosen because it was shown in section 9.1.2 that it is computationally less demanding than the Runge-Kutta scheme while its accuracy is similar in purely scattering media. The grid spacing was set to $\Delta x = 0.0004$ m after a grid independence study.

Because the directional emission characteristics of the light source as well as reflectivity and refractions at the material interfaces were unknown, a rough estimate of the incoming light intensity was applied, which is that light enters the domain with intensity $I_{0,\lambda}$ in normal direction to the column wall. An additional influx of intensity $0.1 I_{0,\lambda}$ was assumed to occur from the opposite wall in the experiment with particles of diameter d_{p1}. Besides, it was assumed that no reflection or refraction occurs. Outgoing radiation was assumed to leave the domain unhindered at all boundaries.

9.4.5. Results

Figure 9.11 depicts the comparison of measured and simulated light intensity profiles along the measuring section of the bubble column with respect to ϕ_v and d_p at $\lambda = 560$ nm. A first observation is that the simulated and measured profiles agree fairly well, which is also the case for other wavelengths, see Appendix B. Regarding the shape of the intensity profiles, a characteristic feature can be found for all cases in the polystyrene system. The light energy accumulates close to the light source and the maximum light intensity is by a factor 2-5 higher than the incoming intensity at the reactor wall. The magnitude of the maximum depends on the particle concentration, particle size and wavelength and therefore on the respective scattering coefficient and anisotropy factor. The phenomenon is observed in both, simulation and experiment, and can be explained by multiple scattering, which increases the effective distance traveled by photons and thus, their residence time in the suspension. In turn, the total energy in the system increases. It should be noted that similar characteristics of the intensity profiles were observed for the Monte Carlo simulation of purely scattering media as shown in sections 9.1.1 - 9.1.3. Also it should be emphasized that the computed asymmetry factors of both particle systems are fundamentally different (0.8632 for d_{p1} vs. 0.0879 for d_{p2} at 560 nm) what shows the capability of the lattice Boltzmann model to simulate both, slight and strong anisotropic scattering.

However, the agreement between simulation and experiment is not perfect, what might be caused by uncertainties regarding the experimental conditions and the simplified assumptions concerning the

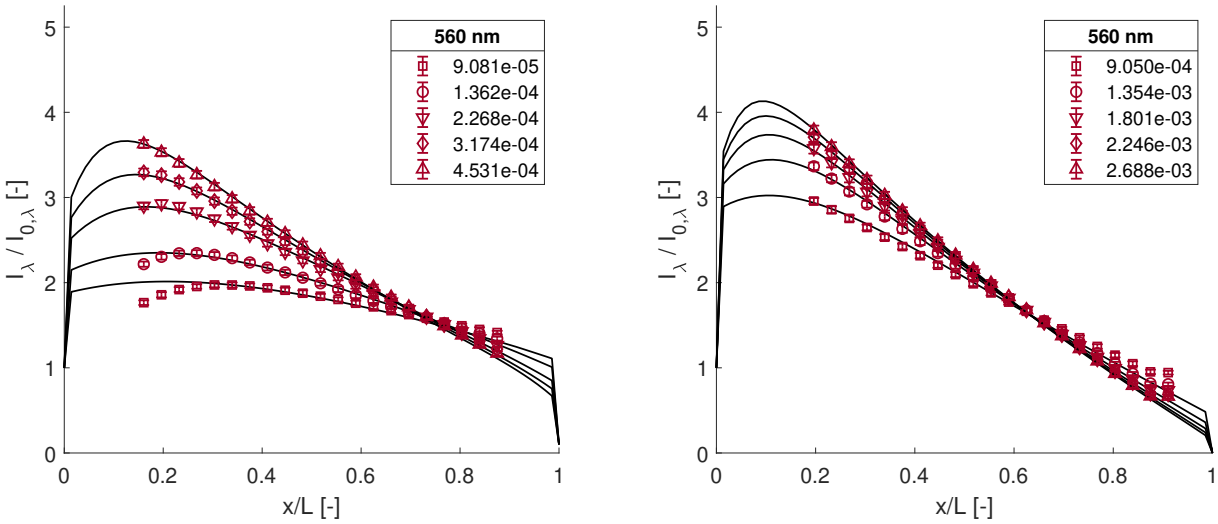

Figure 9.11.: Comparison of simulated (lines) and measured (symbols) profiles of the light intensity at $\lambda = 560$ nm in polystyrene suspensions. Different symbols encode the particle volume fraction ϕ_v as denoted in the legend. Left: Suspension with particles of $d_1 = 555$ nm. Right: Suspension with particles of $d_2 = 95$ nm.

boundary conditions. The applied boundary condition for the light source definitively does not reflect the real conditions which can be expected to be affected by reflections, refraction and a non-parallel light flux into the domain. Despite of the challenge to characterize the boundary conditions experimentally, it is also evident that future developments in the field of RT-LBM should focus on proper boundary modeling including reflecting boundaries. Due to the fact that RT-LBM is a quite new method, very little work has been done on the development of boundary conditions as it was also discussed in section 9.2.3. Nevertheless it can be summarized that the comparison of experimental and numerical data shows that the model correctly predicts the scattering of light in turbid suspensions for a wide range of conditions. Lastly, as a final remark for this section it shall be said that also experiments in a culture of *Chlorella vulgaris* were conducted, but not shown here due to the large uncertainties in the determination of the radiation characteristics.

9.5. Concluding remarks

The chapter discussed the developed lattice Boltzmann model and several approaches for its further improvement were presented. The modification of the original model with an interpolation or extrapolation step yielded a more consistent formulation. It was shown that the Euler time integration scheme is sufficient for the simulation of scattering media while it becomes limiting in strongly absorbing ones. The utilization of Runge-Kutta time integration schemes is an effective way to improve the accuracy and to decrease the computational costs for these cases. Hypothetically, mixed-order grid convergence is achieved with the modified method but further research is needed for the clarification of this question. Scaling of the transport coefficients based on the similarity relations lead to reliable results in purely

scattering media in the diffusive regime but to errors in scattering and absorbing media. Therefore, the application of the scaling is not recommended. Generally, the method works well in scattering media, while at higher Knudsen number it may suffer from ray effects. For the application in photobioreactors with simple geometry, the one-dimensional model variant might be a good tool for fast and flexible computation of light transfer. In contrast to analytical models, e.g. Lambert's law or Cornet's model, the 1D RT-LBM is also able to account for spatial variations of the radiation characteristics. Finally, it was also shown that reasonable agreement with experimental data can be achieved, but future developments should focus on the modeling of realistic domains rather than the investigation of simplified test cases.

10. Discussion of light modeling, light distribution and light-dependent growth kinetics

Chapters 7 and 8 dealt with the growth of microalgae in bubble column photobioreactors and the enhancement of the reactor productivity by intensifying the exposure of cells to flashing light. With regard to this topic, a discussion of light propagation models and their application in photobioreactors is provided in this section. The technological potential of the flashing-light effect in different reactor types is discussed and new research needs are outlined.

10.1. Impact of light modeling on the prediction of light absorption

10.1.1. Comparison of light propagation models

In chapter 3, different models for light propagation were introduced, all being common to compute light distributions in photobioreactors. Since the availability of light is the major determinant for phototrophic cell growth, the questions arise how the different models differentiate and how sensitive the prediction of cell growth reacts to the chosen model. In this section, four analytical and numerical models for light propagation are compared with respect to their prediction of light distribution and light absorption. The selection of models contains Lambert's law (Eq. (3.8)), Cornet's model (Eqs. (3.16), (3.17)), the 1D RT-LBM (Eqs. (9.28), (9.29)) and the 3D RT-LBM (Eqs. (9.6), (9.7) and (9.12)), of which the two latter utilized the RK time integration.

A plane-parallel geometry with light path L_0 is considered, which is quasi one-dimensional and representative for a flat-panel photobioreactor [69]. A similar type of geometry was already considered in chapter 6. In such a setup, the spatial light distribution $I_\lambda(x)$ is fully determined by the surface intensity $I_{0,\lambda}$, the optical depth $\tau_\lambda = (A_{abs,\lambda} + A_{sca,\lambda})XL_0$ [287] and additionally in scattering media by the asymmetry factor g_λ and the single scattering albedo $\omega_\lambda = A_{sca,\lambda}/(A_{abs,\lambda} + A_{sca,\lambda})$. All quantities depend on the wavelength as indicated by the index λ, which is dropped from now on. In order to reduce the number of input variables (I_0, L_0, X, A_{abs}, A_{sca}, g), the non-dimensional intensity $I_{nd}(x) = I(x)/I_0$ is considered and the parameters L_0 and X are lumped together to the surface area specific biomass concentration $X_A = XL_0$, which defines the optical depth in case of given radiation characteristics. From the spectral radiation characteristics of *Chlamydomonas reinhardtii* (see chapter 8, table 4) one finds that the scattering albedo varies in the range of $\omega = 0.6...0.96$, with the largest values in the green part. Further, it can be estimated from literature data [89] that an upper bound for

X_A in the order of 0.2 kg/m^2 can be found in typical PBR configurations. However, on average[1] one finds $X_{A,max} \approx 0.1$ so that the range $X_A = 0...0.1$ kg/m^2 is assumed here to represent different stages of the cultivation.

Figure 10.1 depicts the outcome of the four models at wavelengths 430 nm and 550 nm. The albedo at 430 nm is $\omega \approx 0.6$ and the relative contribution of absorption to the light-matter interaction is at its maximum. Almost no visible difference exists between all models. This means firstly, that the numerical predictions agree with the analytical ones and secondly, that scattering is irrelevant under these conditions, as it is not considered by Lambert's law at all. This also underlines the statement made in section 9.2.1 that the ray effect does not play a role for the 3D RT-LBM if the dimension of the source is in the order of the boundary dimension. At wavelengths where the albedo is larger, deviations between the models become visible, which are caused by the different treatments of scattering. This is a likely explanation, since it was shown in section 9.3 that the 1D RT-LBM yields results similar to Cornet's law if the scattering matrix is computed based on the backscattering ratio, while its computation is based on the asymmetry factor in the present simulations. All models accounting for scattering predict higher intensities than the source intensity near the wall due to backscattering and steeper intensity profiles so that the highest intensities in the rear part of the reactor are predicted by Lambert's law. Particularly, the effect of scattering becomes visible in the result of the three-dimensional RT-LBM for $X_A = 0.02$ kg m^{-2}, where it predicts intensities more than 20% higher in magnitude compared with Lambert's law. Additional three-dimensional Monte Carlo simulations at 550 nm agree reasonably well with the results of the 3D RT-LBM, what indicates that lateral photon propagation affects the intensity distribution even in quasi one-dimensional geometries and that one-dimensional approximations leads to erroneous intensity profiles. However, 1D models are without doubt superior over the three-dimensional counterparts in terms of computational costs.

The volumetric light absorption rate[2] q_{abs} links the light intensity profile to the growth kinetics, and is therefore a good measure for quantifying the impact of the light model on the predicted growth rate. This quantity was also used in chapter 8 in order to compare the effects of pneumatic mixing on the rate of photosynthesis. For the purpose of comparing the different light propagation models, the spatial average of q_{abs} will be used, which reads in a non-dimensional formulation

$$q_{abs,nd} = \frac{X_A}{L_0} \int_0^{L_0} I_{nd}(x) A_{Abs} \mathrm{d}x \tag{10.1}$$

Note that $q_{abs,nd}$ depends on the wavelength and can be transformed into physical units by multiplication with I_0/L_0. Figure 10.2 depicts the difference between the models which include scattering and Lambert's law in terms of $q_{abs,nd}$ with respect to the single scattering albedo. The transformation into

[1] The statement is based on 36 evaluated data sets for submerged cultures, which are listed in Ref. [89].
[2] The physical dimensions are [μE m^{-3} s^{-1}].

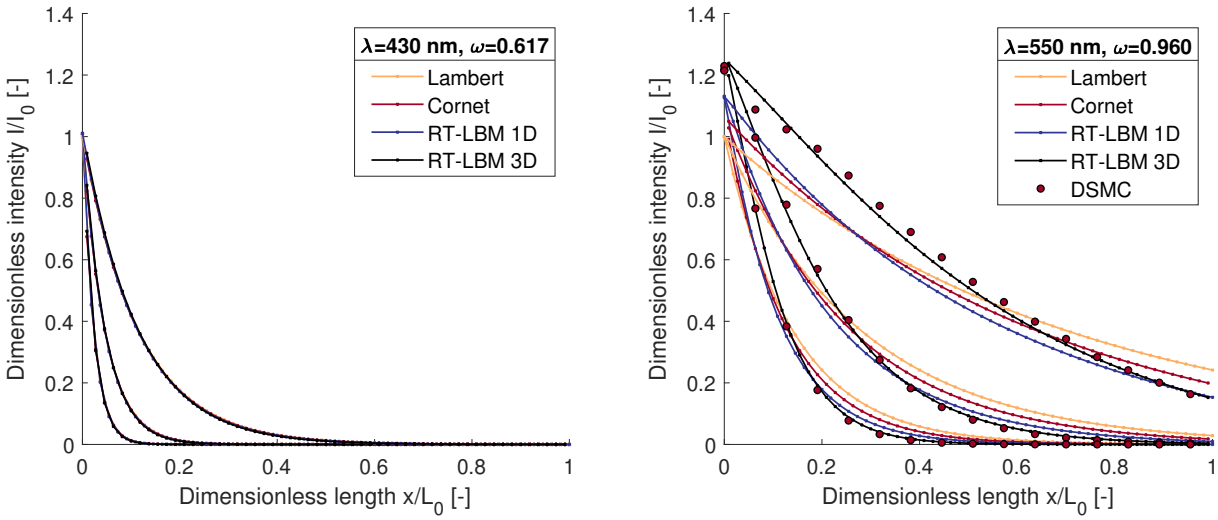

Figure 10.1.: Comparison of light intensity profiles from different models at 430 nm and 550 nm. The parameter X_A was set in the simulations to the values 0.02, 0.05 and 0.1 kg m^{-2}, whereby the top set of curves corresponds to the lowest value. The absorption and scattering cross-sections were set according tp the values listed in chapter 8, table 4, and the asymmetry factor was set to 0.97 for all simulations. For $\lambda = 550$ nm additional Monte Carlo simulations (DSMC) were performed with settings similar to the ones in chapter 9.

physical units is similar as for $q_{abs,nd}$. It can be seen that deviations of the predicted intensity distribution are also reflected in the rate of light absorption and the difference increases steadily with the single scattering albedo, which is also the case for other values of X_A (not shown). The overall impact of the chosen model on the prediction of cell growth must be evaluated in physical quantities so that the geometry of the photobioreactor and the source spectrum as additional factors need to be considered. For example, if $I_0 = 100$ μE m^{-2} s^{-1} and $L_0 = 0.1$ m for $\omega = 0.95$, the predicted absorbed energy differs by 50 μE m^{-3} s^{-1} between the three-dimensional RT-LBM and Lambert's law, which corresponds to about 5% of the overall absorbed energy. However, the above mentioned transformation of Eq. (10.1) into physical quantities shows, that the volumetric light absorption rate scales with $1/L_0$ which means that the absolute deviation between the model outcomes becomes largest for short light paths. The source spectrum, on the other hand, acts as a weighting function by determining the light absorption in parts of the spectrum where the albedo is high. Therefore, the choice of the light model can be expected to affect the prediction of growth kinetics the most in case of short light paths, high biomass concentration and sources emitting a significant amount of light at wavelengths, where the scattering albedo is $\omega > 0.85$, which, for *C. reinhardtii*, is the case in range from 510 to 650 nm and for $\lambda > 690$ nm . It should be emphasized that for this species the asymmetry factor g was set to the value of 0.97. For other species it is known that the scattering is characterized by stronger isotropy [189], so that the effects of scattering on the light distribution already become important at lower values of ω.

The comparison of the different models shows that scattering should be always considered in computations of the light distribution, especially because simple models like the 1D RT-LBM and Cornet's

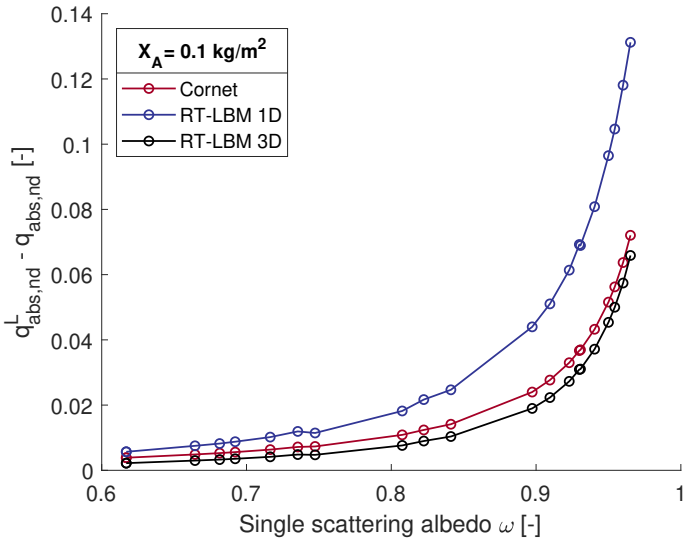

Figure 10.2.: Difference of the predicted average non-dimensional rate of light absorption between light propagation models including scattering and Lambert's law. The superscript L indicates the rate of light absorption predicted by Lambert's law.

model are available. For quasi one-dimensional geometries these models provide a sufficient degree of accuracy and are therefore superior over Lambert's law. However, in strongly absorbing cultures of microalgae, the deviations between the respective predictions are not too large, even if scattering is ignored. Generally, the usage of numerical methods might enable a higher flexibility compared to analytical models, for instance, if spatial variations of the radiation characteristics or reflective boundaries must be taken into account. In common PBR designs, spatial inhomogeneities are not too likely because of the small dimensions being necessary to reach the required high surface-to-volume ratios, while in other disciplines of radiation transfer like climate forecasts, spatial inhomogeneities might be more important and 3D computations of radiation transfer become necessary [245]. The application of 3D models might also become a necessity in cultures of microalgae in case of complex PBR geometries. For example, the positioning of many light sources in a three-dimensional space [97] may cause radiation fields which might be too complex for their reduction to quasi one-dimensional or two-dimensional computations. In order to compute light distributions in pipes or columns, a two-dimensional version of the RT-LBM might be a good complement to the numerical tools which have been developed in this work. The development of such a model on the basis of the existing ones is straightforward and essentially requires the adaption of the quadrature rule.

10.1.2. Uncertainty analysis

An interesting question for the application of light propagation models is to quantify how much their outcome is affected by uncertain input parameters. Cells adapt their cellular composition in response to different environmental conditions, what leads to variations of the absorption and scattering character-

Table 10.1.: Observed variation of different uncertain quantities and their respective assumed degree of uncertainty. The organism used in the respective experiments is specified in parenthesis. Note that the values given for the observed variation are approximates since it is usually not constant across the spectrum.

Affected quantity	Observed variation	Source of uncertainty	Ref.	Degree of uncertainty
A_{abs}	-40%	Photoacclimation (*C. reinhardtii*)	[62]	-40% of base value
	-40%	Photoacclimation (various species)	[64]	
	-50%	Photoacclimation (*C. vulgaris*)	[121]	
A_{sca}	-10%	Cell shape and size (*C. reinhardtii*)	[62]	$\pm 25\%$ of base value
	$\pm 30\%$	Cultivation time and light intensity (*N. oculata*)	[120]	
	+50%	Cultivation time (*C. vulgaris*)	[121]	
g	-0.02	Cell composition (*I. galbana*)	[189]	-0.02 from base value
	-0.01	Cultivation time (*C. vulgaris*)	[121]	
X	$\pm 5\%$	Measurement uncertainty	[288]	$\pm 5\%$ of base value
	$5 - 13\%$	Measurement uncertainty (*C. vulgaris*)	[289]	

istics [64, 120]. Also the biomass concentration is often not exactly known during cultivation processes and therefore an object of uncertainty [288, 289]. The propagation of uncertain input parameters and their effect on light intensity and light absorption shall be estimated by a stochastic Monte Carlo procedure, which follows the approach of Sin et al. [290]. Briefly, the first step of the methodology consists of specifying the uncertainty of the input parameters. Based on literature data, table 10.1 depicts the observed variation of uncertain quantities and the consequential assumed degree of uncertainty. In a second step, a set of input parameters is sampled randomly within the specified range of uncertainty and utilized in simulations of the light distributions in order to quantify the uncertainty of the model output, which, in the present case, is the local light intensity and the non-dimensional volumetric rate of light absorption according to Eq. (10.1). Because the procedure requires many simulations to obtain results with statistical evidence, only one-dimensional models are evaluated due to their low computational costs. In total, 900 base cases were evaluated, whereby a base case is defined by the radiation characteristics at a certain wavelength (300 levels between 400 nm and 700 nm) and the parameter X_A (3 levels: 0.02, 0.05 and 0.1 kg m^{-2}). 1000 light profiles were simulated for every base case and each of the one-dimensional models (Lambert's law, Cornet's model, 1D RT-LBM).

Figure 10.3 depicts the light distribution at 430 and 550 nm and the respective output uncertainty, which is indicated by quantiles of the local light intensity. The utilized light propagation model for this figure is the 1D RT-LBM. It can be seen that the absolute output uncertainty is a function of the parameter X_A and scales roughly with the local light intensity. In order to further quantify the output uncertainty, the interquartile range

$$IQR = Q_{75} - Q_{25} \tag{10.2}$$

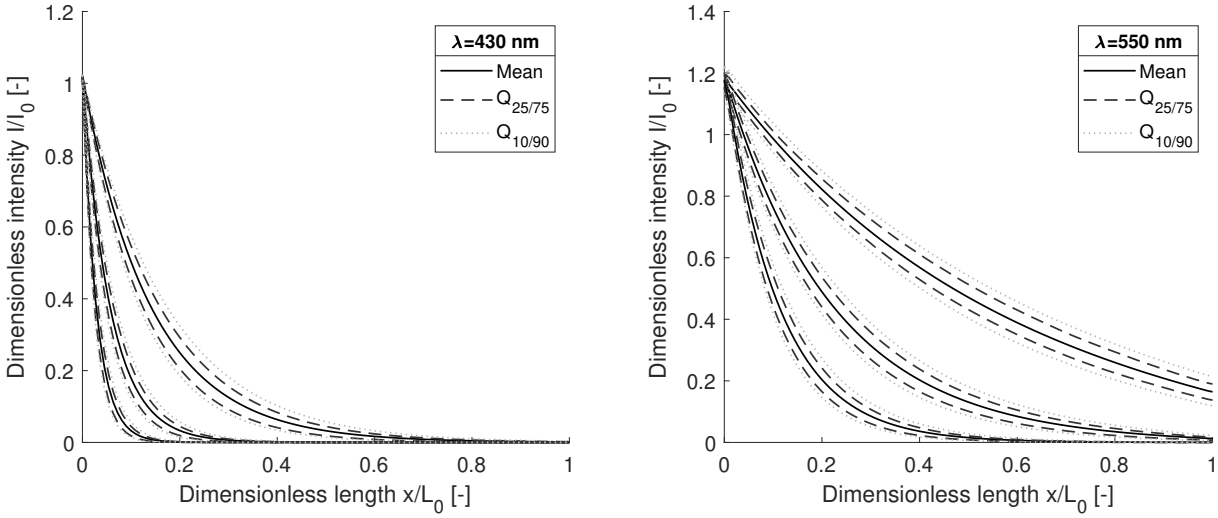

Figure 10.3.: Uncertainty of light intensity profiles due to uncertain input parameters. The quantiles indicate the uncertainty of the local light intensity. The base values for the absorption and scattering cross-sections are listed in chapter 8, table 4. The base value of the anisotropy factor is 0.97 and the ones of the parameter X_A are 0.02, 0.05 and 0.1 kg m^{-2}, whereby the top set of curves corresponds to the lowest value. The sampling of random parameter sets was carried out according to table 10.1. The utilized light propagation model is the 1D RT-LBM.

of the non-dimensional rate of light absorption (see Eq. (10.1)) is calculated for each light propagation model and base case. Figure 10.4 shows the results of the computation with respect to the single scattering albedo and X_A. In the case of $X_A = 0.02$, the output uncertainty is positively correlated to ω, what means that light absorption is mainly uncertain in the green part of the spectrum. As X_A increases, the uncertainty of light absorption becomes increasingly important also in parts of the spectrum where absorption dominates over scattering. Interestingly, the IQR of the light absorption rate is found in a similar order of magnitude than the difference between light propagation models, what can be seen by comparing figures 10.2 and 10.4. It should be mentioned that curves similar to figure 10.4 were also obtained for Cornet's model and Lambert's law, with IQR of almost identical magnitudes. The similarity of the measured uncertainty for different models indicates that the uncertainty of the scattering-cross section plays a minor role for the overall result in the here considered case of strong forward scattering, because scattering is not considered by Lambert's law. In summary, the major result of the analysis is that the accuracy of predicting light distribution and light absorption is affected in a similarly by the choice of the light propagation model and by the uncertainty of the input parameters. To date, radiation characteristics are not measured online, so that additional work in this field can contribute to a better understanding and control of physical environments in photobioreactors.

10.1.3. Sensitivity analysis

In the previous section it was shown that the prediction of light distribution and light absorption in PBR is much affected by the uncertainty of the input parameters. However, the analysis did not explain the

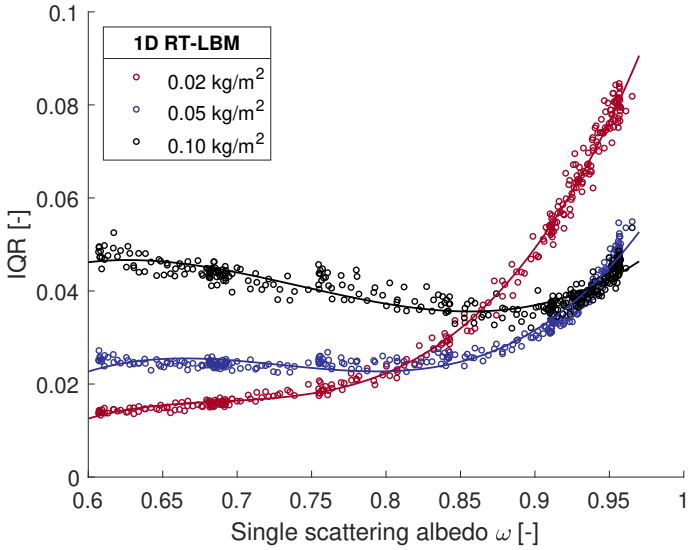

Figure 10.4.: Uncertainty of the averaged volumetric rate of light absorption in terms of the interquartile range IQR with respect to the scattering albedo ω and the surface area-specific biomass concentration X_A. Computations were carried out by means of the 1D RT-LBM.

contribution of individual parameters to the overall uncertainty, which shall therefore be investigated now. The importance of a parameter's uncertainty is high, if the model output is sensitive to changes of the parameter value. A common way to estimate the sensitivity of a model to variations of its inputs is Differential Analysis [290], where the partial derivative

$$S_{k,j} = \frac{\partial y_k}{\partial \theta_j}|_{\boldsymbol{\theta_0}} \tag{10.3}$$

of the k^{th} model output y_k with respect to the j^{th} input θ_j is evaluated for a set of input parameters on a certain level, which define a base state $\boldsymbol{\theta_0}$. For the present analysis, the model output is $q_{abs,nd}$ and the inputs are given by the parameters X_A, A_{abs}, A_{sca} and g. In order to compare the effects of the different inputs, Eq. (10.3) can be scaled by normalization to the values of the respective inputs and local outputs, thus

$$S_j = \frac{\partial q_{abs,nd}}{\partial \theta_j} \frac{\theta_j}{q_{abs,nd}} \tag{10.4}$$

Now, the quantity S_j measures the percentage change of $q_{abs,nd}$ in response to a percentage change of θ_j at a base state $\boldsymbol{\theta_0}$. In order to estimate S_j numerically, the partial derivative in Eq. (10.4) can be approximated by central differences, which leads to the expression

$$S_j \approx \frac{q_{abs,nd}(\theta_j + \Delta\theta_j) - q_{abs,nd}(\theta_j - \Delta\theta_j)}{2\Delta\theta_j} \frac{\theta_j}{q_{abs,nd}} \tag{10.5}$$

for the relative sensitivity of $q_{abs,nd}$ to a variation of θ_j. Similar as in section 10.1.2, S_j was evaluated for 900 base cases to investigate the parameter sensitivity at different wavelengths (A_{abs}, A_{sca}, g) and

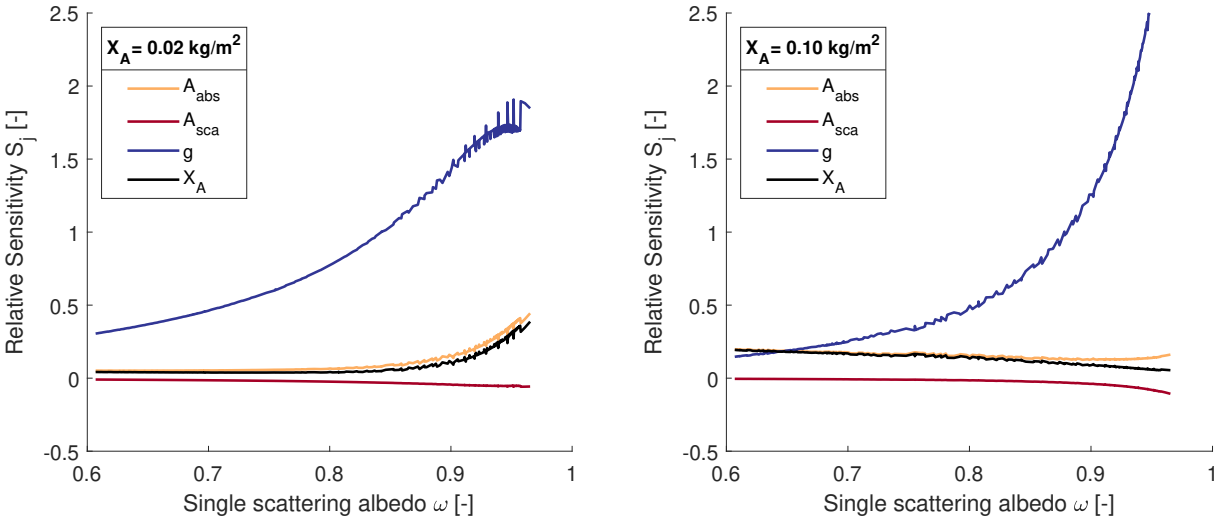

Figure 10.5.: Relative sensitivity of the average rate of light absorption to model input parameters at various base states. The output sensitivity was calculated by means of Eq. (10.5) and (10.1). The underlying simulations of light distribution were performed with the 1D RT-LBM. The input parameter variation $\Delta\theta_j$ was set to 0.1% of the respective base value in case of A_{abs}, A_{sca} and X_A and to an absolute variation of 0.001 for g. Left: Sensitivity at $X_A = 0.02$ kg m^{-2}. Right: Sensitivity at $X_A = 0.10$ kg m^{-2}.

process states (X_A). The base value of the anisotropy factor was kept constant in all simulations at $g = 0.97$.

Figure 10.5 depicts the relative sensitivity of the rate of light absorption to the model inputs. The underlying light propagation model is the 1D RT-LBM. It can be seen that $q_{abs,nd}$ is more or less insensitive to variation of the scattering cross-section A_{sca} over the complete range of the scattering albedo. Only at large levels of X_A and ω a slightly negative impact can be observed. This means that scattering counteracts the absorption of light, which is in agreement to figure 10.2 and the result that the predicted light absorption is the highest, if the intensity distribution is computed with Lambert's law. The sensitivity of $q_{abs,nd}$ to a change of A_{abs} or X_A is similar to each other. It can be seen from figure 10.5 that $q_{abs,nd}$ is positively correlated with these quantities. While at low levels of X_A the most sensitive part of the spectrum is the green one ($\omega > 0.85$), the picture changes at high levels of X_A, where $q_{abs,nd}$ becomes also sensitive to variation of A_{abs} or X_A at lower values of ω. Interestingly, the highest relative sensitivity of the model output is found for the anisotropy factor, which is positively correlated to $q_{abs,nd}$, what means that stronger forward scattering enhances the rate of light absorption. This is a likely result since the RTE converges towards Lambert's law for perfect forward scattering. It should be noted that the sensitivity of $q_{abs,nd}$ to A_{sca} is tightly connected to the level of the anisotropy factor and increases for stronger isotropy. At the same time, the sensitivity of $q_{abs,nd}$ to g decreases.

The results of this section confirm the findings of the previous one that the uncertainty of model outputs is basically caused by not precisely known absorption characteristics, which include both, the absorption cross-section and the biomass concentration (see Eq. (3.1)). The picture will change in case

of organisms scattering light more isotropically, though many algae species are characterized by strong forward scattering [121, 178, 190, 191]. With regard to the parameter sensitivity of the analytical light propagation models, similar result as shown in figure 10.5 were also observed for Cornet's model, while Lambert's law is of course insensitive to changes of A_{sca} and g. It should be emphasized at this point, that different results must be expected if the average light intensity is the investigated model output. However, since the amount of absorbed light determines the rate of photosynthesis, the rate of light absorption seems to be a more relevant model output to evaluate.

Generally, the prediction error of light propagation models, output uncertainty and parameter sensitivity are rarely addressed in the context of photobioreactor research and just few examples exist for their study [291]. The results of the present analysis emphasize the need for suitable process monitoring tools for algal pigmentation, which are not readily available to date [292]. The coupling of simple light transmittance sensors [293] or optical fibers (see section 9.4) with computational tools like neural networks might be a promising way to improve the prediction of light distribution in future. An additional benefit of such developments is given by the fact that the radiation characteristics of phototrophic cells are closely related to the cell physiology and composition. Therefore, these properties might be accessed with help of optical models and optimization algorithms by fitting the cell composition and the resulting cellular radiation characteristics to the measured ones [189].

10.2. Technological potential of utilizing the flashing-light effect

10.2.1. Mixing-induced flashing-light effect

One of the major results of chapter 8 was that pneumatic mixing in the investigated bubble column PBR did not induce the FLE. Recalling that the evaluation of the FLE and its technological potential are the primary scopes of this work, the question arises whether the obtained result can be generalized with regard to different conventional PBR types, what shall be discussed in this section.

In order to investigate the interplay of light distribution, hydrodynamics and kinetics in different PBR, Olivieri et al. [30] developed a Lagrangian model, which is in principle similar to the one used in chapter 8, but simplified in the sense that the motion of individual microalgae cells was treated as a random walk rather than being obtained from full CFD simulations. In their model, the dispersion coefficients were related to the operation parameters of different PBR types, and for the case of bubble column PBR the frequencies of L/D cycles were found in a similar order of magnitude as in chapter 8. Tubular PBR are among the most frequently used configurations in microalgae production. Based on their simulations Olivieri et al. [30] state that turbulent mixing can partially compensate light limitations in tubular reactors by shuttling algae cells between light and dark parts of the reactor, but for this a Reynolds number of $Re > 10^5$ is required. The estimated order of magnitude is essentially similar to the simulation results of Marshall and Sala [81] for a similar configuration. Accordingly, the required

conditions for the occurrence of the FLE in tubular reactors seem to be clearly different from the usual operation points with Re in the order of 10^3 to 10^4 (see section 2.2.1), what means that the FLE does not take place under normal operation conditions.

The characteristics of turbulent eddies on different scales provide further estimates for the relevance of certain flow conditions to facilitate the FLE in tubular PBR, if one assumes that the eddy lifetime is a characteristic for the L/D cycling frequency. The characteristic time and length scales of the smallest eddies in isotropic turbulence can be estimated from the Kolmogorov microscale [294]. With adequate assumptions for a tubular PBR, one finds the characteristic time scale t_K in the order of 10^{-3} to 10^{-4} seconds and the associated length scale l_K in the order of 10^{-5} meters, see Appendix C. While mixing on such time scales is sufficient to induce the FLE, the length scale over which mixing occurs is at least one order of magnitude smaller than the characteristic length scale of the light intensity distribution, which is approximately equal to μ_a^{-1} in strongly absorbing media[3]. Therefore, mixing on the scale of the smallest eddies cannot contribute to the FLE.

On intermediate scales between the largest and the smallest eddies, the Taylor scale provides an estimate for the characteristic time and length scales of the turbulent eddies. According to [294], the Taylor length scale is related to the characteristic length scale of the system L_0 and to the one of the smallest eddies l_K by $l_T = (L_0 l_K^2)^{1/3}$ and the corresponding time scale can be computed as $t_T = l_T/u_0$, where u_0 is the average velocity of the flow. Computing these quantities with respect to Re for a pipe of $D_0 = 0.05$ m shows that l_T is of similar order than μ_a^{-1} in dense algae cultures for $Re > 10^4$ and also the inverse time scale seems to be sufficient for adequate light/dark shuttling. Therefore, turbulent mixing on intermediate scales seems to be effective to enhance the productivity of PBR. However, simulations of Olivieri et al. [30] for similar conditions do not confirm this estimate on the reactor scale. Even if turbulent eddies of intermediate size create conditions which support the FLE, the improvement is still restricted to a small part of the pipe around the light/dark border so that the overall effect must be determined by mixing on the largest scales. Thus, eddies at the Taylor scale can only induce the FLE in a small fraction of the cell population[4], which can hardly cause a significant productivity gain. In addition, one should consider that the mixing must occur near the reactor walls, since PBR are usually illuminated externally. It is clear that mixing near walls is affected by the viscous sublayer, whose thickness δ_0 can be roughly approximated[5] as $\delta_0 \approx 10^{-3}$ m, which is in a similar order of magnitude as μ_a^{-1} in high density cultures.

[3] Referring to chapter 8, table 4, one finds that the maximum absorption cross-section of *C. reinhardtii* is $A_{abs} \approx 430$ m^2 kg^{-1}. According to Eq. (3.1), a biomass concentration of 5 g/L leads to $\mu_a^{-1} \approx 5 \cdot 10^{-4}$ m.

[4] A rough estimate for the fraction of unaffected cells is based on the presumption that the decay of the light intensity in thick cultures is steep and the boundary between light and dark parts of the culture is near the wall of the pipe. If one assumes that the FLE occurs in a layer of thickness l_T next to the wall and that cells are equally distributed in the liquid, the fraction of unaffected cells can be estimated from the ratio of the geometrical cross-sections of the thin layer and the remaining part of the pipe, which gives $(D_0 - l_T)^2/D_0^2$.

[5] The underlying assumption is that the time averaged velocity profile in the considered range of Re is approximately given by $u/u_0 = (2y/D_0)^{1/7}$ and that $u(y = D_0/2 - \delta_0) = 0.99u_0$. This yields $\delta_0 = D_0/2(1 - 0.99^{1/7})$.

The characteristic time and length scales for the largest eddies are given by the mean flow rate and a macroscopic characteristic length L_0, which is the pipe diameter D_0 for a tubular PBR [294]. Thus, a characteristic frequency for turbulent mixing by the largest eddies is given by the expression

$$f_t = \frac{u_0}{D_0} \propto \frac{Re}{D_0^2} \tag{10.6}$$

At high values of the Reynolds number ($Re \approx 10^4...10^5$) and $D_0 \leq 0.05$ m, f_t takes values in the order of 10^1 to 10^2 Hz, so that the FLE becomes potentially relevant. As stated in chapter 8, a positive effect of flashing light on *C. reinhardtii* starts to occur at flash frequencies of 50 Hz, though frequencies of at least one order of magnitude are required to realize the full potential of the FLE. Although for other species lower flash frequencies might be already sufficient [52], it seems that mixing of algae by the largest eddies is too slow, even at high Re.

It is often mentioned that mechanical stress might become an issue under intensive mixing, what leads to an increase of the cell mortality [295–297]. Obviously, a further increase of the mean flow rate in order to reach higher Reynolds numbers is accomplished with higher mechanical stress on individual cells. An estimate for the shear rate in isotropic turbulence can be obtained by calculating the length and velocity of the smallest turbulent eddies under the presumption that the size of the cells does not differ too much from the length scales of the turbulent eddies [298, 299]. Following this approach with reasonable assumptions for the properties of the culture broth and the reactor dimensions, it can be calculated that the resulting shear stress on individual cells is in the order of several Pascal, see Appendix C for details. It is known that the resistance of several species to shear stress becomes critical at the determined or even lower levels [295–297, 300, 301], although other species should be able to grow without problems under the estimated conditions [297]. An open question is the impact of tensile stresses on the physiology of microalgae since there is a lack of literature data about this topic. However, the discussion so far implies that mechanical stresses in turbulent pipe flow may become critical at flow rate which are required to counteract light limitation. In line with this statement, Gao et al. [84] showed in CFD simulations that mechanical stress also counteracts beneficial effects of pneumatic mixing in airlift photobioreactors above a certain gas superficial velocity.

In summary, it seems unlikely that turbulent mixing induces the FLE in tubular PBR under suitable operation conditions, which are limited by mechanical cell damage and costs for mixing energy. This conclusion also accounts for different modified tubular systems with static mixers, which have been reviewed by Abu-Gosh [56]. As reported there, L/D cycles in different configurations took place over times in the order of seconds. In a recent study [302] it was shown by means of CFD simulation that in twisted tubes or tubes with static mixers, L/D cycles with frequencies of 4 Hz can be obtained. Although it depends on the cultivated species, it seems unlikely that the FLE significantly improves the photon conversion efficiency under such conditions. Therefore, the results of chapter 8, namely that

the FLE is not induced by pneumatic mixing, seem also to apply to hydrodynamic mixing in tubular PBR. However, gains in productivity were observed to a greater or lesser extend in response to higher mixing intensity [56] so that some kind of effect must take place.

Based on the results of Oliveri et al. [30] an interesting point is discussed by Janssen [303], who argues that the improvement of PBR productivity under high-light conditions and intensive mixing is due to a reduced amount of photoinhibition rather than to the induction of the flashing-light effect. More precisely, the hypothesis states that the rate of photosystem inactivation decreases under flashing light because light absorption in excess is reduced as a consequence of the dark periods and, thereby, the ratio of PSU damage and PSU repair is shifted in favor of the latter. Clearly, this mechanism differs from the flashing-light effect, which is explained by a buffer of reduction equivalents which can be used to bridge periods of darkness [53]. In order to assess the impact of both effects, simulations of the dynamics response of photosynthesis to light fluctuations can be carried out. A suitable starting point is the kinetic model [76], which was utilized in chapter 8, see Eqs. 21 and 22 therein. For a quick simulation, the model is simplified in the sense that only monochromatic light in the absorption maximum (430 nm) is considered and the effects of mixing on the temporal light exposure are approximated by a binary pulse function being characterized by the pulse frequency ν_F and the duty cycle τ_F. Therefore, the simulation approximates the light exposure of a single cell in a mixed culture and how it reacts to different light regimes. The three PSU states in the model are initialized at their steady-state under constant light exposure at a light intensity of $I_0 = 2000$ μE m^{-2}s^{-1} so that the effect of L/D cycles can be evaluated with regard to their to photoinhibition and the FLE. The total simulation time is 3000 seconds for each case under consideration. Note that the flash intensity is equal to I_0 and kept constant at all duty cycles, what is different to the simulations shown in chapter 8.

Terry [45] introduced the degree of light integration (see also section 2.1.2)

$$\Gamma(I, \nu_F, \tau_F) = \frac{P(I_0, \nu_F, \tau_F) - \tau_F P(I_0)}{P(\tau_F I_0) - \tau_F P(I_0)} \tag{10.7}$$

as a measure for the FLE which takes values between 0 and 1. In Eq. (10.7), P is the rate of photosynthesis which is related to the time-averaged fraction of activated PSU, $\nu_F = (t_F + t_D)^{-1}$ is the flash frequency and $\tau_F = t_F/(t_F + t_D)$ is the duty cycle, which relates the flashing time to the total period of the L/D cycle. Another measure for the FLE can be obtained with the ratio of the fractions of activated PSU during the dark period and the total L/D cycle, which is

$$\phi_{x_1} = \frac{\langle x_1(t_D)\rangle}{\langle x_1(t_L)\rangle} \tag{10.8}$$

where $\langle\cdot\rangle$ stands for the temporal average and the indexes L and D indicate the light and dark periods of the light pulse. Similar to Γ, ϕ_{x_1} varies between 0 and 1, where a value of 1 means that the

average amount of activated PSU is similar during the dark period and the flash, thus, that the FLE is fully exploited. Additionally, the fraction of damaged PSUs can be evaluated as a direct measure for photoinhibition.

Figure 10.6 shows the simulated kinetic response of *C. reinhardtii* to monochromatic flashing light with different flash frequencies and duty cycles. From the illustration on the top left it can be seen that flashing indeed reduces photoinhibition over the whole range of frequencies and duty cycles. Thereby, the effect is inversely related to the duty cycle, what makes sense because photodamage can only occur during the flash. An increase of the flash frequency causes a linear decrease of the fraction of damaged PSU, whereby the slope is a function of the duty cycle and gets steeper for shorter light periods as indicated by the regression lines. In consequence of both, the number of PSU which can actively contribute to photosynthesis increases under flashing light. This finding can be seen as an indication for the validity of Janssen's hypothesis, although it is not clear yet whether the repaired PSU contribute to the factions of resting or activated PSU. Only in the latter case, a positive effect of less photoinhibition on the rate of photosynthesis will be observed.

Turning to the fraction of activated PSU (illustration top right), one finds a positive correlation to the flash frequency. Only for very low flash frequencies ($\nu_F < 1$ Hz), the simulation predicts a level below the solution for continuous light, which is in accordance to the observation of low reactor productivities under low frequency flashing [41, 58, 59]. For low flash frequencies, the observed increase is linear and the slope of the correlation (indicated by the dashed lines) is closely related to the change of the damaged PSU fraction (not shown). This means that a constant proportion of repaired PSU can be found in the time-averaged activated state, what supports Janssen's argument that flashing light also indirectly contributes to higher productivity by reducing the amount of damaged PSU. At frequencies higher than 50 Hz the simulation data deviates increasingly from the linear regression. With regard to the results of chapter 8, it is likely that this deviation results from the flashing-light effect what will be substantiated later in this section. Clearly, the contribution of the FLE depends on the duty cycle. For $\tau_F = 0.5$ actually no effect can be observed what means that an increase of productivity is entirely a result of reduced photodamage. If τ_F decreases, the FLE becomes more pronounced.

The conclusions having been drawn so far are also supported by the ratio ϕ_{x_1} of activated PSU during the light and dark periods, which is depicted on the bottom left of figure 10.6. The quantity ϕ_{x_1} increases steadily with the flash frequency, which can be explained easily by the fact that activated PSU need a certain time for the complete relaxation to the resting state after the end of a light flash. The ratio of this time to the length of dark period becomes larger for higher flash frequencies so that the relaxation process affects ϕ_{x_1}. Strictly speaking, this effect is similar to the FLE because activated PSU are present during dark periods and enable the progress of the dark reaction (see 2.1.1). However, the small values of ϕ_{x_1} at low frequencies show that the reaction rates during the dark period are almost

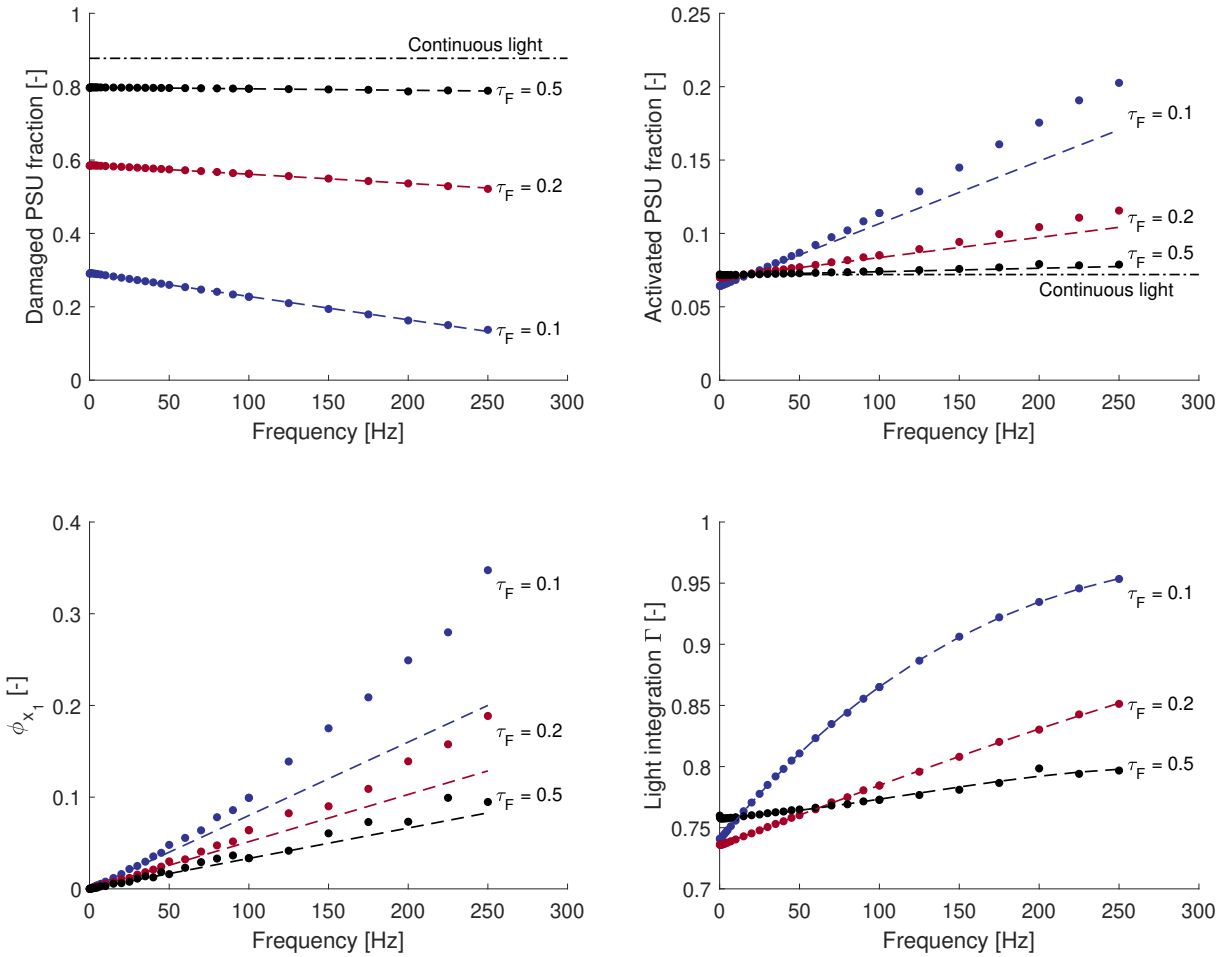

Figure 10.6.: Kinetics of photosynthesis under flashing light. The intensity of continuous and flashing light is $I_0 = 2000$ μE m^{-2}s^{-1} for all simulations. The dynamic simulations are evaluated by computing the time-average of the state variables over the last 10 flashes within the simulated physical time of 3000 seconds. Symbols denote simulation results and dashed lines indicate regression curves (see text for details). Top left: time-averaged fraction of damaged PSU. Top right: time-averaged fraction of activated PSU. Bottom left: time-averaged ratio of activated PSU during dark and light periods according to Eq. (10.8). Bottom right: Degree of light integration according to Eq. (10.7).

negligible. As long as all activated PSU relax during the dark period, one can expect a linear relation between ϕ_{x_1} and the flash frequency, what is also confirmed by the simulation data as indicated by the dashed regression lines, which were computed with data for $\nu_F < 10$ Hz. It can be seen that for $\nu_F > 50$ Hz the simulation data starts to deviate from the linear relation, what means that activated PSU exists during the entire dark period and the FLE becomes increasingly significant for the overall rate of photosynthesis. A quite good agreement exists between the frequencies at which the activated PSU fraction and ϕ_{x_1} start to deviate from the linear relations ($\tau_F = 0.1$: $\nu_F \approx 50$ Hz, $\tau_F = 0.2$: $\nu_F \approx 90 - 100$ Hz, $\tau_F = 0.5$: completely linear), what substantiates the aforementioned interpretation of the relationship between flash frequency and the fraction of activated PSU.

With regard to the degree of light integration as defined by Terry [45], one sees that the results of the analysis are only partially reflected therein. At low flash frequencies the highest degree of

light integration is predicted for $\tau_F = 0.5$, although the simulation results indicate that the FLE is induced only to a negligible extend under these conditions and that the positive effects of flashing light can entirely be explained by a reduced amount of damaged PSU. However, at higher frequencies and shorter duty cycles, Γ provides an adequate measure to compare effects of flashing light on the kinetics of photosynthesis. One should also keep in mind that such integral measures are required to evaluate experimental studies, where no or only limited information about PSU states and their dynamics are available.

Generally, the findings of the simulation study support the hypothesis of Janssen and also indicate a number of conclusions. The kinetic response of cells to flashing light consists of two superimposing effects, which are (i) an increase of activated PSU that is proportional to the decrease of damaged PSU and (ii) the actual flashing light effect. While the first effect dominates at low flash frequencies, both effects take place at higher frequencies, whereby their relative contribution depends on the light regime. It is likely that the cell species, the absolute light intensity, the light spectrum and gradients of light intensity additionally impact the extend of both effects on the culture scale, though this was not evaluated in the present section. An indicator for the strength of both effects can be achieved based on the regression between activated PSU and the flash frequency at low flash frequencies (see figure 10.6, top right), which provides a measure for the effect of reduced photoinhibition, as discussed before. An absolute estimate for this effect can be achieved by comparing the regression curve with the activated fraction of PSU under continuous light, thus

$$\phi_{PD} = x_{1,R}(\nu_F, \tau_F) - x_{1,C} \tag{10.9}$$

where $x_{1,R}(\nu_F)$ stands for the linear regression curve and $x_{1,C}$ for the fraction of activated PSU under continuous light. On the other hand, the difference between the activated fraction under flashing light and the regression line can be seen as a measure for the FLE.

$$\phi_{FLE} = x_{1,F}(\nu_F, \tau_F) - x_{1,R}(\nu_F, \tau_F) \tag{10.10}$$

where $x_{1,F}$ is the fraction of activated PSU under flashing light. As an example, the result for $\tau_F = 0.1$ is depicted in figure 10.7. Under the simulated conditions, the reduction of photoinhibition is the dominating effect for the simulated parameter range. Based on the presented results and the presumption of a linear decrease of damaged PSU with the flash frequency, it can be calculated that the effect of reduced photoinhibition reaches its maximum at $\nu_F \approx 460$ Hz for $\tau_F = 0.1$ and remains constant from thereon. In the present example, a light intensity of $I_0 = 2000\ \mu$E m^{-2}s^{-1} was assumed, which is already relatively high so that significant photodamage occurs under continuous light, what might overestimate the effect of reduced photoinhibition. Also, no spectral effects or the presence of light intensity gradi-

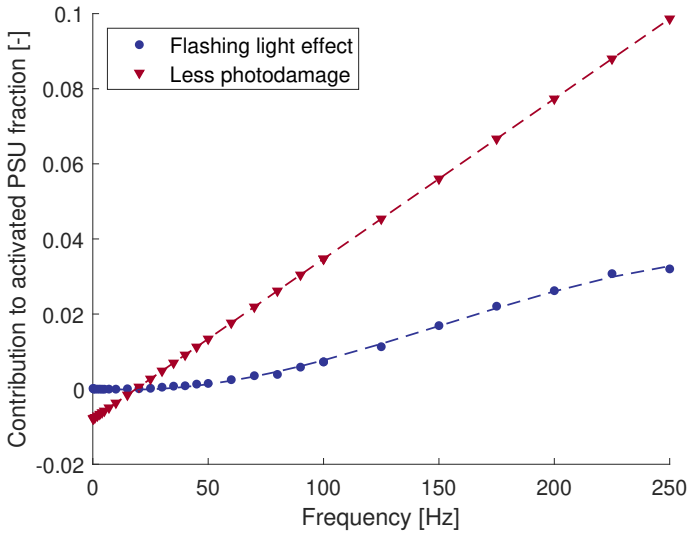

Figure 10.7.: Impact of the flashing-light effect and reduction of photodamage on the amount of activated PSU under flashing light for $\tau_F = 0.1$. The curves were computed with Eqs. (10.9) and (10.10) with data shown in figure 10.6. Further details for the computation of the curves are given in the text.

ents were considered for this simple estimate, but they can significantly affect the overall picture. This becomes clear if one considers that photodamage is only relevant in regions near the light source due to the attenuation of light in cell cultures. In contrast, if cells are shuttled between light and dark parts of the reactor, the FLE would also be induced in cells with lower degree of photodamage. Therefore, a systematic variation of parameters on the culture scale is required to obtain a general picture. Thereby, the distinction between two effects which both result from flashing light exposure might also help to explain scattered experimental data without clear trends [52] and provide a better understanding of the effects of different light regimes. The approach presented in this section might be a good starting point to investigate the relative contribution of both effects on productivity enhancement in more future studies to provide further clarification of the topic. Thereby, a computational difficulty lies in the stiff nature of the differential algebraic equation system, which results from the flashing light signal and needs careful selection of the numerical solvers and parameters to avoid erroneous simulations and data interpretation.

Returning to a technological point of view, the results of this section confirm that hydrodynamic mixing is not a suitable strategy to induce the FLE in populations of microalgae. It is possible that experimental results for the relationship of mixing and productivity enhancement were misinterpreted in the past and that observed effects were attributed erroneously to an induction of the FLE by means of hydrodynamic mixing. In contrast, the results of this work indicate that mixing in different PBR types is far too slow to induce the FLE. Therefore, the only possible solution for utilizing the FLE in order to enhance PBR productivity is the decoupling of light exposure and the flow, which can only be obtained by the dynamic modulation of artificial illumination sources. This does not necessarily mean that PBR operation should always occur under artificial light. But it indicates that the photon

conversion efficiency in PBR is determined by the light intensity gradient under natural light and can only be improved to a limited extend by reducing photoinhibition.

10.2.2. Decoupling the light regime from hydrodynamics by artificial illumination

The results presented in chapter 8 and the previous section indicate that hydrodynamic mixing is not suitable to tune the temporal light exposure towards a desired light regime in order to improve the operation of photobioreactors. Therefore, it seems reasonable to treat hydrodynamics and light supply separately as well as their respective functions in PBR. Without doubt, mixing of submersed cultures is important for gas-liquid mass transfer, nutrient supply and the prevention of sedimentation or biofouling but according to the results of this work, it should not be considered as the key to realize a tailored light exposure of individual cells.

In comparison to natural light sources, artificial sources provide a higher degree of flexibility and the opportunity to exactly control the illumination conditions. Agreement exists that light emitting diodes (LED) are most promising among the common light sources and that they will be the dominant type of light source in future [57, 304, 305]. They combine several beneficial operation characteristics like low heat emission and relatively high efficiency [304], but most importantly, LED are characterized by narrow emission spectra, different peak wavelengths and very fast reaction times, which are all important properties to design tailored light regimes.

The idea of employing LED for microalgal production is not new. Early applications proved that microalgae can grow under red light and that even higher cell densities can be reached in comparison to a full spectrum control [108]. In fact, the physiological response of various microalgae to specific wavelengths has been investigated in recent years and it was shown that productivity can be tuned by a proper selection of the emission spectrum by combining different types of LED [306–310]. In these works it was also observed that the biochemical composition is greatly affected by the provided light spectrum and that the up- and downregulation of different metabolites like pigments [306, 309] or lipids [308] can be triggered by exposing algae to light of certain wavelengths. Thereby, it must be taken into account that the definition of an optimal emission spectrum highly depends on the cultivated species [306]. Also the photon conversion efficiency can be improved by tuning the light emission spectrum under high light conditions [50], which was also observed experimentally by de Mooij et al. [311], who state that "*productivity and biomass specific light absorption are inversely correlated*". This is not surprising, because the strong absorption of red or blue light leads to the saturation of the dark reaction of photosynthesis, while yellow light penetrates more deeply into the culture and the rate of absorption becomes more homogeneous. With regard to the application of LED to microalgae cultivation, these examples show that the adaption of the light emission spectrum during the cultivation might enable

higher productivities and efficiencies as well as new possibilities to trigger the expression of target molecules.

In addition to the opportunity to change the light emission spectrum, artificial sources provide the possibility to adapt the emitted overall light intensity dynamically. Thereby, the modulation of the emission intensity can occur on different time scales. On very short time scales, high frequency pulsation of light can induce the FLE and enhance the reactor productivity as it was shown in chapter 8. Although this strategy for improving PBR operation was already suggested by Gordon and Polle in 2007 [50], continuous light supply is still the standard way of illumination, even on the lab scale. This lack of implementation might be due to the need for signal generators which are able to produce high frequency flashing light [106] and the related equipment costs. To date, the maximum frequencies which can be obtained by pulse width modulation range between 150 and 300 Hz [106], what is too low to exploit the full potential of the FLE, at least for some species. Higher frequencies can be obtained by so-called overloading at the cost of lower wall-plug efficiencies [106]. However, the utilization of cheap microcontrollers was shown to be a feasible mean to create high frequency light flashes [27], which seems promising for future studies. On longer time scales, the modulation of the time-averaged light intensity might be advantageous. If the biomass concentration increases with time, light penetration into the culture becomes increasingly limiting for the course of the process. A common way to react to such a situation is to dilute the culture in order to maintain an optimal operation point (Turbidostat mode). Alternatively, PBR operation in a Luminostat mode was suggested [312, 313], which is characterized by the optimization of the source intensity with respect to the energy demand of the biomass. It was shown that this approach led to faster cell growth, higher final concentrations and improved energy efficiency [312] but clearly, it is coupled to artificial illumination sources.

Summarizing the aforementioned, light supply by LED sources in principle enables to tune the light regime dynamically with respect to a certain process state in order to provide optical conditions for cell growth and the production of desired metabolites. The idea of a dynamic optimization of illumination conditions was already discussed in chapter 7, see section 4 therein, and seems to be one of the most promising approaches to enhance the capabilities of artificially illuminated PBR. Ideally, an optimization should address the light quality (e.g. the spectrum) as well as high frequency and long term modulations of the light intensity. Accompanied with this, several research needs arise. As mentioned above, cheap and efficient controllers for LED sources must be integrated in PBR control systems. Moreover, real-time multi-parameter optimization requires fast algorithms and a robust formulation of the optimization problem. Also, prior to application, the light requirements of different species must be known so that future research is needed to provide more experimental data to calibrate models like photosynthetic factory models or metabolic flux models, which can predict the cellular response to a dynamic light regime. Another unsolved issue is the development of cheap and accurate (soft-)sensors

for the online monitoring of optical cell properties and pigmentation, which are not readily available. Usually, process monitoring of algae cultures is based on turbidity measurements at single wavelengths [292], which alone is definitively not sufficient to obtain information about optical cell properties. The measurement of pigmentation might be a key issue, since it determines the spatial and spectral light distribution and mirrors the physiological state of the cell culture. Optical fibers and spectrometers like the ones being used in section 9.4 can be used to collect data with high spectral resolution and coupled with equation-based or data driven models to obtain the information of interest. The technological level of microalgae production in terms of sensing and control is still relatively low and several possibilities for improvements exist, which altogether might enhance the efficiency of light utilization in photobioreactors. Thereby, internally illuminated PBR [97] can be a suitable complement to artificial light sources.

Immediately, the question arises how feasible microalgae production by means of artificial illumination can be beyond the lab scale. While sunlight for outdoor cultivation is freely available, artificial lightning requires additional electric power. Blanken et al. [314] estimated the electricity costs and conducted a case study to compare the energetic efficiency of microalgae production under sunlight and artificial light, whereby the electric power was assumed to be generated via different pathways (photovoltaics, coal). According to their result, the energetic efficiency, measured as the amount of primary energy being stored into biomass, is always worse in comparison to the direct use of sunlight for PBR illumination and the costs for electric energy cause a significant increase of the biomass production costs. The results of the analysis were also confirmed in other works [57]. This is somehow disillusioning but one should consider that (i) illumination with red LED was assumed, which is inefficient from an energetic point of view [311], (ii) continuous illumination was assumed, thus no benefits of high frequent light flashing were considered, (iii) technological improvements in photovoltaics and renewable energies as well as in LED technology may lead to better efficiencies what would improve the energy balance. Indeed, under flashing light the energy requirement per gramm dry weight was shown to be significantly reduced (about factor of 5) by means of light integration [27], what changes the picture drastically. Therefore, a tailored light regime affects additional costs for electricity and the efficiency of energy utilization, which however, has not yet been demonstrated beyond the lab scale. The economic reasonableness of applying artificial illumination will also depend on the long term evolution of electricity costs against the background of climate change. In any case, cultivating microalgae under artificial illumination seems not to be reasonable to substitute agricultural products on large scales, thus exploiting them as a source of food protein or biofuels. It is more likely that this type of cultivation offers opportunities to produce high valuable products under industrial conditions in optimized and well-controlled physical environments. For these products energy efficiency is less

important and constraints for the costs can be relaxed due to the higher products value [314]. Further research on artificially illuminated PBR should therefore focus on these kind of applications.

10.3. Concluding remarks

The objective of this chapter was to discuss the distribution of light in PBR and how it affects the cellular growth kinetics and their prediction. It was shown that the outcome of different light propagation models is strongly affected by parameter uncertainty, what may result in prediction errors with a similar order of magnitude as the difference between different light propagation models. The achievement of full light integration by means of hydrodynamic mixing seems to be unrealistic and even partial light integration is limited by mechanical damage of cells. Observed correlations between the mixing intensity and gains of PBR productivity might be explained by a reduction of photoinhibition under high light conditions rather than by the induction of the FLE. Tailoring the light exposure to physiological requirements seems possible by artificial illumination, if technological improvements in the fields of sensing and control can be realized under the constraint of low capital and operation costs. In future, these technologies could enable well-defined photobiotechnological production processes of products with high value under industrial conditions.

11. Conclusions and Outlook

The objective of this work was to evaluate the interplay of light distribution, hydrodynamic mixing and cellular reaction kinetics in photobioreactors with a special focus on the flashing-light effect. For this purpose, numerical techniques were developed and applied in simulation studies to estimate the impact of different physical environments in bubble column photobioreactors on the kinetics of microalgal photosynthesis and cell growth. Therefore, the green microalgae *Chlamydomonas reinhardtii* was chosen as a model organism.

The spatio-temporal distribution of light is the key element for efficient photobiotechnological production processes. In order to enable a comprehensive examination of the light distribution in photobioreactors, a new numerical model for three-dimensional light propagation was developed within the lattice Boltzmann framework. The model takes absorption and three-dimensional scattering into account and was validated by means of Monte Carlo simulations and experiments. It was shown that it is capable of simulating light transfer within a broad range of optical properties, although further research is needed to improve boundary conditions and enable the simulation of light transfer in more complex geometries. In its recent state, the model is already implemented in the open source lattice Boltzmann library *openLB* [315] and will be available in one of the upcoming code releases. By this, important benefits of lattice Boltzmann methods like efficient parallelization can be utilized in future studies, which can of course concern also other types of radiation and different applications than radiative transfer in microalgae culture.

Concerning the transport of light in photobioreactors, it was shown that considering the presence of a gaseous phase in light propagation models is of minor importance for the prediction of cellular growth. This finding was explained by two reasons, namely that light absorption by the cell culture is clearly the dominating feature at most wavelengths and consequently, the light intensity is low at locations where gas bubble are located so that effects of the gas phase on light distribution are weak. In addition, the consideration of gas bubbles in light propagation models only makes sense if the optical properties of a cell culture can be precisely determined, which is still not straightforward today so that predictions of light distributions are uncertain anyway. The results may be different for other sparger types, much higher gas superficial velocities or smaller bubbles which tend to move towards the reactor wall due to the action of lift forces. However, the general trend that an increasing biomass concentration counteracts any beneficial effect of the gas phase on the distribution of light can also be expected in these cases.

In accordance with these findings, the presence of the gas phase was not further considered for the computation of light distributions and additional simulations focused on the effects of pneumatic mixing on the kinetics of the photosynthetic reactions, in particular on the induction of the flashing-light effect. For different operation points of a bubble column photobioreactor, it was shown that the shuttling of algae cell between light and dark zones of the culture is not fast enough to induce the flashing-light effect in *C. reinhardtii*. A further discussion of the topic indicated that the flashing-light effect will also be not induced by hydrodynamic mixing in tubular photobioreactors because shear damage of cells and the increasing demand for mixing energy limit the reachable light/dark frequencies. This leads to the conclusion that the productivity of conventional solar-irradiated photobioreactors can not be improved significantly by the induction of the flashing-light effect. However, additional simulations indicated that hydrodynamic mixing might contribute to a higher reactor productivity by reducing the degree of photoinhibition. The quantification of this effect should be part of future work.

In contrast, it was found that the productivity of photobioreactors can be enhanced by means of pulsed light sources, even on the scale of conventional photobioreactors. Clearly, pulsed illumination can only be realized by means of artificial light sources and LED appear most promising for this purpose because they unify several beneficial operation characteristics and offer additional opportunities such as the adaption of emission spectra and intensity during cultivation processes in order to achieve tailored light regimes. However, the functionality for high frequency pulsation is not yet a standard feature and needs further development.

What comes next? How can the cultivation of microalgae look like in future and are the goals of substituting or complementing fossil and agricultural resources with microalgae biomass realistic perspectives? Genetic engineering seems to be a major requirement for a successive production of microalgae and especially for algae-based biofuels, either by engineering the photosynthetic apparatus [50] or metabolic pathways involved in the biosynthesis of lipids [316, 317]. Concerning the production of food or feed, the situation may be more complicated with regard to regulatory constraints and consumer expectations. Turning back to a process engineering perspective, the results of this work and recent research imply different scenarios for future production technologies.

The hope that the productivity of solar-irradiated photobioreactors can be significantly increased by hydrodynamic mixing and the induction of the flashing-light effect seems not to be justified. Therefore, the current constraints of the availability of solar energy and the efficiency of its utilization will also determine the cultivation process in future. To date, the production cost of microalgae biomass is still in the order of several EUR/kg dry biomass [318], so that in comparison to conventional agriculture microalgae can not be considered as a competitive feedstock for the production of feed and food protein or even biofuels. If the productivity under sunlight can not be increased significantly, production must become cheaper. In fact, current trends point towards the installation of simple cultivation systems

like open ponds in greenhouses or systems made out of plastics [318], which are cheap and require little maintenance and manpower. Thus, for the production of microalgae under sunlight, one must orientate on conventional agricultural production systems, where crops are grown with a minimum of effort and energy. Besides, the added value of the biomass in this scenario should ideally be increased by means of biorefinery approaches and the gain of multiple products [13]. Also, a production in an agricultural environment can or should make usage of synergistic effects, like the coupling of algae production facilities to co-generation units to provide thermal power or to wastewater treatments for nutrient recovery [14]. Of course, these possibilities might be restricted by the type of products and related legal regulations. In summary, in a first scenario, microalgae will be produced in low-cost facilities under sunlight and low to medium efficiency of light utilization in an agricultural environment.

Another scenario is the outdoor production of metabolites like pigments in closed photobioreactors, e.g. tubular photobioreactors. This scenario has been already realized today in countries where ideal conditions for microalgae cultivation exists, e.g. high solar irradiation, adequate temperatures and the possibility for production over the whole year [318]. Such production sites are limited and additionally must be attractive in terms of labor costs.

A different scenario becomes possible, if artificial illumination sources are employed. The benefits of these, and especially LED, were discussed earlier. However, the related costs for installation and energy are still high so that the production might become even more costly in comparison to the common cultivation under sunlight [314]. Thus, artificially illuminated photobioreactors only make sense for products with high market values like pharmaceuticals, which in addition must be unique for microalgae. A possible future scenario could then be the efficient production of microalgae in high-tech indoor cultivation systems with tailored light regimes under industrial conditions. Due to the limited available space in factories, emerging concepts like the cultivation of immobilized algae in biofilms [319] could be part of this scenario since the achievable biomass concentrations are much higher in comparison to conventional photobioreactors. However, the proof of the concept beyond the lab scale has not yet been demonstrated. In summary, a third scenario of algae production consists of high-tech production facilities for the production of metabolites with a high market value, which operate under well-defined conditions and contain artificial light sources. It is questionable whether such a way of production would be still sustainable, but it could contribute to replace even less sustainable ways of production.

The drawn scenarios indicate that there will be no ultimate way to cultivate microalgae. Rather, the decision of a way of cultivation will depend on location, costs and the desired products [320]. To promote a breakthrough of microalgae biotechnology, the investigation of new potential products and their applications is one of the most important tasks for researchers in the near future because each of the scenarios is more probable to be realized if the added value of the biomass is maximized.

References

[1] M. Vigani et al. “Food and feed products from micro-algae: Market opportunities and challenges for the EU”. In: *Trends in Food Science & Technology* 42.1 (2015), pp. 81–92.

[2] Y. Chisti. “Biodiesel from microalgae”. In: *Biotechnology Advances* 25.3 (2007), pp. 294–306.

[3] M. van Krimpen et al. *Cultivation, processing and nutritional aspects for pigs and poultry of European protein sources as alternatives for imported soybean products*. Tech. rep. Lelystad: Wageningen UR Livestock Research, 2013.

[4] F. Acién et al. “Production cost of a real microalgae production plant and strategies to reduce it”. In: *Biotechnology Advances* 30.6 (2012), pp. 1344–1353.

[5] R. Kothari et al. “Microalgal cultivation for value-added products: a critical enviro-economical assessment”. In: *3 Biotech* 7.4 (2017).

[6] R. Halim, M. K. Danquah, and P. A. Webley. “Extraction of oil from microalgae for biodiesel production: A review”. In: *Biotechnology Advances* 30.3 (2012), pp. 709–732.

[7] L. Batan et al. “Net Energy and Greenhouse Gas Emission Evaluation of Biodiesel Derived from Microalgae”. In: *Environmental Science & Technology* 44.20 (2010), pp. 7975–7980.

[8] M. Tredici et al. “Energy balance of algal biomass production in a 1-ha “Green Wall Panel” plant: How to produce algal biomass in a closed reactor achieving a high Net Energy Ratio”. In: *Applied Energy* 154 (2015), pp. 1103–1111.

[9] P. K. Naraharisetti, P. Das, and P. N. Sharratt. “Critical factors in energy generation from microalgae”. In: *Energy* 120 (2017), pp. 138–152.

[10] L. Probst et al. *Sustainable, Safe and Nutritious Food - New nutrient sources*. Tech. rep. European Union, 2015.

[11] J. O. Westman and C. J. Franzén. “Current progress in high cell density yeast bioprocesses for bioethanol production”. In: *Biotechnology Journal* 10.8 (2015), pp. 1185–1195.

[12] F. Bumbak et al. “Best practices in heterotrophic high-cell-density microalgal processes: achievements, potential and possible limitations”. In: *Applied Microbiology and Biotechnology* 91.1 (2011), pp. 31–46.

[13] K. W. Chew et al. “Microalgae biorefinery: High value products perspectives”. In: *Bioresource Technology* 229 (2017), pp. 53–62.

[14] J. Trivedi et al. “Algae based biorefinery—How to make sense?” In: *Renewable and Sustainable Energy Reviews* 47 (2015), pp. 295–307.

[15] Â. P. Matos. “The Impact of Microalgae in Food Science and Technology”. In: *Journal of the American Oil Chemists’ Society* 94.11 (2017), pp. 1333–1350.

[16] M. P. Caporgno and A. Mathys. “Trends in Microalgae Incorporation Into Innovative Food Products With Potential Health Benefits”. In: *Frontiers in Nutrition* 5 (2018).

[17] E. S. Garcia et al. “Techno-Functional Properties of Crude Extracts from the Green Microalga Tetraselmis suecica”. In: *Journal of Agricultural and Food Chemistry* 66.29 (2018), pp. 7831–7838.

[18] D. Jha et al. “Microalgae-based Pharmaceuticals and Nutraceuticals: An Emerging Field with Immense Market Potential”. In: *ChemBioEng Reviews* 4.4 (2017), pp. 257–272.

[19] J. C. Ogbonna and H. Tanaka. “Light requirement and photosynthetic cell cultivation - Development of processes for efficient light utilization in photobioreactors”. In: *Journal of Applied Phycology* 12.3/5 (2000), pp. 207–218.

[20] P. J. le B. Williams and L. M. L. Laurens. “Microalgae as biodiesel & biomass feedstocks: Review & analysis of the biochemistry, energetics & economics”. In: *Energy & Environmental Science* 3.5 (2010), p. 554.

[21] J. Wolf et al. “Multifactorial comparison of photobioreactor geometries in parallel microalgae cultivations”. In: *Algal Research* 15 (2016), pp. 187–201.

[22] M. Barceló-Villalobos et al. “Evaluation of photosynthetic light integration by microalgae in a pilot-scale raceway reactor”. In: *Bioresource Technology* 280 (2019), pp. 404–411.

[23] B. Kok. “Photosynthesis in flashing light”. In: *Biochimica et Biophysica Acta* 21.2 (1956), pp. 245–258.

[24] J. U. Grobbelaar. “The influence of light/dark cycles in mixed algal cultures on their productivity”. In: *Bioresource Technology* 38.2-3 (1991), pp. 189–194.

[25] J. Degen et al. “A novel airlift photobioreactor with baffles for improved light utilization through the flashing light effect”. In: *Journal of Biotechnology* 92.2 (2001), pp. 89–94.

[26] K.-H. Park and C.-G. Lee. “Effectiveness of flashing light for increasing photosynthetic efficiency of microalgal cultures over a critical cell density”. In: *Biotechnology and Bioprocess Engineering* 6.3 (2001), pp. 189–193.

[27] A. A. Lunka and D. J. Bayless. “Effects of flashing light-emitting diodes on algal biomass productivity”. In: *Journal of Applied Phycology* 25.6 (2013), pp. 1679–1685.

[28] P. Hartmann, Q. Béchet, and O. Bernard. “The effect of photosynthesis time scales on microalgae productivity”. In: *Bioprocess and Biosystems Engineering* 37.1 (2013), pp. 17–25.

[29] A. M. J. Kliphuis et al. “Photosynthetic efficiency of Chlorella sorokiniana in a turbulently mixed short light-path photobioreactor”. In: *Biotechnology Progress* 26.3 (2010), pp. 687–696.

[30] G. Olivieri et al. “Photobioreactors for microalgal cultures: A Lagrangian model coupling hydrodynamics and kinetics”. In: *Biotechnology Progress* 31.5 (2015), pp. 1259–1272.

[31] A. Richmond, ed. *Handbook of Microalgal Culture*. Blackwell Publishing Ltd, 2003.

[32] P. G. Laura Barsanti. *Algae*. CRC Press, 2014. 361 pp.

[33] N. A. Campbell and J. B. Reece. *Biologie*. Spektrum-Akademischer Vlg, 2003.

[34] C. Vejrazka et al. “Photosynthetic efficiency and oxygen evolution of Chlamydomonas reinhardtii under continuous and flashing light”. In: *Applied Microbiology and Biotechnology* 97.4 (2012), pp. 1523–1532.

[35] C. Wilhelm and D. Selmar. “Energy dissipation is an essential mechanism to sustain the viability of plants: The physiological limits of improved photosynthesis”. In: *Journal of Plant Physiology* 168.2 (2011), pp. 79–87.

[36] S. Aiba. “Growth kinetics of photosynthetic microorganisms”. In: *Advances in Biochemical Engineering/Biotechnology*. Springer Berlin Heidelberg, 1982, pp. 85–156.

[37] Q. Béchet, A. Shilton, and B. Guieysse. “Modeling the effects of light and temperature on algae growth: State of the art and critical assessment for productivity prediction during outdoor cultivation”. In: *Biotechnology Advances* 31.8 (2013), pp. 1648–1663.

[38] C. Wilhelm and T. Jakob. “Balancing the conversion efficiency from photon to biomass”. In: *Microalgal Biotechnology: Potential and Production*. Ed. by C. Posten and C. Walter. DE GRUYTER, 2012.

[39] A. Richmond. “Principles for attaining maximal microalgal productivity in photobioreactors: an overview”. In: *Asian Pacific Phycology in the 21st Century: Prospects and Challenges*. Springer Netherlands, 2004, pp. 33–37.

[40] J. Pruvost, J.-F. Cornet, and J. Legrand. “Hydrodynamics influence on light conversion in photobioreactors: An energetically consistent analysis”. In: *Chemical Engineering Science* 63.14 (2008), pp. 3679–3694.

[41] C. Posten. “Design principles of photo-bioreactors for cultivation of microalgae”. In: *Engineering in Life Sciences* 9.3 (2009), pp. 165–177.

[42] P. G. Falkowski, H. Lin, and M. Y. Gorbunov. “What limits photosynthetic energy conversion efficiency in nature? Lessons from the oceans”. In: *Philosophical Transactions of the Royal Society B: Biological Sciences* 372.1730 (2017), p. 20160376.

[43] E. M. Grima et al. “Evaluation of photosynthetic efficiency in microalgal cultures using averaged irradiance”. In: *Enzyme and Microbial Technology* 21.5 (1997), pp. 375–381.

[44] M. Cuaresma et al. “Horizontal or vertical photobioreactors? How to improve microalgae photosynthetic efficiency”. In: *Bioresource Technology* 102.8 (2011), pp. 5129–5137.

[45] K. L. Terry. “Photosynthesis in modulated light: Quantitative dependence of photosynthetic enhancement on flashing rate”. In: *Biotechnology and Bioengineering* 28.7 (1986), pp. 988–995.

[46] Y. Zarmi, G. Bel, and C. Aflalo. “Theoretical Analysis of Culture Growth in Flat-Plate Bioreactors: The Essential Role of Timescales”. In: *Handbook of Microalgal Culture*. John Wiley & Sons, Ltd, 2013, pp. 205–224.

[47] D. Iluz, I. Alexandrovich, and Z. Dubinsky. “The Enhancement of Photosynthesis by Fluctuating Light”. In: *Artificial Photosynthesis*. InTech, 2012.

[48] J. U. Grobbelaar, L. Nedbal, and V. Tichý. “Influence of high frequency light/dark fluctuations on photosynthetic characteristics of microalgae photoacclimated to different light intensities and implications for mass algal cultivation”. In: *Journal of Applied Phycology* 8.4-5 (1996), pp. 335–343.

[49] M. Janssen et al. “Photosynthetic efficiency of Dunaliella tertiolecta under short light/dark cycles”. In: *Enzyme and Microbial Technology* 29.4-5 (2001), pp. 298–305.

[50] J. M. Gordon and J. E. W. Polle. “Ultrahigh bioproductivity from algae”. In: *Applied Microbiology and Biotechnology* 76.5 (2007), pp. 969–975.

[51] S. Xue, Z. Su, and W. Cong. “Growth of Spirulina platensis enhanced under intermittent illumination”. In: *Journal of Biotechnology* 151.3 (2011), pp. 271–277.

[52] E. Sforza et al. “Adjusted Light and Dark Cycles Can Optimize Photosynthetic Efficiency in Algae Growing in Photobioreactors”. In: *PLoS ONE* 7.6 (2012). Ed. by A. Webber, e38975.

[53] C. Vejrazka et al. “The role of an electron pool in algal photosynthesis during sub-second light–dark cycling”. In: *Algal Research* 12 (2015), pp. 43–51.

[54] C. Brindley et al. “Light regime optimization in photobioreactors using a dynamic photosynthesis model”. In: *Algal Research* 16 (2016), pp. 399–408.

[55] D. Simionato et al. “Optimization of light use efficiency for biofuel production in algae”. In: *Biophysical Chemistry* 182 (2013), pp. 71–78.

[56] S. Abu-Ghosh et al. “Flashing light in microalgae biotechnology”. In: *Bioresource Technology* 203 (2016), pp. 357–363.

[57] M. D. Ooms et al. “Photon management for augmented photosynthesis”. In: *Nature Communications* 7 (2016), p. 12699.

[58] M. Janssen et al. “Specific growth rate of Chlamydomonas reinhardtii and Chlorella sorokiniana under medium duration light/dark cycles: 13–87 s”. In: *Journal of Biotechnology* 70.1-3 (1999), pp. 323–333.

[59] M. Janssen et al. “Efficiency of light utilization of Chlamydomonas reinhardtii under medium-duration light/dark cycles”. In: *Journal of Biotechnology* 78.2 (2000), pp. 123–137.

[60] M. J. Barbosa et al. “Microalgae cultivation in air-lift reactors: Modeling biomass yield and growth rate as a function of mixing frequency”. In: *Biotechnology and Bioengineering* 82.2 (2003), pp. 170–179.

[61] H. Takache, J. Pruvost, and H. Marec. “Investigation of light/dark cycles effects on the photosynthetic growth of Chlamydomonas reinhardtii in conditions representative of photobioreactor cultivation”. In: *Algal Research* 8 (2015), pp. 192–204.

[62] J. Yarnold, I. L. Ross, and B. Hankamer. “Photoacclimation and productivity of Chlamydomonas reinhardtii grown in fluctuating light regimes which simulate outdoor algal culture conditions”. In: *Algal Research* 13 (2016), pp. 182–194.

[63] Y. Nishiyama, S. I. Allakhverdiev, and N. Murata. “Protein synthesis is the primary target of reactive oxygen species in the photoinhibition of photosystem II”. In: *Physiologia Plantarum* 142.1 (2011), pp. 35–46.

[64] H. L. MacIntyre et al. “Photoacclimation of Photosynthesis Irradiance Response Curves and Photosynthetic Pigments in Microalgae and Cyanobacteria”. In: *Journal of Phycology* 38.1 (2002), pp. 17–38.

[65] E. Erickson, S. Wakao, and K. K. Niyogi. “Light stress and photoprotection in Chlamydomonas reinhardtii”. In: *The Plant Journal* 82.3 (2015), pp. 449–465.

[66] E. Lee, M. Jalalizadeh, and Q. Zhang. “Growth kinetic models for microalgae cultivation: A review”. In: *Algal Research* 12 (2015), pp. 497–512.

[67] P. Darvehei, P. A. Bahri, and N. R. Moheimani. “Model development for the growth of microalgae: A review”. In: *Renewable and Sustainable Energy Reviews* 97 (2018), pp. 233–258.

[68] A. D. Jassby and T. Platt. “Mathematical formulation of the relationship between photosynthesis and light for phytoplankton”. In: *Limnology and Oceanography* 21.4 (1976), pp. 540–547.

[69] W. Blanken et al. “Predicting microalgae growth”. In: *Algal Research* 14 (2016), pp. 28–38.

[70] P. Eilers and J. Peeters. “A model for the relationship between light intensity and the rate of photosynthesis in phytoplankton”. In: *Ecological Modelling* 42.3-4 (1988), pp. 199–215.

[71] B.-P. Han. “Photosynthesis–Irradiance Response at Physiological Level: a Mechanistic Model”. In: *Journal of Theoretical Biology* 213.2 (2001), pp. 121–127.

[72] X. Wu and J. C. Merchuk. “A model integrating fluid dynamics in photosynthesis and photoinhibition processes”. In: *Chemical Engineering Science* 56.11 (2001), pp. 3527–3538.

[73] B.-P. Han. “A Mechanistic Model of Algal Photoinhibition Induced by Photodamage to Photosystem-II”. In: *Journal of Theoretical Biology* 214.4 (2002), pp. 519–527.

[74] F. C. Rubio et al. “A mechanistic model of photosynthesis in microalgae”. In: *Biotechnology and Bioengineering* 81.4 (2002), pp. 459–473.

[75] I. A. Papadakis, K. Kotzabasis, and K. Lika. “Modeling the dynamic modulation of light energy in photosynthetic algae”. In: *Journal of Theoretical Biology* 300 (2012), pp. 254–264.

[76] F. García-Camacho et al. “A mechanistic model of photosynthesis in microalgae including photoacclimation dynamics”. In: *Journal of Theoretical Biology* 304 (2012), pp. 1–15.

[77] A. Nikolaou et al. “Dynamic coupling of photoacclimation and photoinhibition in a model of microalgae growth”. In: *Journal of Theoretical Biology* 390 (2016), pp. 61–72.

[78] A. Bernardi et al. “High-Fidelity Modelling Methodology of Light-Limited Photosynthetic Production in Microalgae”. In: *PLOS ONE* 11.4 (2016). Ed. by I. D. Smet, e0152387.

[79] P. Rudnicki et al. “A comparative study of photosynthetic unit models for algal growth rate and fluorescence prediction under light/dark cycles”. In: *Algal Research* 24 (2017), pp. 227–236.

[80] X. Wu and J. C. Merchuk. “Simulation of algae growth in a bench-scale bubble column reactor”. In: *Biotechnology and Bioengineering* 80.2 (2002), pp. 156–168.

[81] J. Marshall and K. Sala. “A stochastic Lagrangian approach for simulating the effect of turbulent mixing on algae growth rate in a photobioreactor”. In: *Chemical Engineering Science* 66.3 (2011), pp. 384–392.

[82] X. Gao, B. Kong, and R. D. Vigil. “Characteristic time scales of mixing, mass transfer and biomass growth in a Taylor vortex algal photobioreactor”. In: *Bioresource Technology* 198 (2015), pp. 283–291.

[83] X. Gao, B. Kong, and R. D. Vigil. “Comprehensive computational model for combining fluid hydrodynamics, light transport and biomass growth in a Taylor vortex algal photobioreactor: Lagrangian approach”. In: *Bioresource Technology* 224 (2017), pp. 523–530.

[84] X. Gao, B. Kong, and R. D. Vigil. “Multiphysics simulation of algal growth in an airlift photobioreactor: Effects of fluid mixing and shear stress”. In: *Bioresource Technology* 251 (2018), pp. 75–83.

[85] P. O. “Photobioreactors: production systems for phototrophic microorganisms”. In: *Applied Microbiology and Biotechnology* 57.3 (2001), pp. 287–293.

[86] A. P. Carvalho, L. A. Meireles, and F. X. Malcata. “Microalgal Reactors: A Review of Enclosed System Designs and Performances”. In: *Biotechnology Progress* 22.6 (2006), pp. 1490–1506.

[87] C. Ugwu, H. Aoyagi, and H. Uchiyama. “Photobioreactors for mass cultivation of algae”. In: *Bioresource Technology* 99.10 (2008), pp. 4021–4028.

[88] R. Singh and S. Sharma. “Development of suitable photobioreactor for algae production – A review”. In: *Renewable and Sustainable Energy Reviews* 16.4 (2012), pp. 2347–2353.

[89] G. Olivieri, P. Salatino, and A. Marzocchella. “Advances in photobioreactors for intensive microalgal production: configurations, operating strategies and applications”. In: *Journal of Chemical Technology & Biotechnology* 89.2 (2013), pp. 178–195.

[90] J. C. G. Cañedo and G. L. L. Lizárraga. “Considerations for Photobioreactor Design and Operation for Mass Cultivation of Microalgae”. In: *Algae - Organisms for Imminent Biotechnology*. InTech, 2016.

[91] Q. Huang et al. “Design of Photobioreactors for Mass Cultivation of Photosynthetic Organisms”. In: *Engineering* 3.3 (2017), pp. 318–329.

[92] L. Travieso et al. “A helical tubular photobioreactor producing Spirulina in a semicontinuous mode”. In: *International Biodeterioration & Biodegradation* 47.3 (2001), pp. 151–155.

[93] I. Perner-Nochta and C. Posten. “Simulations of light intensity variation in photobioreactors”. In: *Journal of Biotechnology* 131.3 (2007), pp. 276–285.

[94] Q. Zhang et al. “Study of hydrodynamic characteristics in tubular photobioreactors”. In: *Bioprocess and Biosystems Engineering* 36.2 (2012), pp. 143–150.

[95] E. Molina et al. “Tubular photobioreactor design for algal cultures”. In: *Journal of Biotechnology* 92.2 (2001), pp. 113–131.

[96] A. S. Mirón et al. “Bubble-column and airlift photobioreactors for algal culture”. In: *AIChE Journal* 46.9 (2000), pp. 1872–1887.

[97] M. Heining and R. Buchholz. “Photobioreactors with internal illumination - A survey and comparison”. In: *Biotechnology Journal* 10.8 (2015), pp. 1131–1137.

[98] J. H. de Vree et al. “Comparison of four outdoor pilot-scale photobioreactors”. In: *Biotechnology for Biofuels* 8.1 (2015).

[99] C. J. Hulatt and D. N. Thomas. “Energy efficiency of an outdoor microalgal photobioreactor sited at mid-temperate latitude”. In: *Bioresource Technology* 102.12 (2011), pp. 6687–6695.

[100] N.-H. Norsker et al. “Microalgal production — A close look at the economics”. In: *Biotechnology Advances* 29.1 (2011), pp. 24–27.

[101] M. R. Tredici et al. “Techno-economic analysis of microalgal biomass production in a 1-ha Green Wall Panel (GWP®) plant”. In: *Algal Research* 19 (2016), pp. 253–263.

[102] A. Melis. “Solar energy conversion efficiencies in photosynthesis: Minimizing the chlorophyll antennae to maximize efficiency”. In: *Plant Science* 177.4 (2009), pp. 272–280.

[103] L. Wobbe and C. Remacle. “Improving the sunlight-to-biomass conversion efficiency in microalgal biofactories”. In: *Journal of Biotechnology* 201 (2015), pp. 28–42.

[104] A. S. Mirón et al. “Shear stress tolerance and biochemical characterization of Phaeodactylum tricornutum in quasi steady-state continuous culture in outdoor photobioreactors”. In: *Biochemical Engineering Journal* 16.3 (2003), pp. 287–297.

[105] A. P. Carvalho et al. “Light requirements in microalgal photobioreactors: an overview of biophotonic aspects”. In: *Applied Microbiology and Biotechnology* 89.5 (2011), pp. 1275–1288.

[106] P. S. Schulze et al. “Flashing LEDs for Microalgal Production”. In: *Trends in Biotechnology* 35.11 (2017), pp. 1088–1101.

[107] S.-K. Wang et al. “Microalgae cultivation in photobioreactors: An overview of light characteristics”. In: *Engineering in Life Sciences* 14.6 (2014), pp. 550–559.

[108] C.-G. Lee and B. Palsson. “High-density algal photobioreactors using light-emitting diodes”. In: *Biotechnology and Bioengineering* 44.10 (1994), pp. 1161–1167.

[109] A. S. Mirón et al. “Comparative evaluation of compact photobioreactors for large-scale monoculture of microalgae”. In: *Journal of Biotechnology* 70.1-3 (1999), pp. 249–270.

[110] H. Berberoglu, J. Yin, and L. Pilon. “Light transfer in bubble sparged photobioreactors for H2 production and CO2 mitigation”. In: *International Journal of Hydrogen Energy* 32.13 (2007), pp. 2273–2285.

[111] M. D. Ooms et al. “Light dilution via wavelength management for efficient high-density photobioreactors”. In: *Biotechnology and Bioengineering* 114.6 (2017), pp. 1160–1169.

[112] B. D. Fernandes et al. “Light Regime Characterization in an Airlift Photobioreactor for Production of Microalgae with High Starch Content”. In: *Applied Biochemistry and Biotechnology* 161.1-8 (2010), pp. 218–226.

[113] E. Lee, R.-L. Heng, and L. Pilon. “Spectral optical properties of selected photosynthetic microalgae producing biofuels”. In: *Journal of Quantitative Spectroscopy and Radiative Transfer* 114 (2013), pp. 122–135.

[114] R. Kandilian et al. “Comparison of experimentally and theoretically determined radiation characteristics of photosynthetic microorganisms”. In: *Journal of Quantitative Spectroscopy and Radiative Transfer* 175 (2016), pp. 30–45.

[115] D. Fuente et al. “Light distribution and spectral composition within cultures of micro-algae: Quantitative modelling of the light field in photobioreactors”. In: *Algal Research* 23 (2017), pp. 166–177.

[116] G. Marotta et al. “Reflection-refraction effects on light distribution inside tubular photobioreactors”. In: *The Canadian Journal of Chemical Engineering* 95.9 (2017), pp. 1646–1651.

[117] A. Jacobi et al. “Advanced photobioreactor LED illumination system: Scale-down approach to study microalgal growth kinetics”. In: *Engineering in Life Sciences* 12.6 (2012), pp. 621–630.

[118] L. López-Rosales et al. “Pilot-scale bubble column photobioreactor culture of a marine dinoflagellate microalga illuminated with light emission diodes”. In: *Bioresource Technology* 216 (2016), pp. 845–855.

[119] R. J. Geider, H. L. MacIntyre, and T. M. Kana. “A dynamic model of photoadaptation in phytoplankton”. In: *Limnology and Oceanography* 41.1 (1996), pp. 1–15.

[120] R.-L. Heng and L. Pilon. “Time-dependent radiation characteristics of Nannochloropsis oculata during batch culture”. In: *Journal of Quantitative Spectroscopy and Radiative Transfer* 144 (2014), pp. 154–163.

[121] C. Y. Ma et al. “Growth-dependent radiative properties of Chlorella vulgaris and its influence on prediction of light fluence rate in photobioreactor”. In: *Journal of Applied Phycology* (2018).

[122] E. M. Grima et al. “Photobioreactors: light regime, mass transfer, and scaleup”. In: *Journal of Biotechnology* 70.1-3 (1999), pp. 231–247.

[123] C. Brindley, F. A. Fernández, and J. Fernández-Sevilla. “Analysis of light regime in continuous light distributions in photobioreactors”. In: *Bioresource Technology* 102.3 (2011), pp. 3138–3148.

[124] H.-P. Luo and M. H. Al-Dahhan. “Analyzing and modeling of photobioreactors by combining first principles of physiology and hydrodynamics”. In: *Biotechnology and Bioengineering* 85.4 (2004), pp. 382–393.

[125] A. S. Mirón et al. “Mixing in Bubble Column and Airlift Reactors”. In: *Chemical Engineering Research and Design* 82.10 (2004), pp. 1367–1374.

[126] A. Jacobi, D. Ivanova, and C. Posten. “Photobioreactors: Hydrodynamics and mass transfer”. In: *IFAC Proceedings Volumes* 43.6 (2010), pp. 162–167.

[127] N. Kantarci, F. Borak, and K. O. Ulgen. “Bubble column reactors”. In: *Process Biochemistry* 40.7 (2005), pp. 2263–2283.

[128] A. A. Kulkarni and J. B. Joshi. “Bubble Formation and Bubble Rise Velocity in Gas-Liquid Systems: A Review”. In: *Industrial & Engineering Chemistry Research* 44.16 (2005), pp. 5873–5931.

[129] A. Shaikh and M. Al-Dahhan. “Scale-up of Bubble Column Reactors: A Review of Current State-of-the-Art”. In: *Industrial & Engineering Chemistry Research* 52.24 (2013), pp. 8091–8108.

[130] G. Besagni, F. Inzoli, and T. Ziegenhein. “Two-Phase Bubble Columns: A Comprehensive Review”. In: *ChemEngineering* 2.2 (2018), p. 13.

[131] K. Kumar and D. Das. “Growth characteristics of Chlorella sorokiniana in airlift and bubble column photobioreactors”. In: *Bioresource Technology* 116 (2012), pp. 307–313.

[132] C. J. Hulatt and D. N. Thomas. “Productivity, carbon dioxide uptake and net energy return of microalgal bubble column photobioreactors”. In: *Bioresource Technology* 102.10 (2011), pp. 5775–5787.

[133] J. P. P. Bitog et al. “Optimised hydrodynamic parameters for the design of photobioreactors using computational fluid dynamics and experimental validation”. In: *Biosystems Engineering* 122 (2014), pp. 42–61.

[134] *WO2016176698: Device for a photochemical process, such as a photocytalytical and/or photosynthetic process.* Patent. 2016.

[135] Y. T. Shah et al. “Design parameters estimations for bubble column reactors”. In: *AIChE Journal* 28.3 (1982), pp. 353–379.

[136] J.-P. Zhang et al. “Flow regime identification in gas-liquid flow and three-phase fluidized beds”. In: *Chemical Engineering Science* 52.21-22 (1997), pp. 3979–3992.

[137] G. Besagni et al. “The effect of aspect ratio in counter-current gas-liquid bubble columns: Experimental results and gas holdup correlations”. In: *International Journal of Multiphase Flow* 94 (2017), pp. 53–78.

[138] R. Clift, J. R. Grace, and M. E. Weber. *Bubbles, Drops, and Particles (Dover Civil and Mechanical Engineering)*. Academic Press, 1978.

[139] T. Ziegenhein and D. Lucas. “Observations on bubble shapes in bubble columns under different flow conditions”. In: *Experimental Thermal and Fluid Science* 85 (2017), pp. 248–256.

[140] B. Thorat et al. “Effect of Sparger Design and Height to Diameter Ratio on Fractional Gas Hold-up in Bubble Columns”. In: *Chemical Engineering Research and Design* 76.7 (1998), pp. 823–834.

[141] D. Lucas, H.-M. Prasser, and A. Manera. “Influence of the lift force on the stability of a bubble column”. In: *Chemical Engineering Science* 60.13 (2005), pp. 3609–3619.

[142] R. C. Chen, J. Reese, and L.-S. Fan. “Flow structure in a three-dimensional bubble column and three-phase fluidized bed”. In: *AIChE Journal* 40.7 (1994), pp. 1093–1104.

[143] W. Warsito and L.-S. Fan. “Dynamics of spiral bubble plume motion in the entrance region of bubble columns and three-phase fluidized beds using 3D ECT”. In: *Chemical Engineering Science* 60.22 (2005), pp. 6073–6084.

[144] R. Mudde, J. Groen, and H. V. D. Akker. “Liquid velocity field in a bubble column: LDA experiments”. In: *Chemical Engineering Science* 52.21-22 (1997), pp. 4217–4224.

[145] D. Bröder and M. Sommerfeld. “An advanced LIF-PLV system for analysing the hydrodynamics in a laboratory bubble column at higher void fractions”. In: *Experiments in Fluids* 33.6 (2002), pp. 826–837.

[146] E. Delnoij et al. “Dynamic simulation of dispersed gas-liquid two-phase flow using a discrete bubble model”. In: *Chemical Engineering Science* 52.9 (1997), pp. 1429–1458.

[147] D. Pfleger and S. Becker. “Modelling and simulation of the dynamic flow behaviour in a bubble column”. In: *Chemical Engineering Science* 56.4 (2001), pp. 1737–1747.

[148] R. Rzehak et al. “Baseline Model for the Simulation of Bubbly Flows”. In: *Chemical Engineering & Technology* 38.11 (2015), pp. 1972–1978.

[149] V. V. Buwa and V. V. Ranade. “Mixing in Bubble Column Reactors: Role of Unsteady Flow Structures”. In: *The Canadian Journal of Chemical Engineering* 81.3-4 (2003), pp. 402–411.

[150] C. T. Crowe et al. *Multiphase Flows with Droplets and Particles, Second Edition*. Taylor & Francis Inc, 2011. 509 pp.

[151] V. V. Buwa and V. V. Ranade. “Characterization of dynamics of gas-liquid flows in rectangular bubble columns”. In: *AIChE Journal* 50.10 (2004), pp. 2394–2407.

[152] F. C. Rubio et al. “Mixing in bubble columns: a new approach for characterizing dispersion coefficients”. In: *Chemical Engineering Science* 59.20 (2004), pp. 4369–4376.

[153] H.-P. Luo et al. “Analysis of photobioreactors for culturing high-value microalgae and cyanobacteria via an advanced diagnostic technique: CARPT”. In: *Chemical Engineering Science* 58.12 (2003), pp. 2519–2527.

[154] A. K. Gebremariam and Y. Zarmi. “Synchronization of fluid-dynamics related and physiological time scales and algal biomass production in thin flat-plate bioreactors”. In: *Journal of Applied Physics* 111.3 (2012), p. 034904.

[155] A. A. Kulkarni and J. B. Joshi. “Measurement of eddy diffusivity in bubble column and validation based on the intermittency models”. In: *Chemical Engineering Science* 60.22 (2005), pp. 6146–6159.

[156] J. B. Joshi et al. “Bubble generated turbulence and direct numerical simulations”. In: *Chemical Engineering Science* 157 (2017), pp. 26–75.

[157] R. Masood and A. Delgado. “Numerical investigation of the interphase forces and turbulence closure in 3D square bubble columns”. In: *Chemical Engineering Science* 108 (2014), pp. 154–168.

[158] R. Masood, C. Rauh, and A. Delgado. “CFD simulation of bubble column flows: An explicit algebraic Reynolds stress model approach”. In: *International Journal of Multiphase Flow* 66 (2014), pp. 11–25.

[159] J. Bitog et al. “Application of computational fluid dynamics for modeling and designing photobioreactors for microalgae production: A review”. In: *Computers and Electronics in Agriculture* 76.2 (2011), pp. 131–147.

[160] X. Gao, B. Kong, and R. D. Vigil. “Simulation of algal photobioreactors: recent developments and challenges”. In: *Biotechnology Letters* 40.9-10 (2018), pp. 1311–1327.

[161] E. K. Nauha and V. Alopaeus. “Modeling method for combining fluid dynamics and algal growth in a bubble column photobioreactor”. In: *Chemical Engineering Journal* 229 (2013), pp. 559–568.

[162] E. K. Nauha and V. Alopaeus. “Modeling outdoors algal cultivation with compartmental approach”. In: *Chemical Engineering Journal* 259 (2015), pp. 945–960.

[163] I.-h. Seo et al. “Numerical investigation of a bubble-column photo-bioreactor design for microalgae cultivation”. In: *Biosystems Engineering* 113.3 (2012), pp. 229–241.

[164] A. Ojha and M. Al-Dahhan. “Local gas holdup and bubble dynamics investigation during microalgae culturing in a split airlift photobioreactor”. In: *Chemical Engineering Science* 175 (2018), pp. 185–198.

[165] N. Schneider and M. Gerber. “Correlation between viscosity, temperature and total solid content of algal biomass”. In: *Bioresource Technology* 170 (2014), pp. 293–302.

[166] A. Morel and A. Bricaud. “Theoretical results concerning light absorption in a discrete medium, and application to specific absorption of phytoplankton”. In: *Deep Sea Research Part A. Oceanographic Research Papers* 28.11 (1981), pp. 1375–1393.

[167] D. Baillis and J.-F. Sacadura. “Thermal radiation properties of dispersed media: theoretical prediction and experimental characterization”. In: *Journal of Quantitative Spectroscopy and Radiative Transfer* 67.5 (2000), pp. 327–363.

[168] J. R. Howell, R. Siegel, and M. P. Menguc. *Thermal Radiation Heat Transfer, 6th Edition*. Taylor & Francis Inc, 2015. 1016 pp.

[169] S. D. Campbell et al. “Light scattering regimes along the optical axis in turbid media”. In: *Physical Review E* 74.6 (2006).

[170] A. Yaroshevsky et al. “The transition from the ballistic to the diffusive regime in a turbid medium”. In: *Optics Letters* 36.8 (2011), p. 1395.

[171] A. Morel. “Optics of Marine Particles and Marine Optics”. In: *Particle Analysis in Oceanography*. Springer Berlin Heidelberg, 1991, pp. 141–188.

[172] C. F. Bohren and D. R. Huffman, eds. *Absorption and Scattering of Light by Small Particles*. Wiley-VCH Verlag GmbH, 1998.

[173] G. F. Miroslaw Jonasz. *Light Scattering by Particles in Water: Theoretical and Experimental Foundations*. ACADEMIC PR INC, 2007. 704 pp.

[174] H. C. van de Hulst. *Light scattering by small particles*. Courier Corporation, 1957.

[175] L. C. Henyey and J. L. Greenstein. “Diffuse radiation in the Galaxy”. In: *The Astrophysical Journal* 93 (1941), p. 70.

[176] J. Dauchet et al. “Calculation of the radiative properties of photosynthetic microorganisms”. In: *Journal of Quantitative Spectroscopy and Radiative Transfer* 161 (2015), pp. 60–84.

[177] R. Kandilian, E. Lee, and L. Pilon. “Radiation and optical properties of Nannochloropsis oculata grown under different irradiances and spectra”. In: *Bioresource Technology* 137 (2013), pp. 63–73.

[178] H. Berberoglu, L. Pilon, and A. Melis. “Radiation characteristics of Chlamydomonas reinhardtii CC 125 and its truncated chlorophyll antenna transformants tla1, tlaX and tla1-CW+”. In: *International Journal of Hydrogen Energy* 33.22 (2008), pp. 6467–6483.

[179] Ø. Svensen, Ø. Frette, and S. R. Erga. “Scattering properties of microalgae: the effect of cell size and cell wall”. In: *Applied Optics* 46.23 (2007), p. 5762.

[180] A. Quirantes and S. Bernard. “Light scattering by marine algae: two-layer spherical and nonspherical models”. In: *Journal of Quantitative Spectroscopy and Radiative Transfer* 89.1-4 (2004), pp. 311–321.

[181] A. Quirantes and S. Bernard. “Light-scattering methods for modelling algal particles as a collection of coated and/or nonspherical scatterers”. In: *Journal of Quantitative Spectroscopy and Radiative Transfer* 100.1-3 (2006), pp. 315–324.

[182] A. Bhowmik and L. Pilon. “Can spherical eukaryotic microalgae cells be treated as optically homogeneous?” In: *Journal of the Optical Society of America A* 33.8 (2016), p. 1495.

[183] A. Solovchenko et al. “Stress-Induced Changes in Optical Properties, Pigment and Fatty Acid Content of Nannochloropsis sp.: Implications for Non-destructive Assay of Total Fatty Acids”. In: *Marine Biotechnology* 13.3 (2010), pp. 527–535.

[184] A. E. Solovchenko, O. B. Chivkunova, and I. P. Maslova. “Pigment composition, optical properties, and resistance to photodamage of the microalga Haematococcus pluvialis cultivated under high light”. In: *Russian Journal of Plant Physiology* 58.1 (2011), pp. 9–17.

[185] X. Li et al. “Optical extinction characteristics of three biofuel producing microalgae determined by an improved transmission method”. In: *Particuology* 33 (2017), pp. 1–10.

[186] A.-M. Sánchez and J. Piera. “Methods to retrieve the complex refractive index of aquatic suspended particles: going beyond simple shapes”. In: *Biogeosciences* 13.14 (2016), pp. 4081–4098.

[187] R. Kandilian et al. “Simple method for measuring the spectral absorption cross-section of microalgae”. In: *Chemical Engineering Science* 146 (2016), pp. 357–368.

[188] L. Pilon, H. Berberoğlu, and R. Kandilian. “Radiation transfer in photobiological carbon dioxide fixation and fuel production by microalgae”. In: *Journal of Quantitative Spectroscopy and Radiative Transfer* 112.17 (2011), pp. 2639–2660.

[189] S. Bellini et al. “Simulation Method Linking Dense Microalgal Culture Spectral Properties in the 400–750 nm Range to the Physiology of the Cells”. In: *Applied Spectroscopy* 70.6 (2016), pp. 1018–1033.

[190] H. Berberoglu and L. Pilon. “Experimental measurements of the radiation characteristics of Anabaena variabilis ATCC 29413-U and Rhodobacter sphaeroides ATCC 49419”. In: *International Journal of Hydrogen Energy* 32.18 (2007), pp. 4772–4785.

[191] H. Berberoglu, P. S. Gomez, and L. Pilon. “Radiation characteristics of Botryococcus braunii, Chlorococcum littorale, and Chlorella sp. used for fixation and biofuel production”. In: *Journal of Quantitative Spectroscopy and Radiative Transfer* 110.17 (2009), pp. 1879–1893.

[192] A. A. Gitelson et al. “Optical Properties of Dense Algal Cultures Outdoors and their Application to Remote Estimation of Biomass and Pigment Concentration in Spirulina Platensis (Cyanobacteria)”. In: *Journal of Phycology* 31.5 (1995), pp. 828–834.

[193] M. N. Merzlyak et al. “Light absorption and scattering by cell suspensions of some cyanobacteria and microalgae”. In: *Russian Journal of Plant Physiology* 55.3 (2008), pp. 420–425.

[194] E. Greenwald, J. M. Gordon, and Y. Zarmi. “Physics of ultra-high bioproductivity in algal photobioreactors”. In: *Applied Physics Letters* 100.14 (2012), p. 143703.

[195] B. Kong and R. D. Vigil. “Simulation of photosynthetically active radiation distribution in algal photobioreactors using a multidimensional spectral radiation model”. In: *Bioresource Technology* 158 (2014), pp. 141–148.

[196] E. M. Grima et al. “A mathematical model of microalgal growth in light-limited chemostat culture”. In: *Journal of Chemical Technology AND Biotechnology* 61.2 (1994), pp. 167–173.

[197] Y.-S. Yun and J. M. Park. “Kinetic modeling of the light-dependent photosynthetic activity of the green microalga Chlorella vulgaris”. In: *Biotechnology and Bioengineering* 83.3 (2003), pp. 303–311.

[198] I. S. Suh and S. B. Lee. “A light distribution model for an internally radiating photobioreactor”. In: *Biotechnology and Bioengineering* 82.2 (2003), pp. 180–189.

[199] K. Kumar, A. Sirasale, and D. Das. “Use of image analysis tool for the development of light distribution pattern inside the photobioreactor for the algal cultivation”. In: *Bioresource Technology* 143 (2013), pp. 88–95.

[200] J. T. O. Kirk. “Volume scattering function, average cosines, and the underwater light field”. In: *Limnology and Oceanography* 36.3 (1972), pp. 455–467.

[201] D. Fuente et al. “Estimation of the light field inside photosynthetic microorganism cultures through Mittag-Leffler functions at depleted light conditions”. In: *Journal of Quantitative Spectroscopy and Radiative Transfer* 204 (2018), pp. 23–26.

[202] J. Ripoll. “Derivation of the scalar radiative transfer equation from energy conservation of Maxwell’s equations in the far field”. In: *Journal of the Optical Society of America A* 28.8 (2011), p. 1765.

[203] J. Oxenius. *Kinetic Theory of Particles and Photons*. Springer Berlin Heidelberg, 1986.

[204] R. Soto. *Kinetic Theory and Transport Phenomena*. OXFORD UNIV PR, 2016. 304 pp.

[205] N. Pottier. *Nonequilibrium Statistical Physics*. Oxford University Press, 2010.

[206] M. F. Modest. *Radiative Heat Transfer*. Elsevier LTD, Oxford, 2013.

[207] F. Krujatz et al. “Light-field-characterization in a continuous hydrogen-producing photobioreactor by optical simulation and computational fluid dynamics”. In: *Biotechnology and Bioengineering* 112.12 (2015), pp. 2439–2449.

[208] J. F. Cornet et al. “A structured model for simulation of cultures of the cyanobacteriumSpirulina platensis in photobioreactors: II. Identification of kinetic parameters under light and mineral limitations”. In: *Biotechnology and Bioengineering* 40.7 (1992), pp. 826–834.

[209] L. Pottier et al. “A fully predictive model for one-dimensional light attenuation byChlamydomonas reinhardtii in a torus photobioreactor”. In: *Biotechnology and Bioengineering* 91.5 (2005), pp. 569–582.

[210] W. Cheng, J. Huang, and J. Chen. “Computational fluid dynamics simulation of mixing characteristics and light regime in tubular photobioreactors with novel static mixers”. In: *Journal of Chemical Technology & Biotechnology* 91.2 (2014), pp. 327–335.

[211] B. H. J. McKellar and M. A. Box. “The Scaling Group of the Radiative Transfer Equation”. In: *Journal of the Atmospheric Sciences* 38.5 (1981), pp. 1063–1068.

[212] H. Lee and R. O. Buckius. “Scaling Anisotropic Scattering in Radiation Heat Transfer for a Planar Medium”. In: *Journal of Heat Transfer* 104.1 (1982), p. 68.

[213] Z. Guo and S. Maruyama. “Scaling anisotropic scattering in radiative transfer in three-dimensional nonhomogeneous media”. In: *International Communications in Heat and Mass Transfer* 26.7 (1999), pp. 997–1007.

[214] H. T. K. Tagne and D. D. Baillis. “Radiative Heat Transfer Using Isotropic Scaling Approximation: Application to Fibrous Medium”. In: *Journal of Heat Transfer* 127.10 (2005), p. 1115.

[215] Z. Guo and S. Kumar. “Equivalent isotropic scattering formulation for transient short-pulse radiative transfer in anisotropic scattering planar media”. In: *Applied Optics* 39.24 (2000), p. 4411.

[216] Z. Guo et al. “Monte Carlo simulation and experiments of pulsed radiative transfer”. In: *Journal of Quantitative Spectroscopy and Radiative Transfer* 73.2-5 (2002), pp. 159–168.

[217] S. Chandrasekhar. *Radiative Transfer*. Dover Publications Inc., 1960. 416 pp.

[218] P. J. Coelho. “Advances in the discrete ordinates and finite volume methods for the solution of radiative heat transfer problems in participating media”. In: *Journal of Quantitative Spectroscopy and Radiative Transfer* 145 (2014), pp. 121–146.

[219] R. Koch et al. “Discrete ordinates quadrature schemes for multidimensional radiative transfer”. In: *Journal of Quantitative Spectroscopy and Radiative Transfer* 53.4 (1995), pp. 353–372.

[220] R. Koch and R. Becker. “Evaluation of quadrature schemes for the discrete ordinates method”. In: *Journal of Quantitative Spectroscopy and Radiative Transfer* 84.4 (2004), pp. 423–435.

[221] B. Hunter and Z. Guo. “Numerical smearing, ray effect, and angular false scattering in radiation transfer computation”. In: *International Journal of Heat and Mass Transfer* 81 (2015), pp. 63–74.

[222] B. Hunter and Z. Guo. “Phase-Function Normalization in the 3-D Discrete-Ordinates Solution of Radiative Transfer—PART I: Conservation of Scattered Energy and Asymmetry Factor”. In: *Numerical Heat Transfer, Part B: Fundamentals* 62.4 (2012), pp. 203–222.

[223] B. Hunter and Z. Guo. “Conservation of asymmetry factor in phase function discretization for radiative transfer analysis in anisotropic scattering media”. In: *International Journal of Heat and Mass Transfer* 55.5-6 (2012), pp. 1544–1552.

[224] B. Hunter and Z. Guo. “A New and Simple Technique to Normalize the HG Phase Function for Conserving Scattered Energy and Asymmetry Factor”. In: *Numerical Heat Transfer, Part B: Fundamentals* 65.3 (2014), pp. 195–217.

[225] P. Coelho. “The role of ray effects and false scattering on the accuracy of the standard and modified discrete ordinates methods”. In: *Journal of Quantitative Spectroscopy and Radiative Transfer* 73.2-5 (2002), pp. 231–238.

[226] Z. C. Wheaton and G. Krishnamoorthy. “Modeling radiative transfer in photobioreactors for algal growth”. In: *Computers and Electronics in Agriculture* 87 (2012), pp. 64–73.

[227] L. Wu, Z. Li, and Y. Song. “Hydrodynamic conditions in designed spiral photobioreactors”. In: *Bioresource Technology* 101.1 (2010), pp. 298–303.

[228] J. R. Howell. “The Monte Carlo Method in Radiative Heat Transfer”. In: *Journal of Heat Transfer* 120.3 (1998), p. 547.

[229] S. L. Jacques. “Monte Carlo Modeling of Light Transport in Tissue (Steady State and Time of Flight)”. In: *Optical-Thermal Response of Laser-Irradiated Tissue*. Springer Netherlands, 2010, pp. 109–144.

[230] B. A. Whitney. “Monte Carlo radiative transfer”. In: *Fluid Flows to Black Holes*. WORLD SCIENTIFIC, 2011, pp. 151–176.

[231] D. Toublanc. “Henyey–Greenstein and Mie phase functions in Monte Carlo radiative transfer computations”. In: *Applied Optics* 35.18 (1996), p. 3270.

[232] K. Evans and A. Marshak. “Numerical Methods”. In: *3D Radiative Transfer in Cloudy Atmospheres*. Springer-Verlag, pp. 243–281.

[233] J. M. Heinrich et al. “Analysis and Design of Photobioreactors for Microalgae Production I: Method and Parameters for Radiation Field Simulation”. In: *Photochemistry and Photobiology* 88.4 (2012), pp. 938–951.

[234] J. M. Heinrich et al. “Stratification of the Radiation Field Inside a Photobioreactor During Microalgae Growth”. In: *Photochemistry and Photobiology* 89.5 (2013), pp. 1127–1134.

[235] J. F. Cornet, C. G. Dussap, and J. B. Gros. “Conversion of radiant light energy in photobioreactors”. In: *AIChE Journal* 40.6 (1994), pp. 1055–1066.

[236] H. Takache, J. Pruvost, and J.-F. Cornet. “Kinetic modeling of the photosynthetic growth of Chlamydomonas reinhardtii in a photobioreactor”. In: *Biotechnology Progress* 28.3 (2012), pp. 681–692.

[237] X. Li and N. Yang. “Modeling the light distribution in airlift photobioreactors under simultaneous external and internal illumination using the two-flux model”. In: *Chemical Engineering Science* 88 (2013), pp. 16–22.

[238] R. Kandilian et al. “Light transfer in agar immobilized microalgae cell cultures”. In: *Journal of Quantitative Spectroscopy and Radiative Transfer* 198 (2017), pp. 81–92.

[239] D. Mihalas and B. W. Mihalas. *Foundations of Radiation Hydrodynamics*. DOVER PUBN INC, 1999. 752 pp.

[240] G. L. Olson, L. H. Auer, and M. L. Hall. “Diffusion, P1, and other approximate forms of radiation transport”. In: *Journal of Quantitative Spectroscopy and Radiative Transfer* 64.6 (2000), pp. 619–634.

[241] Z. Guo et al. “Comparing Diffusion Approximation with Radiation Transfer Analysis for Light Transport in Tissues”. In: *Optical Review* 10.5 (2003), pp. 415–421.

[242] G. N. Minerbo. “Maximum entropy Eddington factors”. In: *Journal of Quantitative Spectroscopy and Radiative Transfer* 20.6 (1978), pp. 541–545.

[243] G. Pomraning. “Maximum entropy Eddington factors and flux limited diffusion theory”. In: *Journal of Quantitative Spectroscopy and Radiative Transfer* 26.5 (1981), pp. 385–388.

[244] C. Levermore. “Relating Eddington factors to flux limiters”. In: *Journal of Quantitative Spectroscopy and Radiative Transfer* 31.2 (1984), pp. 149–160.

[245] A. B. Davis and A. Marshak. “Solar radiation transport in the cloudy atmosphere: a 3D perspective on observations and climate impacts”. In: *Reports on Progress in Physics* 73.2 (2010), p. 026801.

[246] M. C. W. van Rossum and T. M. Nieuwenhuizen. “Multiple scattering of classical waves: microscopy, mesoscopy, and diffusion”. In: *Reviews of Modern Physics* 71.1 (1999), pp. 313–371.

[247] D. Hänel. *Molekulare Gasdynamik*. Springer Berlin Heidelberg, 2004. 236 pp.

[248] G. R. McNamara and G. Zanetti. “Use of the Boltzmann Equation to Simulate Lattice-Gas Automata”. In: *Physical Review Letters* 61.20 (1988), pp. 2332–2335.

[249] D. A. Wolf-Gladrow. *Lattice-Gas Cellular Automata and Lattice Boltzmann Models*. Springer-Verlag GmbH, 2000.

[250] S. Succi. *The Lattice Boltzmann Equation for Fluid Dynamics and Beyond (Numerical Mathematics and Scientific Computation)*. Clarendon Press, 2001.

[251] Z. Guo and C. Shu. *Lattice Boltzmann Method and Its Applications in Engineering*. WORLD SCIENTIFIC, 2013.

[252] T. Krüger et al. *The Lattice Boltzmann Method*. Springer-Verlag GmbH, 2016.

[253] T. Zeiser. “Simulation und Analyse von durchströmten Kugelschüttungen in engen Rohren unter Verwendung von Hochleistungsrechnern”. PhD thesis. Friedrich-Alexander Universität Erlangen, 2008.

[254] E. M. Viggen. “The lattice Boltzmann method: Fundamentals and acoustics”. PhD thesis. Norwegian University of Science and Technology, 2014.

[255] S. Chen and G. D. Doolen. “Lattice Boltzmann Method for Fluid Flows”. In: *Annual Review of Fluid Mechanics* 30.1 (1998), pp. 329–364.

[256] C. K. Aidun and J. R. Clausen. “Lattice-Boltzmann Method for Complex Flows”. In: *Annual Review of Fluid Mechanics* 42.1 (2010), pp. 439–472.

[257] X. He and L.-S. Luo. “Theory of the lattice Boltzmann method: From the Boltzmann equation to the lattice Boltzmann equation”. In: *Physical Review E* 56.6 (1997), pp. 6811–6817.

[258] J. W. y. Robert Geist Karl Rasche and R. Schalkoff. “Lattice-Boltzmann Lighting”. In: *Eurographics Symposium on Rendering*. Ed. by A. K. H. W. Jensen. The Eurographics Association, 2004.

[259] T. Abe. “Derivation of the Lattice Boltzmann Method by Means of the Discrete Ordinate Method for the Boltzmann Equation”. In: *Journal of Computational Physics* 131.1 (1997), pp. 241–246.

[260] P. Asinari, S. C. Mishra, and R. Borchiellini. “A Lattice Boltzmann Formulation for the Analysis of Radiative Heat Transfer Problems in a Participating Medium”. In: *Numerical Heat Transfer, Part B: Fundamentals* 57.2 (2010), pp. 126–146.

[261] Y. Ma, S. Dong, and H. Tan. “Lattice Boltzmann method for one-dimensional radiation transfer”. In: *Physical Review E* 84.1 (2011).

[262] H. Bindra and D. V. Patil. “Radiative or neutron transport modeling using a lattice Boltzmann equation framework”. In: *Physical Review E* 86.1 (2012).

[263] R. McCulloch and H. Bindra. “Coupled radiative and conjugate heat transfer in participating media using lattice Boltzmann methods”. In: *Computers & Fluids* 124 (2016), pp. 261–269.

[264] A. Gairola and H. Bindra. “Lattice Boltzmann method for solving non-equilibrium radiative transport problems”. In: *Annals of Nuclear Energy* 99 (2017), pp. 151–156.

[265] Y. Zhang, H. Yi, and H. Tan. “One-dimensional transient radiative transfer by lattice Boltzmann method”. In: *Optics Express* 21.21 (2013), p. 24532.

[266] Y. Zhang, H.-L. Yi, and H.-P. Tan. “The lattice Boltzmann method for one-dimensional transient radiative transfer in graded index gray medium”. In: *Journal of Quantitative Spectroscopy and Radiative Transfer* 137 (2014), pp. 1–12.

[267] Y. Zhang, H.-L. Yi, and H.-P. Tan. “Lattice Boltzmann method for short-pulsed laser transport in a multilayered medium”. In: *Journal of Quantitative Spectroscopy and Radiative Transfer* 155 (2015), pp. 75–89.

[268] Y. Zhang, H.-L. Yi, and H.-P. Tan. “Short-pulsed laser propagation in a participating slab with Fresnel surfaces by lattice Boltzmann method”. In: *International Journal of Heat and Mass Transfer* 80 (2015), pp. 717–726.

[269] Y. Zhang et al. “Transient Radiative Transfer in a Graded Index Slab with Fresnel Surfaces”. In: *Journal of Thermophysics and Heat Transfer* 30.3 (2016), pp. 513–522.

[270] S. Patidar et al. “Dual phase lag model-based thermal analysis of tissue phantoms using lattice Boltzmann method”. In: *International Journal of Thermal Sciences* 103 (2016), pp. 41–56.

[271] S. Patidar et al. “Lattice Boltzmann method-based solution of radiative transfer equation for investigating light propagation through laser-irradiated tissue phantoms”. In: *International Communications in Heat and Mass Transfer* 84 (2017), pp. 144–149.

[272] A. Mink et al. “A 3D Lattice Boltzmann method for light simulation in participating media”. In: *Journal of Computational Science* 17 (2016), pp. 431–437.

[273] H.-L. Yi, F.-J. Yao, and H.-P. Tan. “Lattice Boltzmann model for a steady radiative transfer equation”. In: *Physical Review E* 94.2 (2016).

[274] S. C. Mishra et al. “Analysis of Conduction-Radiation Heat Transfer in a 2D Enclosure Using the Lattice Boltzmann Method”. In: *Numerical Heat Transfer, Part A: Applications* 66.6 (2014), pp. 669–688.

[275] J. C. Butcher. *Numerical Methods for Ordinary Differential Equations*. John Wiley & Sons Inc, 2016. 538 pp.

[276] J. H. Ferziger and M. Peric. *Numerische StrÃ¶mungsmechanik*. Springer Berlin Heidelberg, 2008.

[277] D. Wilde et al. “Multistep lattice Boltzmann methods: Theory and applications”. In: *International Journal for Numerical Methods in Fluids* (2019).

[278] C. McHardy, D. Becker, and C. Rauh. “Similarity of Field Quantities in Scaled Radiation Transfer Lattice Boltzmann Simulations (RT-LBM)”. In: *PAMM* (2018).

[279] H. T. K. Tagne and D. Baillis. “Isotropic scaling limits for one-dimensional radiative heat transfer with collimated incidence”. In: *Journal of Quantitative Spectroscopy and Radiative Transfer* 93.1-3 (2005), pp. 103–113.

[280] A. Liemert and A. Kienle. “Analytical solution of the radiative transfer equation for infinite-space fluence”. In: *Physical Review A* 83.1 (2011).

[281] F. Toschi and S. Succi. “Lattice Boltzmann method at finite Knudsen numbers”. In: *Europhysics Letters (EPL)* 69.4 (2005), pp. 549–555.

[282] C. S. Zhaoli Guo. *Lattice Boltzmann Method and Its Applications in Engineering*. World Scientific Publishing Company, 2013. 420 pp.

[283] J. C. Chai, H. S. Lee, and S. V. Patankar. "Ray Effect and False Scattering in the Discrete Ordinates Method". In: *Numerical Heat Transfer, Part B: Fundamentals* 24.4 (1993), pp. 373–389.

[284] H. Lee, S. Bawazeer, and A. Mohamad. "Boundary conditions for lattice Boltzmann method with multispeed lattices". In: *Computers & Fluids* 162 (2018), pp. 152–159.

[285] C. Mätzler. *MATLAB Functions for Mie Scattering and Absorption - Version 2*. Research Report No. 2002-11. University of Bern, 2002.

[286] R. Hass et al. "Industrial applications of Photon Density Wave spectroscopy for in-line particle sizing". In: *Applied Optics* 52.7 (2013), p. 1423.

[287] C. Martínez, F. Mairet, and O. Bernard. "Theory of turbid microalgae cultures". In: *Journal of Theoretical Biology* 456 (2018), pp. 190–200.

[288] M. Chioccioli, B. Hankamer, and I. L. Ross. "Flow Cytometry Pulse Width Data Enables Rapid and Sensitive Estimation of Biomass Dry Weight in the Microalgae Chlamydomonas reinhardtii and Chlorella vulgaris". In: *PLoS ONE* 9.5 (2014). Ed. by R. V. Duhalt, e97269.

[289] M. J. Griffiths et al. "Interference by pigment in the estimation of microalgal biomass concentration by optical density". In: *Journal of Microbiological Methods* 85.2 (2011), pp. 119–123.

[290] G. Sin, K. V. Gernaey, and A. E. Lantz. "Good modeling practice for PAT applications: Propagation of input uncertainty and sensitivity analysis". In: *Biotechnology Progress* 25.4 (2009), pp. 1043–1053.

[291] J. Dauchet et al. "Photobioreactor Modeling and Radiative Transfer Analysis for Engineering Purposes". In: *Photobioreaction Engineering*. Elsevier, 2016, pp. 1–106.

[292] I. Havlik et al. "On-line monitoring of large cultivations of microalgae and cyanobacteria". In: *Trends in Biotechnology* 31.7 (2013), pp. 406–414.

[293] B. Franco et al. "Monoalgal and mixed algal cultures discrimination by using an artificial neural network". In: *Algal Research* 38 (2019), p. 101419.

[294] F. Durst. *Grundlagen der Strömungsmechanik*. Springer Berlin Heidelberg, 2007.

[295] C. Wang and C. Q. Lan. "Effects of shear stress on microalgae – A review". In: *Biotechnology Advances* 36.4 (2018), pp. 986–1002.

[296] W. H. Thomas and C. H. Gibson. "Effects of small-scale turbulence on microalgae". In: *Journal of Applied Phycology* 2.1 (1990), pp. 71–77.

[297] M. H. A. Michels et al. "Cultivation of shear stress sensitive and tolerant microalgal species in a tubular photobioreactor equipped with a centrifugal pump". In: *Journal of Applied Phycology* 28.1 (2015), pp. 53–62.

[298] E. Molina et al. "Scale-up of tubular photobioreactors". In: *Journal of Applied Phycology* 12.3/5 (2000), pp. 355–368.

[299] Y. Chisti. “Shear Sensitivity”. In: *Encyclopedia of Bioprocess Technology*. Ed. by M. C. Flickinger. American Cancer Society, 2002.

[300] S. Mitsuhashi et al. “Effects of shear flow on photosynthesis in a dilute suspension of microalgae”. In: *Applied Microbiology and Biotechnology* 42.5 (1995), pp. 744–749.

[301] D. Kokkinos et al. “Deformation and rupture of Dunaliella salina at high shear rates without the use of thickeners”. In: *Biorheology* 1 (2016), pp. 1–11.

[302] C. Gómez-Pérez et al. “Twisted tubular photobioreactor fluid dynamics evaluation for energy consumption minimization”. In: *Algal Research* 27 (2017), pp. 65–72.

[303] M. Janssen. “Chapter Four - Microalgal Photosynthesis and Growth in Mass Culture”. In: *Photobioreaction Engineering*. Ed. by J. Legrand. Vol. 48. Advances in Chemical Engineering. Academic Press, 2016, pp. 185–256.

[304] P. S. Schulze et al. “Light emitting diodes (LEDs) applied to microalgal production”. In: *Trends in Biotechnology* 32.8 (2014), pp. 422–430.

[305] E. G. Nwoba et al. “Light management technologies for increasing algal photobioreactor efficiency”. In: *Algal Research* 39 (2019), p. 101433.

[306] S. Baer et al. “Optimization of spectral light quality for growth and product formation in different microalgae using a continuous photobioreactor”. In: *Algal Research* 14 (2016), pp. 109–115.

[307] I. Wagner, C. Steinweg, and C. Posten. “Mono- and dichromatic LED illumination leads to enhanced growth and energy conversion for high-efficiency cultivation of microalgae for application in space”. In: *Biotechnology Journal* 11.8 (2016), pp. 1060–1071.

[308] P. S. Schulze et al. “Effect of light quality supplied by light emitting diodes (LEDs) on growth and biochemical profiles of Nannochloropsis oculata and Tetraselmis chuii”. In: *Algal Research* 16 (2016), pp. 387–398.

[309] G. Markou. “Effect of Various Colors of Light-Emitting Diodes (LEDs) on the Biomass Composition of Arthrospira platensis Cultivated in Semi-continuous Mode”. In: *Applied Biochemistry and Biotechnology* 172.5 (2014), pp. 2758–2768.

[310] D. da Fontoura Prates et al. “Spirulina cultivated under different light emitting diodes: Enhanced cell growth and phycocyanin production”. In: *Bioresource Technology* 256 (2018), pp. 38–43.

[311] T. de Mooij et al. “Impact of light color on photobioreactor productivity”. In: *Algal Research* 15 (2016), pp. 32–42.

[312] R. Kandilian, T.-C. Tsao, and L. Pilon. “Control of incident irradiance on a batch operated flat-plate photobioreactor”. In: *Chemical Engineering Science* 119 (2014), pp. 99–108.

[313] S. Tebbani et al. “Optimal Operation of a Lumostatic Microalgae Cultivation Process”. In: *Developments in Model-Based Optimization and Control*. Springer International Publishing, 2015, pp. 209–235.

[314] W. Blanken et al. “Cultivation of microalgae on artificial light comes at a cost”. In: *Algal Research* 2.4 (2013), pp. 333–340.

[315] M. Krause et al. *OpenLB Release 1.2: Open Source Lattice Boltzmann Code*. online. https://www.openlb.net/. 2018.

[316] R. Miao, H. Xie, and P. Lindblad. "Enhancement of photosynthetic isobutanol production in engineered cells of Synechocystis PCC 6803". In: *Biotechnology for Biofuels* 11.1 (2018).

[317] I. S. Yunus et al. "Synthetic metabolic pathways for photobiological conversion of CO2 into hydrocarbon fuel". In: *Metabolic Engineering* 49 (2018), pp. 201–211.

[318] S. Leu and S. Boussiba. "Advances in the Production of High-Value Products by Microalgae". In: *Industrial Biotechnology* 10.3 (2014), pp. 169–183.

[319] B. Podola, T. Li, and M. Melkonian. "Porous Substrate Bioreactors: A Paradigm Shift in Microalgal Biotechnology?" In: *Trends in Biotechnology* 35.2 (2017), pp. 121–132.

[320] T. J. Johnson et al. "Photobioreactor cultivation strategies for microalgae and cyanobacteria". In: *Biotechnology Progress* 34.4 (2018), pp. 811–827.

Appendices

A. Comparison of time integration schemes for the RT-LBM

The appendix extends the comparison of different time integration schemes in section 9.1.2.

Table A.1.: Simulation results for different time integration schemes in medium 1.

Euler	$N = 55^3$	$N = 76^3$	$N = 110^3$	$N = 156^3$	$N = 220^3$
Steps until convergence	674	912	1234	1682	2285
Av. time per step [s]	0.379	1.092	3.091	8.880	24.144
Total time [s]	255.65	995.62	3813.83	14935.56	55168.47
RMSE	0.031	0.034	0.023	0.029	0.025
MAPE	0.073	0.094	0.056	0.087	0.063
Heun	$N = 55^3$	$N = 76^3$	$N = 110^3$	$N = 156^3$	$N = 220^3$
Steps until convergence	623	866	1191	1642	2247
Av. time per step [s]	0.583	1.677	4.702	13.474	69.973
Total time [s]	363.05	1452.62	5599.68	22123.53	157229.08
RMSE	0.026	0.031	0.023	0.028	0.025
MAPE	0.074	0.102	0.059	0.092	0.065
Runge-Kutta	$N = 55^3$	$N = 76^3$	$N = 110^3$	$N = 156^3$	$N = 220^3$
Steps until convergence	626	868	1193	1643	2248
Av. time per step [s]	1.005	2.863	8.008	22.824	127.467
Total time [s]	628.84	2485.09	9553.09	37500.39	286545.59
RMSE	0.026	0.031	0.023	0.028	0.025
MAPE	0.073	0.101	0.059	0.092	0.065

Table A.2.: Simulation results for different time integration schemes in medium 2.

Euler	$N = 55^3$	$N = 76^3$	$N = 110^3$	$N = 156^3$	$N = 220^3$
Steps until convergence	193	268	371	515	712
Av. time per step [s]	0.377	1.098	3.078	8.866	22.646
Total time [s]	72.75	294.26	1141.92	4565.86	16123.76
RMSE	0.018	0.023	0.018	0.022	0.019
MAPE	0.260	0.215	0.190	0.205	0.191
Heun	$N = 55^3$	$N = 76^3$	$N = 110^3$	$N = 156^3$	$N = 220^3$
Steps until convergence	189	265	368	512	709
Av. time per step [s]	0.584	1.673	4.702	13.457	64.099
Total time [s]	110.29	443.24	1730.39	6890.29	45445.93
RMSE	0.018	0.023	0.019	0.022	0.019
MAPE	0.222	0.260	0.212	0.251	0.215
Runge-Kutta	$N = 55^3$	$N = 76^3$	$N = 110^3$	$N = 156^3$	$N = 220^3$
Steps until convergence	190	265	368	512	709
Av. time per step [s]	1.009	2.858	8.014	22.843	120.635
Total time [s]	191.68	757.33	2949.24	11695.44	85530.22
RMSE	0.018	0.023	0.019	0.022	0.019
MAPE	0.210	0.253	0.210	0.250	0.215

Table A.3.: Simulation results for different time integration schemes in medium 3.

Euler	$N = 55^3$	$N = 76^3$	$N = 110^3$	$N = 156^3$	$N = 220^3$
Steps until convergence	2142	2580	3260	4250	56011
Av. time per step [s]	0.378	1.093	3.073	8.889	23.015
Total time [s]	809.15	2820.00	10017.71	37779.22	128905.19
RMSE	0.069	0.049	0.029	0.037	0.044
MAPE	0.156	0.120	0.124	0.096	0.122
Heun	$N = 55^3$	$N = 76^3$	$N = 110^3$	$N = 156^3$	$N = 220^3$
Steps until convergence	1426	2034	2810	3861	5255
Av. time per step [s]	0.590	1.682	4.696	13.455	71.038
Total time [s]	840.66	3420.90	13195.99	51948.44	373303.22
RMSE	0.032	0.030	0.031	0.039	0.047
MAPE	0.095	0.080	0.103	0.082	0.114
Runge-Kutta	$N = 55^3$	$N = 76^3$	$N = 110^3$	$N = 156^3$	$N = 220^3$
Steps until convergence	1528	2095	2847	3885	5271
Av. time per step [s]	1.002	2.859	7.992	22.872	130.538
Total time [s]	1531.66	5988.49	22753.44	88856.55	688063.71
RMSE	0.035	0.031	0.031	0.038	0.047
MAPE	0.106	0.085	0.105	0.083	0.114

Table A.4.: Simulation results for different time integration schemes in medium 4.

Euler	$N = 55^3$	$N = 76^3$	$N = 110^3$	$N = 156^3$	$N = 220^3$
Steps until convergence	155	205	279	384	530
Av. time per step [s]	0.377	1.093	3.081	8.879	22.169
Total time [s]	58.431	224.017	859.643	3409.472	11749.37
RMSE	0.029	0.026	0.018	0.020	0.017
MAPE	0.893	0.780	0.663	0.501	0.414
Heun	$N = 55^3$	$N = 76^3$	$N = 110^3$	$N = 156^3$	$N = 220^3$
Steps until convergence	137	193	269	376	523
Av. time per step [s]	0.586	1.674	4.712	13.471	63.550
Total time [s]	80.288	323.132	1267.644	5065.260	33236.73
RMSE	0.025	0.025	0.019	0.021	0.018
MAPE	0.790	0.474	0.317	0.323	0.273
Runge-Kutta	$N = 55^3$	$N = 76^3$	$N = 110^3$	$N = 156^3$	$N = 220^3$
Steps until convergence	141	195	270	377	523
Av. time per step [s]	1.006	2.865	8.025	22.867	119.539
Total time [s]	141.791	558.659	2166.671	8620.560	62518.88
RMSE	0.025	0.025	0.019	0.021	0.018
MAPE	0.367	0.336	0.281	0.298	0.265

B. Additional details and results of the experimental validation of the RT-LBM

Figure B.1 shows the refractive index of water and polystyrene with respect to the wavelength in the visible range. The data was used to compute the asymmetry factor (figure B.2) and the scattering coefficients (figure B.3) by means of Mie theory [285]. The scattering coefficient is depicted for the same particle volume fractions ϕ_v as being used in the simulations of the light fields. The detailed comparison of simulated and experimentally determined profiles of the light intensity is shown in figures B.4 - B.7.

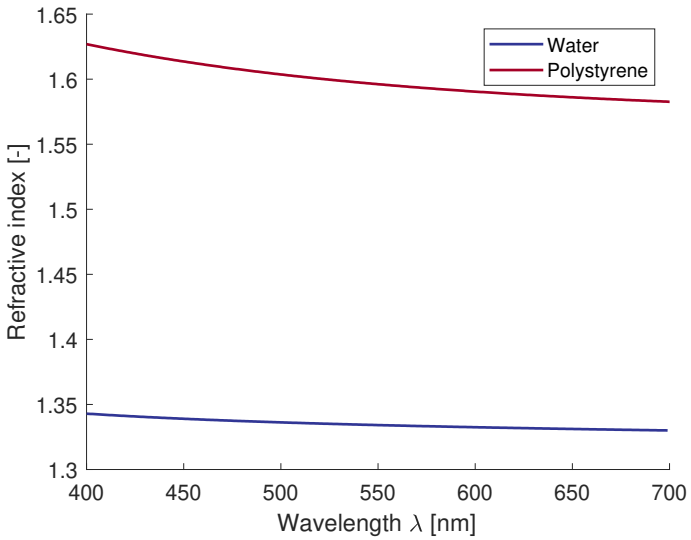

Figure B.1.: Refractive index of water and polystyrene for the visible part of the light spectrum.

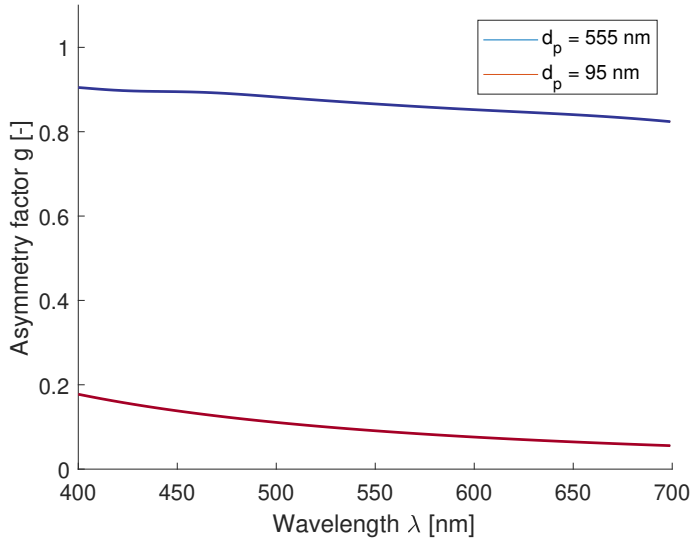

Figure B.2.: Computed asymmetry factors of polystyrene particles of different sizes used in the experiments with respect to wavelength in the visible part of the light spectrum.

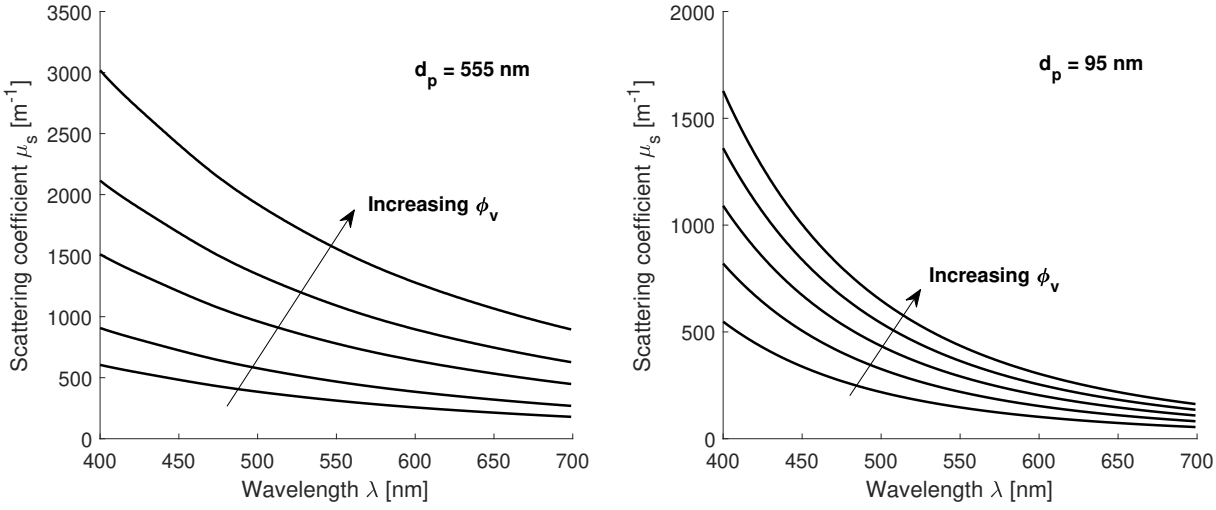

Figure B.3.: Computed scattering coefficients in polystyrene suspensions with particles of different sizes with respect to wavelength in the visible part of the light spectrum. ϕ_v denots for the particle volume fraction. Left: Suspension with particles of $d_1 = 555$ nm. Right: Suspension with particles of $d_2 = 95$ nm.

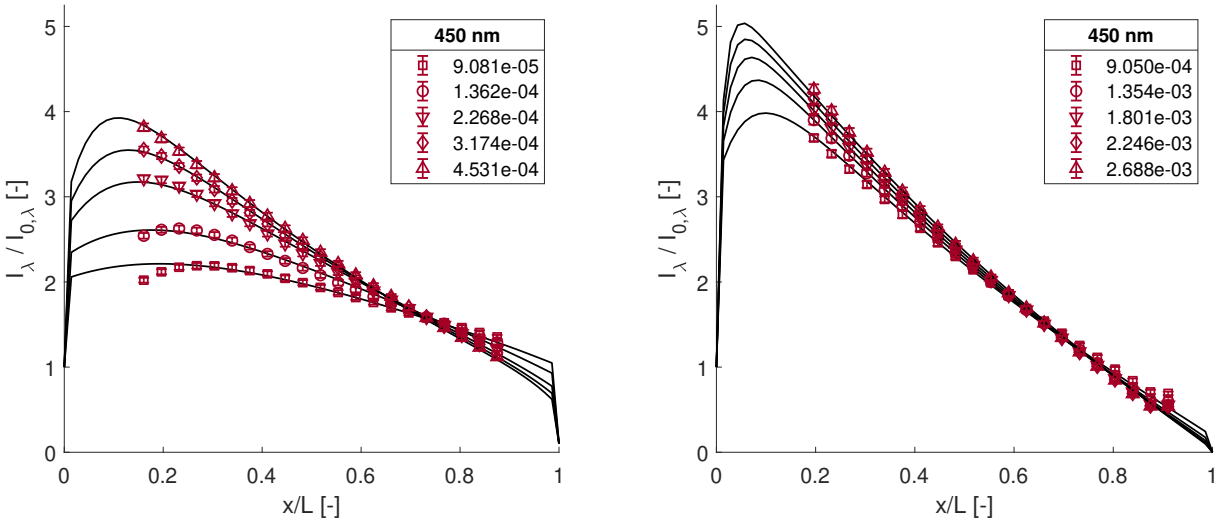

Figure B.4.: Comparison of simulated (lines) and measured (symbols) profiles of the light intensity at $\lambda = 450$ nm in polystyrene suspensions. Different symbols encode the particle volume fraction ϕ_v as denoted in the legend. Left: Suspension with particles of $d_1 = 555$ nm. Right: Suspension with particles of $d_2 = 95$ nm.

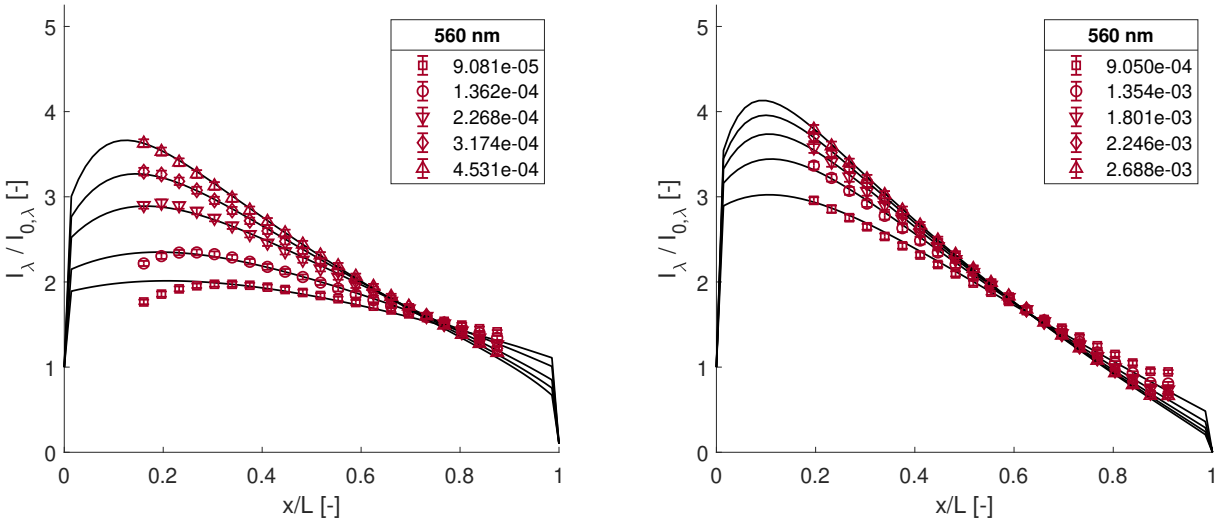

Figure B.5.: Comparison of simulated (lines) and measured (symbols) profiles of the light intensity at $\lambda = 560$ nm in polystyrene suspensions. Different symbols encode the particle volume fraction ϕ_v as denoted in the legend. Left: Suspension with particles of $d_1 = 555$ nm. Right: Suspension with particles of $d_2 = 95$ nm.

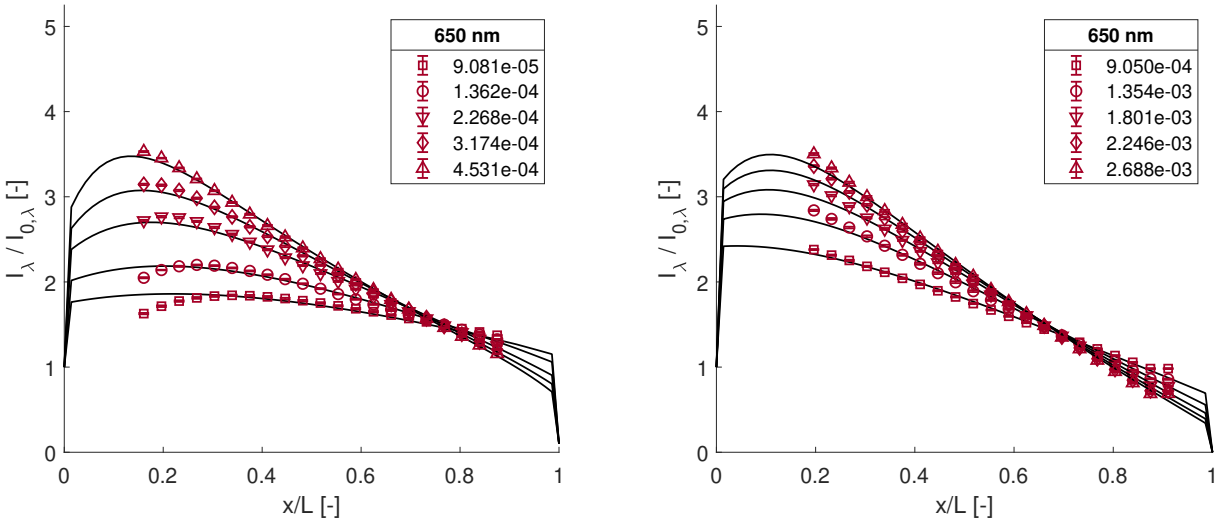

Figure B.6.: Comparison of simulated (lines) and measured (symbols) profiles of the light intensity at $\lambda = 650$ nm in polystyrene suspensions. Different symbols encode the particle volume fraction ϕ_v as denoted in the legend. Left: Suspension with particles of $d_1 = 555$ nm. Right: Suspension with particles of $d_2 = 95$ nm.

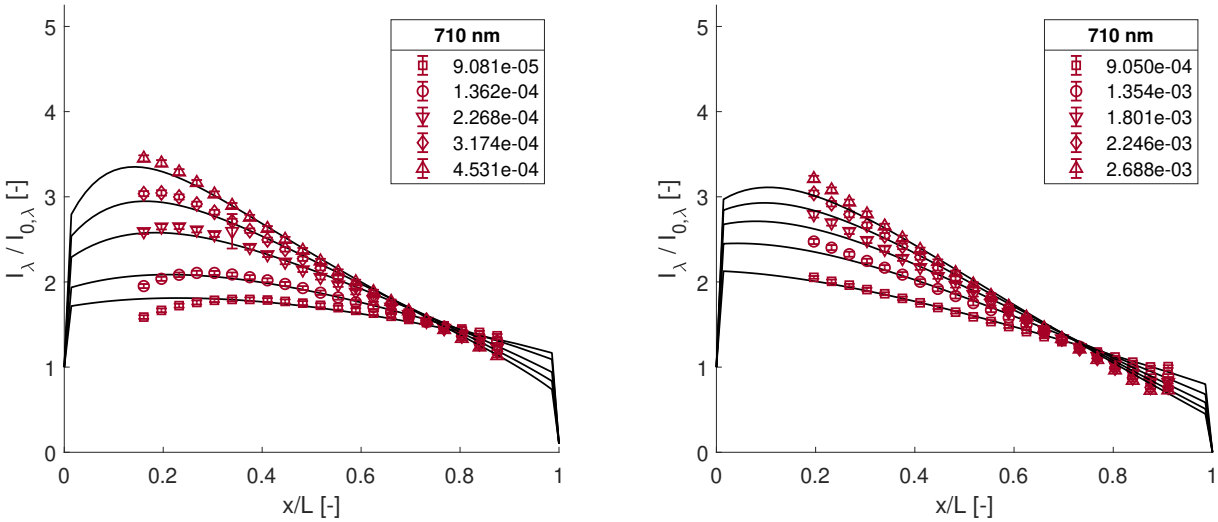

Figure B.7.: Comparison of simulated (lines) and measured (symbols) profiles of the light intensity at $\lambda = 710$ nm in polystyrene suspensions. Different symbols encode the particle volume fraction ϕ_v as denoted in the legend. Left: Suspension with particles of $d_1 = 555$ nm. Right: Suspension with particles of $d_2 = 95$ nm.

C. Estimation of shear stress on individual cells in turbulent flow

The following estimation of the shear stress acting on algae cells in isotropic turbulence follows the calculations of Chisti [299]. It is assumed that turbulence is isotropic, if the length scale l_K of the terminal microeddies on the Kolmogorov microscale is much smaller than the length scale of the largest eddies, which are in the order of the characteristic length of the considered apparatus, thus the pipe diameter D_0. Therefore, the condition $l_K/D_0 \ll 1$ is a requirement for isotropic turbulence. It is also assumed that the contribution of the viscous shear to the total shear stress on a cell is dominating so that the stress induced by turbulent mixing is the major cause of cell damage.

It is further assumed that the local shear rates can be approximated from the length and velocity scales of terminal microeddies, thus

$$\dot{\gamma} = \frac{u_K}{l_K} \tag{C.1}$$

The length scale l_K is related to the dissipation rate of the turbulent energy ϵ_k by

$$l_K = \left(\frac{\nu_l^3}{\epsilon_k}\right)^{1/4} \tag{C.2}$$

while the eddy velocity u_K is computed as $u_K = l_K/t_K$, where the time scale t_K is given by

$$t_K = \left(\frac{\nu_l}{\epsilon_k}\right)^{1/2} \tag{C.3}$$

The dissipation rate of the turbulent energy is related to the macroscopic, time-average properties of the flow by

$$\epsilon_k = \frac{u_0}{\rho_l}\frac{dp_l}{dx} \tag{C.4}$$

where the mean velocity of the flow u_0 in a certain pipe can be computed from the Reynolds number

$$u_0 = \frac{\nu_L Re}{D_0} \tag{C.5}$$

and the pressure gradient from the wall shear stress τ_w

$$\frac{dp_l}{dx} = \frac{4\tau_w}{D_0} \tag{C.6}$$

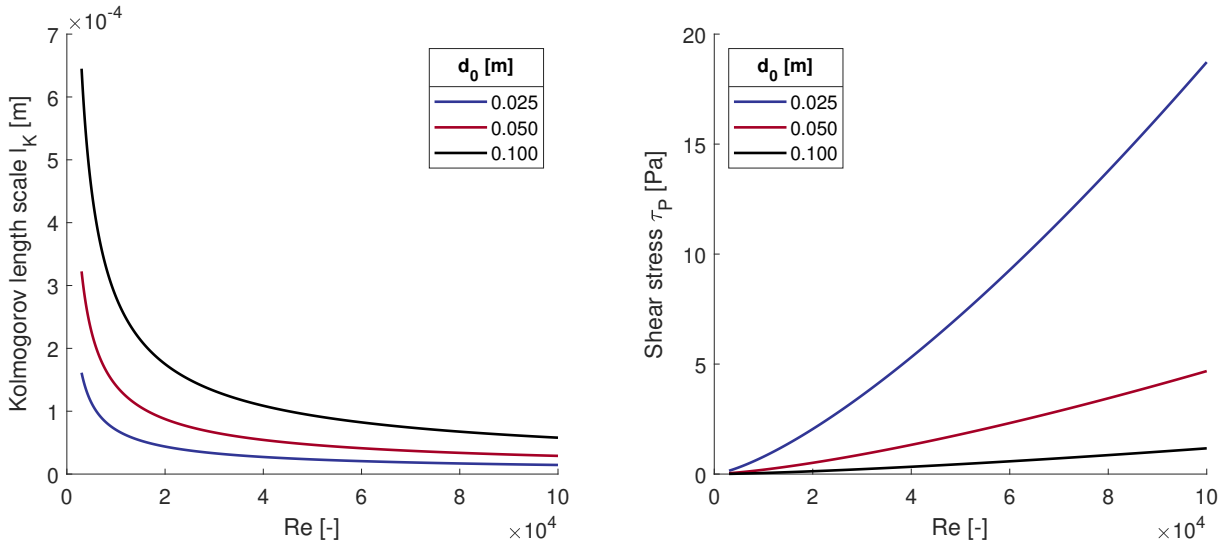

Figure C.1.: Impact of the Reynolds number Re on the Kolmogorov length scale (left) and the shear stress on microalgae cells caused by turbulent eddies (right).

which is related to u_0 by

$$\tau_w = \frac{1}{2} C_f \rho_l u_0^2 \tag{C.7}$$

where the Fanning friction factor is given by

$$C_f = 0.0792 Re^{-1/4}. \tag{C.8}$$

Since cell concentrations are restricted to a few gram per liter in photobioreactors, the physical properties of the culture broth are approximately similar to those of water. Typical pipe dimensions of tubular photobioreactors can be found in the single digit centimeter range. With these assumptions the local turbulent shear rate can be calculated by means of Eqs. (C.1)-(C.8). The shear stress on the cells can be obtained by

$$\tau_p = \dot{\gamma} \eta_l \tag{C.9}$$

where η_l is the dynamic viscosity of the fluid. Note that this deviation differs from the usual definition of turbulent shear stress, which models the diffusion of momentum in turbulent flows by means of a representative shear rate and the eddy viscosity [294]. In contrast, Eq. (C.9) estimates the viscous shear stress on particulate cell which results from the motion of the liquid phase [296].

Figure C.1 shows the computed Kolmogorov length scale and the shear stress with respect to the Reynolds number and the pipe diameter. The liquid properties were assumed with $\eta_l = 0.002$ Pas and $\rho_l = 1020$ kg m^{-3}.

D. Overview of included publications

1. McHardy, C., Horneber, T., Rauh, C. (2016). New lattice Boltzmann method for the simulation of three-dimensional radiation transfer in turbid media. Optics Express, 24 (15), 16999-17017, 2016. doi: 10.1364/OE.24.016999.
   The publication is included in this thesis as chapter 5: New lattice Boltzmann method for the simulation of three-dimensional radiation transfer in turbid media.

   Included version: Author Accepted Manuscript
   Reprinted with permission from ©The Optical Society.

2. McHardy, C., Horneber, T., Rauh, C. (2018). Spectral Simulation of Light Propagation in Participating Media by Using a Lattice Boltzmann Method for Photons. Appl. Math. Comput. 319(15), 59-70, 2018. doi: 10.1016/j.amc.2017.01.045.
   The publication is included in this thesis as chapter 6: Spectral Simulation of Light Propagation in Participating Media by Using a Lattice Boltzmann Method for Photons.

   Included version: Publisher's version
   Reprinted with permission from Elsevier.

3. McHardy, C., Luzi, G., Lindenberger, C., Agudo, J.R., Delgado, A., Rauh, C. (2018). Numerical Analysis of the Effects of Air on Light Distribution in a Bubble Column Photobioreactor. Algal Research, 31, 311-325, 2018. doi: 10.1016/j.algal.2018.02.016.
   The publication is included in this thesis as chapter 7: Numerical Analysis of the Effects of Air on Light Distribution in a Bubble Column Photobioreactor.

   Included version: Publisher's version
   Reprinted with permission from Elsevier.

4. Luzi, G., McHardy, C., Lindenberger, C., Rauh, C., Delgado, A. (2019). Comparison between different strategies for the realization of flashing-light effects - pneumatic mixing and flashing illumination. Algal Research, 101404, 2019. doi: 10.1016/j.algal.2018.1014040.
   The publication is included in this thesis as chapter 8: Comparison between different strategies for the realization of flashing-light effects - pneumatic mixing and flashing illumination.

   Included version: Publisher's version
   Reprinted with permission from Elsevier.